High-Resolution Observations of the Molecular Gas in Luminous Infrared Galaxies

Thesis by

Peter M. Bryant

In Partial Fulfillment of the Requirements

for the Degree of

Doctor of Philosophy

California Institute of Technology

Pasadena, California

1997

(Submitted September 16, 1996)

Acknowledgments

Whatever first inspired my interest in astronomy has faded into the mists of my childhood. All I know is that, from my earliest memory, I knew I wanted to study the universe. A doctorate in astronomy is thus truly a dream come true for me. Achieving this dream would have been impossible without the help, support, and encouragement of innumerable people over the years. It would be impossible to thank all these people if this brief space, but nonetheless I will make my best attempt.

First and foremost, thanks go to my parents, Eugenia and Arch Bryant, who not only put up with my crazy fascinations with all things beyond the Earth, but encouraged me to pursue them and spend a lifetime studying them. From reading me astronomy books as bedtime stories when I was a toddler, to staying outside under the night sky with me as I learned the constellations, to being forced to sleep in the back seat of the car in a deserted campground in downstate Illinois when I finally got my telescope out to a dark site, and much much more, they allowed my astronomical interests to flourish and laid the foundation for any success I may achieve.

Also from my childhood, I owe thanks to the staff of the Adler Planetarium of Chicago. They produced a wonderful resource that provided me with endless hours of fascination and stimulation; I never tired of the place. It is one of the things I miss most about my home town.

In the academic arena, Bob Rosner, at the University of Chicago, and Bruce Bills, then at the Lunar and Planetary Institute, were the first to allow me the opportunity

to learn about the pleasures and pains of scientific research, for which I am eternally grateful. At Caltech, I discovered radio astronomy in Shri Kulkarni's class on astronomical instrumentation, and it changed the course of my career.

Of course, no doctorate is possible without an advisor, and Nick Scoville has been near ideal in performing that role for me: pointing me towards studies of luminous infrared galaxies, starbursts, AGNs, and their ilk; providing innumerable insights and suggestions along the way; and still allowing me the freedom to pursue my own course.

Dave Sanders, with his encyclopedic knowledge of luminous infrared galaxies, gave me helpful advice early in my thesis while I was selecting which objects to concentrate on. This work was much improved due to those efforts. I am grateful to Dave, Joe Mazzarella, and their collaborators for providing me with their near-IR images prior to publication. I also thank Sterl Phinney for useful discussions.

Working amongst the entire millimeter group at Caltech has been a tremendous experience. Special thanks go to Anneila Sargent and John Carlstrom, both of whose great knowledge of and enthusiasm for astronomy can hardly help but rub off on those around them, and to Claire Chandler and Tony Phillips, who were very patient with my questions about reducing interferometric data back when most of it was still new to me. I am thankful to have had the opportunity to interact with the staff at the Owens Valley Radio Observatory during my frequent stays there. I am especially grateful to Tim Clark, Ray Finch, Curt Giovanine, Colin Hall, Ron Lawrence, Steve Padin, Steve Scott, and Dave Woody, who were always patient and generous with their time in helping me and answering my questions about the millimeter array. Thanks

also go to Rachel Akeson, Eugene DeGeus, Chris Fassnacht, Dave Koerner, Oliver Lay, Angela Putney, Kevin Rauch, Todd Small, Greg Taylor, Hien Tran, Gautam Vasisht, Min Yun, and many others for the help, advice, and companionship they have provided during my time in Robinson.

It has been wonderful to share my last year in Pasadena with Susanne Aalto Bergman, Per Bergman, and their four year old son Henrik. They have not only been great friends, but Susanne and Per have been great colleagues as well. Susanne has been an endless source of ideas and inspiration, as well as being very patient with me while explaining the physical interpretations of molecular line ratios and their importance. Any remaining misunderstandings I may have are certainly no fault of hers. I am glad they decided to come to Caltech for a short time.

I cannot imagine having kept my sanity during the course of writing my thesis without athletic activities, so I must also thank the many members of the intramural volleyball, softball, and soccer teams I have played with for providing many enjoyable and exhausting diversions from work. I am grateful for the Sierra Club and its wonderful outings program, which allowed me to meet many new and interesting people from all over the Los Angeles area who shared my enthusiasm for nature and hiking. Thanks also to Art Zirger for being an enthusiastic hiking partner for much of the last few years.

Of my dearest friend, Lauren Browning, not enough kind words can be said, so I shall not try. But without her, who knows what may have become of me.

Abstract

I have performed a high-resolution imaging survey of the molecular gas in seven luminous infrared galaxies using the Owens Valley millimeter array. This work has produced 2″-resolution maps of the CO 1→0 emission. Further high-resolution data has been obtained for subsets of these galaxies in CO 2→1, HCN 1→0, HCO^+ 1→0, and CS 1→0.

The CO maps reveal a systematic variation in the morphology of the molecular gas with the interaction state of the system. The three mergers with a single IR/radio nucleus show very bright and compact CO cores that peak at the stellar nucleus. The two mergers with double IR/radio nuclei also possess bright CO cores, but these peak roughly midway between the nuclei and show an extent nearly equal to the nuclear separation. In these objects, the gas cores of the individual merging galaxies appear to be coalescing while the stellar nuclei still remain distinct.

Based on dynamical arguments, the Galactic conversion factor from CO luminosity to molecular gas mass is overestimating the gas mass in Mrk 231 by at least a factor of 3.6 and in NGC 6240 by at least a factor of 1.5. Nonetheless, the molecular gas likely dominates the nuclear gravitational potential. The probable cause of the severe overestimate in Mrk 231 is the high brightness temperature of the CO 1→0 emission ($T_b > 34$ K).

Starbursts remain a viable explanation for the powerful output of luminous infrared galaxies. Upper limits to the free-free mm-wave continuum are used to con-

strain a starburst model from the literature, with the result that starbursts can reasonably explain all the systems studied here except perhaps Mrk 231. In several cases, though, they are required to be older than several 10^7 yr. Furthermore, the extreme mid-IR optical depths implied by the CO surface brightnesses confirm a prediction of the compact starburst model of Condon et al. (1991).

The trend of increasing $L_{\rm FIR}/L_{\rm CO}$ ratio with increasing CO surface brightness is confirmed. The high concentrations of molecular gas thus appear intimately related to the high luminosities of these systems.

The CO/HCN ratio varies by an order of magnitude even in this small sample of luminous mergers, suggesting that the gas properties are dramatically variable.

Table of Contents

List of Figures

List of Tables

Chapter 1

Introduction

Lurking at the hearts of large, colliding galaxy systems lie the most powerful energy generators in our neighborhood of the universe. Due to the thick shrouds of dust surrounding the cores of these galaxies, nearly all of this energy emerges at far-infrared wavelengths (40–400μm) that are completely absorbed by our planet's atmosphere. This significant population of luminous galaxies thus remained unnoticed until the 1970s and 1980s. Now in the 1990s, the mechanism responsible for these powerhouses is still a controversial subject. Is a burst of star formation extending over hundreds of parsecs at rates near to or higher than those in the most active OB star formation regions in our own Galaxy responsible for the incredible luminosities? Or are other phenomena necessary—such as the accretion onto a massive black hole which may power quasars and other AGN? This thesis indirectly attacks these questions,

among others, by studying the molecular gas—the fuel that apparently stokes the engines of the luminous infrared galaxies.

1.1. Luminous IR galaxies before IRAS

Early ground-based infrared observations at wavelengths of 1–25 μm suggested for the first time that a large fraction of the nuclei of bright spirals, plus virtually all Seyfert galaxies, contain very strong infrared emission that could dominate their bolometric luminosities (Rieke & Lebofsky 1978; Kleinmann & Low 1970; Rieke & Low 1972; Kleinmann & Wright 1974; Neugebauer et al. 1976; Dyck et al. 1978; Rieke & Lebofsky 1979). The 10 μm silicate absorption, seen in several nuclei, led to the notion that thermal emission from large columns of dust was the source of the infrared emission (e.g., Lebofsky & Rieke 1979). The blackbody dust temperatures were estimated to be 30–50 K based on observations from airplane-based telescopes that enabled the broad-band spectra of a number of bright galaxies to be traced out to wavelengths 300 μm (e.g., Telesco & Harper 1980; Harper & Low 1973).

Most of the first observed IR galaxies had luminosities of order 10^{10}–10^{11} $L_\odot$, (see Rieke & Lebofsky 1979 and references therein) and only a small number of the earliest objects were found to have IR luminosities over 10^{11} $L_\odot$ (e.g., Rieke & Low 1972)—for example, NGC 1068, NGC 1614, Arp 299, and Mrk 231. These infrared-luminous galaxies tended to contain active, emission-line nuclei, such as Seyferts. It was recognized, however, that, due to the empirical anti-correlation

of ultraviolet and infrared fluxes (Rieke 1978), the known sample of Seyfert galaxies was probably biased against strong infrared sources. An all-sky survey at far-infrared wavelengths was required to discover if a large population of infrared-bright, visually-faint galaxies existed. This was one of the motivations behind the Infrared Astronomy Satellite (IRAS) mission of 1983–1984 (Soifer, Houck, & Neugebauer 1987).

1.2. Luminous IR galaxies after IRAS

IRAS indeed resulted in the discovery of a population of galaxies with exceptional infrared luminosities of up to several times 10^{12} $L_\odot$—one to two orders of magnitude greater than their optical luminosities (Soifer et al. 1984ab; Aaronson & Olszewski 1984; Houck et al. 1985). The IRAS survey also revealed for the first time that these objects are a very significant population in our local universe: at luminosities over 10^{11} $L_\odot$, the space density of IR galaxies is comparable to or larger than those of other classes of luminous extragalactic objects, such as Seyferts (Soifer et al. 1986). Hereafter, those galaxies with $L_{\rm IR}(8\text{–}1000\mu{\rm m}) > 10^{11}$ $L_\odot$ are referred to as luminous IR galaxies or LIRGs.

1.2.1. Interactions and mergers of gas-rich galaxies

Galactic mergers appear to play a significant role in the production of high IR luminosities—the fraction of IR galaxies that have undergone strong tidal interactions, as revealed by their large-scale optical morphology, increases as the luminosity increases. At luminosities below 10^{11} $L_\odot$, only 18% of galaxies appear to be involved

in strong interactions; at luminosities above 10^{11} $L_\odot$, however, nearly half are strongly interacting (Lawrence et al. 1989); and at the highest luminosities—above 10^{12} $L_\odot$—more than two-thirds and perhaps over nine-tenths appear to be strongly interacting or merging (Leech et al. 1993; Sanders et al. 1988; Murphy et al. 1996).

LIRGs are, nearly universally, bright emitters of CO $J = 1 \rightarrow 0$. Using the empirical conversion factor from CO luminosity to molecular gas mass measured for Milky Way disk giant molecular clouds (GMCs), the implied molecular gas masses usually approach or exceed 10^{10} $M_\odot$ (e.g., Sanders, Scoville, & Soifer 1991). The first aperture synthesis observations of CO showed that these large amounts of molecular gas are often highly concentrated towards the cores (e.g., Scoville et al. 1991). Only a small number—for example VV 114 and Mrk 273 (Yun, Scoville & Knop 1994; Yun & Scoville 1995)—have shown CO distributions comparable in size to the stellar disks. The highest-resolution CO observations prior to this thesis revealed that Arp 220 and IC 694 contain bright cores of less than 400 pc radius, in which the estimated gas mass approaches the nuclear dynamical mass (Scoville et al. 1991; Sargent & Scoville 1991). The CO cores in many other LIRGs remained essentially unresolved at resolutions of 1–3 kpc (e.g., Scoville et al. 1989; Planesas, Mirabel, & Sanders 1991), suggesting that very compact, massive CO cores are common in LIRGs. Simulations of galactic mergers have produced similarly extreme nuclear concentrations of gas as a result mergers of equal-mass gas-rich galaxies (Noguchi 1988, 1991; Hernquist 1989; Barnes & Hernquist 1991).

1.2.2. The nature of the luminosity source

The large amounts of dust and gas in the cores of luminous IR galaxies extinguish much of the optical and near-IR radiation emerging from their nuclei, greatly complicating the study of the phenomena responsible for their intense activity. As a result, a controversy concerning the nature of the luminosity source has raged ever since IR-luminous galaxies were discovered. At least three mechanisms have been proposed to be the dominant energy source: a prodigious burst of star formation (e.g., Wright, Joseph, & Meikle 1984; Rieke et al. 1985; Joseph & Wright 1985; Condon et al. 1991, hereafter CHYT), a dust-enshrouded Seyfert or quasar-like AGN (e.g., Sanders et al. 1988; DePoy, Becklin, & Geballe 1986; Lonsdale, Smith & Lonsdale 1995), and the kinetic energy of colliding galaxies (Harwit et al. 1987). Furthermore, it has been argued that the interstellar radiation field from the old stellar population also contributes significantly to the IR luminosity of these objects (Thronson et al. 1990). Much of the work on LIRGs in the last decade has focused on the problem of which mechanism is dominant and how much does each contribute, yet no satisfactory conclusions have been reached.

1.2.2.1. Starbursts

There is plenty of observational evidence to suggest that star formation is occurring at exceptional rates in and around the nuclei of luminous IR galaxies. The nuclei of a large fraction show narrow-line optical spectra with line ratios reminiscent of Galactic H II regions (e.g., Joseph & Wright 1985); even those that show LINER or Seyfert nuclear spectra often exhibit substantial evidence for starburst activity in

the area immediately surrounding the nucleus (e.g., Veilleux et al. 1995; Boksenberg et al. 1977; Cutri et al. 1984; Wilson et al. 1986; Ashby, Houck, & Matthews 1995). Several near- and mid-IR spectral features also point to significant star formation: many LIRGs exhibit deep absorption in the 2.3 μm ro-vibrational absorption bands of CO, which are believed to arise in the photospheres of red supergiants (Rieke et al. 1985; Lester, Harvey, & Carr 1988; Ridgway, Wynn-Williams, & Becklin 1993); many also exhibit strong silicate absorption at 10 μm and a bright emission feature at 3.3 μm that are commonly observed in starburst galaxies and frequently absent in optically-selected Seyferts and quasars (Lebofsky & Rieke 1979; Roche et al. 1984; Rieke et al. 1985). Global ratios of IR luminosity to CO luminosity comparable to those in high-mass star formation cloud cores in the Milky Way—implying gas depletion timescales of $\lesssim 10^8$ yr—also suggest that powerful starburst activity is occurring in most LIRGs (Sanders et al. 1991). The strongest evidence suggesting that star formation is actually the dominant source of luminosity is that most LIRGs closely follow the tight correlation between far-IR and non-thermal radio fluxes seen for the disks of spiral galaxies (Sanders & Mirabel 1985; Helou, Soifer, & Rowan-Robinson 1985). Even those LIRGs that exhibit raw ratios of far-IR to radio flux too high to fit this correlation agree with it after their radio flux is corrected for the free-free absorption at frequencies above 1.4 GHz that likely plagues these very compact objects (CHYT). After correction for this effect, only 1 of the 40 LIRGs studied by CHYT does not follow the spiral galaxy far-IR/radio correlation, a result which suggests starburst-dominance in the vast majority of LIRGs.

1.2.2.2. AGNs

Despite the proliferation of evidence for powerful starbursts in LIRGs, Sanders et al. (1988) argue that the most luminous LIRGs—the "ultraluminous" objects, $L_{IR} > 10^{12}$ $L_{\odot}$—are dominantly powered by dust-enshrouded quasars. The best case for this is the one LIRG that CHYT found to disagree with the spiral far-IR/radio correlation: the Seyfert 1 galaxy Mrk 231, which, at $L_{IR} = 3.5 \times 10^{12}$ $L_{\odot}$ is the most luminous object in the local universe (Sanders et al. 1988). Not only is its radio emission, after correcting for free-free absorption, too strong for its far-IR emission relative to star-forming galaxies, but its radio source is variable on timescales of years (Condon, Frayer, & Broderick 1991), implying an extremely compact size of ~1 pc. Many other LIRGs also show evidence for the existence of dust-enshrouded AGNs, especially amongst the highest luminosity objects (Sanders et al. 1988), but also at more moderate luminosities. The most direct evidence is that a significant fraction of LIRGs show nuclear emission-line optical spectra that are classified as Seyfert 1, Seyfert 2, or LINERs (e.g., Veilleux et al. 1995). Some objects that show only relatively narrow emission lines at optical wavelengths reveal broad lines at near-IR wavelengths where the dust extinction is decreased (e.g., DePoy et al. 1986). Relatively flat cm-wave radio spectra have also been interpreted as evidence for the presence of AGNs (e.g., Gehrz, Sramek, & Weedman 1983), though CHYT argue that free-free absorption in very compact starbursts can also explain the flat cm-wave spectra. Many LIRGs show compact, cm-wave VLBI radio cores (Lonsdale, Smith, &

Lonsdale 1993). In fact, Lonsdale et al. (1995) claim that LIRGs follow the same relation between core radio power and bolometric luminosity as do radio-quiet quasars, albeit with large scatter. They argue that enshrouded AGNs may thus account for the bulk of the IR luminosity—especially if the far-IR/radio correlation is due to "fundamental properties of the dusty gas," rather than a common link to star formation. On the other hand, Rieke (1988) argues that the weakness of hard X-ray emission from LIRGs implies that AGNs are not energetically significant; however, subsequent high-resolution observations of the molecular gas in Arp 220, IC 694, and the bulk of the objects presented in this thesis have revealed that the gas column densities in front of the nucleus are so great as to extinguish even hard X-rays. So it remains uncertain if the AGNs produce more energy than the nuclear starbursts that are often simultaneously observed. It is also possible that the AGNs and nuclear starbursts are intimately related via a process that is not understood.

1.2.2.3. Other possibilities

Two other mechanisms have also been proposed to power at least some LIRGs: the kinetic energy of colliding galaxies (Harwit et al. 1987) and the interstellar radiation field from the old stellar population (Thronson et al. 1990). The former hypothesis was designed to explain the commonly observed LINER optical spectra and the powerful near-IR H_2 lines seen in some LIRGs such as NGC 6240. CHYT point out, however, that this mechanism requires a special collision geometry (face-on) that implies an luminosity source extended over several kpc, contrary to the compact sources (< 1 kpc) seen in most LIRGs. Also, the observed space density of LIRGs is difficult

to explain with the short timescales for the high-luminosity phase in this scenario (few 10^6 yr). Thronson et al. (1990) argue that the old stellar population from two merging galaxies provides a substantial portion of the luminosity in the $L_{IR} = 6.6 \times 10^{11}$ $L_\odot$ object NGC 6240. Again, however, the compact nature of the radio and mid-IR emission argues against this mechanism playing a significant role in the majority of LIRGs, especially when combined with the abundant and prominent evidence for the more exotic phenomena described above.

1.3. The importance of studying the molecular gas

Whatever the nature of the luminosity source of LIRGs, the dense concentrations of molecular gas in their cores likely serve as the fuel. It is therefore important to learn more about the spatial distribution, kinematics, and properties of the molecular gas in order to better understand the phenomena that are occurring at the cores of these mysterious objects. In particular, parameters of starburst models can be constrained, revealing whether or not it is possible for star formation to be the dominant luminosity source. Furthermore, CO emission of such extreme surface brightness is not seen in any other known objects; LIRGs thus provide a laboratory for studying the behavior of the molecular gas in extreme environments not found anywhere else.

Two crucial parameters for constraining starburst models are the total nuclear mass and the nuclear molecular gas mass. The difference between the two is the maximum mass allowable in the form of already-formed stars. This number, together with the IR luminosity, constrains the age and initial mass function of the starburst

(e.g., Scoville & Soifer 1991). The gas mass constrains the future evolution of the starburst.

The total nuclear mass can be measured dynamically with maps of any spectral line that probes the entire nuclear region. Due to the large extinction at optical and near-IR wavelengths, radio and mm-wave spectral lines—in particular CO $J = 1 \rightarrow 0$, the brightest non-maser tracer of molecular gas—are the most easily observed lines that can do this. A major uncertainty in the observational estimate of the dynamical mass arises if the gas is aspherically-distributed, so that inclination effects can cause the observed line width to be smaller than the actual range of velocities. If the gas distribution can be spatially resolved, however, its geometry can be modeled and the inclination uncertainties minimized.

The nuclear molecular gas mass is significantly harder to reliably estimate. As an initial guess, many authors have used the empirical conversion factor from CO luminosity to molecular gas mass as measured for Milky Way GMCs. It has long been understood, however, that this conversion factor may not apply to molecular gas where the cloud densities or CO brightness temperatures are substantially different than for local GMCs or where clouds are not self-gravitating (e.g., Dickman, Snell, & Schloerb 1986). The molecular gas cores in LIRGS are almost certainly much hotter and denser and at higher pressure than GMCs in the Milky Way disk. Also, due to the powerful activity, the interstellar ultraviolet radiation field is much more intense. Without observational demonstration, there is no compelling reason to expect the same gas mass conversion factor to be appropriate in such an extreme environment.

Previous observational estimates of the gas mass conversion factor in LIRGs have produced ambiguous results. Radford, Solomon, & Downes (1991) use single dish observations of the CO 2→1/CO 1→0 ratio in four LIRGs (IC 883, Arp 220, Mrk 231, and VII Zw 31) to argue that the conversion factor is within a factor of a few of the Galactic value. On the other hand, Shier, Rieke, & Rieke (1994) estimate dynamical masses in two LIRGs (NGC 1614 and IC 694) using the dispersion of the stellar $\lambda 2.3\mu$m CO absorption bands and claim that the conversion factor is 4–10 times smaller than the Galactic value. In fact, neither of these studies is definitive. Aperture synthesis observations of Mrk 231 reported here (Chapter 2) reveal that the brightness temperature of the CO is at least 34 K and likely much higher, contradicting the inference of Radford et al. that T_b is only $\sim$10 K and raising the possibility that the Galactic conversion factor overestimates the gas mass. The claim of Shier et al. is also highly doubtful, because they assume isotropic velocity distributions and relatively little internal extinction at near-IR wavelengths in LIRGs; in fact, as I argue in Chapter 3, the mean extinctions through the nuclei of LIRGs are likely to be several magnitudes or more, and it is therefore unlikely that near-IR tracers reveal the full range of velocities.

By resolving the gas distributions and probing through the entire nucleus, aperture synthesis observations of the molecular gas in LIRGs can provide improved estimates of the total nuclear mass and the nuclear molecular gas mass—two of the most crucial parameters for understanding if starbursts provide the energy that powers

the LIRGs. Knowledge of the properties of the starbursts in LIRGs will also contribute understanding to the broader problems related to starbursts—in particular, the formation and evolution of galaxies.

1.4. Thesis overview

With this motivation, I undertook an observational study of the spatial distribution, kinematics, and properties of the molecular gas in luminous IR galaxies for my Ph. D. thesis. The best and brightest tracer of the entire molecular gas content is the 115 GHz CO $J = 1 \rightarrow 0$ transition. Prior to this work, due to the relatively large distance of all but the very nearest LIRGs, only a handful had been mapped in CO 1→0 with the resolution necessary to resolve the compact molecular gas distributions (2–4″, or 1–2 kpc at 100 Mpc; see Scoville et al. 1991). Furthermore, only a single LIRG, Arp 220, had been mapped at such high-resolution in a tracer of high-density molecular gas—HCN 1→0 in this case (Radford et al. 1991), and none had been mapped at this resolution in higher rotational transitions such as CO 2→1. The brightness of high-density tracers relative to CO provide qualitative estimates of the mean density of the molecular gas, while observations of higher rotational transitions help to constrain the excitation of the gas in addition to providing superior resolution. When I began my thesis, these observations were becoming more feasible due to the rapid improvements in the sensitivity and the number of baselines of the Owens Valley millimeter array. Thus I have incorporated such observations into this work, in addition to the high

signal-to-noise, high-resolution CO 1→0 observations that provide the fundamental starting point for studies of molecular gas.

The bulk of this thesis constitutes papers I have written for publication in peer-reviewed journals. Chapter 2, previously published in a similar version as Bryant & Scoville (1996a), contains the description and analysis of high-resolution aperture synthesis CO 1→0 and CO 2→1 maps of the Seyfert 1 merger remnant Mrk 231—the most luminous galaxy in the local universe and the LIRG that is most likely to be energetically-dominated by an AGN. The emphasis of the conclusions has been altered slightly from the published version to improve the fit of Chapter 2 within the broader context of this thesis. Chapter 3, to be published as Bryant & Scoville (1996b), contains the results of a high-resolution aperture synthesis survey of 7 LIRGs ranging in luminosity from 3.2×10^{11} to 3.5×10^{12} $L_{\odot}$, five of which are mergers and two of which are members of interacting pairs of galaxies. This survey more than doubles the number of LIRGs for which high-resolution ($\sim 2''$) CO spectral line maps have been published and reveals further exceptionally-massive and compact gas cores. Chapter 4, to be published as Bryant & Scoville (1996c), describes the results of an aperture synthesis survey of the high-density tracer emission in six of the systems studied in the Chapter 3. The HCN 1→0 line was imaged in 6 objects, HCO^+ 1→0 in 3, and CS 1→0 in one. Measurements of the 3 mm radio continuum are also presented here, and the extra constraints they place on starburst models are discussed. In conclusion, Chapter 5 summarizes the results of

the thesis and presents possibilities for future work. The Appendix, originally published as an appendix to Bryant & Scoville (1996a), describes a detailed theoretical analysis of the behavior of the conversion factor from CO luminosity to molecular gas mass; the variation of the conversion factor relative to the empirical value is studied in several different gas configurations and in different physical environments.

References

Aaronson, M. & Olszewski, E. W. 1984, Nature, 309, 414

Ashby, M. L. N., Houck, J. R., & Matthews, K. 1995, ApJ, 447, 545

Barnes, J. E. & Hernquist, L. E. 1991, ApJ, 370, L65

Boksenberg, A., Carswell, R. F., Allen, D. A., Fosbury, R. A. E., Penston, M. V., & Sargent, W. L. W. 1977, MNRAS, 178, 451

Bryant, P. M. & Scoville, N. Z. 1996a, ApJ, 457, 678

Bryant, P. M. & Scoville, N. Z. 1996b, ApJ, submitted

Bryant, P. M. & Scoville, N. Z. 1996c, ApJ, submitted

Condon, J. J., Frayer, D. T., & Broderick, J. J. 1991, AJ, 101, 362

Condon, J. J., Huang, Z. P., Yin, Q. F., & Thuan, T. X. 1991, ApJ, 378, 65 (CHYT)

Cutri, R. M., Rudy, R. J., Rieke, G. H., Tokunaga, A. T., & Willner, S. P. 1984, ApJ, 280, 521

DePoy, D. L., Becklin, E. E., & Geballe, T. R. 1986, ApJ, 316, L63

Dickman, R. L., Snell, R. L., Schloerb, F. P. 1986, ApJ, 309, 326

Dyck, H. M., Becklin, E. E., & Capps, R. W. 1978, BAAS, 10, 422

Gehrz, R. D., Sramek, R. A., & Weedman, D. W. 1983, ApJ, 267, 551

Harper, D. A. & Low, F. J. 1973, ApJ, 182, L89

Harwit, M., Houck, J. R., Soifer, B. T., & Palumbo, G. C. C. 1987, ApJ, 315, 28

Helou, G., Soifer, B. T., & Rowan-Robinson, M. 1985, ApJ, 298, L7

Hernquist, L. 1989, Nature, 340, 687

Houck, J. R., Schneider, D. P., Danielson, G. E., Beichman, C. A., Lonsdale, C. J., Neugebauer, G., & Soifer, B. T. 1985, ApJ, 290, L5

Joseph, R. D. & Wright, G. S. 1985, MNRAS, 214, 87

Kleinmann, D. E. & Low, F. J. 1970, ApJ, 161, L203

Kleinmann, D. E. & Wright, E. L. 1974, ApJ, 191, L19

Lawrence, A., Rowan-Robinson, M., Leech, K., Jones, D. H. P., & Wall, J. V. 1989, MNRAS, 240, 329

Lebofsky, M. J. & Rieke, G. H. 1979, ApJ, 229, 111

Leech, K. J., Rowan-Robinson, M., Lawrence, A., & Hughes, J. D. 1993, MNRAS, 267, 253

Lester, D. F., Harvey, P. M., & Carr, J. 1988, ApJ, 329, 641

Lonsdale, C. J., Smith, H. E., & Lonsdale, C. J. 1993, ApJ, 405, L9

Lonsdale, C. J., Smith, H. E., & Lonsdale, C. J. 1995, ApJ, 438, 632

Murphy, T. W. et al. 1996, AJ, 111, 1025

Neugebauer, G., Becklin, E. E., Oke, J. B., & Searle, L. 1976, ApJ, 205, 29

Noguchi, M. 1988, A&A, 203, 259

Noguchi, M. 1991, MNRAS, 251, 360

Planesas, P., Mirabel, I. F., & Sanders, D. B. 1991, ApJ, 370, 172

Radford, S. J. E. et al. 1991, in Dynamics of Galaxies and Their Molecular Cloud Distributions, ed. F. Combes & F. Casoli (Dordrecht: Kluwer) p. 303

Radford, S. J. E., Solomon, P. M., & Downes, D. 1991, ApJ, 368, L15

Ridgway, S. E., Wynn-Williams, C. G., & Becklin, E. E. 1994, ApJ, 428, 609

Rieke, G. H. 1978, ApJ, 226, 550

Rieke, G. H. 1988, ApJ, 331, L5

Rieke, G. H., Cutri, R. M., Black, J. H., Kailey, W. F., McAlary, C. W., Lebofsky, M. J., & Elston, R. 1985, ApJ, 290, 116

Rieke, G. H. & Lebofsky, M. J. 1978, ApJ, 220, L37

Rieke, G. H. & Lebofsky, M. J. 1979, ARA&A, 17, 477

Rieke, G. H. & Low, F. J. 1972, ApJ, 176, L95

Roche, P. F., Aitken, D. K., Phillips, M. M., & Whitmore, B. 1984, MNRAS, 207, 35

Sanders, D. B. & Mirabel, I. F. 1985, ApJ, 298, L31

Sanders, D. B., Scoville, N. Z., & Soifer, B. T. 1991, ApJ, 370, 158

Sanders, D. B., Soifer, B. T., Elias, J. H., Madore, B. F., Matthews, K., Neugebauer, G., & Scoville, N. Z. 1988, ApJ, 325, 74

Sargent, A. I. & Scoville, N. Z. 1991, ApJ, 366, L1

Scoville, N. Z., Sanders, D. B., Sargent, A. I., Soifer, B. T., & Tinney, C. G. 1989, ApJ, 345, L25

Scoville, N. Z., Sargent, A. I., Sanders, D. B., & Soifer, B. T. 1991, ApJ, 366, L5

Scoville, N. Z. & Soifer, B. T. 1991, in Massive Stars in Starbursts, eds. C. Leitherer, N. R. Walborn, T. M. Heckman, & C. A. Norman (Cambridge: Cambridge Univ. Press) p. 233

Shier, L. M., Rieke, M. J., & Rieke, G. H. 1994, ApJ, 433, L9

Soifer, B. T. et al. 1984a, ApJ, 278, L71

Soifer, B. T. et al. 1984b, ApJ, 283, L1

Soifer, B. T., Houck, J. R., & Neugebauer, G. 1987, ARA&A, 25, 187

Soifer, B. T., Sanders, D. B., Neugebauer, G., Danielson, G. E., Lonsdale, C. J., Madore, B. F., & Persson, S. E. 1986, ApJ, 303, L41

Telesco, C. M. & Harper, D. A. 1980, ApJ, 235, 392

Thronson, H. A., Majewski, S., Descartes, L., & Hereld, M. 1990, ApJ, 364, 456

Veilleux, S., Kim, D. C., Sanders, D. B., Mazzarella, J. M., & Soifer, B. T. 1995, ApJS, 98, 171

Wilson, A. S., Baldwin, J. A., Sun, S. D., & Wright, A. E. 1986, ApJ, 310, 121

Wright, G. S., Joseph, R. D., & Meikle, W. P. S. 1984, Nature, 309, 430

Yun, M. S. & Scoville, N. Z. 1995, ApJ, 451, L45

Yun, M. S., Scoville, N. Z., & Knop, R. A. 1994, ApJ, 430, L109

Chapter 2

The Molecular Core of Markarian 231

2.1. Introduction

Luminous infrared galaxies constitute a significant population in the local universe (Soifer et al. 1986), yet the source of their luminosity remains uncertain: nuclear starbursts (Rieke et al. 1985), dust-enshrouded quasars (Sanders et al. 1988), and the kinetic energy of colliding galaxies (Harwit et al. 1987) have all been proposed. A possible clue to the nature of the luminosity source is that galactic interactions (Sanders et al. 1988; Lawrence et al. 1989) and powerful, yet highly-compact CO emission (e.g., Scoville et al. 1991) appear to be intimately associated with the high infrared luminosities. According to numerical simulations, a strong interaction between two galaxies, at least one of which is gas-rich, can cause the rapid accumulation of large amounts of molecular gas in the nuclear regions (Barnes & Hernquist 1991).

This massive gas concentration can then serve as the fuel for a powerful starburst, a central AGN, or both. High resolution observations of the spatial distribution and kinematics of the molecular gas in these systems yield critical constraints on the central concentration of the molecular gas, its physical conditions, and the dynamical mass of the nuclear region. These constraints can then provide understanding of the nature of the luminosity source and the evolutionary status of these systems.

The CO $J = 1 \rightarrow 0$ transition is the most easily observed tracer of the total molecular gas content in galaxies, yet only a few luminous infrared galaxies have been observed in this transition with the angular resolution necessary ($\sim 2''$) to resolve the kiloparsec-size central concentrations of molecular gas (e.g., Scoville et al. 1991 and references therein). We have therefore undertaken a high-resolution imaging survey of a sample of luminous IR galaxies in the CO 1→0 transition. With followup observations in the CO $J = 2 \rightarrow 1$ transition we can achieve a resolution of approximately $1''$. This paper presents the first results of this project—on the ultraluminous galaxy Mrk 231.

Mrk 231 (UGC 8058) is an unusual object, even amongst the population of luminous IR galaxies. At a distance of 174 Mpc (using $H_0 = 75$ km s^{-1} Mpc^{-1} and the Virgocentric flow model of Aaronson et al. 1982), Mrk 231 is the most luminous object in the local universe, with an infrared luminosity, $L_{\rm IR}$(8–1000 μm), of 3.5×10^{12} L$_\odot$ (see Sanders et al. 1988). From its optical morphology, the galaxy appears to be the product of a recent merger—it is an asymmetrical object with two linear, low surface brightness features that may be tidal tails (Hutchings & Neff 1987; Sanders

et al. 1987; Hamilton & Keel 1987). The optical spectrum of the Seyfert 1 nucleus of Mrk 231 shows further peculiarities, including highly reddened continuum and line emission ($A_V \approx 2$, Boksenberg et al. 1977), strong Fe II emission, very little narrow line emission, and several systems of low ionization absorption lines at blueshifts up to 8240 km s^{-1} relative to the systemic velocity (Adams & Weedman 1972; Boksenberg et al. 1977; Rudy, Foltz, & Stocke 1985; Boroson et al. 1991). One of these absorption line systems is variable on a time scale of a few years (Boroson et al. 1991; Kollatschny et al. 1992). Also, the X-ray (0.1–4.5 keV) to bolometric luminosity ratio of Mrk 231 is two orders of magnitude lower than other broad line galaxies (Eales & Arnaud 1988). Finally, several observations directly suggest that Mrk 231 contains large amounts of gas and dust in the vicinity of its nucleus: it possesses a very broad neutral hydrogen line, entirely in absorption, with a full width at zero intensity of 240 km s^{-1} (Heckman, Balick, & Sullivan 1978), a strong 10 μm silicate absorption feature (Roche, Aitken, & Whitmore 1983), and a bright, previously unresolved CO emission region immediately surrounding the nucleus (Scoville et al. 1989).

2.2. Observations

Our observations were carried out at the Owens Valley millimeter array at Big Pine, California, between 1993 April 28 and 1993 May 14 in the CO 1→0 transition, and on 1995 January 2 in the CO 2→1 transition. During the earlier period, the array consisted of four 10.4m telescopes; on the latter date, five telescopes (of the six telescope array) were in operation. Table 2–1 lists details of the observations. For

Table 2–1. Observational parameters for Mrk 231

Pointing center (B1950.0)	RA $12^h\,54^m\,05^s.01$, Dec $57°\,08'\,38''.1$		
Center of passband	$cz = 12660$ km s^{-1}		
Bandwidth of spectrometer	464 MHz		
Resolution	4 MHz		
Dates of tracks	28 Apr 1993	CO 1→0	4 telescopes
	06 May 1993	CO 1→0	4
	14 May 1993	CO 1→0	4
	02 Jan 1995	CO 2→1	5

CO 1→0, good spatial frequency (uv) coverage was achieved by tracking Mrk 231 for several hours on both sides of transit using two configurations of the array, while for CO 2→1, a single configuration was used. Data were obtained simultaneously with a digital spectrometer and an analog continuum correlator (500 MHz bandwidth in 1993; upgraded to 1000 MHz bandwidth by 1995). The digital correlator consists of four independent modules (Padin et al. 1993). For our observations, the modules were set up to cover adjacent, partially-overlapping, portions of the IF, covering a bandwidth of 464 MHz with 116 clean frequency channels. A single field (HPBW = 63″ at 110.6 GHz) was observed, centered at the position of the peak centimeter-wave emission (Condon et al. 1990), and the phase calibrator (1150+497) was observed every thirty minutes.

Initial phase, passband, and flux calibration of the data was done using Owens Valley millimeter array software (Scoville et al. 1993). The instrumental passband was derived from spectra of the bright quasars 3C 273, 3C 454.3, and 3C 279. The absolute flux scale was determined from integrations on Uranus and Neptune, after correcting the planet fluxes for resolution effects. We estimate the accuracy of the flux calibration

to be 10% at 110 GHz and 15% at 220 GHz. For CO 1→0 only, we performed self-calibration of the antenna phases on the line-center emission using the CIT DIFMAP software package (Shepherd, Pearson, & Taylor 1994); a 30-minute averaging time was used to achieve sufficient signal-to-noise ratio for each gain solution. Following calibration, we subtracted the continuum emission from the *uv* data with the task 'UVLIN' from the NRAO AIPS software package, using the average of two regions of line-free emission (120 MHz for CO 1→0 and 80 MHz for CO 2→1) on either end of the spectrometer bandwidth. We extracted continuum *uv* data near 111 GHz from the entire spectrometer bandwidth in the opposite sideband to the CO 1→0 emission and from the line-free portion of the spectrometer in the same sideband. We extracted continuum data near 222 GHz from the analog correlator data in the opposite sideband to the CO 2→1 and from the line-free spectrometer channels in the same sideband. After Fourier transforming the line and continuum *uv* data, channel maps were deconvolved using the CLEAN algorithm, as implemented in the AIPS task 'MX.'

2.3. Results

2.3.1. CO line emission

Maps of the integrated CO emission and the intensity-weighted mean velocities in Mrk 231 are presented in Figure 2–1 for CO 1→0 and Figure 2–2 for CO 2→1. Quantitative properties derived from the CO maps are summarized in Table 2–2. The CO 1→0 emission is only barely resolved by the $2''.5 \times 2''.0$ beam, and the deconvolved source

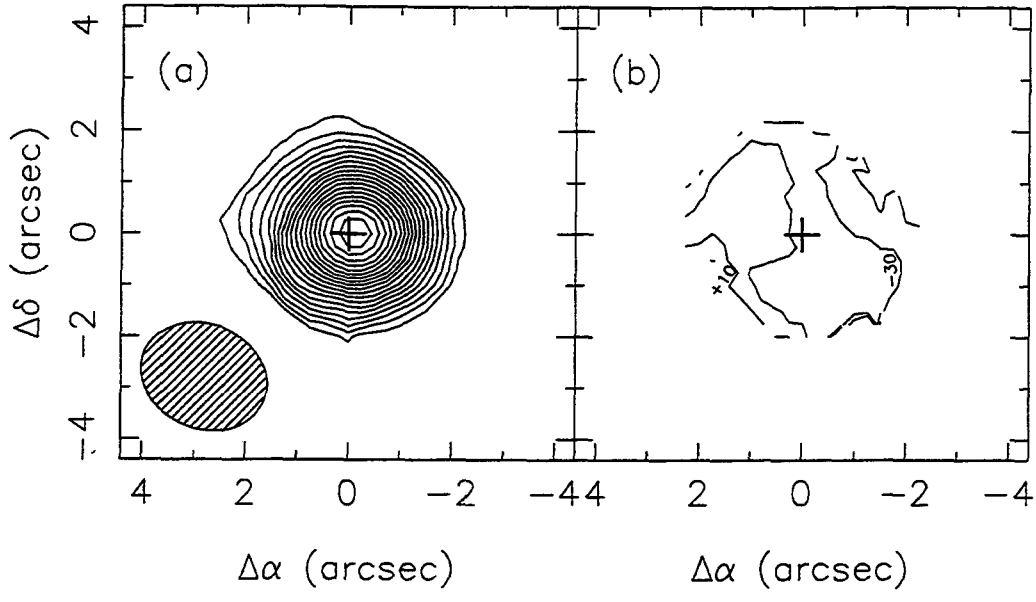

Figure 2–1. Aperture synthesis maps (uniform weighting) of CO 1→0 emission from the nucleus of Mrk 231. The reference point for the right ascension and declination axes is $12^h\,54^m\,05^s.01$, $+57°\,08'\,38''.1$ (B1950.0), representing the position of the peak of the 1.49 GHz continuum flux ("+"; Condon et al. 1990). The hatched ellipse at lower left represents the half-power beam size. (a) Velocity-integrated emission; contours are uniformly spaced at 2.12 Jy beam^{-1} km s^{-1} intervals, starting at 4.24 Jy beam^{-1} km s^{-1}. (b) Mean velocities (intensity-weighted); contours are uniformly spaced at 20 km s^{-1} intervals and are labeled relative to $cz = 12660$ km s^{-1}. To produce these maps, we smoothed the data cubes to eight times the inherent velocity resolution (from 5.4 to 43.4 km s^{-1}) and blanked pixels below 2σ (28 mJy).

size is required to be under $1''.5$. The velocity map indicates a significant east-west velocity gradient, however, and the CO 2→1 map, at much higher resolution, confirms this structure. In CO 2→1, the source is well resolved in the east-west direction by the $0''.8$ beam, showing a deconvolved size of $1''.0 \pm 0''.1$. At the adopted distance, this size corresponds to a radius $R = 420$ pc. The source is still only marginally resolved along its minor axis, showing a deconvolved size of $0''.3 \pm 0''.2$. The velocity gradient is much stronger in the CO 2→1 map, and it is closely aligned with the major axis of the CO emission distribution. The CO velocity gradient also matches

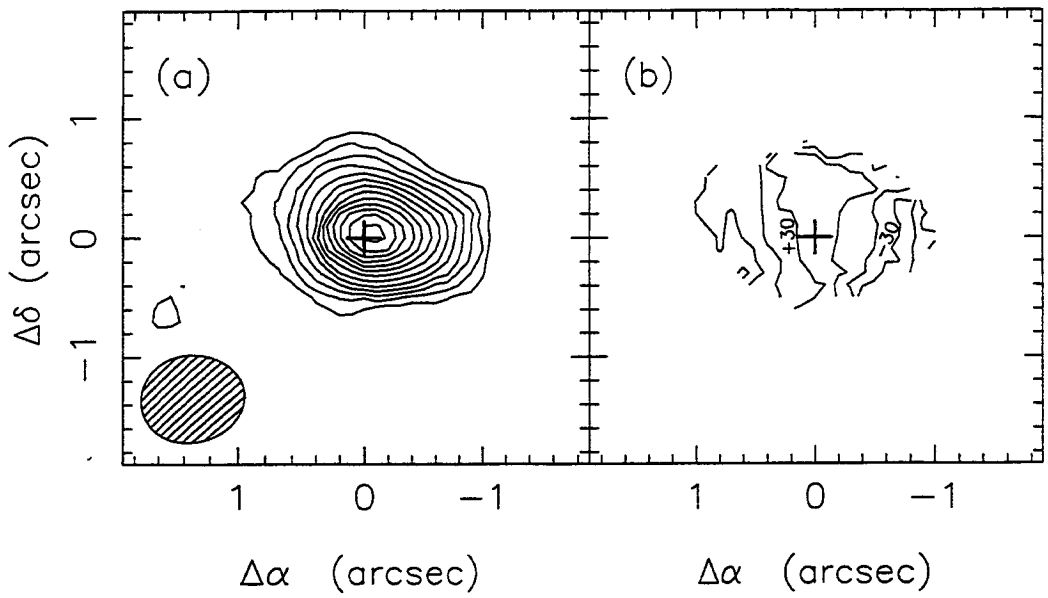

Figure 2–2. Same as Figure 1, but for CO 2→1. (a) Velocity-integrated emission; contours are uniformly spaced at 4.23 Jy beam^{-1} km s^{-1} intervals, starting at 8.46 Jy beam^{-1} km s^{-1}. (b) Mean velocities (intensity-weighted); contours are uniformly spaced at 20 km s^{-1} intervals and are labeled relative to $cz = 12660$ km s^{-1}. To produce these maps, we smoothed the data cubes to eight times the inherent velocity resolution (from 5.4 to 43.4 km s^{-1}) and blanked pixels below 2σ (66 mJy).

the direction and slope of that seen optically in the extended narrow line gas (Keel & Hamilton 1995).

Spectra measured in an aperture containing the entire emission are depicted in Figure 2–3. Both lines are consistent with having Gaussian profiles with a full width at half maximum $\Delta v = 186$ km s^{-1}; however, the CO 2→1 line is redshifted by 22 ± 6 km s^{-1} relative to CO 1→0.

The integrated CO 1→0 flux detected by the millimeter array is 62 Jy km s^{-1}, corresponding to a CO 1→0 luminosity $L'_{\rm CO} = 5.0 \times 10^9$ K km s^{-1} pc^2; the integrated CO 2→1 flux detected is 180 Jy km s^{-1}. Both of these numbers are about 65% of the fluxes detected by single-dish telescopes (Radford, Solomon, & Downes 1991; Aalto-Bergman 1995). While the existence of extended CO emission cannot be ruled out,

Table 2–2. Mrk 231 CO line emission parameters[a]

	CO 1→0	CO 2→1
Synthesized beam	2″.5 × 2″.0, PA 64°	0″.80 × 0″.73, PA 109°
Gaussian fit to source	2″.7 × 2″.2, PA 105°	1″.2 × 0″.8, PA 73°
Source size (deconv.)	< 1″.5	1″.0 × 0″.3, PA 69°
$\bar{v}$ (cz)	12645 (4) km s^{-1}	12667 (4) km s^{-1}
$\Delta v_{\rm FWHM}$	186 (9) km s^{-1}	189 (10) km s^{-1}
$I_{\rm CO}$	62 Jy km s^{-1}	180 Jy km s^{-1}
$T_{\rm b,peak}$	4.7 K	14 K

[a] Numbers in parentheses are formal uncertainties from Gaussian fits to the line profiles.

given the combined uncertainties in the single dish and interferometer flux scales of around 20%, it is not required.

The peak beam-diluted brightness temperature of the CO 1→0 line is 4.7 K above the background, while that of the CO 2→1 line is 14 K. If we assume that the lower-J transition arises from the same regions as the higher-J transition so that the area of the (unresolved) 1→0 source is the same as the measured area of the 2→1 source, then the intrinsic brightness temperatures are $T_{\rm b,1\rightarrow0} \approx 83$ K and $T_{\rm b,2\rightarrow1} \approx 33$ K. These numbers are highly uncertain, however, since one dimension of the CO 2→1 source is nearly unresolved. If instead we utilize the 3σ upper limit to the deconvolved area of the CO 2→1 source (1″.20 × 0″.66), we can place confident limits: $T_{\rm b,1\rightarrow0} > 34$ K and $T_{\rm b,2\rightarrow1} > 19$ K. If the CO 1→0 source is larger than the CO 2→1 source, then the lower limit to $T_{\rm b,1\rightarrow0}$ is somewhat smaller than the value quoted above.

We have not detected CO emission in either transition at the position of the "secondary nucleus"—roughly 3″.5 south of the Seyfert nucleus (Armus et al. 1994). The possibility still exists that this region shows CO emission outside our bandpass (cz = 12030–13290 km s^{-1}), because one of the two optical narrow line components

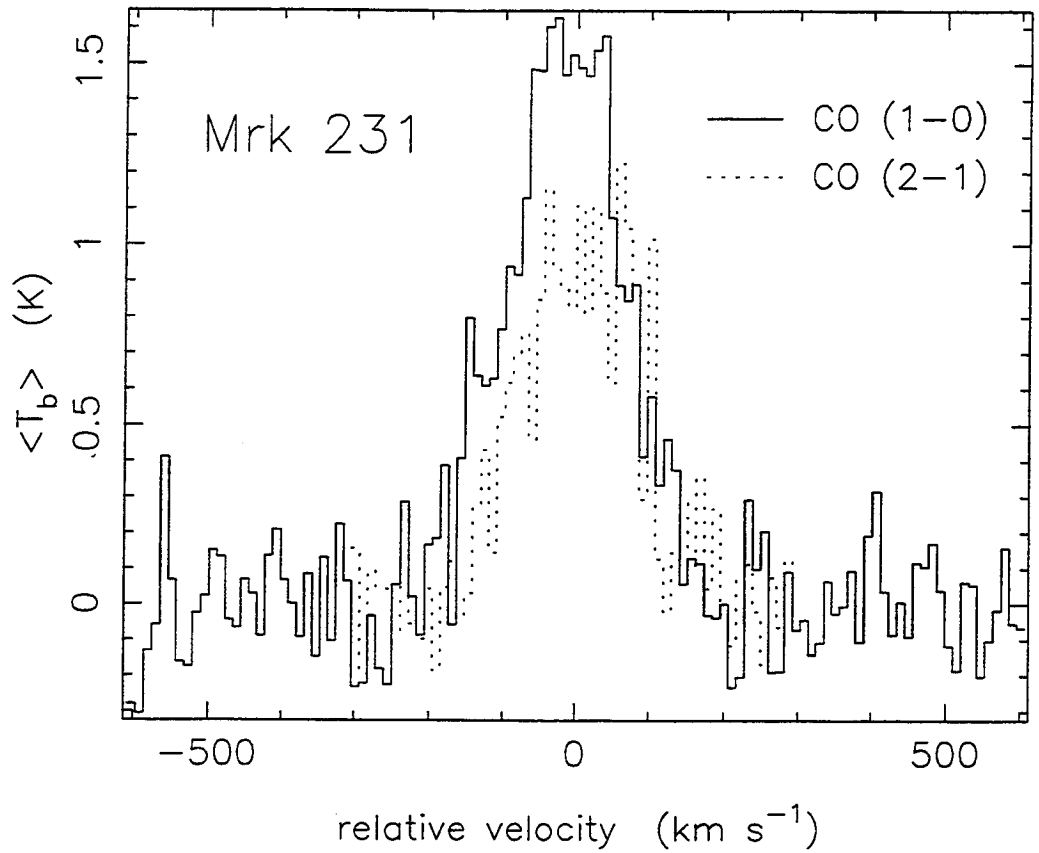

Figure 2–3. Average spectra of the CO 1→0 and CO 2→1 lines from the nucleus of Mrk 231. We calculated velocities according to $v = (\nu_0 - \nu)/\nu_0$, where $\nu_0 = \nu_{\rm rest}/(1+z_0)$, and $cz_0 = 12660$ km s^{-1}. In order to compare the line profiles of the two lines, we convolved the natural-weighted CO 2→1 map to the same resolution as the natural-weighted CO 1→0 map (HPBW 3″.0 × 2″.4), and then extracted the spectra of each line using the same aperture—a rectangle 4″.4 long in the east-west direction and 4″.0 long in the north-south direction, centered on the phase center.

at this position shows a velocity of 12160 ± 200 km s^{-1}(Hamilton & Keel 1987). If CO 1→0 emission is present is our bandpass at this position, it must have a peak (beam diluted) surface brightness less than 0.39 K (2σ) averaged over 8 MHz (21.6 km s^{-1}) channels.

2.3.2. Continuum emission

We measured the continuum emission in the unresolved core of Mrk 231 to be 49 mJy at an effective frequency of 109.0 GHz by averaging the line free portion of the up-

Table 2–3. Mrk 231 continuum emission[a]

Epoch (UT)	$S_{109.0\ \mathrm{GHz}}$ (mJy)	$S_{223.3\ \mathrm{GHz}}$ (mJy)
28.4 Apr 1993	48 (6)	...
06.1 May 1993	55 (8)	...
14.2 May 1993	46 (6)	...
02.5 Jan 1995	...	24 (9)

[a] Numbers in parentheses are uncertainties that include both map noise and calibration uncertainties.

per sideband with the entire lower sideband passband. Our data consist of three separate observations of Mrk 231 over the course of two weeks, and are consistent with a constant flux to within the calibration errors (Table 2–3). Based on only two measurements, McCutcheon & Gregory (1978) claimed that the 23 GHz continuum of Mrk 231 varied by a factor of two in a single day. No other radio frequency measurements of Mrk 231 in the literature suggest such extreme, rapid variability, and indeed, we see no evidence for such behavior at 109 GHz during the course of our observations.

Examination of the literature does reveal that the non-thermal continuum of Mrk 231 is dramatically variable on time scales of months to years at frequencies from 1.5 to 23 GHz. By extrapolating earlier lower frequency observations (Condon et al. 1991b; Condon, Frayer, & Broderick 1991a; Israel, Seielstad, & Berge 1988; Edelson 1987; Preuss & Fosbury 1983; Biermann et al. 1980; McCutcheon & Gregory 1978; Kojoian et al. 1976; Sulentic 1976; Sramek & Tovmassian 1975) to 109 GHz using a spectral index $\beta = -0.6$ ($S_\nu \propto \nu^\beta$, Edelson 1987; Kojoian et al. 1976), we would expect a non-thermal continuum at 109 GHz of anywhere between 18 and

65 mJy. The 109 GHz continuum is thus consistent with being either entirely non-thermal or mostly thermal. We are therefore unable to significantly constrain the contribution of thermal bremsstrahlung emission to the continuum flux at 109 GHz.

We measured the continuum emission at an effective frequency of 223.3 GHz on 2 January 1995 by averaging the line free portion of the lower sideband spectrometer passband with the upper sideband data from the 1000 MHz bandwidth analog correlator. The resultant map shows a 3σ detection of 24 mJy bm^{-1}. If the bulk of the flux we see at 109.0 GHz is non-thermal (with a spectral index of -0.6), this detection is consistent with being entirely non-thermal emission (32 mJy would be expected if Mrk 231 did not vary). If the bulk of the flux at 109.0 GHz is thermal bremsstrahlung emission (e.g., 18 mJy non-thermal, 31 mJy thermal), then 41 mJy would be expected at 223.3 GHz for a non-varying Mrk 231; this disagrees with our detection by 2σ. Unfortunately, uncertainties due to the possible variation of Mrk 231's non-thermal flux prevent significant constraints on the thermal contribution.

2.4. Discussion

2.4.1. Total nuclear mass

We can estimate the total mass in the CO-emitting region by assuming that the CO-emitting gas is in dynamical equilibrium with the central gravitational potential of Mrk 231; however, the dynamical mass estimate is dependent upon the assumed geometry of the gas. In the Appendix (§A.3), we discuss the derivation of dynamical mass for two simple geometries: a sphere and a rotating disk.

For a spherical gas distribution, the dynamical mass is given by equation A–26. Using the observed values for the line-width and the CO radius gives

$$M_{\rm dyn}({\rm sphere}) = 3.4 \times 10^9 \alpha^{-1}(1+q)^{-1}\ {\rm M}_\odot, \tag{2–1}$$

where α is a constant of order unity that relates the observed line-width to the physical velocities in the gas. A probable value for α is 1.5, though it can range from around 0.55 to 2.4 (see §A.2.2). The term q measures the strength of confining pressure (thermal and magnetic) relative to gravity (see §A.2.1). For gravitationally-bound clouds, $q \ll 1$; clouds confined by external pressure have $q > 1$.

For a rotating disk, the expression for the dynamical mass is slightly altered (see equation A–27):

$$M_{\rm dyn}({\rm disk}) = 3.4 \times 10^9 \alpha_{\rm d}^{-1}(\sin^2 i)^{-1}\ {\rm M}_\odot, \tag{2–2}$$

where i is the inclination of the disk axis relative to the line-of-sight, and $\alpha_{\rm d}$ is a constant similar to α, but for a disk geometry. $\alpha_{\rm d}$ is nearly equal to one in most cases (see §A.3).

2.4.2. Nuclear gas mass

Analysis of observations of Galactic molecular clouds shows that the masses required to gravitationally bind the observed internal motions, $M_{\rm VT}$, agree well with the gas masses determined by independent techniques. This result implies that Galactic molecular clouds are in gravitational virial equilibrium, with the molecular gas mass,

M_g, roughly equal to the virial mass, M_{VT}. Empirically, M_{VT} is nearly linearly related to the CO "luminosity":

$$M_{VT} \propto (L'_{CO})^{0.85} , \tag{2-3}$$

where $L'_{CO} \equiv \iint T_b dv dS$ is the CO brightness temperature integrated over velocity and area of the cloud (Scoville & Good 1989). Theoretically, assuming gravitational virial equilibrium and optically thick CO line emission, the M_g/L'_{CO} conversion factor is proportional to $\bar{n}^{1/2}/\bar{T}_b$, where $\bar{n}$ is the mean density of the cloud, and $\bar{T}_b$ is the brightness temperature averaged over the face of the cloud (see §A.2.2 and references therein). Both M_g and L'_{CO} are integral quantities for the clouds, and the same result will hold for observations where many clouds are averaged in a single beam, as long as the clouds do not shadow each other. Thus, in other galaxies, the M_g/L'_{CO} conversion factor will be proportional to a weighted average of $\bar{n}^{1/2}/\bar{T}_b$ over the cloud ensemble, for clouds in gravitational virial equilibrium.

The environment of the molecular gas in luminous IR galaxies likely is quite different from that in the Galactic disk, due to much higher radiation energy densities and the possibility of frequent cloud collisions and shock fronts. There is no *a priori* reason to expect that the value of $\bar{n}^{1/2}/\bar{T}_b$ for molecular clouds in these objects is the same as seen locally, or even that the assumption of gravitational virial equilibrium for individual clouds still holds. Furthermore, Downes, Solomon, & Radford (1993) suggest for the case of Arp 220 that the molecular gas may be distributed smoothly throughout the entire central region several hundred parsecs in radius rather than in numerous smaller clouds. L'_{CO} would then no longer directly trace M_g, but instead

would trace the geometric mean of the gas mass and the dynamical mass; this quantity will only be the same as the gas mass if the gas mass fraction is nearly unity. The application of the Galactic M_g/L'_{CO} conversion factor to luminous IR galaxies as is often done in the literature is thus a controversial matter.

With this in mind, we were motivated to re-examine how different assumptions about the geometry and physical state of the molecular gas can affect the relation between L'_{CO} and M_g, and thus to better understand the uncertainties involved in the use of the Galactic conversion factor in other galaxies. We consider several cases, the details of which are given in the Appendix: (1) optically thin CO emission, where the results are independent of geometry; and, for optically thick CO emission, (2) a clumpy gas distribution, and (3) a smooth gas distribution. The optically thick, clumpy distribution case is also independent of the large-scale geometry in which the clumps exist; however, this is not the case for smoothly-distributed gas. We consider two possible geometries for smoothly-distributed gas: (3a) a spherical region, and (3b) a thin, rotating disk. A summary of some of the results of this analysis of the behavior of the M_g/L'_{CO} conversion factor is presented in Figure 2–4.

For Mrk 231, the Galactic conversion factor, 4.9 $M_\odot$ (K km s^{-1} $pc^2)^{-1}$ (Solomon & Barrett 1991), which we hereafter refer to as the "standard" conversion factor, yields a molecular gas mass estimate of 2.4×10^{10} $M_\odot$ in the nuclear concentration. If this is correct, it implies that a molecular gas mass ten times greater than that in the entire Milky Way is confined to a region less than a kiloparsec in diameter about the nucleus of Mrk 231. We need to know how strongly we can trust this gas

Optical depth	Geometry		M_g/L'_{CO}	Notes
$\tau < 1$	all		$0.079x^{-1}\xi_{ul}$	independent of geometry; dependent on abundance and excitation of CO
$\tau > 1$	clumpy		$k_1 \frac{\bar{n}^{1/2}}{\bar{T}_b} \frac{f^{1/2}}{(1+q)^{1/2}}$	independent of large-scale gas distribution as long as no cloud shadows another, in which case M_g/L'_{CO} will be greater than the given function
	smooth	sphere	$k_1 \frac{\bar{n}^{1/2}}{\bar{T}_b} \frac{f^{1/2}}{(1+q)^{1/2}}$	equivalent to case of single spherical clump
		disk: self-gravitating	$k_2 \frac{\bar{n}^{1/2}}{\bar{T}_b} \sec i$	face-on: $M_g/L'_{CO} < 0.5b^*$ for similar $\bar{n}$, $\bar{T}_b$; as disk becomes edge-on, M_g/L'_{CO} increases
		disk: externally-bound	$k_3 \frac{\bar{n}^{1/2}}{\bar{T}_b} \left(\frac{\rho_{g0}}{\rho_{*0}}\right)^{1/2} \sec i$	since density ratio is necessarily much less than one in this case, M_g/L'_{CO} will be much less than b^* for similar $\bar{n}$, $\bar{T}_b$

Figure 2–4. Behavior of M_g/L'_{CO} conversion factor in selected geometries. Constant values adopted in text: $k_1 = 2.1$, $k_2 = 0.6$, $k_3 = 0.77$. Full range: $k_1 \approx 1.7$–3.5, $k_2 \approx 0.51$–0.75, $k_3 \approx 0.65$–0.96. Definitions: $x = X_{CO}/10^{-4}$; $\xi_{ul} = f_u^{-1}\left[1 - \frac{\exp(h\nu/kT_x)-1}{\exp(h\nu/kT_{bg})-1}\right]^{-1}$; f = gas mass fraction of individual clumps; $q = k_4 f(\Pi_e/k)/\Sigma_g^2$, where $k_4 \approx 0.20$–0.34 (0.20 is adopted in the text). Units: M_g/L'_{CO} ($M_\odot$ (K km s^{-1} pc^2)$^{-1}$), $\bar{n}$ (cm^{-3}), $\bar{T}_b$ (K), Π_e/k (cm^{-3} K), Σ_g ($M_\odot$ pc^{-2}).

mass estimate before we can begin to understand the nuclear phenomena in Mrk 231. Below, in an attempt to understand the uncertainties in the standardly-derived value for the molecular gas mass, we apply the results of our analysis on the behavior of the conversion factor to Mrk 231.

2.4.2.1. Optically thick CO assumption

For optically thick emission, the relation between $L'_{\rm CO}$ and $M_{\rm g}$ depends upon the assumed geometrical configuration of the gas, as discussed in the Appendix. A fortunate situation exists for Mrk 231, however, that allows us to place constraints upon the geometry of the gas even though our observations do not yet spatially resolve the structure of the CO emission. This situation is that the value of $M_{\rm g}$ derived from certain geometrical scenarios is larger than $M_{\rm dyn}$. By avoiding this unphysical result, we are able to significantly constrain models for the geometry of the nuclear molecular gas.

2.4.2.1.1. Spherical gas distribution hypothesis

As described above, the dynamical mass implied by the CO emission of Mrk 231 must be less than roughly 2.3×10^9 $M_\odot$ for a spherical distribution of clumps; however, the standard conversion factor combined with the observed $L'_{\rm CO}$ implies a mass in molecular gas alone of 2.4×10^{10} $M_\odot$. Reconciling these numbers places tight constraints on the parameter-space allowed for the hypothesis that the gas is distributed spherically about the nucleus of Mrk 231.

For both a clumpy and a smooth spherical gas distribution, M_g is given by an expression of the form (see equations A–15 to A–18):

$$M_g = bL'_{CO} f^{1/2} (1+q)^{-1/2} \ , \tag{2–4}$$

where $b \equiv (2.57/\alpha^{1/2})(\bar{n}^{1/2}/\bar{T}_b)$ $M_\odot$ (K km s^{-1} pc^2)$^{-1}$, q is the ratio of pressure to gravitational confinement as defined in the Appendix ($q \approx 0$ for pure self-gravitating clouds and $q > 1$ for pressure-confined clouds), and f is the gas mass fraction of individual clumps in the clumpy case and of the entire nuclear cloud (which can be thought of as one large clump) in the smooth case. Note that bL'_{CO} is equal to M_g for pure gas clouds in gravitational virial equilibrium ($f \approx 1$ and $q \ll 1$). Since Galactic disk molecular clouds meet those criteria, $M_g = b^* L'_{CO}$, where $b^* = 4.9$ $M_\odot$ (K km s^{-1} pc^2)$^{-1}$ is the standard conversion factor.

For clouds in a spherically-symmetric distribution, we can place three constraints upon the value of b in Mrk 231. The first constraint, an upper limit, arises from the requirement that the nuclear gas mass fraction be less than the single-clump gas mass fraction. The second, a lower limit, results from direct calculation of b from limits on the mean density and mean brightness temperature of the gas clumps. The third, another lower limit, comes from the lower limit to M_g, obtained by assuming that the CO emission is optically thin.

First, whether the gas is clumpy or smoothly-distributed, the gas mass fraction averaged over the entire nucleus, $f_{nuc} \equiv M_g/M_{dyn}$, must be less than or equal to the single-cloud gas mass fraction f. This leads to the inequality

$$\left(\frac{bL'_{CO}}{M^*_{dyn}}\right)^2 (1+q)^{-1} \leq f \leq 1 \ , \tag{2–5}$$

where $M^*_{\rm dyn} \equiv \delta v^2 R/(\alpha G) \approx 3.4 \times 10^9 \alpha^{-1}$ $M_\odot$, is the dynamical mass for a spherical gas distribution uncorrected for any confining pressure (§2.4.1). We later argue that $q \ll 1$ for the molecular gas in Mrk 231, i.e., that pressure confinement is unimportant (§2.4.2.1.2). In this case, $bL'_{\rm CO}$ must be less than or equal to $M^*_{\rm dyn}$. Expressing $bL'_{\rm CO}$ for Mrk 231 in terms of the standard conversion factor gives $bL'_{\rm CO} = 2.4 \times 10^{10}(b/b^*)$ $M_\odot$. Hence, inequality (5) implies

$$b/b^* \leq 0.14\alpha^{-1} \approx 0.09 \qquad (2\text{–}6)$$

must hold for Mrk 231. In other words, if the gas is spherically distributed (clumpy or uniform) in Mrk 231, the maximum value for the molecular gas mass, $bL'_{\rm CO}$, is only nine percent of the value given by the standard conversion factor.

A lower limit to the value of b in Mrk 231 can be estimated by using a lower limit to the mean cloud density and an upper limit to the mean cloud brightness temperature, since $b \propto \bar{n}^{1/2}/\bar{T}_{\rm b}$. The dust temperature serves as a useful upper limit to the brightness temperature of the CO emission at densities of greater than 10^5 cm^{-3} since the dust and gas will come into thermal equilibrium with the dust keeping the gas from cooling. The 60-800 μm spectrum of Mrk 231 yields an upper limit to the dust temperature of 85 K (Roche & Chandler 1993), which we adopt as an upper limit to $\bar{T}_{\rm b}$. (Note that since $\bar{T}_{\rm b} > 19$ K for CO 2→1, this requires the area covering factor of the CO emission to be large—at least 0.2.) A lower limit to the mean cloud density can be estimated using the lower limit to $M_{\rm g}$ obtained by assuming that the CO emission is optically thin: $M_{\rm min} = 1.3 \times 10^9 x^{-1}$ $M_\odot$ (§2.4.2.2), with $x \equiv X_{\rm CO}/10^{-4}$, where $X_{\rm CO}$ is the relative abundance of CO molecules to H_2 molecules. If this amount of molecular

gas were spread uniformly throughout a spherical region of the observed radius, $\bar{n}$ would be $63x^{-1}$ cm^{-3}; however, this configuration is inconsistent with observations as it implies $A_V \approx 100$ (for a normal dust to gas ratio) towards the nucleus of Mrk 231, yet the Seyfert core is readily observable with $A_V \approx 2$ (Boksenberg et al. 1977). Hence the gas must be clumped, and the density of the emitting gas must be higher: $\bar{n} = 63x^{-1}\phi_V^{-1}$ cm^{-3}, where ϕ_V is the fraction that the gas occupies of the volume of a 420 pc radius sphere about the nucleus. Combining this information with the limit on $\bar{T}_b$ above implies that $b > 0.24(\alpha x \phi_V)^{-1/2} \approx 0.20(x\phi_V)^{-1/2}$ M$_\odot$ (K km s^{-1} pc^2)$^{-1}$. Therefore,

$$b/b^* > 0.049(\alpha x \phi_V)^{-1/2} \approx 0.040(x\phi_V)^{-1/2} \ . \qquad (2\text{–}7)$$

For this lower limit to be consistent with the upper limit derived above, $x\phi_V > 0.13\alpha \approx 0.19$. Hence, for the spherical gas distribution hypothesis to remain valid, either the CO abundance or the volume filling factor of the gas must be relatively large; in fact, X_{CO}must be greater than 1.9×10^{-4} for any value of ϕ_V less than 0.1, and X_{CO} must be greater than 1.5×10^{-5} in any situation.

An additional lower limit to the value of b/b^* in Mrk 231, one that is independent of the assumed geometry, comes from the optically-thin limit to the molecular gas mass, M_{min}. Since bL'_{CO} is the maximum possible value for M_g, bL'_{CO} must be greater than M_{min}. This condition implies

$$b/b^* \geq 0.055x^{-1} \ . \qquad (2\text{–}8)$$

This lower limit on the value of b in Mrk 231 can only be reconciled with the upper limit above if $x > 0.39\alpha \approx 0.59$, i.e., $X_{CO} > 5.9 \times 10^{-5}$. This is a slightly tighter

constraint on the CO abundance than the one derived in the previous paragraph, and is independent of the volume filling factor of the gas.

The preceding analysis provides strong constraints on the hypothesis that the gas is spherically distributed about the nucleus of Mrk 231. This hypothesis forces the product of the CO abundance and the volume filling factor of the gas to be relatively high, despite the fact that the gas must be clumped to allow us to see the Seyfert nucleus optically. This condition cannot yet be confidently ruled out since Mrk 231 is an extremely luminous and unusual object. For example, starburst activity could contribute to a super-abundance of CO relative to H_2 ($X_{CO} \gg 10^{-4}$). A spherical geometry for the gas in Mrk 231 remains a possibility, albeit an unlikely one.

2.4.2.1.2. Gas disk hypothesis

As an alternative, we hypothesize that the molecular gas occupies a rotating disk. Note that the velocity gradient is aligned with the major axis of the emission distribution, which is consistent with this hypothesis. In this section, we consider the implications of the disk hypothesis on the mass conversion factor and on other properties of such a disk.

If the gas disk consists of discrete clouds, whatever the large-scale geometry, M_g is given by equation 2–4, and pressure-confinement may reduce the mass conversion factor; however, the pressure needed for this effect to be significant in Mrk 231 is quite large. Figure 2–5 graphically depicts how the parameters Π_e, Σ_g, and q are related for given value of b (hence for given value of $\bar{n}^{1/2}/\bar{T}_b$). The optically thin mass limit, $M_{min} = 1.3 \times 10^9$ $M_\odot$, implies a minimum gas surface density of $2.4 \times 10^3 x^{-1}$ $M_\odot$ pc^{-2}.

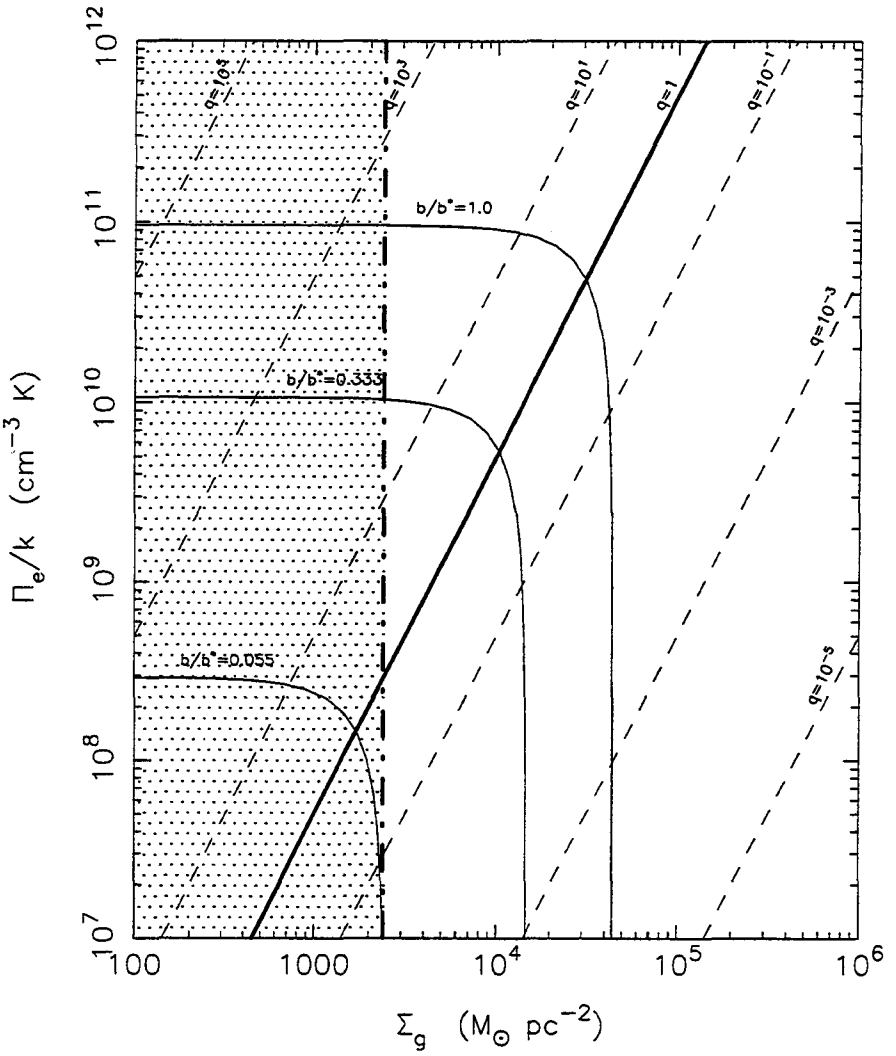

Figure 2–5. This figure illustrates how the pressure confinement term q affects the derived value for the gas mass (represented by the gas surface density Σ_g on the abscissa) for a population of gas clumps in virial equilibrium with fixed values of $\bar{n}$ and $\bar{T}_b$, and hence fixed values for $b \propto \bar{n}^{1/2}/\bar{T}_b$. For the purposes of this diagram, the parameters x and f (see text) have both been fixed at 1.0. As described in the text, the ordinate Π_e/k represents the total thermal and magnetic confining pressure. Thin solid lines trace the loci of $b/b^* = 0.055$ (lower limit), 0.333, and 1.0. (b^* is the standard, Galactic M_g/L'_{CO} conversion factor.) Dashed lines trace loci of constant q; the thick solid line at $q = 1$ represents the boundary between gravitationally-confined clumps (lower right) and pressure-confined clumps (upper left). The dash-dot line represents the optically thin lower limit to the gas surface density (for $x = 1$, i.e., $X_{CO} = 10^{-4}$), and thus the shaded region of the parameter space is ruled out by the CO observations. For pressure confinement to be important for the molecular gas in Mrk 231, Π_e/k must be over 2.8×10^8 cm^{-3} K (for $x = 1$ and $f = 1$). For the purposes of comparison, note that the interstellar pressure in the local Galactic disk lies three orders of magnitude below the bottom of the diagram.

Defining $\Pi_{e,crit}$ as the value for the total confining pressure needed to have $q = 1$, equation A–12 implies $\Pi_{e,crit}/k \geq 2.8 \times 10^8 f^{-1} x^{-2}$ cm^{-3} K. This confining pressure can consist of either magnetic or thermal pressure or a combination of both. Pure magnetic confinement would imply external field strengths of over a milligauss—nearly three orders of magnitude greater than the Galactic magnetic field (e.g., Han & Qiao 1994; Rand & Lyne 1994; Thomson & Nelson 1980; Manchester 1974)—unless CO is super-abundant relative to H_2.

Pure thermal pressure confinement is only consistent with the data for Mrk 231 if the molecular gas surface density is near the lower end of the permitted values. If we assume that the confining medium is at a temperature of 5×10^7 K (4.3 keV), the minimum $\Pi_{e,crit}$ implies a thermal bremsstrahlung luminosity of 2.2×10^8 $L_\odot$ (Rybicki & Lightman 1979; this assumes that the hot medium occupies a sphere of 420 pc radius); about 64% of this energy would emerge in the *Einstein* bandpass (0.1–4.5 keV) in the limit of no absorbing gas column. In fact, *Einstein* X-ray data yield an upper limit of 2.0×10^8 $L_\odot$ to the 0.1–4.5 keV luminosity of Mrk 231 (Eales & Arnaud 1988; limit converted to $H_0 = 75$ km s^{-1} Mpc^{-1}). If Σ_g is greater than the optically-thin limit, $\Pi_{e,crit}$ is raised, and thus so is the thermal bremsstrahlung luminosity, which varies as $\Pi_e^2 T^{-3/2}$. If the gas surface density is even 20% higher than the optically thin lower limit of 2.4×10^3 $M_\odot$ pc^{-2}, the expected X-ray luminosity from free-free radiation is over twice the observational limit, and an atomic hydrogen column density of over 10^{22} cm^{-2} is required (using the absorption cross-sections in Morrison & McCammon 1983); this implies an unreasonable $A_V > 5$ over the entire nuclear region if the

dust to gas ratio is normal. (Note that this hypothetical absorption cannot be due to the molecular gas, which by assumption must be enveloped by the hot medium.) The data thus rule out pure thermal pressure confinement of the molecular gas for $\Sigma_g > 2.9 \times 10^3$ $M_\odot$ pc^{-2} with a 5×10^7 K confining medium. This constraint is further tightened if the confining medium has a somewhat lower temperature. Only for hot medium temperatures above 5×10^7 K and below about 2.5×10^6 K do the constraints on thermal pressure confinement start to loosen. Therefore, we conclude that pressure confinement is likely unimportant ($q < 1$) for the molecular gas in Mrk 231.

The inclination of the gas disk in Mrk 231 can be constrained using the expression for the dynamical mass for a rotating disk (equation 2–2) and the requirement that the disk mass be less than the dynamical mass. This leads to the constraint:

$$\sin^2 i \leq \left(\frac{M'_{\rm dyn}}{b^* L'_{\rm CO}}\right) \left(\frac{b}{b^*}\right)^{-1} (1+q)^{1/2} \ , \qquad (2\text{–}9)$$

where $M'_{\rm dyn} \equiv \delta v^2 R/(\alpha_{\rm d} G) \approx 3.4 \times 10^9 \alpha_{\rm d}^{-1}$ $M_\odot$, is the dynamical mass for a rotating gas disk uncorrected for inclination effects. Taking $\alpha_{\rm d} = 1.0$ and $q \ll 1$ leads to $\sin i \leq 0.37 (b/b^*)^{-1/2}$. If b/b^* is near its minimum (optically thin) value of $0.055 x^{-1}$, and $x \approx 1$ (i.e., CO abundance is approximately that of Galactic GMCs), then $M_{\rm g}$ is then less than $M'_{\rm dyn}$, and i is unconstrained. If b/b^* is greater than one-third, however, then the inclination of the disk axis with respect to our line-of-sight is restricted to be less than 40°, and if $b/b^* \approx 1$, then $i < 22°$. Since $b/b^* = M_{\rm g}/M_{\rm g}^*$ for a self-gravitating molecular clouds (Equation 2–4), where $M_{\rm g}^* \equiv b^* L'_{\rm CO}$ is the gas mass derived using the standard conversion factor, a disk of such clouds in Mrk 231 is constrained to be

within 40° of face-on unless the molecular gas mass is being overestimated by over a factor of three by the standard conversion factor.

If the nuclear disk in Mrk 231 consists of a smooth distribution of gas rather than discrete clouds, the constraints on i are somewhat looser. For a self-gravitating smooth gas disk, the gas mass is given by equation A–22. The inclination constraint becomes $\sin i \tan i \leq 0.48\alpha_{\rm d}^{-1}(b/b^*)^{-1}$. Note that b/$b^*$, which relates the ratio of $\bar{n}^{1/2}/\bar{T}_{\rm b}$ in a gas distribution to the same ratio in Galactic GMCs, is not equal to $M_{\rm g}/M_{\rm g}^*$ in this scenario; instead, the conversion factor is reduced for similar $\bar{n}$ and $\bar{T}_{\rm b}$ by roughly a factor of three relative to what it is in Galactic GMCs: $M_{\rm g}/M_{\rm g}^* \approx$ 0.15–0.44(b/b^*) (§A.2.4.1). For $\alpha_{\rm d} = 1.0$ and $b/b^* \geq 1/3$ in a self-gravitating smooth gas disk, the inclination constraint is $i \leq 59°$. While the disk is not constrained to be face-on in this case, a disk within 30° of edge-on is ruled out unless the ratio of $\bar{n}^{1/2}/\bar{T}_{\rm b}$ is over a factor of three smaller than in Galactic GMCs. For a non-self-gravitating smooth gas disk, the gas mass is given by equation A–25. It is not known explicitly unless the ratio of gas to stellar density at the mid-plane is known. While this knowledge will generally not be available, as it is not for Mrk 231, the fact that the gas mass fraction must be less than this density ratio, which in turn must be much less than one (so that the disk is indeed non-self-gravitating), allows the inclination of a Mrk 231 gas disk to be constrained as in the scenarios considered above: $\sin i \tan i < 0.38\alpha_{\rm d}^{-1}(b/b^*)^{-1}$. For $\alpha_{\rm d} = 1.0$ and $b/b^* > 1/3$, the constraint is $i < 54°$. In either of these smooth disk scenarios for Mrk 231, if the ratio $b \propto \bar{n}/\bar{T}_{\rm b}$ for the molecular gas is within a factor of three of the value for Galactic GMCs, the

gas disk cannot be within 30° of edge-on to our line-of-sight—the larger the value of b, and hence the larger the amount of molecular gas, the more the disk is constrained to be face-on.

The entire preceding discussion has assumed no *a priori* knowledge of the inclination of a gas disk in Mrk 231. The aspect ratio of the CO 2→1 emission, however, yields independent information. That ratio is $1.0/0.3 \approx 3.3$, which implies $i \approx 73°$. For such a nearly edge-on orientation, $M_{\rm dyn}$ is only 3.7×10^9 $M_\odot$, requiring that that the molecular gas mass be over six times smaller than indicated by the standard $M_{\rm g}/L'_{\rm CO}$ conversion factor (2.4×10^{10} $M_\odot$, §2.4.2). The minor axis measurement is highly uncertain, however, so it is quite possible that the inclination is as low as 45° (aspect ratio 1.41), though it is unlikely that is much lower than that. In this case, $M_{\rm dyn}$ is still only 6.8×10^9 $M_\odot$, and the molecular gas mass is required to be 3.6 times smaller than the value given by the standard conversion factor.

As argued above, pressure-confinement is unlikely to be contributing to such an overestimate. Instead, a likely cause is the very high brightness temperature of the CO emission ($T_{\rm b} > 34$ K, §2.3.1)—because the conversion factor for gravitationally-confined gas clouds is proportional to $\bar{T}_{\rm b}^{-1}$ (Equation 2–4). As the conversion factor is also proportional to $\bar{n}^{1/2}$, high densities can act to counter the effect of high brightness temperature. The brightness temperature effect likely triumphs in Mrk 231, though, as the CO 2→1/CO 1→0 line temperature ratio of 0.7 (see Figure 2–3; Radford et al. 1991), considered together with the high brightness temperatures, suggests that the mean density of the bulk of the CO-emitting gas is not much over 10^3 cm^{-3}.

If the gaseous disk consists of numerous clumps of gas, collisions between these clumps would create a viscosity that would cause mass to flow inward. In fact, this effect can account for the infall rate necessary to power Mrk 231's luminosity via accretion onto a central black hole. To obtain a rough estimate of the size of this effect in a molecular disk in Mrk 231, we use the expression for the mass infall rate in a viscous disk given in Canzian (1990) and assume constant kinematic viscosity, constant mass surface density, and a rotation curve that is solid body at the inner radius, and flat at the outer radius of the disk. A rotation curve similar to this would be expected if the gas disk constitutes most of the nuclear mass, as seems likely from the constraints on $M_{\rm g}$ and $M_{\rm dyn}$. We estimate the kinematic viscosity in a similar fashion to Canzian (1990); we take the area covering factor of clumps in Mrk 231 to be approximately 0.5 (§2.4.2.1.1), and for the scale height, we substitute the expression for a self-gravitating disk. This results in the mass infall rate

$$\dot{M} = 0.79\left(\frac{\sigma_v}{10\,\mathrm{km\ s^{-1}}}\right)^3 \mathrm{M_\odot\ yr^{-1}},$$

where σ_v is the (one-dimensional) clump-clump velocity dispersion. Using an accretion luminosity $L_{\rm accr} = 0.1\dot{M}c^2$ results in $L_{\rm accr} = 1.1 \times 10^{12}(\sigma_v/10\,\mathrm{km\ s^{-1}})^3\ \mathrm{L_\odot}$. To account for the entire luminosity of Mrk 231, σ_v need be only about 15 km s^{-1}, well within the range permitted by the observed line width. Hence, while a dominant starburst contribution to the luminosity of Mrk 231 cannot be conclusively ruled out (although strong constraints are possible, §2.4.3), a massive, viscous molecular gas disk can account for the sustained, high accretion rate required to power the ultraluminous nucleus.

2.4.2.2. Optically thin CO assumption

A lower limit to the mass of molecular gas can be obtained by assuming that the observed CO emission is optically thin, as we discuss in the Appendix. To estimate the excitation of the gas, we use the lower limit to the intrinsic peak brightness temperature of the CO 2→1 transition, $\bar{T}_b > 19$ K, as a lower limit to the actual excitation temperature of the gas. By assuming LTE level populations at this excitation temperature, we obtain a minimum molecular gas mass for Mrk 231, $M_{min} = 1.3 \times 10^9 x^{-1}$ $M_\odot$. Even this conservative lower limit is comparable to the entire molecular mass of the Milky Way Galaxy (Sanders, Solomon, & Scoville 1984).

The self-consistency of this number can be checked by estimating the minimum possible optical depth of this amount of gas in a region of the observed size (equation 2–6), which occurs for the case of the gas spread uniformly in a spherical region. Using the upper limit to the dust temperature from Roche & Chandler (1993) (§2.4.2.1.1) as the upper limit to the LTE excitation temperature and the lower limit to $T_{b,1\rightarrow0}$ of 34 K (§2.3.1), the minimum optical depth of the CO 1→0 emission is approximately 0.1. This illustrates that the gas in Mrk 231 is so concentrated that, even for the smallest permitted gas mass, only a relatively modest degree of clumping results in optically thick gas.

2.4.3. Constraints on starburst luminosity

Whether a nuclear starburst or a Seyfert AGN can account for the bulk of the luminosity of Mrk 231 has not yet been established. Several observations indicate a large amount of recent star formation, including blue continuum colors and relatively

strong stellar absorption features in regions surrounding the nucleus (Adams 1972; Kodaira, Iye, & Nishimura 1979; Hamilton & Keel 1987). Double-peaked (800 km s^{-1} separation, Boksenberg et al. 1977; Hamilton & Keel 1987) [O II] λ3727 and [O III] λ5007 narrow emission lines in nearby regions suggest a superwind-like outflow that could be caused by a massive starburst (Lipari, Colina, & Macchetto 1994). Furthermore, Cutri, Rieke, & Lebofsky (1984) state that the strong silicate absorption feature seen in Mrk 231 seems to be typical of starburst galaxies, and Hutchings & Neff (1987) claim that the OH megamaser seen by Baan (1985) is evidence for ongoing starburst activity. Mrk 231 also shows ample evidence for the presence of a compact non-thermal AGN, however. Both its radio (Condon et al. 1991a) and optical continuum (Miller 1979) are variable on time scales that suggest a source size of less than a parsec. Centimeter-wave VLBI observations directly reveal a compact core that contributes a large fraction of the radio flux of Mrk 231 (Preuss & Fosbury 1983; Neff & Ulvestad 1988; Lonsdale, Smith, & Lonsdale 1993; Taylor et al. 1994). In an attempt to quantitatively estimate the relative contribution of a starburst and an AGN to the bolometric luminosity of Mrk 231, Cutri et al. (1984) model the near-infrared spectrum of Mrk 231 as a linear combination of the spectra of M82 (starburst) and NGC 4151 (Seyfert 1.5) and conclude that the luminosity of Mrk 231 is divided roughly equally between starburst and Seyfert activity. Such a spectral modeling technique is necessarily highly uncertain, especially in view of its ambiguous results; the relative contribution of starburst and AGN activity to the luminosity of Mrk 231 thus remains undetermined.

An ultimate aim of our study of the molecular gas in luminous infrared galaxies is to use starburst models in conjunction with data on the molecular gas (which provides the fuel for star formation) to place constraints on the fraction of the infrared luminosity which can be generated in a starburst. If one can constrain this fraction to be much less than unity in a number of objects, this would be a major piece of evidence in favor of the dust-enshrouded quasar hypothesis (Sanders et al. 1988). The compact, variable radio source in Mrk 231 suggests that the Seyfert 1 AGN, and not star formation, powers the dominant fraction of its infrared luminosity (Condon et al. 1991b). Hence Mrk 231 is a good candidate for attempting to constrain the starburst luminosity to be much less than $L_{\rm IR}$.

We estimate the ratio, $L_{\rm sb}/M_*$, of starburst luminosity to the total mass of stars in a starburst by using the constant-rate starburst model of Scoville & Soifer (1991). The results depend upon the upper and lower cutoffs of the stellar IMF ($m_{\rm u}$, $m_{\rm l}$; shape is assumed to be Miller-Scalo) and the age of the starburst ($t_{\rm sb}$). Maximizing the luminosity of a starburst of a given mass requires a very young and top-heavy IMF; for instance, $L_{\rm sb}/M_*$ is as large as 600 $\rm L_\odot\ M_\odot{}^{-1}$ for $t_{\rm sb} = 10^7$ yr, $m_{\rm l} = 3\ \rm M_\odot$, $m_{\rm u} = 80\ \rm M_\odot$. (In Mrk 231, any starburst is unlikely to be much younger than 10^7 yr, since the dynamical time scale for its nucleus is $840\,\rm pc\,/186\,km\ s^{-1} \approx 5 \times 10^6$ yr.) Even for such an extreme IMF, the total stellar mass is required to be $6 \times 10^9 f_{\rm sb}\ \rm M_\odot$, where $f_{\rm sb}$ denotes the fraction of the $3.5 \times 10^{12}\ \rm L_\odot$ luminosity of Mrk 231 that is supplied by starburst activity. Along with the derived values for the dynamical mass

(§2.4.1), this reasonable lower limit to the expected stellar mass of a starburst imposes tight constraints on f_{sb}.

For the spherical large-scale gas distribution discussed in §2.4.2.1.1, the upper limit to M_{dyn} is 2.3×10^9 $M_\odot$. Hence, f_{sb} must be less than $\sim$0.4. In fact, if we allow for the minimum amount of gas ($1.3 \times 10^9 x^{-1}$ $M_\odot$, §2.4.2.2), f_{sb} must be less than 0.17 unless CO is both super-abundant and optically thin. Thus, the spherical gas distribution hypothesis requires a powerful additional source of luminosity in Mrk 231 besides starburst activity. For older and less top-heavy starburst IMFs, M_* is even greater, and this constraint is tightened.

We can also constrain f_{sb} in Mrk 231 for the gas disk hypothesis if we adopt an inclination for the disk. We conservatively adopt $i = 45°$, though the CO 2→1 axis ratio suggests the inclination may be more edge-on (§2.4.2.1.2). (A more edge-on inclination would tighten the following constraint on f_{sb}.) The dynamical mass for a disk of this inclination is 6.8×10^9 $M_\odot$. For normal CO abundance, the minimum gas mass pushes the available mass in stars down to 5.5×10^9 $M_\odot$. This is roughly comparable to the lower limit given above to the stellar mass of the starburst with the luminosity of Mrk 231. Any starburst in Mrk 231 is likely to be significantly older than 10^7 yr, however, even if it does have a top-heavy IMF. For an age of 5×10^7 yr, the lower limit to the stellar mass rises to $1.0 \times 10^{10} f_{sb}$ $M_\odot$, and thus the upper limit to f_{sb} falls from unity to $\sim$0.5.

Our observations thus indicate that only for very extreme circumstances can a starburst account for the bulk of the luminosity in Mrk 231. The molecular disk must

be distributed in a disk at an inclination of 45° and the starburst must be less than a few 10^7 yr old and have a very top-heavy IMF. More edge-on disk inclinations tighten the starburst constraints further, while more face-on inclinations disagree with our measurement of the aspect ratio of the CO 2→1 emission. This result is consistent with the suggestion by Condon et al. (199b) that Mrk 231 is dominated by compact (~1 pc) AGN.

2.5. Conclusions

Our high-resolution CO 1→0 and CO 2→1 observations of the extremely luminous IR galaxy Mrk 231 have resolved a compact emission region with a diameter of around 1″.0 (840 pc). In both transitions, a significant velocity gradient is seen closely aligned with the major axis of the emission distribution. The area covering factor of the CO emission must be greater than ~0.2 due to the high brightness temperature of the emission ($T_{b,1\rightarrow0} > 34$ K, and possibly is as high as 83 K). No emission is detected in either transition at the position of the "secondary nucleus" described by Armus et al. 1994, roughly 3″.5 south of the Seyfert nucleus.

In order to more fully understand the uncertainties involved in converting the observed CO luminosity into a molecular gas mass, we have analyzed in detail the behavior of the M_g/L'_{CO} conversion factor for a variety of different geometries and physical conditions. The main results of this analysis as applied to Mrk 231 are the following.

1. The large-scale distribution of the nuclear molecular gas in Mrk 231 cannot be spherically-symmetric unless the product of the CO abundance relative to H_2

(X_{CO}) and the volume filling factor (ϕ_V) is high: $(X_{CO}/10^{-4})\phi_V > 0.19$. If the large-scale gas distribution is indeed spherically symmetric, the standard, Galactic M_g/L'_{CO} conversion factor must be overestimating the molecular gas mass by at least a factor of 11. Also, in this case, a starburst can generate no more than forty percent of the L_{IR} of Mrk 231, suggesting that the Seyfert 1 AGN would be the dominant luminosity source. A uniform spherical distribution of gas and dust is ruled out from comparison of the observed visual extinction to the nucleus with the extremely large obscuration expected in this case.

2. The large-scale distribution of the nuclear molecular gas is likely disk-like. The aspect ratio of the CO 2→1 emission constrains the inclination of this disk to be 45° or more from the line-of-sight. The molecular gas mass is thus required to be less than 6.8×10^9 $M_\odot$—3.6 times less than the value derived from the standard value of the conversion factor. For such a gas disk, a starburst cannot account for the majority of the luminosity of Mrk 231 unless it is younger than a few 10^7 yr and has a very top-heavy IMF, so that $L_{sb}/M_* \gtrsim 300$ $L_\odot$ $M_\odot{}^{-1}$. This is consistent with the suggestion of Condon et al. (1991) that the luminosity of Mrk 231 is dominated by a compact (1 pc) AGN. Along these lines, we show that a massive, viscous accretion disk with properties consistent with the molecular gas in Mrk 231 can account for the accretion luminosity necessary to power the infrared luminosity of Mrk 231.

Irrespective of the large scale geometry of the nuclear molecular gas, we conclude:

3. Thermal and magnetic pressure confinement of clumps are unlikely to account for a significant lowering of the M_g/L'_{CO} conversion factor below the Galactic value.

The medium required for thermal confinement would, via thermal bremsstrahlung, produce a higher X-ray luminosity than is reported by Eales & Arnaud (1988) unless M_g is within a factor of two of the optically thin lower limit or the gas temperature of the confining medium is outside the range 2.5×10^6 K to 5×10^7 K. Magnetic confinement requires fields of over a milligauss over a region 420 pc in radius.

References

Aalto, S. 1995, private communication

Aaronson, M., Huchra, J., Mould, J., Schechter, P. L., & Tully, R. B. 1982, ApJ, 258, 64

Adams, T. F. 1972, ApJ, 176, L1

Adams, T. F. & Weedman, D. W. 1972, ApJ, 173, L109

Antonucci, R. 1993, ARA&A, 31, 473

Armus, L., Surace, J. A., Soifer, B. T., Matthews, K., Graham, J. R., & Larkin, J. E. 1994, AJ, 108, 76

Baan, W. A. 1985, Nature, 315, 26

Barnes, J. E. & Hernquist, L. E. 1991, ApJ, 370, L65

Biermann, P., Clarke, J. N., Fricke, K. J., Pauliny-Toth, I. I. K., Schmidt, J., & Witzel, A. 1980, A&A, 81, 235

Boksenberg, A., Carswell, R. F., Allen, D. A., Fosbury, R. A. E., Penston, M. V., & Sargent, W. L. W. 1977, MNRAS, 178, 451

Boroson, T. A., Meyers, K. A., Morris, S. L., & Persson, S. E. 1991, ApJ, 370, L19

Danzian, B. 1990, Ph. D. thesis, Caltech

Condon, J. J., Frayer, D. T., & Broderick, J. J. 1991a, AJ, 101, 362

Condon, J. J., Helou, G., Sanders, D. B., & Soifer, B. T. 1990, ApJS, 73, 359

Condon, J. J., Huang, Z. P., Yin, Q. F., & Thuan, T. X. 1991b, ApJ, 378, 65

Cutri, R. M., Rieke, G. H., & Lebofsky, M. J. 1984, ApJ, 287, 566

Downes, D., Solomon, P. M., & Radford, S. J. E. 1993, ApJ, 414, L13

Eales, S. A., & Arnaud, K. A. 1988, ApJ, 324, 193

Edelson, R. A. 1987, ApJ, 313, 651

Hamilton, D. & Keel, W. C. 1987, ApJ, 321, 211

Han, J. L. & Qiao, G. J. 1994, A&A, 288, 759

Harwit, M., Houck, J. R., Soifer, B. T., & Palumbo, G. C. C. 1987, ApJ, 315, 28

Heckman, T. M., Balick, B., & Sullivan, W. T. 1978, ApJ, 224, 745

Hutchings, J. B. & Neff, S. G. 1987, AJ, 92, 14

Israel, F. P., Seielstad, G. A., & Berge, G. L. 1988, A&A, 189, 7

Keel, W. C. & Hamilton, D. 1995, private communication

Kodaira, K., Iye, M., Nishimura, S. 1979, PASJ, 31, 451

Kojoian, G., Sramek, R. A., Dickinson, D. F., Tovmassian, H., & Purton, C. R. 1976, ApJ, 203, 323

Kollatschny, W., Dietrich, M., & Hagen, H. 1992, A&A, 264, L5

Lawrence, A., Rowan-Robinson, M., Leech, K., Jones, D. H. P., & Wall, J. V. 1989, MNRAS, 240, 329

Lipari, S., Colina, L., & Macchetto, F. 1994, ApJ, 427, 174

Lonsdale, C. J., Smith, H. E., & Lonsdale, C. J. 1993, ApJ, 405, L9

Manchester, R. N. 1974, ApJ, 188, 637

McCutcheon, W. H. & Gregory, P. C. 1978, AJ, 83, 566

Miller, H. R. 1979, A&AS, 35, 387

Morrison, R. & McCammon, D. 1983, ApJ, 270, 119

Neff, S. G. & Ulvestad, J. S. 1988, AJ, 96, 841

Padin, S. et al. 1993, IEEE Trans. Instr. Meas., 42, 793

Preuss, E. & Fosbury, R. A. E. 1983, MNRAS, 204, 783

Radford, S. J. E., Solomon, P. M., & Downes, D. 1991, ApJ, 368, L15

Rand, R. J. & Lyne, A. G. 1994, MNRAS, 268, 497

Rieke, G. H., Cutri, R. M., Black, J. H., Kailey, W. F., McAlary, C. W., Lebofsky, M. J., & Elston, R. 1985, ApJ, 290, 116

Roche, P. F., Aitken, D. K., & Whitmore, B. 1983, MNRAS, 205, 21P

Roche, P. F., & Chandler, C. J. 1993, MNRAS, 265, 486

Rudy, R. J., Foltz, C. B., & Stocke, J. T. 1985, ApJ, 288, 531

Rybicki, G. B. & Lightman, A. P. 1979, Radiative Processes in Astrophysics, (New York: John Wiley & Sons)

Sanders, D. B., Soifer, B. T., Elias, J. H., Madore, B. F., Matthews, K., Neugebauer, G., & Scoville, N. Z. 1988, ApJ, 325, 74

Sanders, D. B., Solomon, P. M., & Scoville, N. Z. 1984, ApJ, 276, 182

Sanders, D. B., Young, J. S., Scoville, N. Z., Soifer, B. T., & Danielson, G. E. 1987, ApJ, 312, L5

Scoville, N. Z., Carlstrom, J. E., Chandler, C. J., Phillips, J. A., Scott, S. L., Tilanus, R. P. J., & Wang, Z. 1993, PASP, 105, 1482

Scoville, N. Z. & Good, J. C. 1989, ApJ, 339, 149

Scoville, N. Z., Sanders, D. B., Sargent, A. I., Soifer, B. T., & Tinney, C. G. 1989, ApJ, 345, L25

Scoville, N. Z., Sargent, A. I., Sanders, D. B., & Soifer, B. T. 1991, ApJ, 366, L5

Scoville, N. Z. & Soifer, B. T. 1991, in Massive Stars in Starbursts, eds. C. Leitherer, N. R. Walborn, T. M. Heckman, & C. A. Norman (Cambridge: Cambridge Univ. Press) p. 233

Shepherd, M. C., Pearson, T. J., & Taylor, G. B. 1994, BAAS, 26, 987

Soifer, B. T., Sanders, D. B., Neugebauer, G., Danielson, G. E., Lonsdale, C. J., Madore, B. F., & Persson, S. E. 1986, ApJ, 303, L41

Solomon, P. M. & Barrett, J. W. 1991, in Dynamics of Galaxies and Their Molecular Cloud Distributions, eds. F. Combes & F. Casoli (Dordrecht: Kluwer Academic) p. 235

Sramek, R. A. & Tovmassian, H. M. 1975, ApJ, 196, 339

Sulentic, J. W. 1976, AJ, 81, 582

Taylor, G. B., Vermeulen, R. C., Pearson, T. J., Readhead, A. C. S., Henstock, D. R., Browne, I. W. A., & Wilkinson, P. N. 1994, ApJS, 95, 345

Thomson, R. C. & Nelson, A. H. 1980, MNRAS, 191, 863

Chapter 3

High-Resolution CO Observations of Luminous Infrared Galaxies

3.1. Introduction

The discovery of large concentrations of molecular gas at the cores of luminous infrared galaxies (e.g., Scoville et al. 1991 and references therein) has revealed a strong candidate for the fuel powering these enigmatic objects. The source of their luminosities of 3×10^{11} $L_{\odot}$ or more remains uncertain, with the leading candidates being compact nuclear super-starbursts (Rieke et al. 1985; Joseph & Wright 1985; Condon et al. 1991, hereafter CHYT) and dust-enshrouded active nuclei (Sanders et al. 1988b; Lonsdale, Smith, & Lonsdale 1995). Using spatially- and velocity-resolved observations to constrain the properties, distribution, and kinematic behavior of the molecular fuel, one can better understand whether the gas is capable of supporting

an outburst of star formation luminous enough to power the bolometric luminosity, or whether a dust-enshrouded AGN is necessary. Because of the distance of the closest of these objects (50–150 Mpc) and the small size ($\lesssim$1 kpc) of the molecular gas complexes, 2–3″ angular resolution is required to significantly resolve the central gas concentrations. Such resolution has become possible with millimeter arrays in the last few years.

The most easily observed tracer of molecular gas is the CO $J = 1 \rightarrow 0$ transition at 115.3 GHz, yet only a handful of luminous infrared galaxies have been imaged at such high resolution (Scoville et al. 1991; Sargent & Scoville 1991; Yun, Scoville & Knop 1994; Yun & Scoville 1995). In order to enlarge this sample, we have undertaken a high-resolution survey of several luminous IR galaxies in several molecular transitions. Our observations of the CO $J = 1 \rightarrow 0$ and CO $J = 2 \rightarrow 1$ transitions in Mrk 231, the most luminous object in our sample, are presented in Chapter 2. Chapter 2 also contains an extensive discussion of the analysis techniques for deriving molecular gas masses and the gas conditions. In the present paper, we present the results of our observations of the CO 1→0 transition for six additional luminous infrared galaxies: NGC 2623, IC 883, NGC 6090, NGC 6240, NGC 7469, and NGC 7674. In §3.2 we describe how the sample was selected; in §3.3 we discuss the observations and the data reduction; in §3.4 we present the results of the observations, with a discussion of each individual object; in §3.5, the implications of these results on our understanding of the general population of luminous infrared galaxies are discussed; and in §3.6 we present a summary of our conclusions.

3.2. Sample selection

The sample of seven objects was chosen from galaxies with $L_{IR} > 10^{11.5}$ $L_\odot$ in the original and extended IRAS Bright Galaxy Samples (BGS1 and BGS2). for which single dish CO 1→0 data exist (Sanders, Scoville, & Soifer 1991; hereafter SSS). BGS1 and BGS2 together include galaxies over nearly the entire sky above galactic latitudes of 5° with $F_\nu(60\ \mu m) \geq 5.24$ Jy (Soifer et al. 1986, 1989; Sanders et al. 1995). SSS obtained single dish CO 1→0 data for a large number of the most luminous of the BGS galaxies; they observed 43 out of 69 BGS1 objects with $L_{IR}(8\text{–}1000\ \mu m) > 10^{11}$ $L_\odot$, plus 6 additional objects from BGS2 in the same luminosity range. SSS selected these objects based on sky position at the time of observation, so their sample is not biased by any galaxy properties. From this list of luminous IR galaxies observed in CO 1→0, we selected our sample. Interested in the most luminous objects, but those close enough so that we could resolve kpc-size structures, we set a lower luminosity limit of $10^{11.5}$ $L_\odot$. This resulted in a reasonably large set of objects, which we narrowed down by selecting objects closer than 125 Mpc, plus the extraordinary object Mrk 231 at a distance of 174 Mpc. In this final selection, we also biased our choices towards single nucleus or close double nucleus systems so that only one pointing center was required, and towards high declination objects so that deconvolution of the aperture synthesis images would be more straightforward.

Table 3–1 summarizes some of the basic properties of the seven luminous infrared galaxies we have studied. The distances used in this paper are those quoted by SSS, which were calculated using the Virgocentric flow model of Aaronson et al. 1982, with

Table 3–1. Basic data for the galaxy sample

object	D	L_{IR}	spectral class	interaction class[a]	nuclear separation	common aliases	ref[b]
	(Mpc)	($L_\odot$)			(″)		
(1)	(2)	(3)	(4)	(5)	(6)	(7)	(8)
NGC 2623	76.1	3.5×10^{11}	LINER	M1	...	UGC 4509, Arp 243, VV 79	1
Mrk 231	173.9	3.5×10^{12}	Sy 1	M1	...	UGC 8508	2
IC 883	97.8	4.0×10^{11}	H II	M1	...	UGC 8387, Arp 193, VV 821	3
NGC 6090	123.3	3.2×10^{11}	H II	M2	5.8	UGC 10267, Mrk 496, VV 626	4
NGC 6240	100.9	6.6×10^{11}	LINER	M2	1.5	UGC 10592, VV 617	5
NGC 7469	66.4	4.0×10^{11}	Sy 1	I	80	UGC 12332, Arp 298, Mrk 1514	6
NGC 7674	115.3	3.2×10^{11}	Sy 2	I	33	UGC 12608, Mrk 533, Arp 182 VV 343a, HCG 96a	7

Columns: (1) object; (2) distance, using $H_0 = 75$ km s^{-1} Mpc^{-1} and the Virgocentric flow model of Aaronson et al. 1982; (3) infrared luminosity from 8–1000μm, as quoted in Sanders et al. 1991; (4) optical spectral class of nuclear emission lines; (5) morphological interaction class (e.g., Sanders et al. 1991); (6) angular separation of double nucleus at radio wavelengths (optical for NGC 7674/HCG 96c and NGC 7469/IC 5283); (7) common aliases, from the NASA/IPAC Extragalactic Database; (8) reference for the optical spectral class.

Notes:
[a] M1: merger, single nucleus; M2: merger, double nucleus; I: member of interacting pair, non-overlapping disks.
[b] Spectral class references: (1) Heckman et al. 1983; (2) Boksenberg et al. 1977; (3) Liu & Kennicutt 1995; (4) Mazzarella & Boroson 1993; (5) Heckman, Armus, & Miley 1987; (6) Khachikian & Weedman 1974; (7) Mazzarella & Balzano 1986.

$H_0 = 75$ km s^{-1} Mpc^{-1}. Except for ultraluminous Mrk 231 at 3.5×10^{12} $L_\odot$, they all have L_{IR} in the range from 3.0 to 6.6×10^{11} $L_\odot$. Based on their optical morphology, five objects are classified as mergers and two as interacting pairs (SSS). Two of the mergers—NGC 6090 and NGC 6240—are known to have double nuclei. The nuclear optical spectra cover a wide range of types (see Table 3–1)—Seyfert 1, Seyfert 2, LINER and H II—underlining the uncertainty in the luminosity source of luminous infrared galaxies.

3.3. Observations

The CO observations were performed with the Owens Valley millimeter array at Big Pine, California. The array was expanded from 3 to 6 telescopes during the period of

Table 3–2. Summary of CO 1→0 observations

object	pointing center (B1950.0) α	δ	center of passband[a] cz (km s^{-1})	dates of tracks	no. of telescopes	synthesized beam natural HPBW (″)	PA	synthesized beam uniform HPBW (″)	PA
NGC 2623 ...	$8^h\,35^m\,25^s.27$	+25° 55′ 50″.2	5538	1993 Sep 18	5	3.46 × 2.43	98°	2.54 × 1.89	95°
				1993 Dec 31	5				
				1994 Feb 16[b]	5				
Mrk 231[c]	$12^h\,54^m\,05^s.01$	+57° 08′ 38″.1	12660	1993 Apr 28	4	2.97 × 2.41	67°	2.51 × 2.03	68°
				1993 May 06	4				
				1993 May 14	4				
IC 883	$13^h\,18^m\,17^s.03$	+34° 24′ 04″.5	7000	1993 Apr 24	4	3.81 × 3.23	95°	2.41 × 1.90	98°
				1993 May 16	4				
				1993 Jun 23	4				
				1993 Dec 10	5				
NGC 6090 ...	$16^h\,10^m\,24^s.56$	+52° 35′ 05″.2	8831	1993 Feb 03	4	3.21 × 2.19	90°	2.69 × 1.83	89°
				1993 Jun 10	4				
				1994 Jan 15[b]	5				
NGC 6240 ...	$16^h\,50^m\,27^s.862$	+2° 28′ 58″.87	7335	1993 Jan 01	3	4.93 × 4.12	11°	3.32 × 2.38	90°
				1993 Jan 26	4				
				1993 Apr 16	4				
				1993 May 22	4				
				1993 Jun 15	4				
				1993 Dec 15	5				
NGC 7469 ...	$23^h\,00^m\,44^s.4$	+8° 36′ 16″.0	4963	1993 Jul 04	4	8.33 × 6.28	175°	...	...
NGC 7674 ...	$23^h\,25^m\,24^s.41$	+8° 30′ 12″.6	8669	1992 Dec 16	3	3.47 × 2.40	102°	3.21 × 1.77	97°
				1992 Dec 30	3				
				1993 Feb 06	4				
				1993 Apr 14	4				
				1993 Jun 11	4				
				1993 Jun 12	4				
				1995 Dec 20	6				
				1995 Dec 29	6				
				1996 Jan 08	6				

Notes:
[a] All spectrometer data has 112 channels of 4 MHz (10.7 km s^{-1}) bandwidth.
[b] Data affected by time round-off error; see text for explanation.
[c] Maps and results discussed in Chapter 2.

the CO 1→0 observations—from 1992 Dec to 1994 Feb. In order to obtain sufficient spatial frequency (uv) coverage to produce reliable aperture synthesis images, tracks of 6 to 12 hours were taken on each galaxy using several different configurations of the telescopes. Occasionally, duplicate tracks were obtained in a single configuration when poor atmospheric transparency or poor coherence reduced the quality of the data or when scheduling conflicts caused a track to be prematurely ended. Table 3–2

lists the pointing and passband centers for each object, as well as the dates and number of operational telescopes for each track. Data were recorded simultaneously with a digital spectrometer and a 1 GHz analog continuum correlator. (For data obtained prior to 1993 Sep, the bandwidth of the analog correlator was 500 MHz.) The digital spectrometer consists of four independent modules (Padin et al. 1993), which were arranged to cover adjacent, partially-overlapping, sections of the IF. In this way, the spectrometer covered a bandwidth of 464 MHz ($\sim$1240 km s^{-1}) with 116 clean frequency channels of 4 MHz resolution ($\sim$10.7 km s^{-1}). The half-power width of the primary beam is 66″ at 112.5 GHz, so only a single pointing center for each object, centered at or near the position of the peak of the centimeter-wave continuum emission (Condon et al. 1990; Carral, Turner & Ho 1990), was needed. To remove time-dependent atmospheric and instrumental phase drifts, we observed unresolved quasars near in the sky to the sample objects every thirty minutes.

Phase, passband, and flux calibration were performed using the OVRO millimeter array software (Scoville et al. 1993). Instrumental passbands were derived from the spectra of bright quasars (e.g., 3C 273, 3C 454.3, 3C 345), and the absolute flux scales were obtained from integrations on Uranus or Neptune, correcting the planet fluxes for resolution effects. The uncertainty of the flux calibrations are roughly 10%.

After the *uv* data for each track had been calibrated and the tracks combined into a single dataset for each object, spectral line maps were made using the NRAO AIPS and CIT DIFMAP (Shepherd, Pearson, & Taylor 1994) software packages. For objects in which continuum emission was detected in the line-free spectrometer channels, we

subtracted a constant continuum value from each *uv* data point with the AIPS task 'UVLIN.' The properties of the millimeter-wave continuum emission are discussed in §4.3.2. Using the AIPS task 'MX,' we Fourier transformed and deconvolved—with the CLEAN algorithm—the individual channel maps to produce CO 1→0 data cubes for both natural and uniform weighting of the *uv* data. (For NGC 7469, we only have data in a single configuration, and the difference between the two weighting cases is minimal; hence we used only natural weighting for this object.) The synthesized beam half-power widths (HPBW) for both weightings are listed in Table 3–2 for each object. Absolute positions in the final maps should be accurate to within 0″.5. For the five-telescope tracks on NGC 2623 and NGC 6240, we used DIFMAP to perform self-calibration of the amplitudes and phases on the line-center emission. Comparison of the maps produced with and without self-calibration reveals that self-calibration had little effect upon the final data cubes.

Two of the CO 1→0 tracks—one for NGC 2623 in an intermediate-resolution configuration and one for NGC 6090 in a high-resolution configuration—are corrupted by a time round-off error that was present in the observing software at the time of the observations. Approximately every 10 minutes, a random timing error from +50 to −50 milliseconds was introduced. This real-time error has two detrimental effects on the data (DeGeus 1994): (1) decorrelation of the signal due to random phase jumps, and (2) beam smearing in the direction of right ascension due to random position errors. The first effect is proportional to the instantaneous length of the projected baseline in the east-west direction (u), while the second effect is proportional to the

cosine of the source declination. For the corrupted track on NGC 2623, the longest east-west baseline is only 115 m, so the decorrelation problem is not overly severe ($\lesssim$13%) and was corrected by self-calibration. The beam smearing, while impossible to correct, amounts to less than a second of arc—significantly less than both the final synthesized beam size and the deconvolved source size, which are both around 2″.5. To verify that the east-west structure seen in our CO map of NGC 2623 is not due to this smearing, we mapped the object using only the two tracks unaffected by the round-off error (one of which was in a high-resolution configuration) and achieved the same result. The corrupted NGC 6090 track contains east-west baselines up to 200 m, and thus it is more seriously affected by the time round-off error. We discarded all data with $|u| > 50$ kλ (11% of the data in the track) to bring the maximum decorrelation to less than 8%. (Because we did not perform self-calibration on this object, we used a more stringent decorrelation criterion than for NGC 2623.) Due to the high declination of NGC 6090, the beam smearing amounts to only 0″.6. This is three times smaller than the smallest dimension of the synthesized beam and ten times smaller than the observed source size; the smearing thus has a negligible effect on the final map.

3.4. Results

3.4.1. General

Measured quantities from the aperture synthesis images of the seven galaxies are listed in Table 3–3 for the global CO emission and in Table 3–4 for the core CO com-

Table 3–3. Global CO 1→0 properties

object	F_T (Jy km s^{-1})	θ_T (″)	F_{sd} (Jy km s^{-1})	F_T/F_{sd}	reference[a]
(1)	(2)	(3)	(4)	(5)	(6)
NGC 2623	153	1.8	110	1.4	1
Mrk 231[b]	62	<1.5	97	0.64	2
IC 883	202	4.1	220	0.9	3
NGC 6090	169	31[c]	99[d]	1.7[d]	1
NGC 6240	324	28[c]	277	1.2	2
NGC 7469	317	4.6	220[e]	1.4[e]	1
NGC 7674	85	22[c]	92	0.9	1

Columns: (1) object; (2) total CO flux detected by the Owens Valley millimeter array observations; (3) maximum (deconvolved) extent of the integrated CO emission in the natural weight maps; (4) single dish CO flux; (5) ratio of the interferometer to the single dish CO flux; (6) reference for the single dish CO flux.

Notes:
[a] References for single dish CO fluxes: (1) Sanders et al. 1991; (2) Solomon, Downes, & Radford 1992; (3) Mazzarella et al. 1993. The first reference directly quotes neither F_{sd} (Jy km s^{-1}) nor a calibration constant (Jy K^{-1}), so we have re-calculated F_{sd} from the quoted F_{CO} (K km s^{-1}) and the primary beam of the telescope used (see Gordon, Baars, & Cocke 1992).
[b] See Chapter 2.
[c] The maximum size scale to which the interferometer is sensitive is 25–30″, so the total CO extent may be greater than these numbers, though due to the large values of F_T/F_{sd}, any undetected component is almost certainly a small fraction of the total CO flux.
[d] The published single dish spectrum shows a line width only two-thirds of that seen in the current observations.
[e] The quoted line width of the single dish spectrum is only three-fourths of that seen in the current observations.

ponents which dominate each object except NGC 7674. Selected derived quantities are presented in Table 3–5. The CO 1→0 data for five of the objects studied here are displayed in Figures 3–1 to 3–15 and Figures 3–17 to 3–20. For Mrk 231, CO 1→0 and CO 2→1 are presented and discussed in detail in Chapter 2; for NGC 7469, our CO 1→0 map is of higher signal-to-noise, but lower spatial resolution, than the earlier map of Sanders et al. (1988a), and so is not shown here.

For all the galaxies except NGC 6090, the aperture synthesis maps have recovered 64–140% of the single dish flux (see Table 3–3)—consistent with the entire single dish flux within the large relative calibration uncertainties (~20%). In NGC 6090, however, the array sees 70% *more* flux. The discrepancy is likely due to spectral

Table 3–4. Core CO 1→0 properties

object	F_c	f_c	θ_c	coordinates of peak (B1950.0)		FWHM	FW20	cz_{mid}
	(Jy km s^{-1})		(″)	α	δ	(km s^{-1})	(km s^{-1})	(km s^{-1})
(1)	(2)	(3)	(4)	(5)	(6)	(7)	(8)	(9)
NGC 2623	153	1.0	1.8 × 1.5	$8^h35^m25^s.28$	+25° 55′ 50″.3	317 (21)	423	5540
Mrk 231[a]	62	1.0	1.0 × 0.3[b]	$12^h54^m05^s.00$	+57° 08′ 38″.1	186 (9)	296	12645
IC 883	202	1.0	4.1 × 2.2	$13^h18^m17^s.09$	+34° 24′ 03″.5	388 (18)	454	6995
NGC 6090	96	0.57	5.4 × 3.0	$16^h10^m24^s.36$	+52° 35′ 03″.8	138 (6)	322	8849
NGC 6240	185	0.57	1.6 × 1.5	$16^h50^m27^s.83$	+2° 28′ 58″.1	469 (15)	731	7313
NGC 7469	317	1.0	4.6 × 3.9	$23^h00^m44^s.42$	+8° 36′ 16″.2	273 (3)	346	4917
NGC 7674	12	0.14	<(1.6 × 0.9)	$23^h25^m24^s.38$	+8° 30′ 12″.8	147 (16)	192	8669

Columns: (1) object; (2) CO 1→0 flux of the core component; (3) fraction of the interferometer CO flux in the core component; (4) deconvolved major and minor axis of the core component; (5) peak value of the velocity-integrated CO flux; (6)–(7) coordinates of the peak; (8) line profile full width at half maximum at the position of the peak; (9) line profile full width at 20% maximum at the same position; (10) line profile midpoint at 20% maximum at the same position.

Notes:
[a] See Chapter 2.
[b] From CO 2→1 map (Chapter 2).

baseline uncertainties in the single dish data, since the single dish spectrum of SSS shows a significantly narrower line width than our data. Thus, there is no compelling evidence for any missing flux in the CO data presented here.

The synthesized beam resolves the CO emission in each object in our sample. In six of the seven objects, nearly all of the detected CO emission is concentrated within a region smaller than 1.6 kpc in radius. In Mrk 231, NGC 2623, and NGC 6240, the small sizes of the powerful CO cores ($R_c < 0.42$ kpc) rival those seen in Arp 220 (Scoville et al. 1991; Scoville, Yun, & Bryant 1996) and IC 694 (Sargent & Scoville 1991; Aalto et al. 1996).

The morphology of the CO emission varies with the interaction class of the object in this small sample. The three single nucleus mergers in our seven-object sample (Mrk 231, NGC 2623, IC 883) exhibit no CO emission outside the core component.

Table 3–5. Derived quantities

	total		core						
object	d_T	$M^*_{g,T}$	R_c	$M^*_{g,c}$	M_{dyn}	$M^*_{g,c}/M_{dyn}$	$<\Sigma^*_{g,c}>$	$<A^*_K>$	T_x^{min}
	(kpc)	(10^9 $M_\odot$)	(kpc)	(10^9 $M_\odot$)	(10^9 $M_\odot$)		($M_\odot$ pc^{-2})	(mag)	(K)
(1)	(2)	(3)	(4)	(5)	(6)	(7)	(8)	(9)	(10)
NGC 2623	0.66	10.4	0.33	10.4	5.37	1.9	21000	56	11
Mrk 231[a].....	0.84	21.6	0.42	21.6	3.38	6.4	27000	72	34[b]
IC 883	1.92	22.7	0.96	22.7	22.6	1.0	5400	14	10
NGC 6090	18.5	29.9	1.61	17.0	4.60	3.7	2600[c]	6.9	7
NGC 6240	13.7	38.6	0.39	22.1	14.3	1.5	32000	85	17
NGC 7469	1.46	16.5	0.73	16.5	8.46 9.53[d]	2.0 1.7[d]	6800	18	8
NGC 7674	12.3	13.2	<0.45	1.86	1.50 26.3[e]	1.2 0.07[e]	>2100	>5.4	11

Columns: (1) object; (2) maximum linear extent of CO emission; (3) total mass of molecular gas seen by the array, estimated using the standard M_g/L'_{CO} conversion factor; (4) linear semi-major axis of core CO component; (5) mass of molecular gas in the core, estimated using the standard conversion factor; (6) dynamical mass of the core, estimated for a spherical geometry from the observed line width and radius; (7) ratio of molecular gas mass to dynamical mass in the core; (8) mean molecular gas surface density in the core, using a source area of $\pi R_c^2/\ln 2$; (9) mean K-band ($\lambda 2.2\mu$m) extinction through the core implied by the molecular gas column density, assuming a standard extinction law (e.g., Mathis 1993); (10) minimum CO 1→0 excitation temperature in the core.

Notes:
[a] From CO 1→0 and CO 2→1 maps (Chapter 2).
[b] Assumes that CO 1→0 arises from a smaller area than the 3σ upper limit on the CO 2→1 source size: $1''.2 \times 0''.66$ (Chapter 2).
[c] Calculated using the deconvolved source solid angle.
[d] Disk with an axis inclined 47° to the line-of-sight.
[e] Disk with an axis inclined 17° to the line-of-sight.

The two double nucleus mergers (NGC 6240 and NGC 6090) show low-level CO emission outside the core, extended over scales greater than 10 kpc. NGC 6090, with the widest double nucleus of the mergers, possesses the CO distribution with the largest core radius (1.6 kpc). On the other hand, the two objects that are members of interacting pairs exhibit different morphologies from each other: NGC 7469 shows all of its CO emission within a radius of 0.73 kpc, and resembles the mergers in that sense; NGC 7674, on the contrary, is the only object to show the bulk of its CO emission extending out to a large fraction of its optical disk radius.

For disk molecular clouds in the Milky Way, the molecular gas mass is nearly proportional to the CO luminosity (Scoville & Good 1989). We have used the empirical constant of proportionality, 4.9 $M_\odot$ (K km s^{-1} $pc^2)^{-1}$ (e.g., Solomon & Barrett 1991), which we hereafter refer to as the "standard conversion factor," to make initial estimates of the masses of the molecular gas concentrations, $M_g = M(H_2 + He)$:

$$M_g^* = 1.20 \times 10^4 \, F_{CO} \, D_{Mpc}^2 \, (1+z)^{-1} \quad [M_\odot] \, . \tag{3–1}$$

(A superscripted asterisk to M_g and other quantities refers to the use of the standard conversion factor.) In equation 3–1, F_{CO} is the interferometric spatial- and velocity-integrated CO flux in Jy km s^{-1}, D_{Mpc} is the adopted luminosity distance in Mpc, and z is the redshift. The standard conversion factor that we adopt is equivalent to $N(H_2)^*/I_{CO} = 2.25 \times 10^{20}$ cm^{-2} (K km $s^{-1})^{-1}$.

We also have used the CO sizes and line widths to dynamically estimate the total mass in the cores of these objects, M_{dyn} (see Appendix A). The dynamical masses in Table 3–5 have not been corrected for inclination effects except where noted.

In the cores of the five mergers, M_g^* is either comparable to or significantly greater than M_{dyn}, and for Mrk 231 and NGC 6090, M_g^* is many times greater than M_{dyn}. This unphysical result can be explained either by inclination effects causing M_{dyn} to underestimate the true dynamical mass (e.g., if we are viewing a gas disk whose rotation axis is nearly along our line-of-sight) or by the standard conversion factor causing M_g^* to overestimate of the actual gas mass, or by a combination of these effects. For Mrk 231, in Chapter 2, we use a detailed analysis of the behavior of the CO conversion factor to argue that M_g^* is unlikely to be overestimating the gas mass

by the minimum factor of 6.4 required, and thus conclude that much of the M_g^*/M_{dyn} discrepancy in that object is due to inclination effects, a conclusion supported by the relatively narrow CO line width of 186 km s^{-1} FWHM. For NGC 6090, similar conversion factor arguments fail to place as strong constraints on the possible overestimate of the gas mass— primarily due to the smaller discrepancy between M_g^* and M_{dyn} and the order of magnitude smaller Σ_g^*. Nonetheless, inclination appears to be the principal culprit in causing M_{dyn} to be smaller than M_g^*: the CO line width of NGC 6090 is an exceedingly narrow 138 km s^{-1}—remarkable due to the relatively large extent (3.2 kpc) of the bright CO emission; the optical morphology of NGC 6090 further reinforces the suggestion that we are viewing this merger from a direction close to its axis of angular momentum. If the angle of inclination between our line-of-sight and the rotation axis is 30°, the intrinsic line width becomes 276 km s^{-1}, still smaller than the line widths in IC 883 and NGC 6240, and the dynamical mass estimate becomes 1.8×10^{10} $M_\odot$, roughly equal to M_g^*. Smaller inclinations can raise M_{dyn} comfortably above M_g^* without any appeal to an overestimate of the gas mass. Such an overestimate, however, remains a possibility.

The nuclear dynamical masses of NGC 7469 and NGC 7674 are also likely being severely underestimated by M_{dyn} when no inclination corrections are performed. The axis of the galactic disk of NGC 7469 is inclined 47° to our line-of-sight (e.g., Genzel et al. 1995); accounting for this still leaves M_{dyn} 1.7 times smaller than M_g^* (see Table 3–5). The nuclear ring of starburst emission from which much of the CO emission arises (§3.4.2.5; Meixner et al. 1990), however, appears nearly circular and

may be at a significantly smaller inclination angle (cf. Genzel et al. 1995). If the inclination of the ring is only 25°, $M_{\rm dyn}$ becomes significantly larger than $M_{\rm g}^{*}$ and no gas mass overestimate is required. The disk of NGC 7674 is also very nearly face-on to our line-of-sight; correcting for this large effect on the observed line widths reveals that $M_{\rm g}^{*}$ is less than 10% of $M_{\rm dyn}$ in the nucleus. NGC 7674 is thus the only object in our sample in which the molecular gas is obviously not the dominant mass component in the core.

On the other hand, the appeal to viewing angle to resolve the discrepancy between $M_{\rm g}^{*}$ and $M_{\rm dyn}$ fails in several of the galaxies studied here. In at least two, and probably three, galaxies in the sample, the standard conversion factor must be overestimating the gas mass by a significant number. In Mrk 231, the CO 2→1 observations reveal a source with an aspect ratio of 3:1, uncertain by 40% (Chapter 2). To be conservative, we adopt an aspect ratio of 1.5:1, which, if it is an inclined disk, suggests that $M_{\rm g}^{*}$ is 3.6 times greater than the inclination-corrected dynamical mass. Thus, $M_{\rm g}^{*}$ is likely overestimating the gas mass of Mrk 231 by more than a factor of 3.6. In NGC 6240, $M_{\rm g}^{*}$ is 1.5 times the dynamical mass implied by the observed line width. Based on the very broad observed line width ($\Delta v = 469$ km s^{-1} FWHM), the highly elongated large-scale optical/infrared morphology, and the prominent dust lane, NGC 6240 is probably an edge-on system; thus the observed $M_{\rm dyn}$ should closely approximate the actual dynamical mass. Hence the true gas mass must be at least 50% smaller than $M_{\rm g}^{*}$, and, accounting for a likely stellar mass of several 10^9 M$_\odot$ in its inner few hundred pc, perhaps significantly smaller still. IC 883 also shows a relatively broad CO line

width ($\Delta v = 388$ km s^{-1} FWHM) and a highly elongated optical infrared morphology indicative of an edge-on orientation. In this galaxy, $M_{\rm g}^{*} \approx M_{\rm dyn}$, but if we account for a reasonable mass of stars within the 1 kpc-radius CO emission region, $M_{\rm g}^{*}$ is at least slightly overestimating the gas mass. While for the other galaxies, the viewing angle uncertainties do not require the gas masses to be smaller than $M_{\rm g}^{*}$, this remains a significant possibility given the results for Mrk 231, NGC 6240, and IC 883.

Even if the actual gas masses are smaller than $M_{\rm g}^{*}$, the molecular gas almost certainly constitutes a major fraction, and possibly the majority, of the nuclear mass. For this not to be the case, the conversion factor would have to be reduced from the standard value by factors of over 3–4 or more. In Mrk 231, the most extreme case, the molecular gas mass is a *minimum* of 40% of the total nuclear mass, even if CO 1→0 is optically thin (§3.5.1.2) and the molecular gas is taken to be a disk inclined 60° to our line-of-sight. More conservative choices for either the optical depth of CO or the viewing geometry raise the nuclear gas mass fraction even higher.

3.4.2. Individual objects

In this section, we briefly summarize previous work on the individual objects, and we discuss the aperture synthesis CO maps. The discussion of the results for the CO 1→0 and the CO 2→1 maps of Mrk 231 is in Chapter 2.

3.4.2.1. NGC 2623

The prominent, long optical tails of NGC 2623 led Toomre (1977) and Joseph & Wright (1985) to infer that this system is the product of a strong tidal encounter

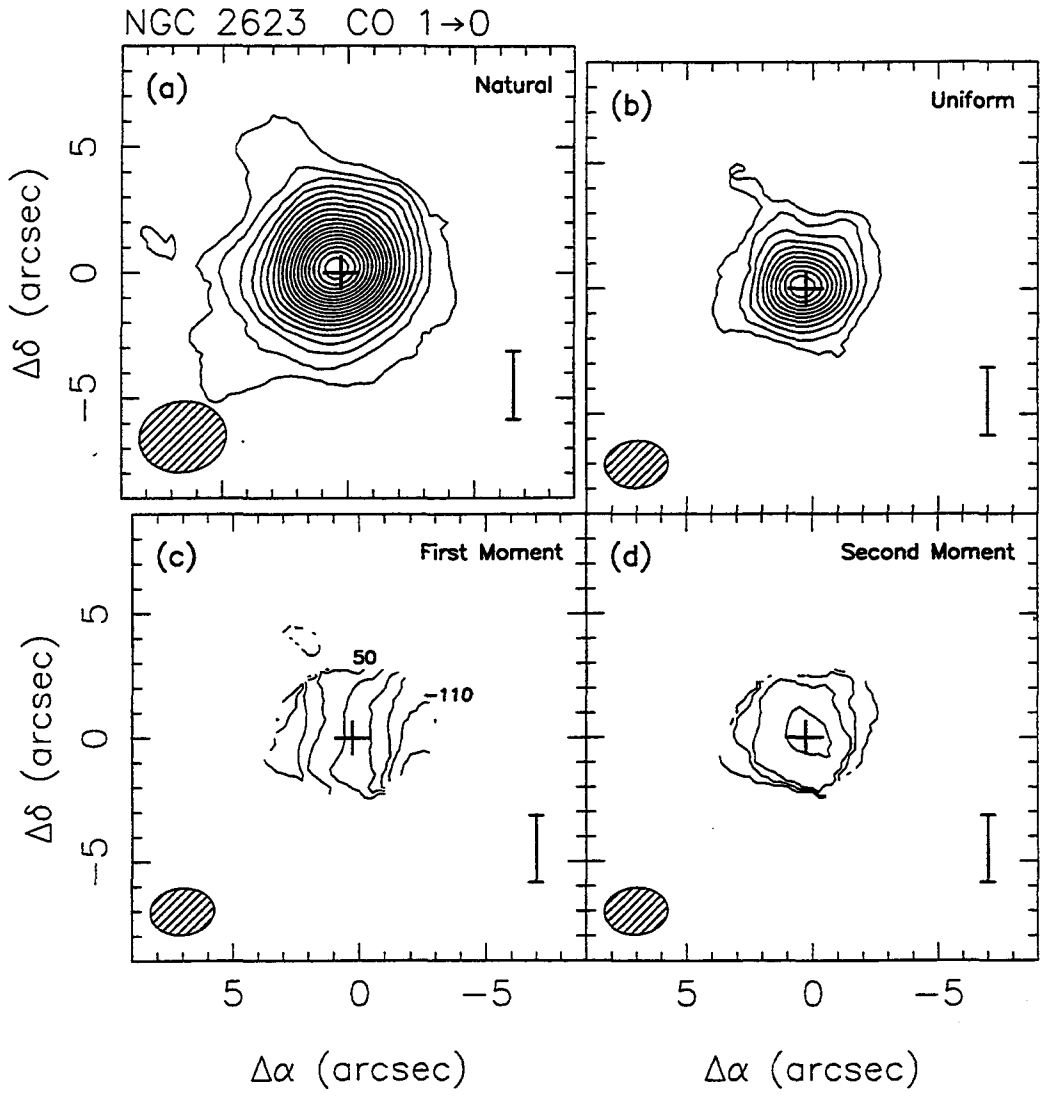

Figure 3–1. CO 1→0 maps of NGC 2623. (a) Velocity-integrated CO emission from the natural-weight aperture synthesis map. Contours are spaced linearly beginning at 4 Jy beam^{-1} km s^{-1}. (b) Velocity-integrated CO emission from the uniform-weight map. Contours are spaced linearly beginning at 5 Jy beam^{-1} km s^{-1}. (c) First velocity moment map of the CO emission from the uniform-weight map. Contours are at intervals of 40 km s^{-1}, and are labeled relative to the central passband velocity of cz = 5538 km s^{-1}. Relative velocities are calculated by the expression $v = c(\nu-\nu_0)/\nu$, where ν_0 is the central passband frequency, $\nu = \nu_R(1+z)^{-1}$, and ν_R = 115.271204 GHz is the rest frequency of the CO 1→0 transition. (d) Second velocity moment map of the CO emission from the uniform-weight map. Contours are spaced linearly beginning at 25 Jy km s^{-1}. The integrated emission maps were produced by summing over all line channels, while blanking pixels below twice the RMS noise level. The first and second moment maps were produced in a similar fashion, but with a blanking threshold of three times the rms noise. The hatched ellipses represent the half-power beam size, and the bars represent a linear dimension of 1 kpc. The "+" symbol represents the position of the sub-arcsecond 8.44 GHz continuum emission (Condon et al. 1991).

between two disk galaxies of similar mass. NGC 2623 shows a single, symmetric

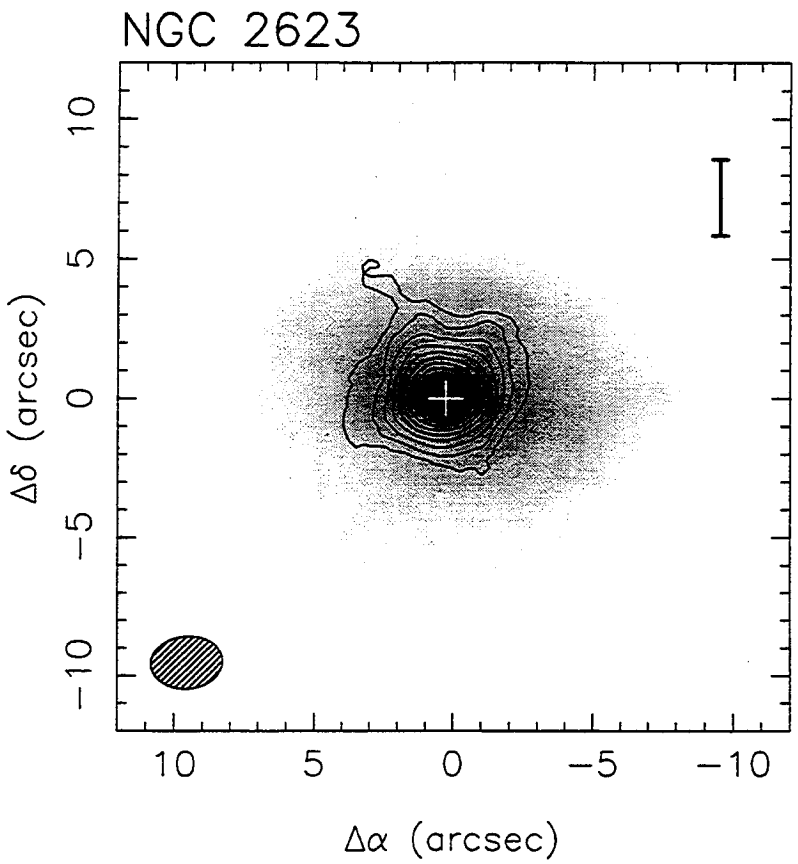

Figure 3–2. CO 1→0 map (uniform weight) in contours, superposed on a grayscale near-infrared K′ image of NGC 2623 from Sanders et al. 1996. To register the images, we assumed that the peak of the K′ emission is spatially coincident with the compact radio continuum source. The symbols have the same meaning as in Figure 3–1.

nucleus in the near-infrared K band (Joy & Harvey 1987), with a radial brightness profile that closely follows a $r^{1/4}$ law out to a radius of 8″ (3 kpc; Wright et al. 1990; Stanford & Bushouse 1991), suggesting that the original nuclei of the two systems have coalesced into a common merged nucleus. Optical emission lines appear in the central 5″ (1.6 kpc), and show a [N II]/Hα ratio around unity, implying a significant degree of shock excitation or a weak LINER source (Joy & Harvey 1987; Bernlöhr 1993; Heckman et al. 1983). Since 10 μm photometry in a 5″.7 aperture detects almost all of the flux seen by IRAS (Wynn-Williams & Becklin 1993), most of the infrared

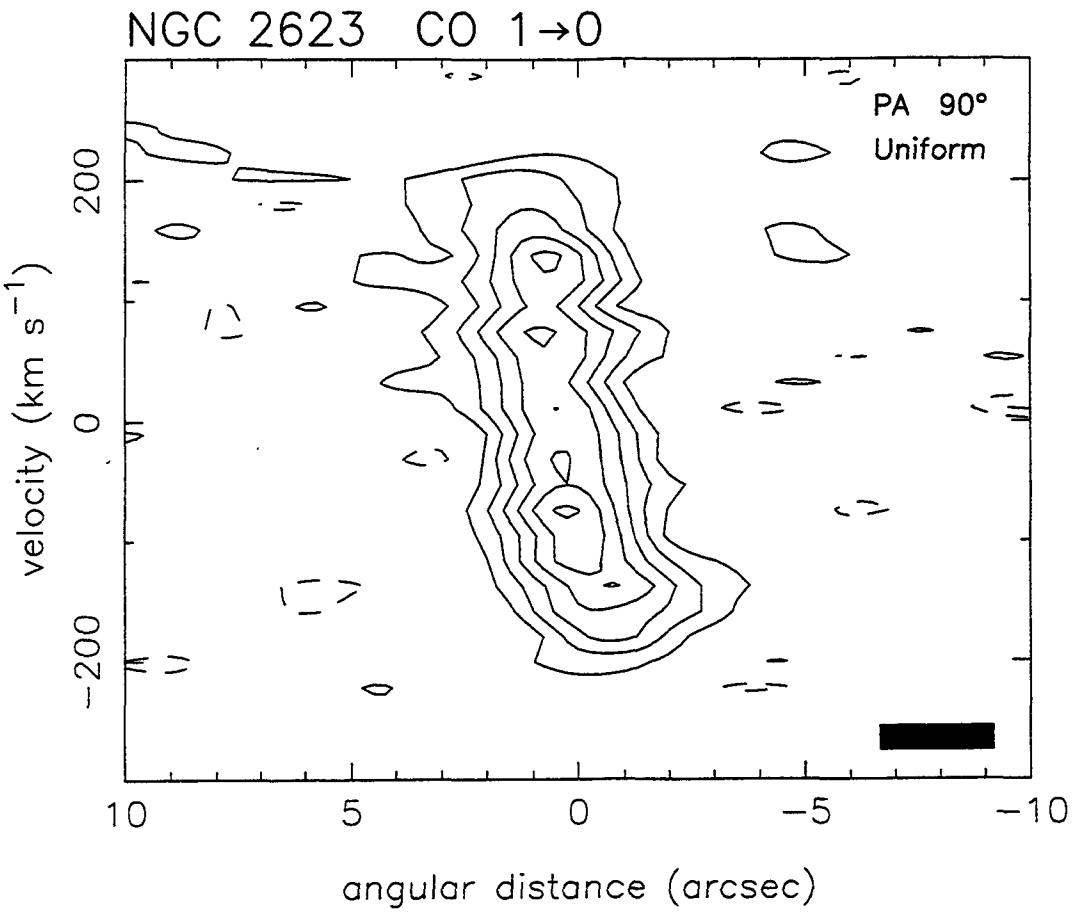

Figure 3–3. Position-velocity cut of the uniform-weight CO data cube for NGC 2623 through the peak of the integrated emission, along position angle 90°. This direction is roughly coincident with the that of the maximum velocity gradient. Contours are spaced linearly beginning at 34 mJy beam^{-1} (2σ for a smoothed frequency resolution of 8 MHz [21.2 km s^{-1}]). Negative contours are shown as dashed lines. The black rectangle represents a single resolution element in both dimensions.

luminosity likely arises from a small region around the single nucleus. In conjunction with $H - K$ infrared photometry (Carico et al. 1988), the strength of the nuclear 2.3 μm CO absorption bands leads to the interpretation that the nuclear K band emission is dominated by reddened light from the photospheres of red supergiants produced in a recent starburst (Ridgway, Wynn-Williams, & Becklin 1994). In fact, using models of starbursts, several authors have suggested that the powerful infrared luminosity of NGC 2623 is dominated by a recent nuclear starburst (CHYT; Bernlöhr

1993; Prestwich, Joseph, & Wright 1994). Norris et al. (1990) and Lonsdale, Smith, & Lonsdale (1993) detect a compact VLBI core in NGC 2623 at centimeter wavelengths with a size of order a milliarcsecond and brightness temperature greater than 10^7 K. This VLBI core, however, is the weakest relative to the infrared luminosity of all the detected objects in the sample of Norris et al., so the existence of the compact radio core in NGC 2623 may still be consistent with the interpretation that a starburst dominates the generation of the infrared luminosity.

The aperture synthesis CO 1→0 map of NGC 2623 (Figures 3–1 to 3–3) shows that the CO emission is dominated by a bright, slightly resolved core. The peak of the CO emission is coincident, within the uncertainties, with the peak of the cm-wave radio continuum core (0″.38 diameter, CHYT; Eales et al. 1990). Deconvolving the synthesized beam from the CO source reveals that the source is slightly resolved, with a major axis of 1″.8 in the north-south direction, and a minor axis of 1″.5. We estimate the uncertainties of these dimensions to be 0″.3 and 0″.5, respectively; so the CO emission region is consistent with being circular. The velocity gradient (Figure 3–1c) is roughly east-west, parallel to the major axis of the near-infrared emission (Figure 3–2). A position-velocity diagram in this direction (Figure 3–3) hints that the velocities may begin to flatten just before the CO emission cuts off, consistent with the hypothesis that the molecular gas mass constitutes the bulk of the mass in the nuclear region. If so, as $M_{\rm g}^*/M_{\rm dyn} = 1.9$ in NGC 2623, after allowing for inclination effects to raise the observed $M_{\rm dyn}$, $M_{\rm g}^*$ may only be overestimating the gas mass by a relatively small factor (<2), if at all. The CO spectrum of the bright

core (Figure 3–22a) reveals a very flat profile, with a full width at zero intensity of 500 km s^{-1}.

3.4.2.2. IC 883

Previous work on IC 883 suggests that IC 883 is a recently-merged system with a high star formation rate and a large mass of gas and dust. Like the other objects in our sample, IC 883 exhibits a peculiar optical morphology (Arp 1966). Its two linear optical "jets" show stellar absorption features, and thus are likely to be tidal tails (Keel 1985). The strong Balmer and [O II] emission lines in the nuclear optical spectrum indicate a large amount of star formation, while the presence of [O I] emission indicates a smaller contribution to the excitation from either shocks or a weak power-law UV source (e.g., Liu & Kennicutt 1995). Further evidence for a recent high rate of star formation is provided by the strong absorption in the 2.3 μm ro-vibrational bands of CO, suggesting prominent continuum emission from young supergiants (Ridgway et al. 1994). Like NGC 2623, IC 883 is an example of the formation of an elliptical-like remnant due to a merger: its near infrared K band profile approximates a $r^{1/4}$ profile out to a radius of 19″.5 (9 kpc), though deviations from the mean profile indicate that the system has not yet completely relaxed (Stanford & Bushouse 1991). Large quantities of gas in IC 883 are revealed by single dish observations, which show very bright CO emission (Radford, Solomon, & Downes 1991; Mazzarella et al. 1993). Indirect evidence for the presence of this gas comes from the colors of the near infrared continuum, which become progressively redder in $H - K$

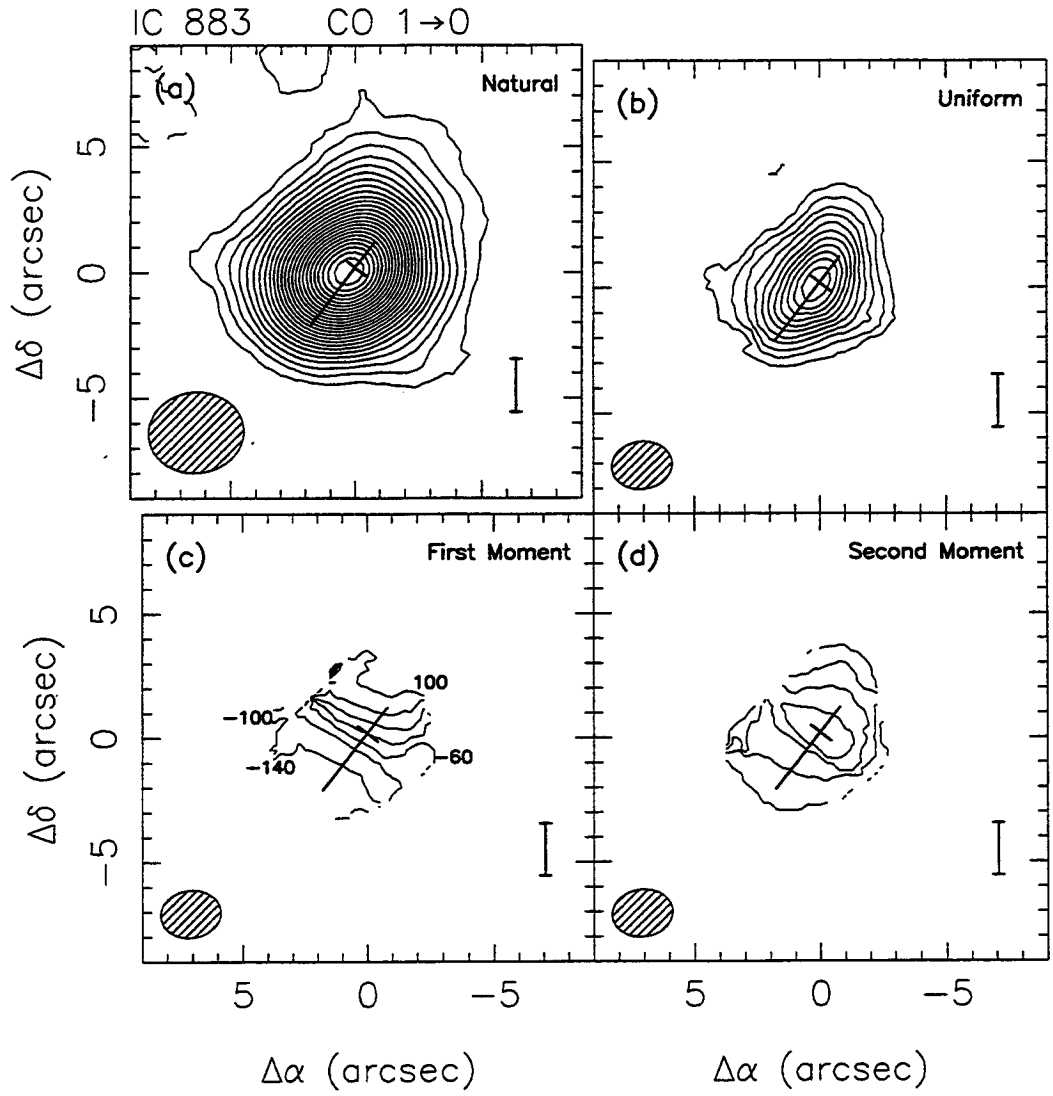

Figure 3–4. CO 1→0 maps of IC 883. (a) Velocity-integrated CO emission from the natural-weight aperture synthesis map. Contours are spaced linearly beginning at 4 Jy beam^{-1} km s^{-1}. (b) Velocity-integrated CO emission from the uniform-weight map. Contours are spaced linearly beginning at 5 Jy beam^{-1} km s^{-1}. (c) First velocity moment map of the CO emission from the uniform-weight map. Contours are at intervals of 40 km s^{-1}, and are labeled relative to the central passband velocity of $cz = 7000$ km s^{-1}. (d) Second velocity moment map of the CO emission from the uniform-weight map. Contours are spaced linearly beginning at 25 Jy km s^{-1}. These maps were produced in the same fashion of Figure 3–1. The hatched ellipses represent the half-power beam size, and the bar represent a linear dimension of 1 kpc. The bold crossed lines represent the peak position and the major and minor axis lengths of the 8.44 GHz continuum emission (Condon et al. 1991).

closer to the nucleus, indicating an obscured mixture of emission from stars and warm dust, and the ratio of Brγ recombination line emission to the thermal radio flux at

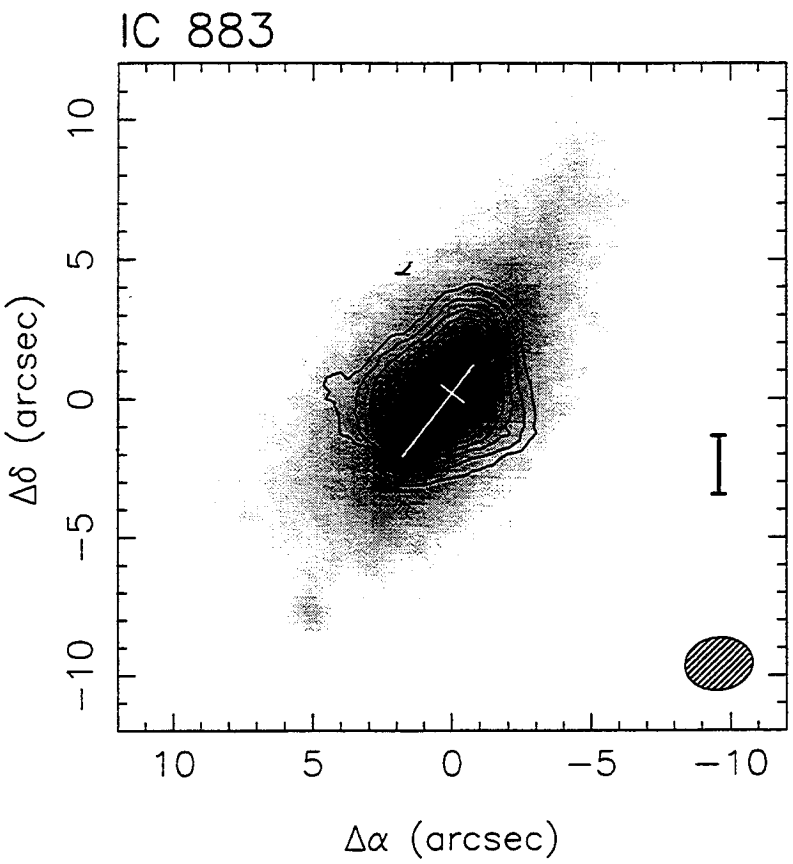

Figure 3–5. CO 1→0 map (uniform weight) in contours, superposed on a grayscale near-infrared K′ image of IC 883 from Sanders et al. 1996. The CO emission shows a similar morphology to both the near infrared and the radio continuum emission. To register the images, we assumed that the peak of the K′ emission is spatially coincident with the peak of the radio continuum emission. The symbols have the same meaning as in Figure 3–4.

8.44 GHz, which implies a very large K band dust optical depth of from 1.7 to 14 (Smith et al. 1995).

The aperture synthesis maps of the CO 1→0 emission are presented in Figures 3–4 to 3–7. The deconvolved CO source size is $4''.1 \times 2''.2$ (1.9×1.0 kpc)—significantly larger than the synthesized beam. Near the CO core and to its south-east, the near-infrared, non-thermal radio continuum, and the major axis and velocity gradient of the CO emission are all elongated along a position angle of 322°. To the north-west of the CO peak, both the major axis and velocity gradient of the CO emission bend

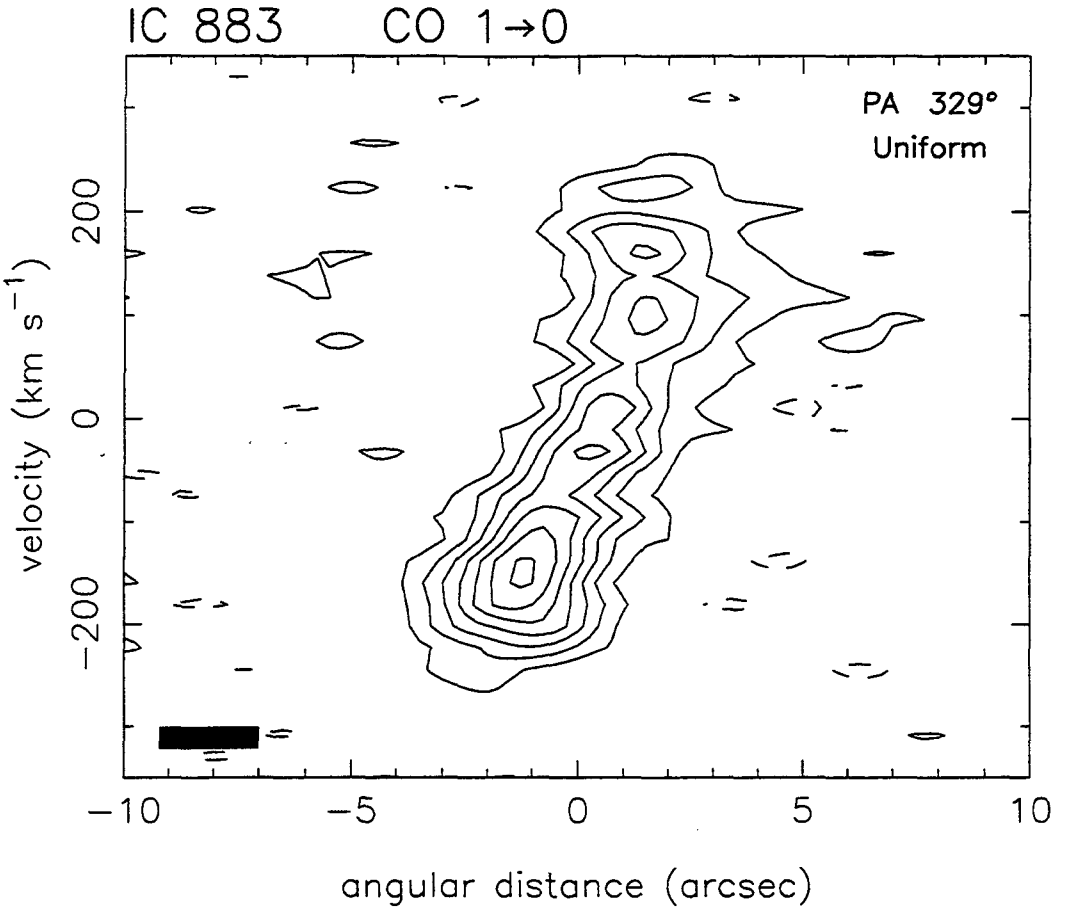

Figure 3–6. Position-velocity cut of the uniform-weight CO data cube for IC 883 through the peak of the integrated emission, along the major axis position angle of 329°. Contours are spaced linearly beginning at 43 mJy beam^{-1} (2σ for a smoothed frequency resolution of 8 MHz [21.3 km s^{-1}]). Negative contours are shown as dashed lines. The black rectangle represents a single resolution element in both dimensions.

towards the north. The near-infrared K′ band emission exhibits a similar bending of its major axis in the north-west (Figure 3–5; Sanders et al. 1996), while the non-thermal radio continuum becomes more diffuse and less collimated to the north-west than it is in the south-east (CHYT).

The lowest contours of the integrated CO emission show an irregular shape, yet the brightest emission is remarkably symmetric, suggesting an ordered gas distribution. The channel maps (Figure 3–7) exhibit the same qualitative behavior as a disk inclined

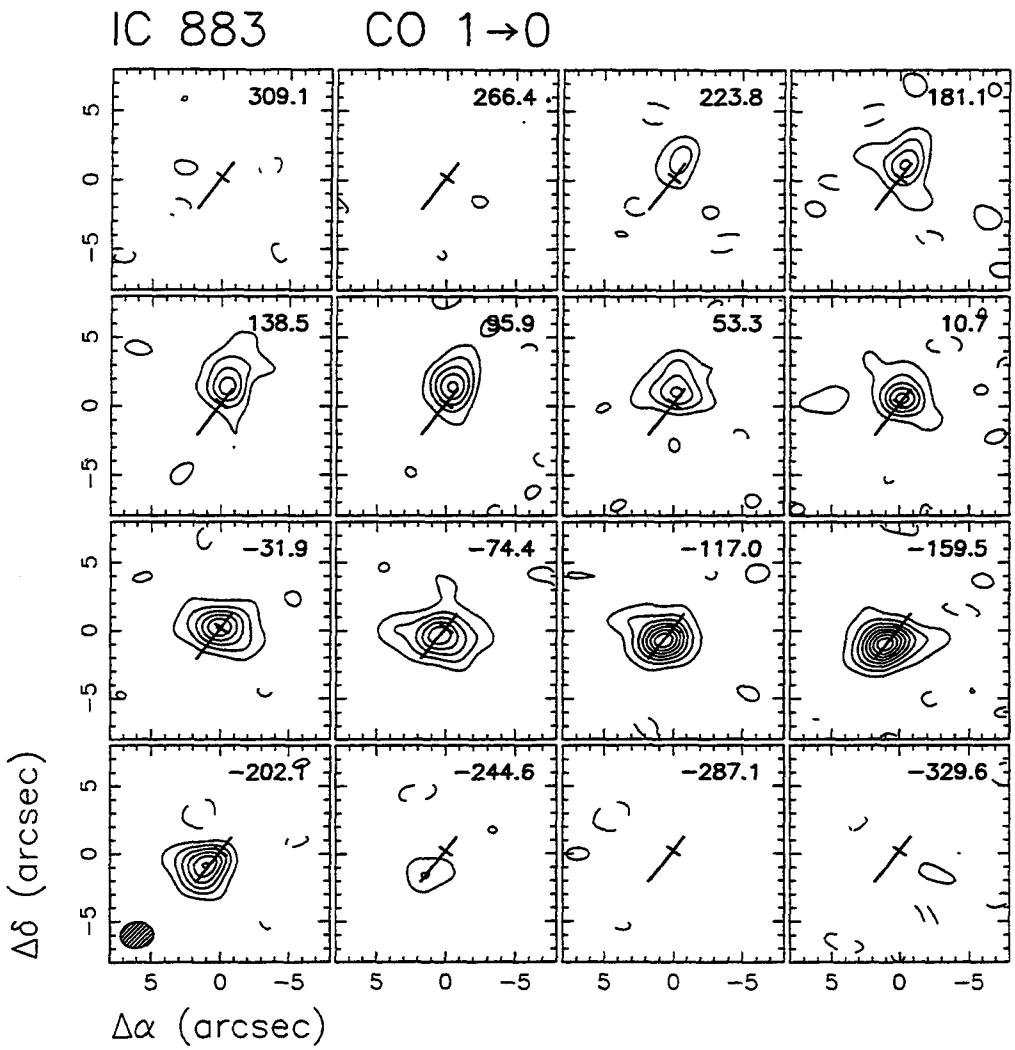

Figure 3–7. Channel maps of the IC 883 uniform-weight CO data cube, binned by 16 MHz (42.6 km s^{-1}), with the central velocities of each map shown at upper right. Contours are spaced linearly beginning at 34 mJy $beam^{-1}$ (2.2σ). As in Figure 4, the bold crossed lines represent the 8.44 GHz radio continuum emission.

at a moderate angle to the line-of-sight (cf. Koerner, Sargent, & Beckwith 1993). The position-velocity diagram along the major axis of IC 883 (Figure 3–6) reveals, however, that the kinematics are more complicated than a symmetric rotating disk, as the north-west region of CO emission exhibits a broader line width and weaker intensity than the south-east region. This asymmetry shows up in the integrated CO spectrum as an asymmetry in the line profile (Figure 3–22b).

3.4.2.3. NGC 6090

Unlike many other luminous infrared galaxies, NGC 6090 shows no evidence at optical or radio wavelengths for a compact AGN. At optical wavelengths, this object appears as a double nucleus system with an asymmetric disk and two arched tails approximately one arcminute (36 kpc) in length (e.g., Mazzarella & Boroson 1993). The nuclei are separated by 6″.4 (3.8 kpc) at B band, and 5″.8 at K band. Mazzarella & Boroson (1993) classify the emission line spectra of both nuclei as H II by the line ratios of [N II], [S II], and [O I] to Hα. Additional evidence points to current starburst activity in the core of NGC 6090: the Hα/L_B luminosity ratio (Calzetti & Kinney 1992), deep CO absorption at 2.3 μm (Ridgway et al. 1994), and the spatially extended non-thermal radio emission (Batuski, Hanisch, & Burns 1992).

The aperture synthesis CO 1→0 map of NGC 6090 shows one dominant component, peaking roughly halfway between the two nuclei seen at optical, infrared, and radio wavelengths (Figures 3–8 and 3–9). The core of the CO emission is well-resolved and elongated along the direction between the radio nuclei (PA 60°). The deconvolved major axis (FWHM) is 5″.4 (3.2 kpc), which is very nearly the same as the distance between the two radio continuum peaks, 5″.3. Perpendicular to the major axis, the CO emission is also resolved, with a deconvolved size of 3″.0 (1.8 kpc).

The complex shape of the isovelocity contours (Figure 3–8c) indicates that the velocity field is rather disordered. A position-velocity slice along the major axis reveals a relatively uniform velocity gradient between the nuclei at low resolution (Figure 3–10a). Thus, much of the gas in the core of NGC 6090 appears to have

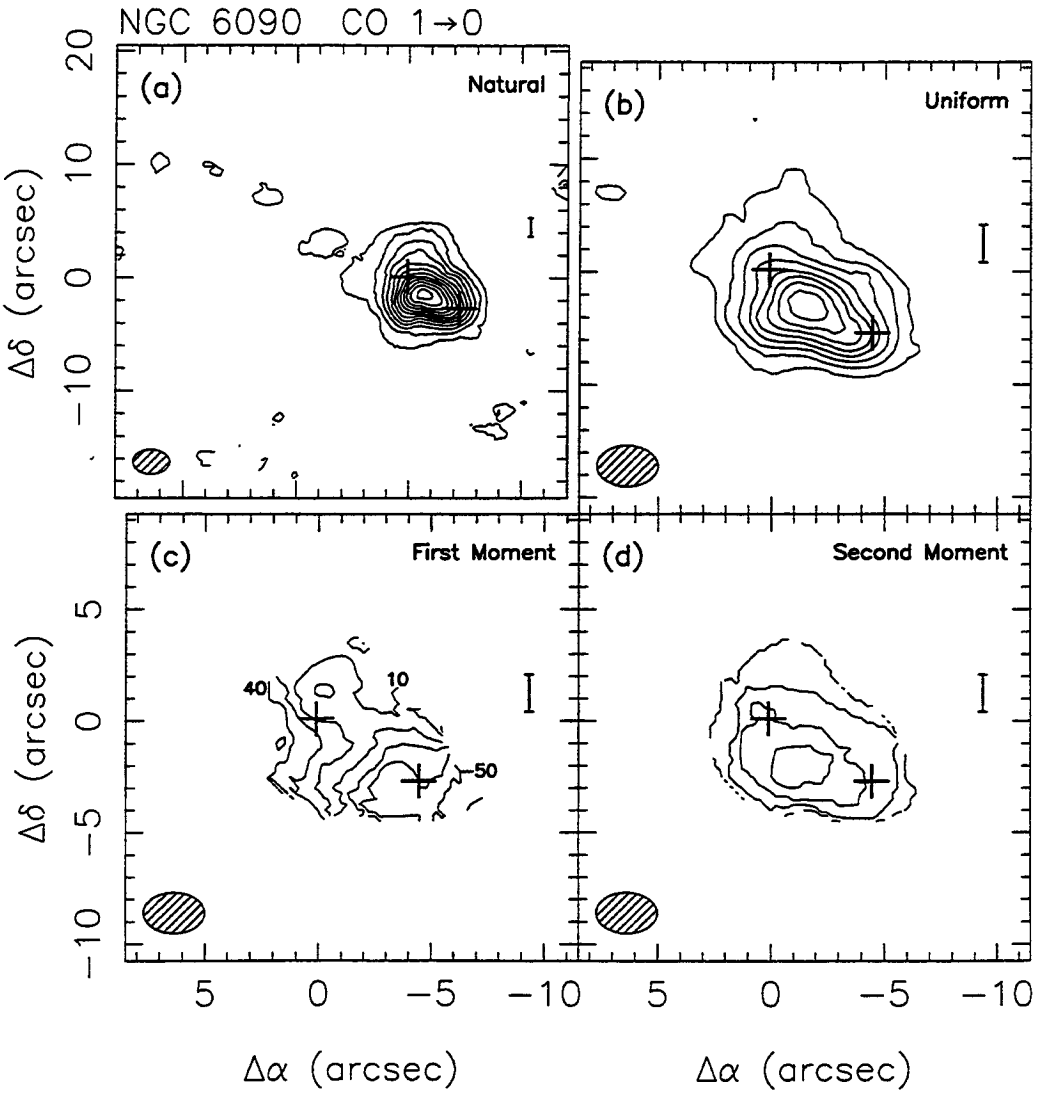

Figure 3–8. CO 1→0 maps of NGC 6090. (a) Velocity-integrated CO emission from the natural-weight aperture synthesis map. Contours are spaced linearly beginning at 2.8 Jy beam^{-1} km s^{-1}. (b) Velocity-integrated CO emission from the uniform-weight map. Contours are spaced linearly beginning at 2.8 Jy beam^{-1} km s^{-1}. (c) First velocity moment map of the CO emission from the uniform-weight map. Contours are at intervals of 15 km s^{-1}, and are labeled relative to the central passband velocity of $cz = 8831$ km s^{-1}. (d) Second velocity moment map of the CO emission from the uniform-weight map. Contours are spaced linearly beginning at 12.5 Jy km s^{-1}. These maps were produced in the same fashion of Figure 3–1. The hatched ellipses represent the half-power beam size, and the bars represent a linear dimension of 1 kpc. The two "+" symbols represent the positions of the peaks of the 1.49 GHz continuum emission (Condon et al. 1990).

relaxed into a coherent structure. Yet some irregularities in the kinematics become apparent in the position-velocity diagram at higher resolution (Figure 3–10b); in fact,

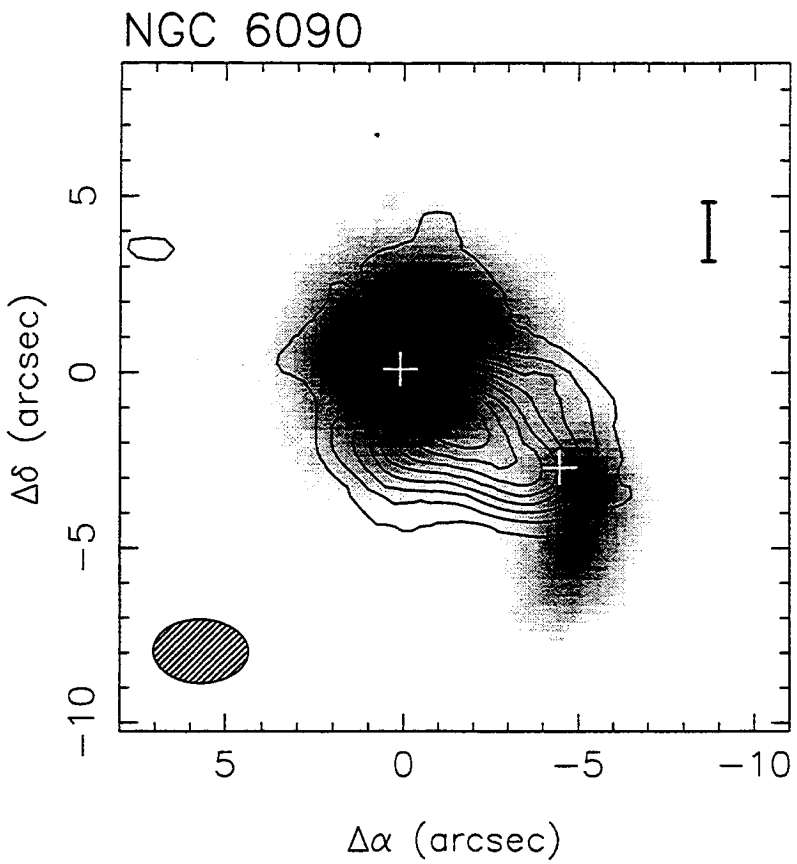

Figure 3–9. CO 1→0 map (uniform weight) in contours, superposed on a grayscale near-infrared K′ image of NGC 6090 from Sanders et al. 1996. The CO emission shows a dramatically different morphology from either the near infrared or the radio continuum emission. To register the images, we assumed that the north-east peak of the K′ emission is spatially coincident with the north-east peak of the radio continuum emission. The symbols have the same meaning as in Figure 3–8.

Figure 3–10b hints that there may be two distinct velocity components which have not completely merged yet. Because the merger is still far from completion (evidence the clearly distinct nuclei at infrared and radio wavelengths, separated by 4 kpc), the current state of the molecular gas is likely a short-lived phase.

The morphology of the CO emission in NGC 6090 is somewhat similar to that of the CO emission in VV 114 (Yun et al. 1994). Like NGC 6090, VV 114 shows a ridge of CO emission between its two infrared nuclei; however, in VV 114 the nuclei are more widely separated than in NGC 6090 (6 kpc compared to 3.2 kpc in NGC 6090).

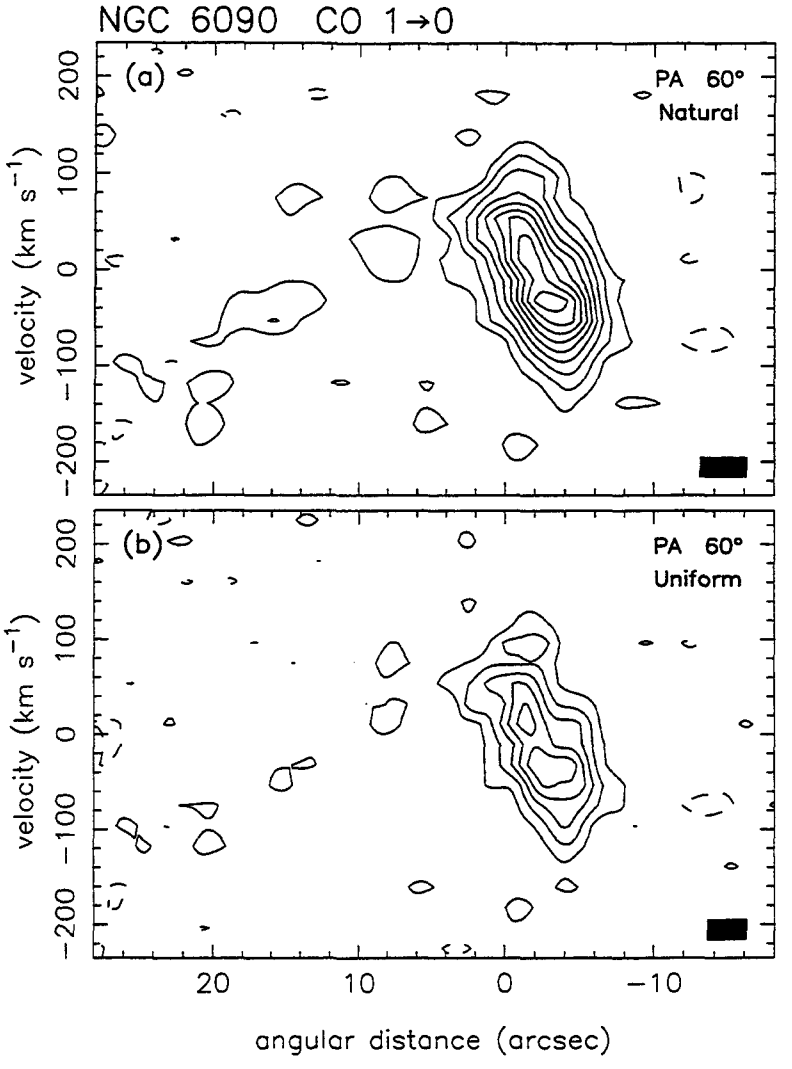

Figure 3–10. Position-velocity cut of the CO data cubes for NGC 6090 through the peak of the integrated emission, along the major axis position angle of 60°. (a) Natural-weight CO data cube. Contours are spaced linearly beginning at 26 mJy beam^{-1} (2σ for a smoothed frequency resolution of 8 MHz [21.4 km s^{-1}]). (a) Uniform-weight CO data cube. Contours are spaced linearly beginning at 31 mJy beam^{-1} (2σ for the same frequency resolution). Negative contours are shown as dashed lines. The black rectangle represents a single resolution element in both dimensions.

VV 114 also shows a larger fraction of its CO emission outside of the central ridge than does NGC 6090. This gas is suggested to be falling into the nuclear ridge (Yun et al. 1994), and it is possible that VV 114 will eventually evolve to exhibit infrared and CO morphology more like NGC 6090. A major difference between the two objects is

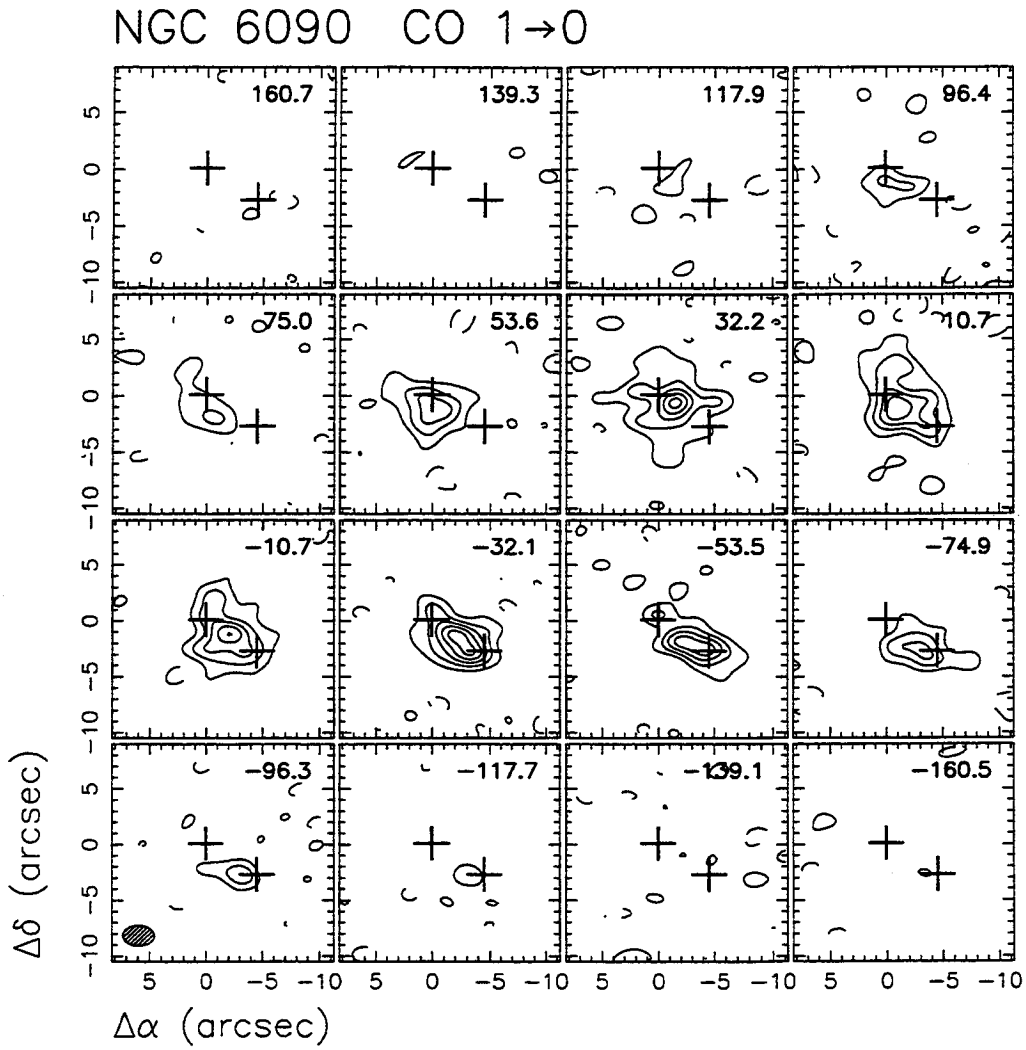

Figure 3–11. Channel maps of the NGC 6090 uniform-weight CO data cube, binned by 8 MHz (21.4 km s^{-1}), with the central velocities of each map shown at upper right. Contours are spaced linearly beginning at 34 mJy $beam^{-1}$ (2.2σ). The symbols have the same meaning as in Figure 3–8.

the relative distribution of the CO emission and the cm-wave continuum. In VV 114 the radio continuum extends over a similar region to the CO bar, while in NGC 6090 the radio continuum exhibits a double structure with peaks at the two near-infrared nuclei, (Hummel et al. 1987) rather unlike the morphology of the CO "bar."

The velocity width of the CO emission is very narrow ($\Delta v = 136$ km s^{-1} FWHM; Figure 3–22c). and the dynamical mass implied by the line width is several times less

than the standard estimate of the mass of molecular gas in the core (see Table 3–5). This discrepancy is discussed in §3.4.1.

The natural-weight CO map reveals knots of CO along a curvilinear feature to the north-east of the core, with nearly the same position angle as the core CO emission. The kinematic gradient in this arc is opposite to that seen in the central CO ridge (Figure 3–10). A corresponding spur of emission is also visible in optical images of NGC 6090 (e.g., Mazzarella & Boroson 1993). This feature is distinct from the tails noted above. In fact, we do not detect CO along the optical tails, although the bulge in the CO contours north of the position of the eastern nucleus does coincide with the base of these tails.

3.4.2.4. NGC 6240

NGC 6240 is one of the most extensively studied of the luminous infrared galaxies. Optically, it appears highly disturbed (Zwicky, Herzog, & Wild 1961) and is believed to be the merger of two disk galaxies (Fosbury & Wall 1979). A double nucleus is apparent at optical, infrared, and radio wavelengths, with a projected separation of 1.5–2″ that decreases as the wavelength increases (Fried & Schulz 1983; Condon et al. 1982; Carral et al. 1990; Eales et al. 1990; Thronson et al. 1990; Herbst et al. 1990; Barbieri et al. 1993). The nucleus of NGC 6240 shows a low-ionization spectrum and has been classified as a LINER by Heckman, Armus, & Miley (1987). In the near-infrared, the nuclear spectrum shows anomalously bright lines of H_2 and [Fe II] and very strong CO absorption bands, while the hydrogen recombination lines are

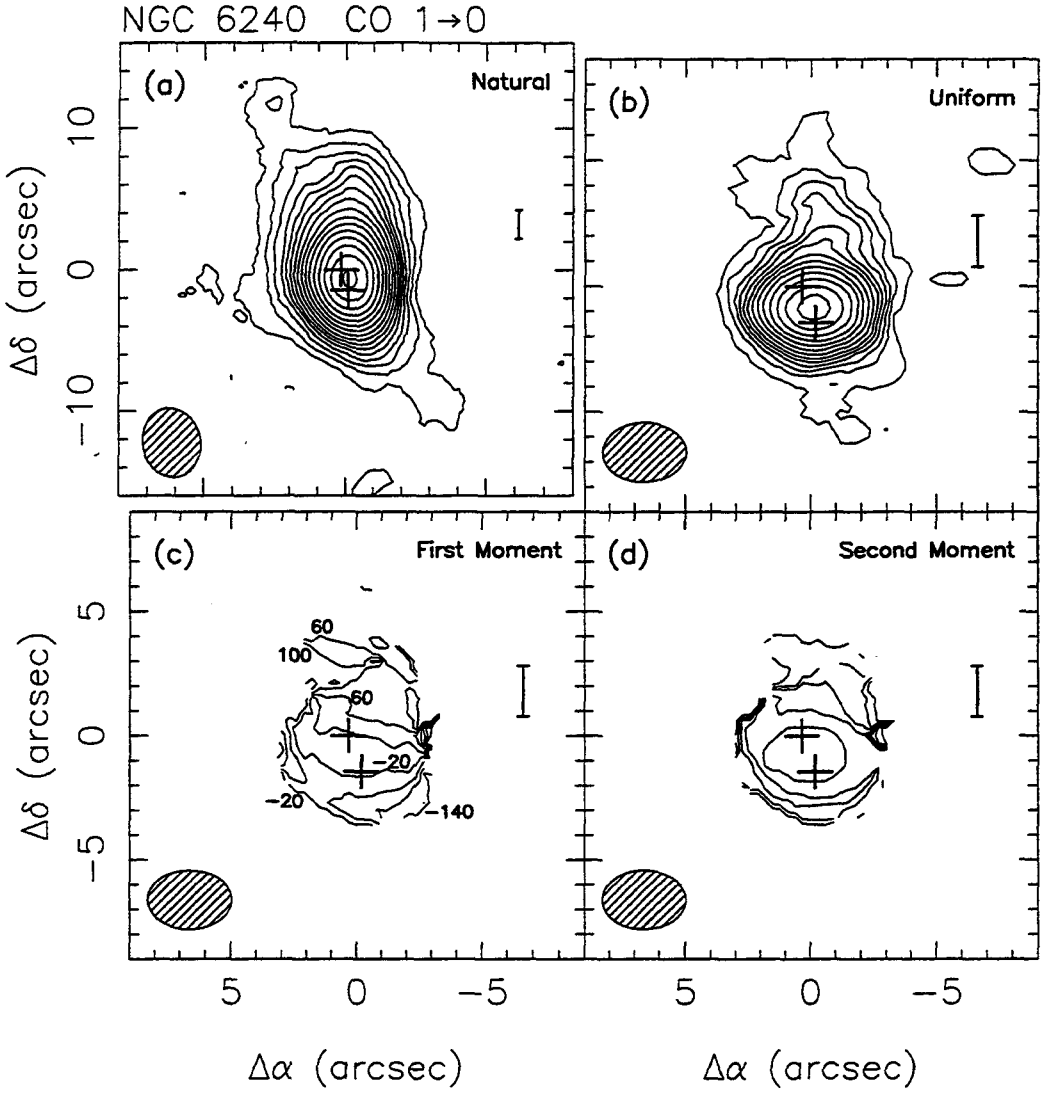

Figure 3–12. CO 1→0 maps of NGC 6240. (a) Velocity-integrated CO emission from the natural-weight aperture synthesis map. Contours are spaced linearly beginning at 4.8 Jy beam^{-1} km s^{-1}. (b) Velocity-integrated CO emission from the uniform-weight map. Contours are spaced linearly beginning at 5.9 Jy beam^{-1} km s^{-1}. (c) First velocity moment map of the CO emission from the uniform-weight map. Contours are at intervals of 40 km s^{-1}, and are labeled relative to the central passband velocity of $cz = 7335$ km s^{-1}. (d) Second velocity moment map of the CO emission from the uniform-weight map. Contours are spaced linearly beginning at 30 Jy km s^{-1}. These maps were produced in the same fashion of Figure 3–1. The hatched ellipses represent the half-power beam size, and the bars represent a linear dimension of 1 kpc. The two "+" symbols represent the positions of the two brightest components of the 15 GHz continuum emission, both of which are well under an arcsecond in size (Carral et al. 1990).

relatively weak by comparison (Rieke et al. 1985; DePoy, Becklin, & Geballe 1986; Lester, Harvey, & Carr 1988). The 12 and 25 μm emission from NGC 6240 is very

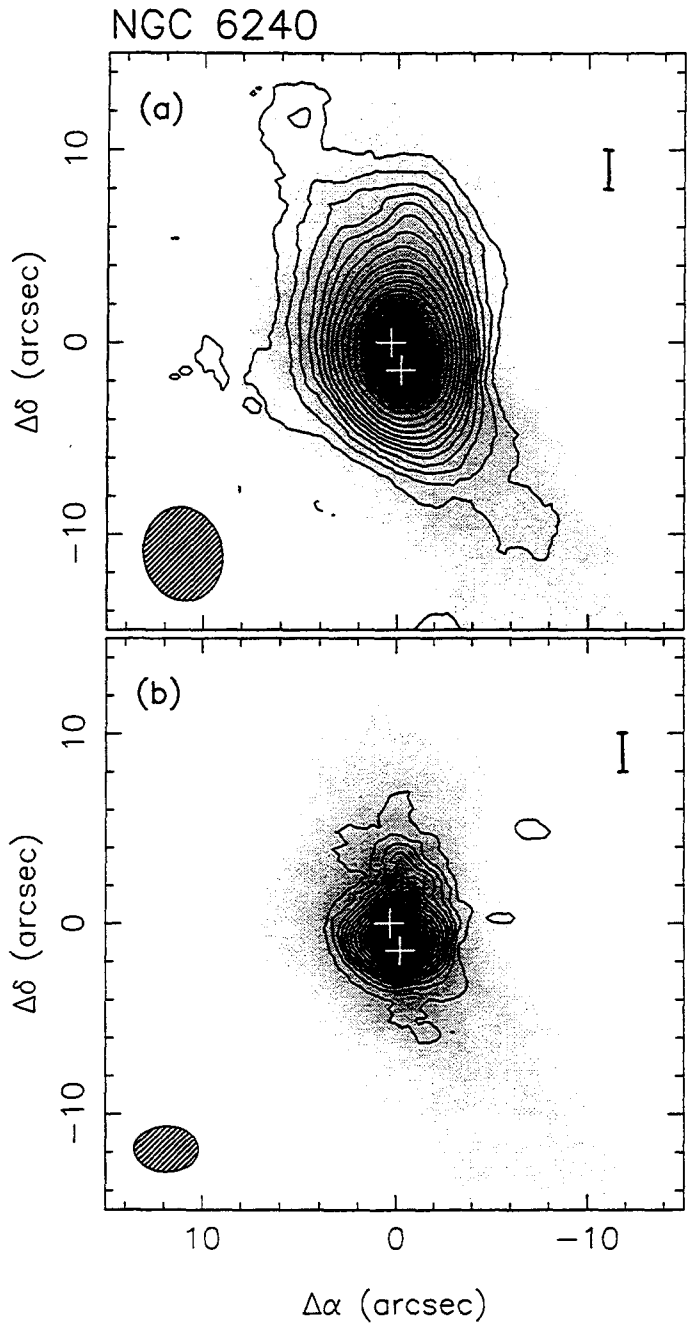

Figure 3–13. CO 1→0 map in contours, superposed on a grayscale near-infrared K′ image of NGC 6240 from Sanders et al. 1996. (a) Natural weight CO map, emphasizing the correlation of the low-level CO contours with the near infrared emission; (b) uniform weight CO map, emphasizing the lack of elongation of the core CO emission along the position angle of the double nucleus. To register the images, we assumed that the south-west peak of the K′ emission is spatially coincident with the south-west peak of the radio continuum emission. The symbols have the same meaning as in Figure 3–12.

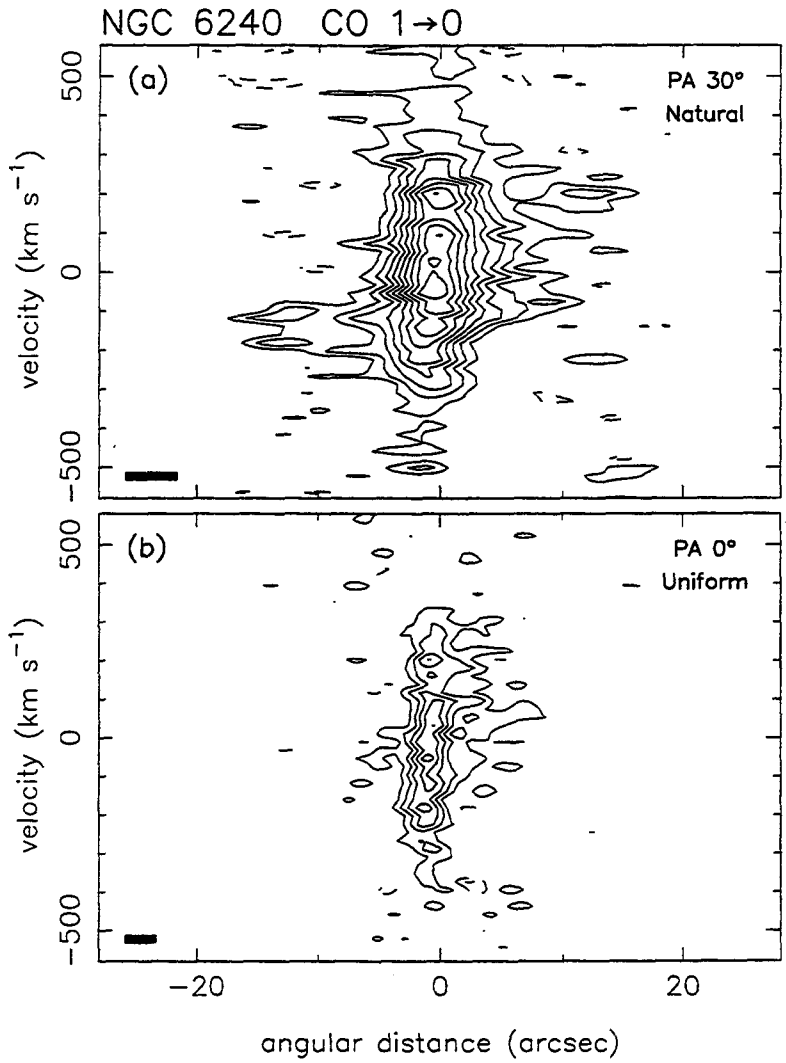

Figure 3–14. Position-velocity cut of the CO data cubes for NGC 6240 through the peak of the integrated emission. (a) Natural-weight CO data cube; cut along position angle 30°, corresponding to the direction of the extension of the low-level CO contours. Contours are spaced linearly beginning at 34 mJy beam^{-1} (2σ for a smoothed frequency resolution of 8 MHz [21.3 km s^{-1}]). (a) Uniform-weight CO data cube; cut along position angle 0°, roughly the direction of maximum velocity gradient. Contours are spaced linearly beginning at 60 mJy beam^{-1} (2σ for the same frequency resolution). Negative contours are shown as dashed lines. The black rectangle represents a single resolution element in both dimensions.

compact, with virtually the entire emission arising from within a 5″.7 (2.7 kpc) aperture (Wynn-Williams & Becklin 1993). The bulk of the cm-wave radio continuum is even more compact, with most of the emission concentrated in the two nuclei, each of

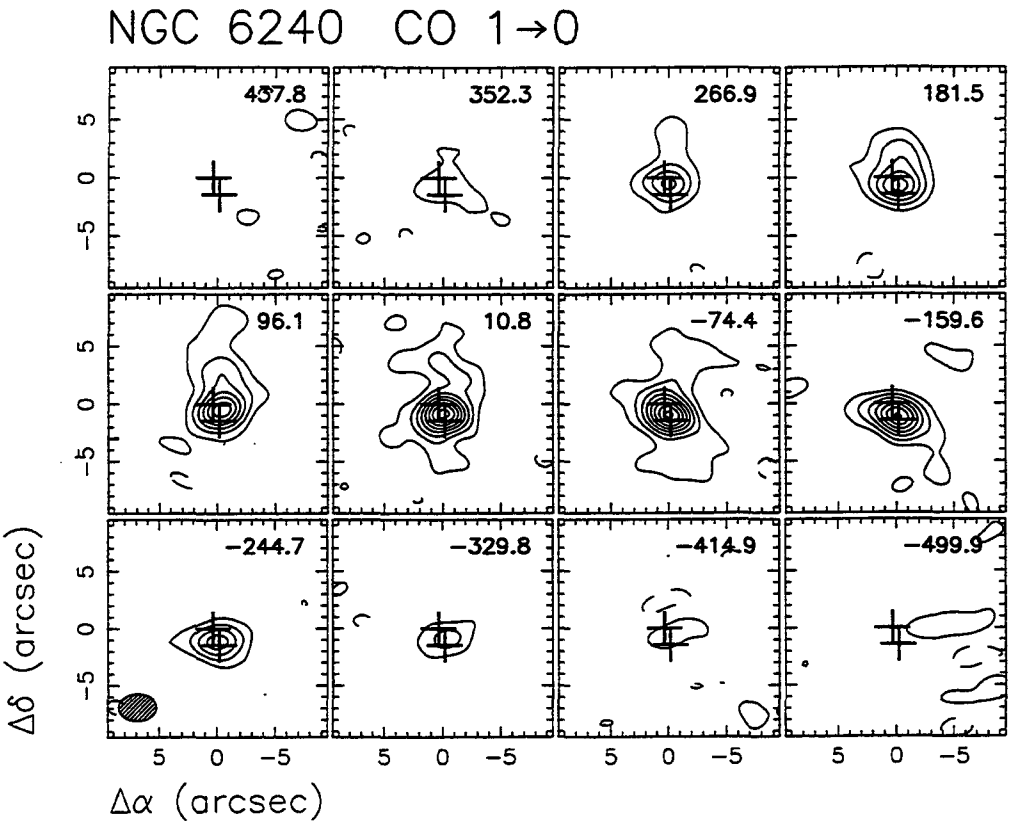

Figure 3–15. Channel maps of the NGC 6240 uniform-weight CO data cube, binned by 32 MHz (85.3 km s^{-1}), with the central velocities of each map shown at upper right. Contours are spaced linearly beginning at 33 mJy $beam^{-1}$ (2.2σ). The symbols have the same meaning as in Figure 3–12.

which is under 0″.15 (0.04 kpc) across (Carral et al. 1990). The low-level radio emission exhibits a complex morphology, extending 15″ to the east of the nuclear region, and may be associated with a "superwind" (Colbert et al. 1994; Armus, Heckman, & Miley 1990).

The nature of the source of the infrared luminosity in NGC 6240 is highly controversial. As such, this source epitomizes the class of luminous infrared galaxies. An extremely powerful burst of star formation is the preferred explanation of many authors (e.g., Wright, Joseph, & Meikle 1984; Rieke et al. 1985; Van der Werf et al. 1993), while the weak recombination line emission leads others to prefer a Seyfert-like

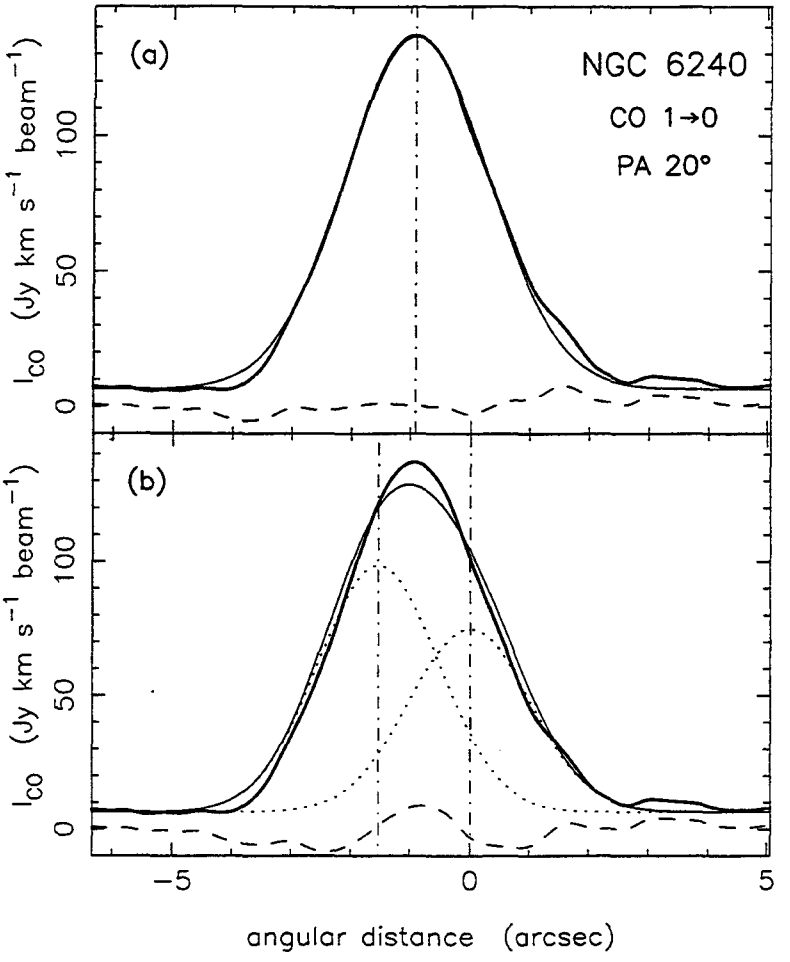

Figure 3–16. A test for consistency of the CO emission distribution in the core of NGC 6240 with a double nucleus. A profile of the integrated CO emission (uniform-weight) along position angle 20°, the position angle of the NIR/radio nuclei, is shown as the thick solid line. In (a), the thin solid line represents a single gaussian fit to this profile (with a fixed "background" level), while in (b), the thin solid line represents a double gaussian fit (fixed "background"), with the centers of the gaussians fixed at the positions of the NIR/radio nuclei (0″.0 and −1″.53 on this diagram) and the widths forced to be equal to the smallest dimension of the synthesized beam. If the widths are left unconstrained, the best double gaussian fit results in profiles of the individual components that are 10% narrower than the synthesized beam. Residuals are shown as the dashed lines; the vertical dot-dash lines indicated the central positions of the gaussians, which were fit in (a) and held constant in (b). The dotted lines in (b) indicate the individual components of the best fit double gaussian.

active nucleus as the luminosity source (DePoy et al. 1986; Carral et al. 1990). Herbst et al. (1990) suggest that shocks generated by the collision of interstellar clouds in

the merger (cf. Harwit et al. 1987) are more likely to account for the infrared luminosity than either a starburst or an active nucleus. Finally, Thronson et al. (1990) argue that only a quarter of the luminosity can come from young stars and that dust heating by the old stellar population can account for most of the rest. Clearly this is a very intriguing object.

The uniform-weight CO 1→0 map of NGC 6240 (Figure 3–12b) shows a slightly resolved core of emission, which peaks between the closely-spaced infrared/radio nuclei (Figure 3–13b). A relatively weak arm of emission to the north and a weaker southern arm are also suggested by the map. The core appears only slightly larger than the synthesized beam. Deconvolved, it is consistent with being circular, with a diameter of 1″.6 (0.78 kpc); the uncertainty in the size is roughly 0″.4 north-south and 0″.7 east-west. The velocity gradient in the core (Figure 3–12c) is roughly parallel to the direction of the infrared/radio nuclear separation (PA 20°). (The gradient reverses itself in the northern arm, similar to the behavior seen in the north-east arc of CO emission in NGC 6090.) The line width in the core is extremely broad, with a full width at zero intensity of over 900 km s^{-1} (Figure 3–22d). In the weak extensions of emission outside the core, the line width drops dramatically, especially to the south, as can be seen in the position-velocity diagrams in Figure 3–14. Channel maps of the core CO emission are presented in Figure 3–15.

Like NGC 6090, the CO source at the core of NGC 6240 appears to peak *between* the radio nuclei rather than on them. The close separation of the nuclei means, however, that this is not immediately apparent by inspection of the integrated emission

map. Nonetheless, it is unlikely that the apparent peak of the CO between the radio nuclei in NGC 6240 is due to the effect of limited resolution on a true double CO nucleus. In Figure 3–16, we compare the fits obtained with a single gaussian component (Figure 3–16a) and with two gaussian components positioned on the two nuclei (Figure 3–16b); the former yields a much better fit. We thus conclude that the integrated CO emission peaks between the two radio nuclei of NGC 6240. In this way, the CO morphology of NGC 6240 is similar to that of the other double nucleus merger in our sample, NGC 6090 (§3.4.2.3).

The natural-weight aperture synthesis map of NGC 6240 (Figure 3–12a) reveals that the low-level CO emission has a morphology similar to the extended K′ band emission (Figure 3–13a). Both show extensions along the optical dust lane to the north-east and south-west of the core, a bulge immediately to the north of the core, and a faint, irregular extension to the west. The secondary CO component seen in an earlier aperture synthesis image of NGC 6240 to the north-east of the core by Wang, Scoville, & Sanders (1991) appears to be associated with the dust-lane CO emission seen in the present map and does not represent a secondary CO nucleus. We do not detect any CO associated with the western extension of radio continuum emission; this result is consistent with the "superwind" interpretation for the western arm (Colbert et al. 1994).

3.4.2.5. NGC 7469

The two galaxies remaining to be discussed are the only two non-mergers in our

sample. Both NGC 7469 and NGC 7674 are barred spiral galaxies with Seyfert nuclei, and are the largest members of interacting galaxy pairs.

NGC 7469 is a prominent example of an object where an AGN and a nuclear starburst are known to co-exist. The Seyfert 1 nucleus was one of the original broad emission line galaxies discussed by Seyfert (1943), but NGC 7469 also contains a bright ring of emission lines at a mean radius of 1″.5 from the nucleus that is hosting a starburst that likely accounts for the majority of the luminosity of the galaxy (Genzel et al. 1995 and references therein). The companion to NGC 7469 is a late-type spiral, IC 5283, and is centered 80″ (26 kpc) away, well outside of the primary beam or our observations.

For NGC 7469, we only performed a track in a low-resolution configuration of the array, and the resulting map does not show much spatial structure and is thus not shown here. The signal-to-noise is excellent, however, as evidenced by the spatially-averaged spectrum (Figure 3–22e), and we are able to measure a source size of 4″.6 × 3″.9, elongated along a position angle of 87°, despite the 8″.3 × 6″.3 synthesized beam. A slightly higher resolution, but lower signal-to-noise, aperture synthesis map of NGC 7469 made with the Owens Valley millimeter array is published in Sanders et al. (1988a). The CO source size we determine is consistent with theirs. Though we measure over twice as much CO flux as Sanders et al., our flux is consistent with that for the aperture synthesis map of Meixner et al. (1990) from the BIMA array. The double-horn shape of the core CO spectrum suggests that the bulk of the CO emission arises in the starburst ring—consistent with the results of Meixner et al. (1990).

3.4.2.6. NGC 7674

NGC 7674, like NGC 7469, is the largest member of an interacting pair. It is a large barred spiral galaxy (e.g., McLeod & Rieke 1995) with faint tidal tails (MacKenty 1990), and it is one of four members of the compact group HCG 96. Its two closest neighbors, a small Sa (HCG 96c) and a small irregular galaxy (HCG 96d), both show signs of having undergone a recent interaction, while the remaining galaxy in the group, NGC 7675, appears to be a relatively normal, quiescent elliptical (Mendes de Oliveira & Hickson 1994). It appears that NGC 7674 and at least one of the nearby small galaxies are undergoing a strong interaction or series of interactions.

NGC 7674 has a Seyfert 2 nucleus, and it is one of the few Seyfert 2s known to harbor a hidden broad line region, visible in polarized light (Miller & Goodrich 1990; Tran 1995). Unlike nearly all other known members of this class, however, dust scattering, rather than electron scattering, is the dominant mechanism for the polarization (Tran 1995). Moderately broad near-infrared He I and Paβ lines are also seen towards the nucleus, though with much narrower line widths ($\sim$1100 km s^{-1}; Ruiz, Rieke, & Schmidt 1994) than are seen in polarized Hβ (2830 km s^{-1}; Tran 1995). A compact, VLBI triple source is also seen (Unger et al. 1988); the brightest components are separated by 0".5 (280 pc) and are less than 0".028 (16 pc) and 0".013 (7 pc) across. Unger et al. are unable to rule out a starburst as the source of the compact radio emission based on the energetics, but they prefer collimated ejection as the source due to the structure of the emission. Other features of NGC 7674 include an extreme blueward asymmetry up to 2000 km s^{-1} in the narrow nuclear emission lines (e.g., Unger

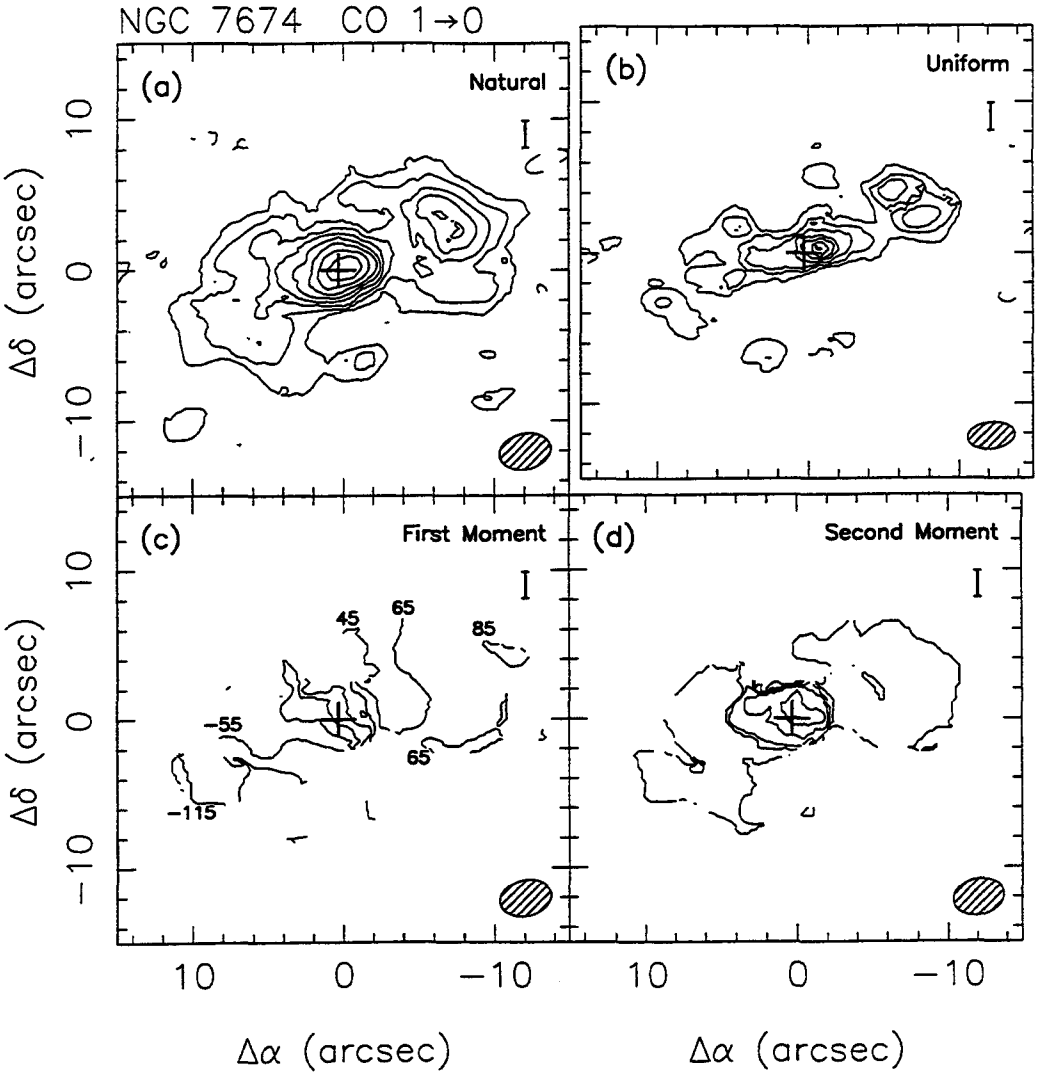

Figure 3–17. CO 1→0 maps of NGC 7674. (a) Velocity-integrated CO emission from the natural-weight aperture synthesis map. Contours are spaced linearly beginning at 1.15 Jy beam^{-1} km s^{-1}. (b) Velocity-integrated CO emission from the uniform-weight map. Contours are spaced linearly beginning at 1.15 Jy beam^{-1} km s^{-1}. (c) First velocity moment map of the CO emission from the uniform-weight map. Contours are at intervals of 20 km s^{-1}, and are labeled relative to the central passband velocity of cz = 8669 km s^{-1}. (d) Second velocity moment map of the CO emission from the uniform-weight map. Contours are spaced linearly beginning at 8 Jy km s^{-1}. These maps were produced in the same fashion of Figure 3–1. The hatched ellipses represent the half-power beam size, and the bars represent a linear dimension of 1 kpc. The "+" symbol represents the position of the brightest component of the compact VLBI triple at the core of NGC 7674 (Unger et al. 1988).

et al. 1988) and an extended narrow line region covering the entire visible extent of the galaxy (Durret et al. 1993). As is the case is many other luminous IR galaxies,

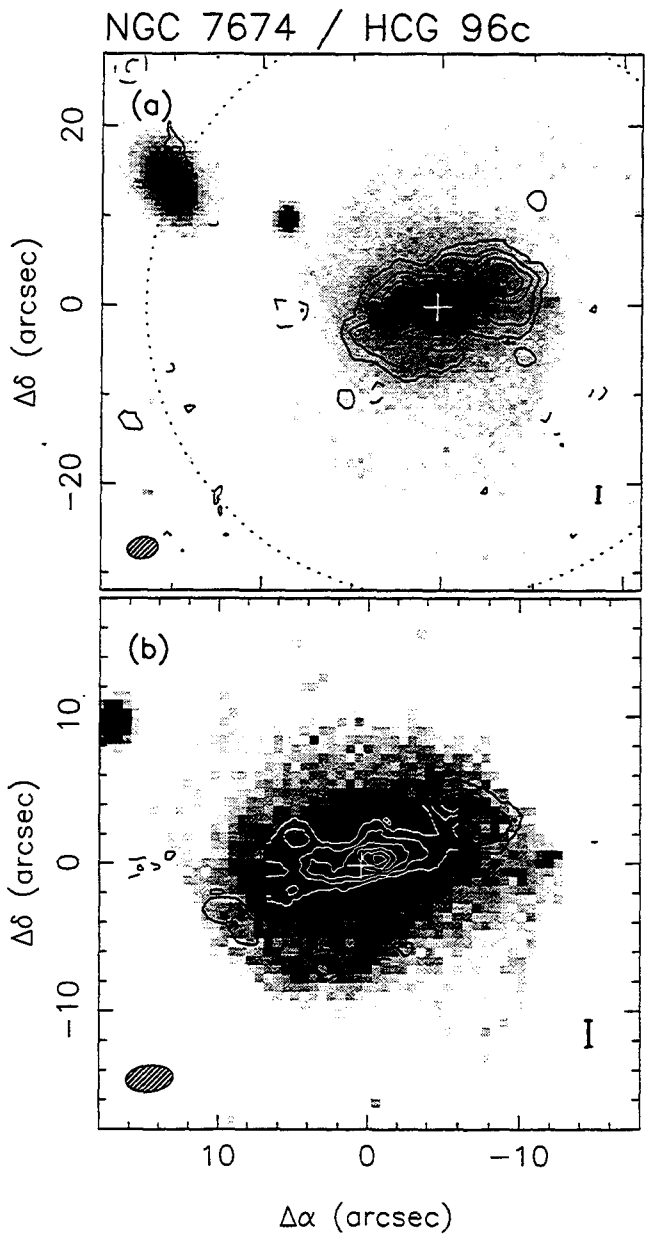

Figure 3–18. CO 1→0 map in contours, superposed on a grayscale near-infrared K′ image of NGC 7674 from Sanders et al. 1996. (a) Natural weight CO map, showing the detection of CO associated with the small galaxy HCG 96c to the north-east of the barred spiral NGC 7674; (b) uniform weight CO map, emphasizing the relative alignment of the CO and stellar bars in NGC 7674. The bright compact object between NGC 7674 and HCG 96c is likely a foreground star. To register the images, we assumed that the peak of the K′ emission is spatially coincident with the peak of the 1.49 GHz radio continuum emission. The dotted circle represents the half-power radius of the primary beam of the Owens Valley millimeter array telescopes. The other symbols have the same meaning as in Figure 3–17.

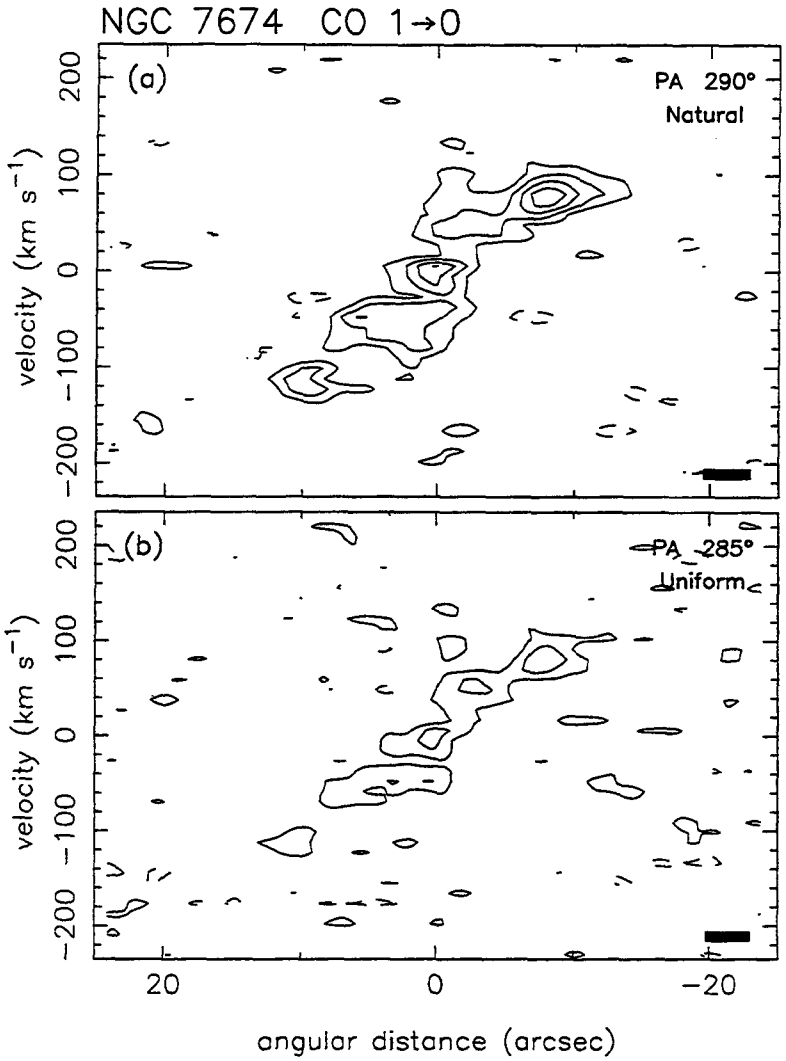

Figure 3–19. Position-velocity cut of the CO data cubes for NGC 7674 through the peak of the integrated emission. (a) Natural-weight CO data cube; cut along position angle 290°, the direction of the bar in the natural-weight integrated CO map. Contours are spaced linearly beginning at 32 mJy beam^{-1} (1.9σ for an unsmoothed frequency resolution of 4 MHz [10.7 km s^{-1}]). (a) Uniform-weight CO data cube; cut along position angle 285°, the direction of the bar in the uniform-weight integrated CO map. Contours are spaced linearly beginning at 40 mJy beam^{-1} (1.8σ for the same frequency resolution). Negative contours are shown as dashed lines. The black rectangle represents a single resolution element in both dimensions.

the 10 μm emission of NGC 7674 is extremely compact, with 77% of the IRAS flux concentrated within a few arcseconds of the nucleus (Wynn-Williams & Becklin 1993).

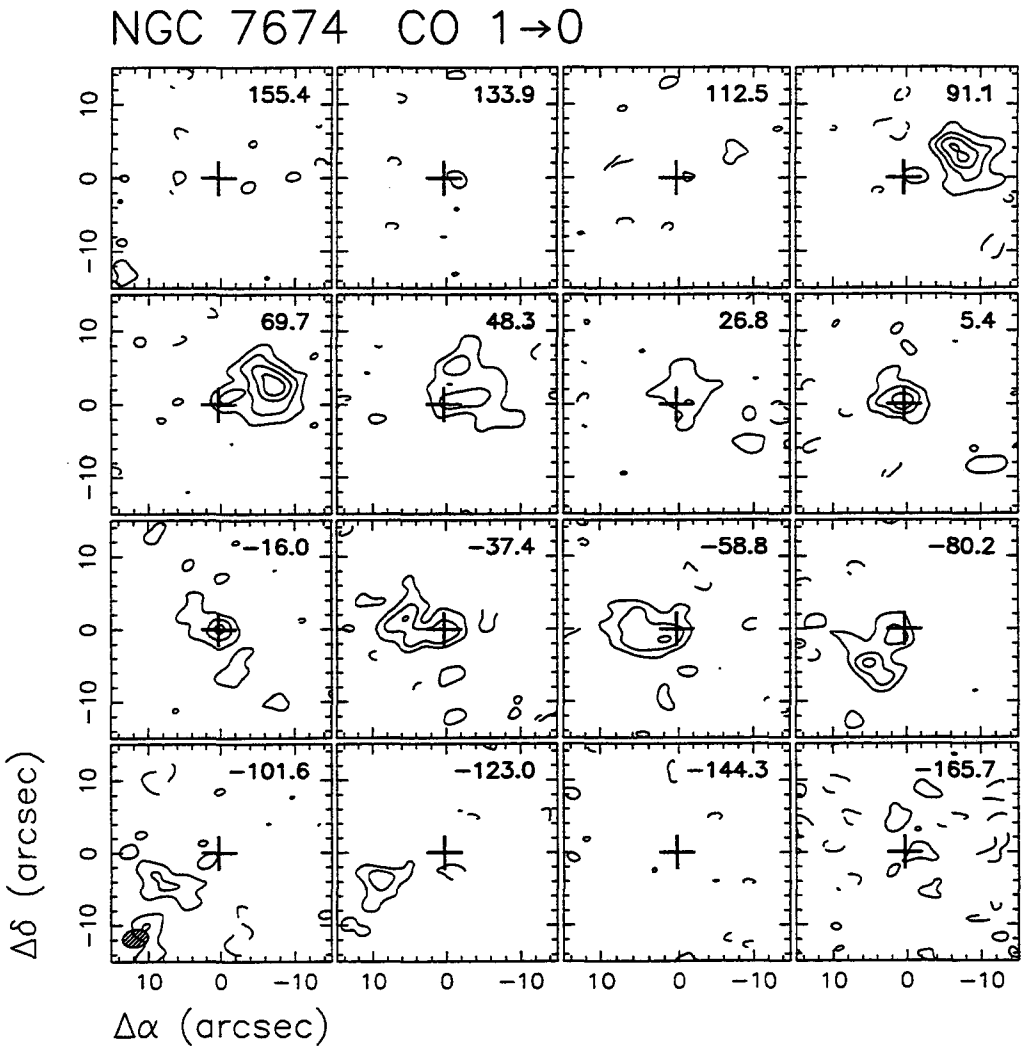

Figure 3–20. Channel maps of the NGC 7674 uniform-weight CO data cube, binned by 8 MHz (21.4 km s^{-1}), with the central velocities of each map shown at upper right. Contours are spaced linearly beginning at 26 mJy $beam^{-1}$ (2.2σ). The symbols have the same meaning as in Figure17.

The aperture synthesis CO map of NGC 7674 reveals a much more extended structure than any of the other objects presented in this paper (Figure 3–17). The CO emission in the natural-weight map shows a broad, irregular ridge 20″ in length at position angle 290° with bright, compact concentrations at the nucleus and at the western end of the ridge. The ridge east of the nucleus appears more irregular in its morphology than that west of the nucleus. The uniform-weight map reveals

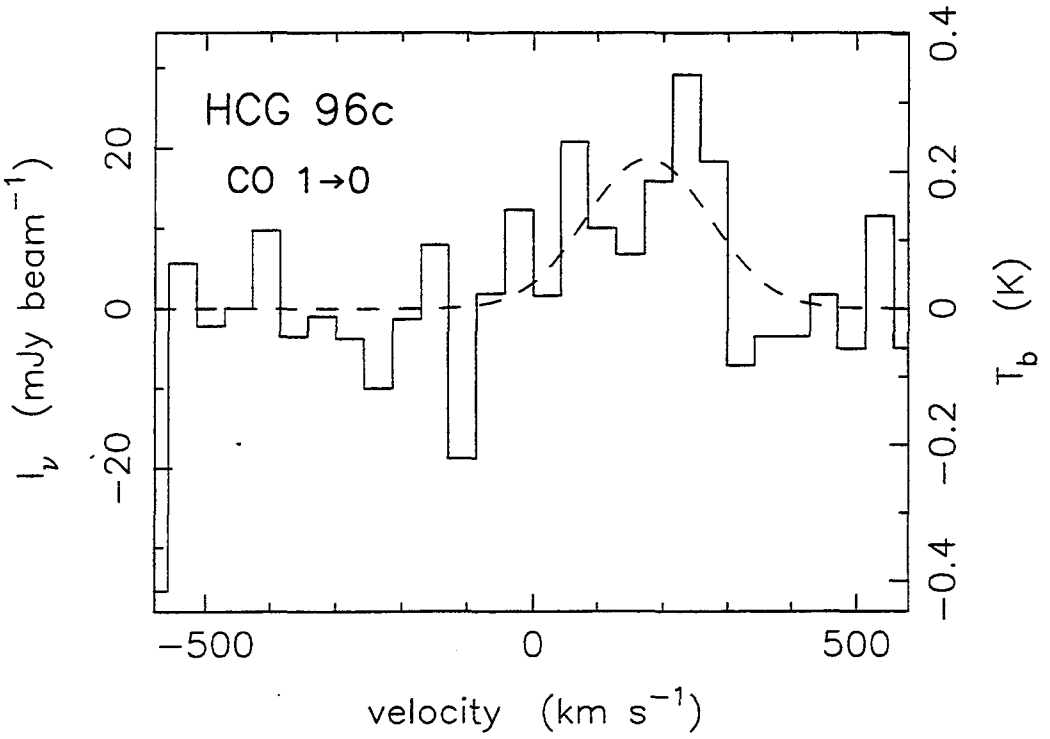

Figure 3–21. CO 1→0 spectrum at the position of HCG 96c, the nearest companion galaxy to NGC 7674, smoothed to a resolution of 16 MHz (42.8 km s^{-1}). The best-fit gaussian is shown as a dashed line. The ordinate is labeled with both the specific intensity (I_ν) and the equivalent brightness temperature (T_b): $T_b \equiv I_\nu c^2/(2k\nu^2)$.

a more linear CO distribution at a slightly different position angle of 285°. Only one-seventh of the CO flux arises from the unresolved concentration near the position of the nuclear VLBI triple. Interestingly, the peak of this concentration is displaced by 0″.9 along the bar from the position of the brightest VLBI component. The peak shows the broadest line width in the object, 150 km s^{-1} FWHM; the other emission regions have line-widths of only ∼20 km s^{-1} FWHM.

The inclination of NGC 7674 is 17° ± 12, based on the axial ratio of the optical isophotes (DeVaucouleurs, DeVaucouleurs, & Corwin 1976)—so it is very nearly face-on. The extended ridge in CO is thus likely a molecular bar. It is nearly coincident with the near-infrared (stellar) bar, as shown in Figure 3–18. A velocity-gradient of

200 km s^{-1} across the length of the bar is apparent in our data. If this motion is rotational, the magnitude of the projected velocity suggests that the inclination of the rotational plane to our line-of-sight is closer to the upper end than the lower end of the range noted above. An inclination of 29° implies a rotational velocity of slightly over 200 km s^{-1} at the end of the bar (6 kpc from the nucleus), while an inclination of 5° would imply an implausibly large rotational velocity of over 1100 km s^{-1}. For an inclination of 17°, the inferred rotational velocity at the end of the bar is 340 km s^{-1}.

We tentatively detect CO 1→0 at the position of the nearest companion to NGC 7674, HCG 96c. A large scale natural-weight map of the CO 1→0 emission around NGC 7674 is shown overlaid on a K′ band image (Sanders et al. 1996) in Figure 3–18a and the spectrum at the position of HCG 96c is shown in Figure 3–21. A gaussian fit to this spectrum, smoothed to a resolution of 75 km s^{-1}, yields a central velocity of $cz = 8749 \pm 30$ km s^{-1} and a FWHM of 220 ± 70 km s^{-1}, where the quoted errors are the formal errors from the fit. The systemic velocity of the optical spectrum of HCG 96c is $cz = 8753$ km s^{-1} (Mendes de Oliveira & Hickson 1994), only 4 km s^{-1} different than the best-fit CO velocity. This tentative detection corresponds to a velocity-integrated flux of 7.9 ± 3.4 Jy $beam^{-1}$ km s^{-1}. Because HCG 96c is 33″ away from the pointing center, a correction factor of approximately 2.2 is needed to compensate for attenuation by the primary beam. Using the standard conversion factor and the adopted distance for NGC 7674, the molecular gas mass in this beam area is then approximately 3×10^9 $M_\odot$, and the mean molecular gas surface density is 400 $M_\odot$ pc^{-2}.

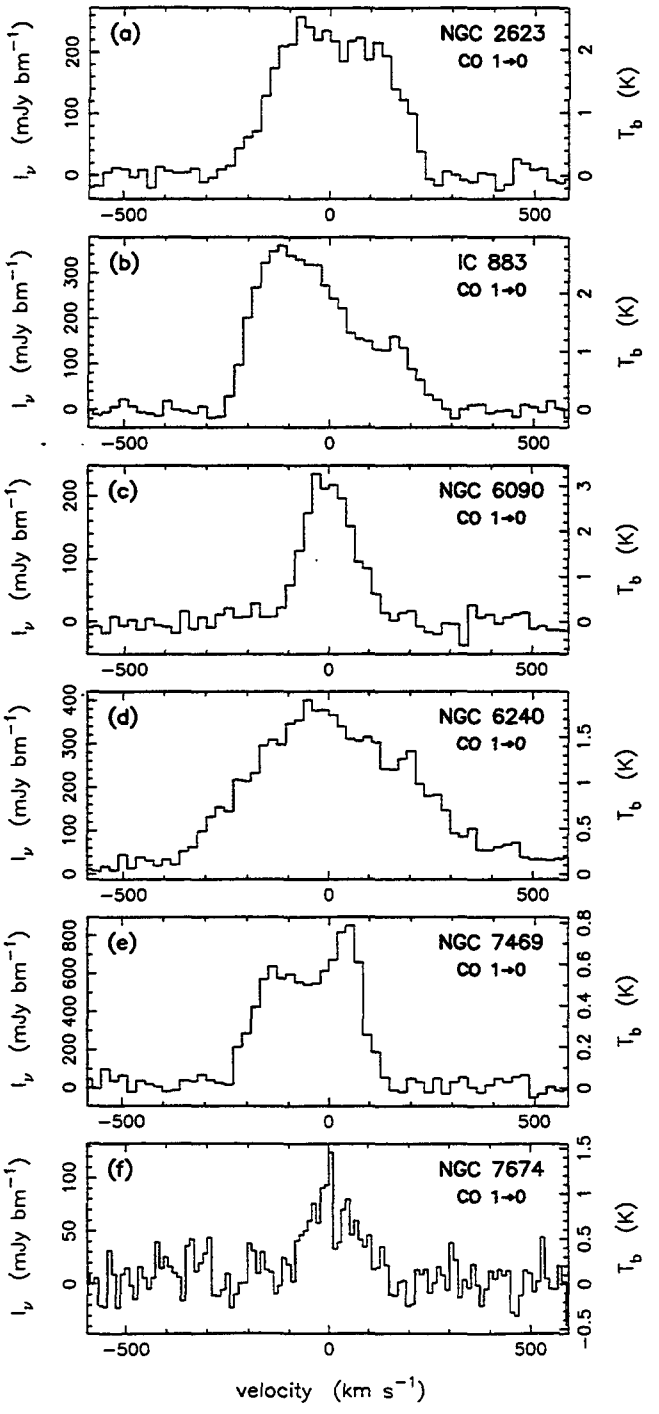

Figure 3–22. CO 1→0 spectra of the peak emission in the natural-weight maps of (a) NGC 2623, (b) IC 883, (c) NGC 6090, (d) NGC 6240, and (e) NGC 7674, smoothed to frequency resolution of 8 MHz. The entire instrumental passband is shown. The ordinate is labeled with both the specific intensity (I_ν) and the equivalent brightness temperature (T_b): $T_b \equiv I_\nu c^2/(2k\nu^2)$.

3.5. Discussion

3.5.1. Gas morphology in double nucleus objects

In both mergers with double near-IR/radio nuclei, NGC 6090 and NGC 6240, the CO emission exhibits a single component that peaks between the stellar nuclei. Recent aperture synthesis CO 2→1 observations of the ultraluminous double nucleus merger Arp 220 have revealed that most of the molecular gas is located between the two stellar nuclei in that system as well (Scoville et al. 1996). On the other hand, all three of the single nucleus mergers studied here show the CO emission coincident with the peak of the near-IR/radio emission. The results for NGC 6090, NGC 6240, and Arp 220 strongly suggest that the gas is in the process of or has already coalesced into a single component, while the stellar cores remain well separated (~0.5–3 kpc). Such a merger of the gas nuclei significantly earlier than the merger of the stellar nuclei has not yet been seen in gas-dynamical simulations of merging galaxies; instead, simulations have indicated that the gas nuclei and the stellar nuclei merge nearly simultaneously (e.g., Barnes & Hernquist 1991; Mihos & Hernquist 1996). The observations reported here, which provide the first observational evidence for gas nuclei merging prior to the stellar nuclei, will serve as constraints for future simulations of at least a subset of mergers. Dissipation in the gas is a likely cause for the early coalescence of the gas cores. Further high-resolution CO observations of mergers with double IR/radio nuclei separated by a few kpc or less are required to determine if the gas morphology seen in NGC 6090, NGC 6240, and Arp 220 represents a typical stage in the evolution of gas-rich mergers.

Due to the empirical correlation between far-IR and non-thermal radio fluxes for galaxies (e.g., Helou, Soifer, & Rowan-Robinson 1985), the regions of bright non-thermal radio emission likely trace the regions of bright far-IR emission and hence the areas from which most of the luminosity arises. Correspondingly, the CO emission traces the molecular gas—the likely fuel for the activity. Because the non-thermal radio emission only encompasses the stellar nuclei, while the CO emission stretches between them, the luminous active nuclei do not appear to be tapping the entire fuel reservoir in NGC 6090, NGC 6240, and Arp 220. The luminosities of these three mergers thus have the potential to rise further as the mergers progress, and we may be seeing a relatively early phase of the strong activity in these systems.

3.5.2. Applicability of the standard $M_{\rm g}/L'_{\rm CO}$ conversion factor

The value of the conversion factor from CO luminosity, $L'_{\rm CO}$, to the molecular gas mass, $M_{\rm g}$, depends on the physical conditions of the molecular gas, its environment, and its geometrical configuration. In Chapter 2, we have analyzed the behavior of the conversion factor for a variety of different conditions and geometries. For a smooth, spherical distribution of gas, and for a clumpy distribution (independent of geometry as long as the clumps do not shadow each other's emission), the gas mass is given by the equation

$$M_{\rm g} = bL'_{\rm CO} f^{1/2}(1+q)^{-1/2} \ , \qquad (3\text{–}2)$$

where $b \equiv (2.57/\alpha^{-1/2})(\bar{n}^{1/2}/\bar{T})\ {\rm M}_\odot\ ({\rm K\ km\ s^{-1}\ pc^2})^{-1}$, $\bar{n}$ and $\bar{T}$ are the mean cloud H_2 density and CO 1→0 brightness temperature, q is the ratio of pressure to gravitational confinement, and f is the gas mass fraction of either the entire cloud (for the single

smooth cloud case) or individual clumps; α is a parameter of order unity, which we adopt as equal to 1.5 as in Chapter 2. The pressure confinement parameter q can be expressed as

$$q = 0.0201 \frac{f}{\alpha_1} \frac{\Pi_e/k \ [\mathrm{cm^{-3}\ K}]}{\Sigma_g^2 \quad [\mathrm{M_\odot\ pc^{-2}}]} , \qquad (3\text{–}3).$$

where Π_e is the sum of the confining thermal and magnetic pressure and α_1 is another parameter of order unity; we adopt $\alpha_1 = 1.0$ as in Chapter 2.

3.5.2.1. Requirements for pressure confinement of gas clouds

If the total (thermal and magnetic) pressure of the medium external to the molecular gas is great enough, the molecular gas clouds can be confined by this pressure rather than by self-gravity. In this case, for a given mass, the line width can be much greater than for a self-gravitating cloud, increasing the line luminosity and hence decreasing the M_g/L'_{CO} conversion factor by an arbitrary amount. The mass of pressure-confined clouds can therefore be severely overestimated by blind use of the standard conversion factor derived for self-gravitating Galactic GMCs.

Estimates of the external pressure that is required for pressure confinement to significantly decrease the conversion factor can be made by setting $q = 1$ in equation 3–3 above:

$$\Pi_{e,crit}/k = 49.8 f^{-1} \Sigma_g^2 \quad [\mathrm{cm^{-3}\ K}] \ . \qquad (3\text{–}4)$$

By using the minimum value for Σ_g, derived for optically thin CO (§3.5.1.2), lower limits to this critical pressure can be derived. These lower limits are listed in column 2 of Table 3–6.

Table 3–6. Minimum Requirements for Pressure Confinement of the Molecular Gas

object	$\Pi_{e,crit}/k$	L_{ff}^{min}	
		5×10^7 K	5×10^6 K
	(cm^{-3} K)	($L_\odot$)	($L_\odot$)
(1)	(2)	(3)	(4)
NGC 2623	4.0×10^7	1.5×10^6	1.5×10^7
Mrk 231[a]	2.4×10^8	9.1×10^7	9.1×10^8
IC 883	2.6×10^6	5.7×10^4	5.7×10^5
NGC 6090	6.0×10^5	8.4×10^3	8.4×10^4
NGC 6240	1.3×10^8	2.2×10^7	2.2×10^8
NGC 7469	3.9×10^6	7.2×10^4	7.2×10^5
NGC 7674	3.8×10^5	2.7×10^2	2.7×10^3

Columns: (1) object; (2) lower limit to the external pressure required for pressure confinement to dominate gravitational confinement of molecular clouds, using the lower limit to the gas surface density shown in Table 3–7; (3) lower limit to the thermal bremsstrahlung luminosity associated with such a hypothetical confining medium for a temperature of 5×10^7 K, using a volume for the medium of $\pi R_c^2 h$, with $h = 100(T/5 \times 10^6\ \mathrm{K})^{0.5}$ pc; (4) same as column 3, but with $T = 5 \times 10^6$ K.

Note:
[a] See Chapter 2.

Even these rather conservative limits are strikingly high in some cases—especially for the most compact objects: Mrk 231, NGC 6240, and NGC 2623. Are there observational consequences of such a high pressure medium if it exists? This hypothetical medium is almost certainly ionized; if it were not ionized, it would be cool, and the high pressures would imply a density high enough so that the external medium would itself be molecular. An ionized gas will produce thermal bremsstrahlung at a rate proportional to $n_e n_i T^{1/2}$, where n_e and n_i are, respectively, the electron and ion volume density and T is the temperature of the confining medium (e.g., Rybicki & Lightman 1979). The bremsstrahlung luminosity is given by $L_{ff}(L_\odot) > 3165\ V(\mathrm{kpc}^3)\ T^{-3/2}\ (\Pi_{e.crit}/k)^2$, where V is the volume of the medium, which must be greater than the volume encompassed by the molecular gas. Using

equation 3–4, the bremsstrahlung luminosity can also be expressed as

$$L_{\rm ff} > 2.22 \times 10^{-5}\ f^{-2}\ V({\rm kpc}^3) \left(\frac{T}{5 \times 10^7\ {\rm K}}\right)^{-3/2} \Sigma_{\rm g}^2 \quad [{\rm L}_\odot]\ . \tag{3–5}$$

Values for these limits, using the optically thin values for $\Sigma_{\rm g}$ and a temperatures of 5×10^7 K (4.3 keV) and 5×10^6 K (0.43 keV), are given in Table 3–6. For a temperatures in the approximate range 2.5×10^6 to 5×10^7 K, the bulk of this luminosity should emerge within the bandpass of typical X-ray satellites.

The strongest constraint is for Mrk 231, which is undetected by the *Einstein* satellite at a limit of 2.0×10^8 $L_\odot$. As discussed in §2.4.2.1.2, this suggests that the molecular gas in that object is unlikely to be confined by thermal pressure. The other objects with published X-ray data, NGC 6240 (Brinkmann, Siebert, & Boller 1994), NGC 7469 (Fabbiano, Kim, & Trinchieri 1992), and NGC 7674 (Awaki et al. 1991), all exhibit X-ray luminosities significantly greater than the minimum expected from a medium that thermally confines the molecular gas; hence the existence of such a medium cannot be ruled out in these objects.

3.5.2.2. Lower limits to the mass of molecular gas

A lower limit to the mass of molecular gas can be obtained by assuming that the CO 1→0 emission is optically thin, though assumptions for the abundance and excitation of CO are required (see Appendix A). We assume a $[CO]/[H_2]$ abundance ratio of 10^{-4} and LTE excitation with the minimum excitation temperatures (7–34 K) listed in Table 3–5. The resulting lower limits to the core gas mass, $M_{\rm g,c}^{\rm min}$, are shown in Table 3–7. These limits are typically 4–5% of the estimates given by the standard

Table 3–7. Optically Thin CO 1→0 Case

object	$M_{g,c}^{min}$ (10^9 $M_\odot$)	τ_{CO}^{min}	$M_{g,c}^{min}/M_{dyn}$	$<\Sigma_{g,c}^{min}>$ ($M_\odot$ pc^{-2})	$<A_K^{min}>$ (mag)	$<A_V^{min}>$ (mag)
(1)	(2)	(3)	(4)	(5)	(6)	(7)
NGC 2623	0.44	0.06	0.083	890	2.4	22
Mrk 231[a]	1.77	0.19	0.52	2200	5.8	54
IC 883	0.94	0.06	0.042	230	0.6	5.6
NGC 6090	0.69	0.04	0.15	110	0.3	2.6
NGC 6240	1.12	0.09	0.079	1600	4.3	40
NGC 7469	0.68	0.05	0.071[b]	280	0.7	6.8
NGC 7674	0.079	0.06	0.003[c]	88	0.2	2.2

Columns: (1) object; (2) minimum molecular gas mass of core, derived by assuming that the CO emission is optically thin, using $[CO]/[H_2] = 10^{-4}$ and LTE level populations with the minimum T_x given in Table 5 (see Chapter 2); (3) minimum optical depth of CO emission, assuming CO uniformly distributed in spherical region of observed radius at a LTE excitation temperature of less than 60 K; (4) ratio of minimum gas mass to dynamical mass of core; (5) mean molecular gas surface density of core in the case of optically thin emission; (6) mean K-band ($\lambda 2.2\mu$m) extinction through the core implied by the minimum molecular gas column density, assuming a standard extinction law (e.g., Mathis 1993); (7) corresponding mean V-band ($\lambda 0.55\mu$m) extinction.

Notes:
[a] See Chapter 2.
[b] For a disk inclined 47° to the line-of-sight.
[c] For a disk inclined 17° to the line-of-sight.

conversion factor, except for Mrk 231 where the strong constraint on T_x requires $M_{g,c}^{min}$ to be 8% of M_g^*.

The minimum optical depth can also be estimated, which allows a self-consistency check for the assumption of optically-thin CO emission (see §2.4.2.2). This minimum optical depth occurs if the CO is assumed to be uniformly distributed in a sphere of the observed radius. Because the dust temperatures of actively star-forming galaxies are almost always between 30 and 50 K (e.g., Chini, Krügel, & Kreysa 1992), we further assume that the CO excitation is LTE with $T_x < 60$ K. In this case, the CO optical depth cannot be smaller than the values listed in column 3 of Table 3–7 (0.04–0.19). While these values are significantly less than one, it would not take much clumping to raise the optical depths to values approaching unity. Also, if

the excitation temperature is only 30 K, a possibility excluded by the data only for Mrk 231, the minimum optical depths jump to values of 0.15–0.35. Optically-thin CO emission cannot be ruled out, but it requires exceptionally warm excitation temperatures and very diffusely-distributed molecular gas.

The core molecular gas masses implied by the CO observations in the five mergers and NGC 7469 range from minimums of 0.4–1.8 $\times$ 10^9 to maximums of 2–3 $\times$ 10^{10}. The possible gas masses for the core of NGC 7674 cover an equally broad range, but for masses about an order of magnitude smaller.

Even at the extreme lower limit, the column densities of gas in the cores of these objects must be very large. The lower limits to the V band extinctions through the cores (A_V = 2.2–54) are very large in all seven objects. Extinction at near-infrared wavelengths is also very significant for the three most compact objects (A_K = 2.4–5.8). If the CO emission is optically thick and from self-gravitating GMCs like those in the Milky Way, the estimated extinctions are much greater, and very substantial in all seven objects (A_K = 7–56; Table 3–5). In all these galaxies—with the possible exceptions of NGC 6090 and NGC 7674 where the lower limits to A_K are only 0.2 and 0.3, respectively—the column density of gas is large enough to have a severe impact upon the emergent K band radiation, because, at extinctions greater than 1 magnitude, the amount and distribution of the observed emission is highly sensitive to the relative geometry of emission and absorption (e.g., Witt, Thronson, & Capuano 1992).

3.5.3. Empirical correlations for a larger sample of gas-rich IR galaxies

We have compiled interferometric CO data for 18 infrared-bright, gas-rich galaxies from the literature to add to the 7 galaxies studied here, in order to search for empirical correlations that can provide insight into the physical properties of such galaxies. We have restricted the compilation to galaxies at distances greater than 20 Mpc, so that the angular size of the CO emission is small enough that relatively little of the CO emission is resolved out. Table 3–8 lists the CO data and derived quantities, as well as other basic data for these galaxies. A similar, but smaller compilation was provided by Scoville et al. (1991).

The original references for the data in Table 3–8 use various conventions for deriving quantities such as distances, luminosities, molecular gas masses, and gas surface densities. In compiling Table 3–8, we have re-calculated these quantities using consistent definitions. We adopt the distances quoted by SSS, calculated as described in §3.2, for the galaxies more distant than 40 Mpc, and by Tully (1988) for the galaxies closer than 40 Mpc. We calculate the molecular gas masses, $M_g = M(\mathrm{H_2} + \mathrm{He})$, from equation 3–1; the value we adopt for the standard CO conversion factor is 25% less than the value originally used by many of the references for the data in Table 3–8. Finally, we calculate the far-infrared luminosities, L_{FIR}, from the luminosity of single-temperature blackbody fits to the IRAS 60 and 100 μm fluxes.

Most of the references listed in Table 3–8 quote velocities in heliocentric cz units. The line width in these units does not correspond to the actual velocities in the gas if the object is significantly redshifted. If Δv and $\Delta v'$ are the actual and cz line

Table 3–8. Compilation of infrared-bright galaxies with interferometric CO data

object	D (Mpc)	log f_{12}/f_{25}	log f_{25}/f_{60}	log f_{60}/f_{100}	log L_{FIR} ($L_\odot$)	R_{bm} (kpc)	R_{CO} (kpc)	F_{CO} (Jy km s^{-1})	log M_g^* ($M_\odot$)	log Σ_g^* ($M_\odot$ pc^{-2})	L_{FIR}/M_g^* ($L_\odot$ $M_\odot^{-1}$)	refs[a]
(1)	(2)	(3)	(4)	(5)	(6)	(7)	(8)	(9)	(10)	(11)	(12)	(13)
Mrk 231	173.9	−0.66	−0.60	+0.04	12.37	0.32	0.42	62	10.33	4.43[b]	108.5	1
17208−0014	175.0	−0.76	−1.31	−0.04	12.35	1.21	1.25	164	10.76	3.91	38.8	2
Arp 220	79.2	−1.09	−1.12	−0.04	12.13	0.38	0.36	391	10.46	4.52[b]	46.7	3
Mrk 273	153.8	−1.00	−0.98	−0.01	12.04	0.82	<0.43	138	10.58	>4.35	29.1	4
VII Zw 31	220.5	−0.47	−0.98	−0.25	11.84	2.93	<1.60	76	10.62	>3.56	16.5	5
Arp 299	48.0	−0.79	−0.70	−0.00	11.77	0.28	0.17	186	10.00	4.46	59.1	6
10173+0828	197.4	−0.78	−0.96	+0.01	11.70	6.39	<3.35	21	9.97	>2.87	53.5	2
NGC 6240	100.9	−0.75	−0.79	−0.08	11.69	0.69	0.39	324	10.59	4.50	12.7	this work
Arp 55	162.7	−0.59	−1.02	−0.19	11.59	3.13	<1.77	86	10.42	>2.96	14.9	7
IC 883	97.8	−0.72	−1.00	−0.26	11.51	0.51	0.96	202	10.36	3.73[b]	14.3	this work
NGC 2623	76.1	−0.89	−1.14	−0.03	11.49	0.40	0.33	153	10.02	4.32	29.7	this work
VV 114	77.7	−0.54	−0.81	−0.14	11.46	0.70	2.87	688	10.69	3.22	5.9	8
NGC 1614	62.3	−0.73	−0.63	−0.04	11.43	0.74	<0.45	105	9.68	>3.72	56.1	5
NGC 7469	66.4	−0.56	−0.68	−0.10	11.41	1.16	0.73	317	10.22	3.83[b]	15.6	this work
NGC 6090	123.3	−0.62	−0.71	−0.17	11.33	0.66	1.61	169	10.48	3.42	7.2	this work
NGC 828	72.6	−0.12	−1.06	−0.31	11.23	1.04	3.68	301	10.27	2.81	9.1	9
NGC 7674	115.3	−0.44	−0.45	−0.18	11.19	1.00	<0.45	85	10.12	>3.31[b]	11.7	this work
Zw 049.057	52.3	−1.07	−1.35	−0.15	11.10	0.34	0.30	122	9.60	3.98	32.0	2
NGC 3079	20.4	−0.14	−1.15	−0.31	10.75	0.35	0.56	1381	9.84	3.68[b]	8.1	10
NGC 520	27.8	−0.52	−1.02	−0.17	10.73	0.37	0.67	327	9.48	3.17	17.8	7
NGC 4038/9	25.4	−0.43	−0.87	−0.23	10.71	0.42	0.91	430	9.52	2.67	15.5	11
NGC 1530	36.6	−0.22	−0.93	−0.41	10.65	0.33	1.33	380[c]	9.78	3.01	7.4	12,13
NGC 7252	63.0	−0.25	−0.97	−0.25	10.58	0.46	1.83	75	9.55	2.60	10.8	14
NGC 3504	26.5	−0.57	−0.73	−0.20	10.56	0.16	0.84	280	9.37	3.08	15.5	15
NGC 6951	24.1	−0.20	−0.90	−0.40	10.50	0.13	0.76	210	9.16	3.01	21.8	15

Column descriptions: (1) object designation; (2) distance (H_0 = 75 km s^{-1} Mpc^{-1}); (3)-(5) infrared colors from IRAS data (Soifer et al. 1989; Sanders et al. 1995); (6) luminosity of single-temperature blackbody fit to IRAS 60–100 μm data; (7) HWHM of CO beam at the adopted distance; (8) deconvolved semi-major axis of the CO emission; (9) interferometric integrated CO flux; (10) nuclear molecular gas mass, from the standard conversion factor; (11) average surface density of densest CO component; (12) ratio of FIR luminosity to nuclear molecular gas mass; (13) reference for CO data.

[a] References for CO data: (1) Bryant & Scoville 1996; (2) Planesas, Mirabel, & Sanders 1991; (3) Scoville et al. 1991; (4) Yun & Scoville 1995; (5) Scoville et al. 1989; (6) Aalto et al. 1996; (7) Sanders et al. 1988; (8) Yun, Scoville, & Knop 1994; (9) Wang, Scoville, & Sanders 1991; (10) Young, Claussen, & Scoville 1988; (11) Stanford et al. 1990; (12) Downes et al. 1996; (13) Regan, Vogel, & Teuben 1995; (14) Wang, Schweizer, & Scoville 1992; (15) Kenney et al. 1992.

[b] Corrected for inclination, by taking the semi-major axis of the deconvolved CO emission region as the disk radius.

[c] Single dish flux from IRAM 30 m telescope.

widths, respectively, then $\Delta v' = (\nu_0/\nu_R)\Delta v = (1+z)^{-1}\Delta v$, where ν_0 is the redshifted line center frequency and ν_R is the rest frequency of the line. As a result, integrated CO fluxes in cz velocity units, which we denote as F'_{CO}, will be less than F_{CO} by a factor of $(1+z)$: $F_{CO} = F'_{CO}(1+z)^{-1}$. When necessary, by using this expression, the integrated CO fluxes in Table 3–8 have been converted to physical velocity units from those originally quoted. These are relatively small corrections due to the low redshifts of the galaxies in Table 3–8.

Correlations involving the total molecular gas mass, $M^*_{g,T}$, and $L_{FIR}/M^*_{g,T}$ are discussed in SSS using single dish CO data for a sample which contains most of the objects in Table 3–8 as a subset. Our analysis differs in that we use interferometric CO fluxes to calculate M^*_g rather than single dish CO fluxes. We thus are measuring the nuclear molecular gas masses rather than the total molecular gas masses. From the numbers in Table 3–8, M^*_g and L_{FIR}/M^*_g exhibit trends consistent with those seen by SSS for $M^*_{g,T}$ and $L_{IR}/M^*_{g,T}$, where L_{IR} is an estimate of the infrared luminosity from 8–1000 μm. L_{FIR}/M^*_g increases as L_{FIR} increases and also as the ratio of IRAS 60 and 100 μm fluxes increases. The latter trend exhibits a slope consistent with that reported by SSS: $L_{IR} \propto T_d^{5.6}$, where SSS have parameterized the 60/100 μm color with the "dust temperature," T_d. L_{FIR}/M^*_g and M^*_g are uncorrelated in our sample, also consistent with the larger sample of SSS.

3.5.3.1. Central gas surface density and IRAS colors

Due to the distances and the compact sizes of the molecular gas distributions of

most of the galaxies in Table 3–8, the central CO surface brightnesses cannot be estimated with single dish CO data. SSS thus do not study correlations with respect to the central gas surface density. With the compilation of interferometric CO data in Table 3–8, we are able to examine how the standard central gas surface densities, Σ_g^*, vary with selected global properties of infrared-bright galaxies.

The central gas surface density is strongly correlated with the IRAS 12/25 μm color. As depicted in Figure 3–23, the objects with higher Σ_g^* generally exhibit redder 12/25 μm colors. The scatter is large, up to an order of magnitude in Σ_g^* on either side of the mean trend, but a Spearman rank correlation test (e.g., Press et al. 1986) yields a probability of only 1.0×10^{-5} that such a trend could arise by chance if the quantities are uncorrelated in the sample. In infrared-selected galaxies, the IRAS 12/25 μm colors are strongly anti-correlated with the 60/100 μm colors (Helou 1986; Soifer et al. 1989; Lutz 1992; Bicay et al. 1995). Thus, because high gas surface densities are associated with cool 12/25 μm colors, they are also associated with warm 60/100 μm colors. This is shown in a Figure 3–24, where the sizes of the symbols represent the surface densities.

The empirical anti-correlation of the IRAS 12/25 and 60/100 μm colors in galaxies has been explained using multi-component dust models as due to an increase in the amount of dust near star-formation regions relative to cool "cirrus"-type dust (Helou 1986; Rowan-Robinson & Crawford 1986, 1989). We suggest that at the warm 60/100 μm end of this trend, where the gas surface densities are over 10^4 $M_\odot$ pc^{-2}, the 12/25 μm color can *also* be affected by a significant amount of reddening due to

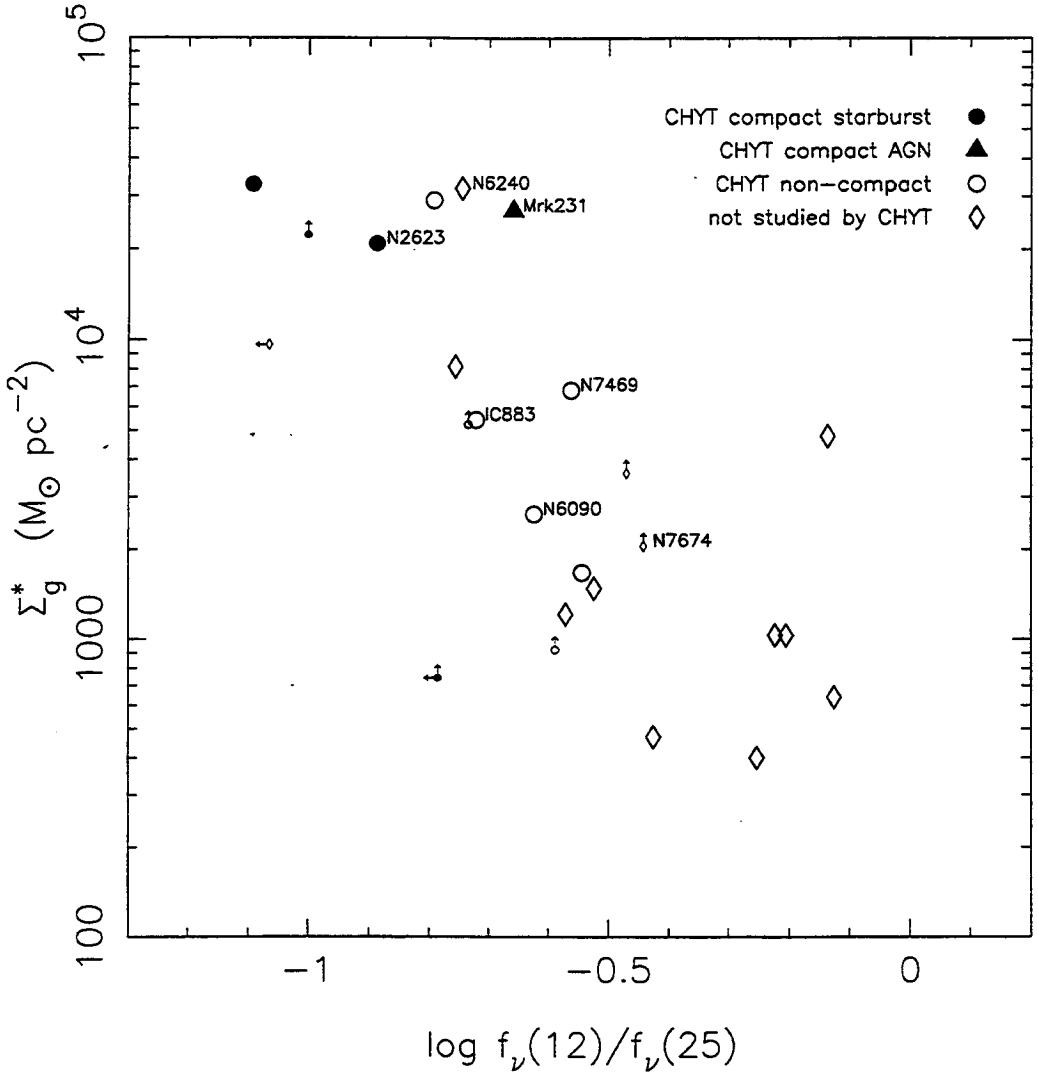

Figure 3–23. The CO surface brightness, parameterized as a gas surface density via the standard conversion factor, is plotted versus the IRAS 12/25 μm colors for the galaxies in Table 3–8. The data from this work are labeled by the galaxy name. The different symbols represent whether the 8.44 GHz radio continuum is more compact than the minimum blackbody size for the IRAS 25–60–100 μm emission (CHYT). Those that are more compact in the radio are tagged as CHYT compact starbursts (or AGN, for Mrk 231, whose radio continuum varies on a timescale of months); those that are not are tagged as CHYT non-compact.

extinction. Optical depth effects have been offered previously as a partial explanation for the behavior of galaxies on IRAS color-color plots (Soifer et al. 1989). As we explain below, we now have strong quantitative evidence for this in our compilation of infrared-luminous galaxies.

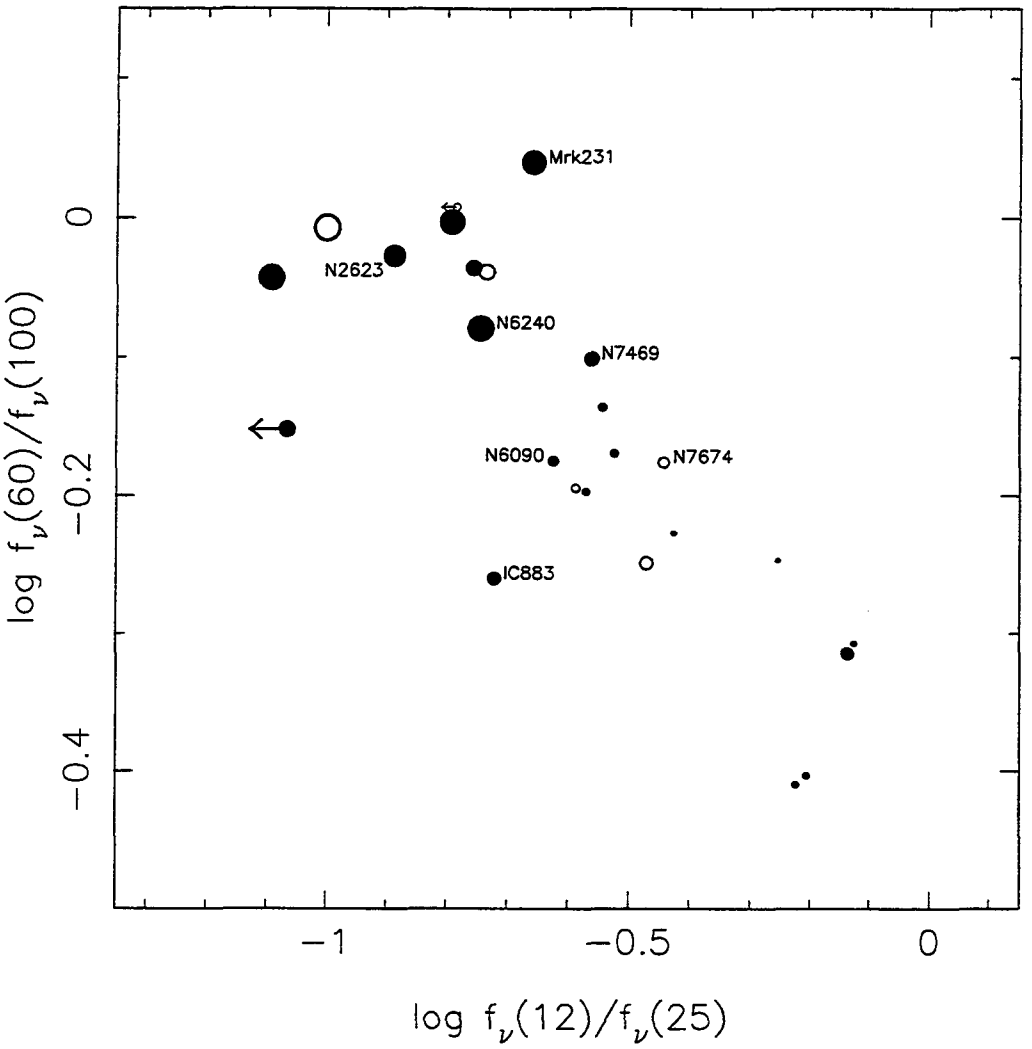

Figure 3–24. The IRAS 12/25 μm colors plotted versus the 60/100 μm colors for the infrared-bright galaxies in Table 3–8 show the well-known anti-correlation. The size of the symbols is proportional to the logarithm of Σ_g^*. Solid symbols are galaxies with measurements of Σ_g^*, while open symbols are galaxies with lower limits to Σ_g^*. High CO surface brightness galaxies concentrate in the upper left portion of the diagram. The data from this work are labeled with the galaxy names.

Extinction and its corresponding reddening can quantitatively account for the size of the correlation in Figure 3–23. The reddest objects, with $\log(f_\nu(12)/f_\nu(25)) \approx -1.0$, show $\Sigma_g^* \approx 2 \times 10^4$ M$_\odot$ pc^{-2}, which corresponds to $A_V \approx 500$ and $A_{12\mu m} \approx 14$, using the extinction law tabulated in Mathis (1993). Accounting for the finite bandwidths of the IRAS filters, such a large column of gas can redden the observed

$\log(f_\nu(12)/f_\nu(25))$ by 0.35 to 1.91. The lesser value corresponds to a uniform mixture of absorbers and emitters, while the greater value corresponds to a foreground absorbing screen. The bulk of infrared-selected galaxies show $\log(f_\nu(12)/f_\nu(25))$ from -0.1 to -0.7, and very rarely show a 12/25 μm color less than -0.8 (Soifer et al. 1989; Sanders et al. 1995). The 7 galaxies from Table 3–8 with the highest Σ_g^* (above 9×10^3 $M_\odot$ pc^{-2}) show extremely red 12/25 μm colors from -0.65 to -1.09. They are thus redder than a typical infrared-selected galaxy ($\log(f_\nu(12)/f_\nu(25)) \approx -0.4$) by 0.25 to 0.69 decades; the most extreme, Arp 220. is redder by 0.3 decades than the sharp edge of the color distribution of infrared-selected galaxies. Furthermore, models of infrared dust emission that neglect extinction have difficulty producing 12/25 μm colors redder than -0.8 (Désert 1986; Rowan-Robinson & Crawford 1989). Hence, the 12/25 μm colors of the densest objects in our sample are entirely consistent with the degree of reddening expected from the column of gas implied by the CO observations. The large scatter in Figure 3–23 is likely due to the high sensitivity of the amount of reddening to the relative geometry of the emitting and absorbing material. Variations in the CO conversion factor, as well as variations in the intrinsic 12/25 μm color due to varying interstellar radiation fields (e.g. Désert 1986), should also contribute to the scatter.

3.5.3.2. Central gas surface density and $L_{\rm FIR}/M_g^*$

In a larger sample, with improved CO data for many objects, we confirm the correlation of central gas surface density (CO surface brightness) with $L_{\rm FIR}/M_g^*$ that was first noted by Scoville et al. (1991). From the Spearman rank correlation test, the

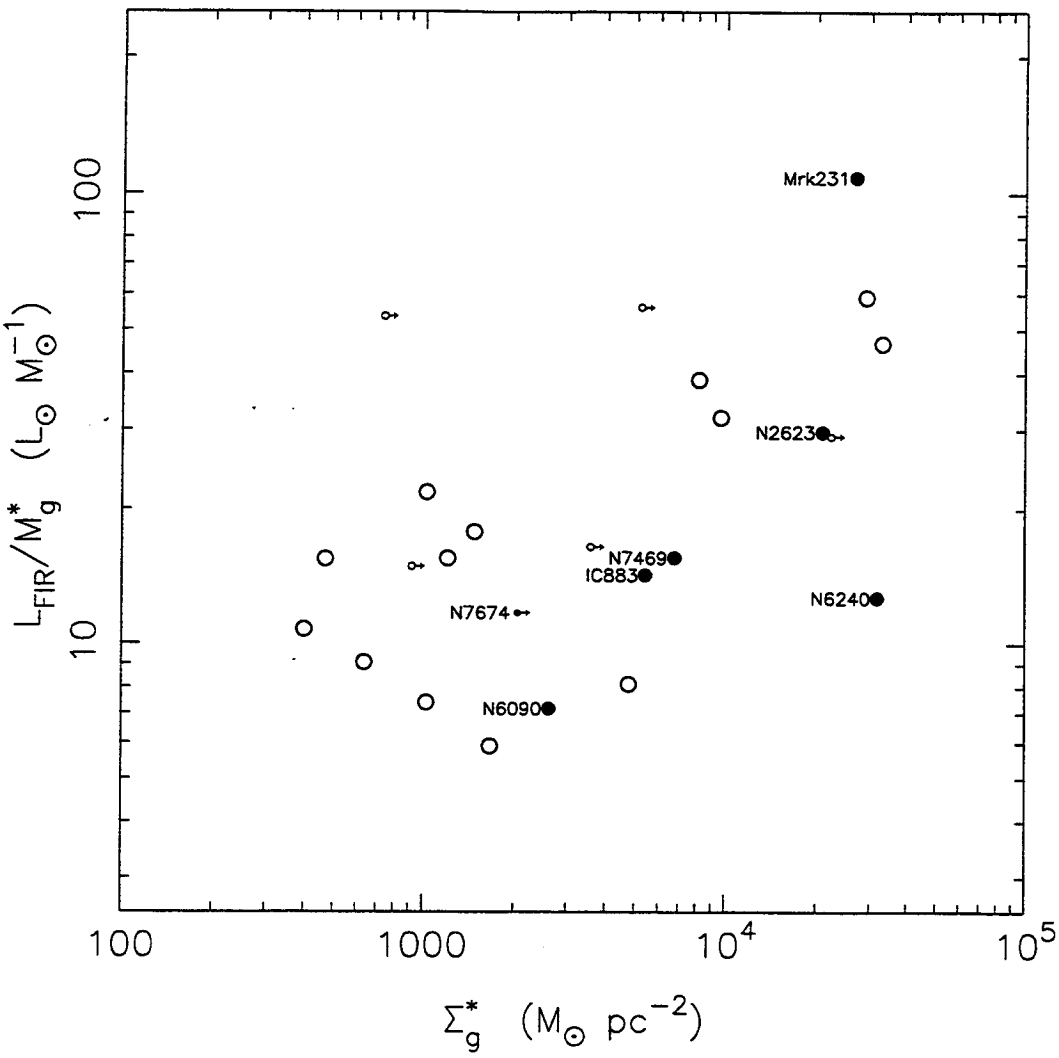

Figure 3–25. The ratio of FIR luminosity to the standard molecular gas mass (proportional to CO luminosity) is plotted versus the standard gas surface density (proportional to the CO surface brightness) for the infrared-bright galaxies in Table 3–8. The data from this work are shown as solid symbols and are labeled with the galaxy names.

probability that the observed trend could be due to the chance alignment of uncorrelated quantities is under 1%. The trend is shown in Figure 3–25. High efficiencies of luminosity generation per unit gas mass are associated with a high central gas densities.

If a starburst dominates the luminosity output, and $L_{\rm FIR}/M_{\rm g}^*$ is interpreted as an efficiency for star formation (which is true as long as the shape and boundaries of the IMF is constant in the sample galaxies), then the empirical correlation in Figure 3–25 implies that the efficiency increases with increasing concentrations of gas. This is consistent with both cloud-cloud collision and gravitational instability models of star formation. In the former case, the timescale for collisions is inversely proportional to $N\sigma v$, where N is the mean density of clouds, σ is the collision cross section, and v is the mean velocity; this timescale hence decreases as the gas mass density, which is proportional to the cloud density, increases. For gravitational instability models, the timescale for collapse is inversely proportional to $n^{1/2}$, where n is the mean particle density in clouds; this timescale also decreases with increasing density, though in this case, the empirical trend suggests that the mean particle density, and not simply the mean cloud density, is higher for higher gas surface density.

Alternatively, high $L_{\rm FIR}/M_{\rm g}^*$ ratios may signify that the bulk of the luminosity is being generated by sources other than star formation, such as a dust-enshrouded AGN. In this case, the empirical trend suggests that the fueling of the AGN becomes more efficient, i.e., the accretion rates increase, at higher gas surface densities. Whatever the source of luminosity, the strong correlation of $L_{\rm FIR}/M_{\rm g}^*$ and $\Sigma_{\rm g}^*$ clearly demonstrates that the high luminosities of these galaxies are related to the high degree of concentration of molecular gas.

Several possible systematic and random errors in the determination of $L_{\rm FIR}/M_{\rm g}^*$ and $\Sigma_{\rm g}^*$ complicate the interpretation of the correlation between these observed quan-

tities. These effects, however, act to mask any correlation between the physical quantities corresponding to the observed $L_{\rm FIR}/M_{\rm g}^*$ and $\Sigma_{\rm g}^*$. The presence of a correlation in the observed quantities in Figure 3–25 thus strongly suggests that there is an actual correlation in the physical quantities as well.

First, the conversion factor from CO luminosity to molecular gas mass can vary from object to object in both a systematic and a random fashion. According to theoretical understanding, the CO conversion factor can vary tremendously depending on the physical conditions in the molecular gas being observed and also upon the geometry and orientation of the molecular gas (see Chapter 2, Appendix A and references therein). Variation of the conversion factor is therefore expected between galaxies and even with position in a single galaxy. Since high $\Sigma_{\rm g}^*$ strictly means nothing more than high CO surface brightness, a systematic variation of the CO conversion factor with $\Sigma_{\rm g}^*$ is a strong possibility. Given the large ratios of $M_{\rm g}^*$ to $M_{\rm dyn}$ for objects of high $\Sigma_{\rm g}^*$, any such systematic variation is likely causing an overestimate of actual gas surface density for high $\Sigma_{\rm g}^*$, and not an underestimate. If the standard conversion factor is causing such an overestimate, it is also overestimating $M_{\rm g}^*$ and causing $L_{\rm FIR}/M_{\rm g}^*$ to be depressed from the actual ratio at high $\Sigma_{\rm g}^*$. This observational effect thus has the potential to reduce, hide, or reverse a positive physical correlation between luminosity-to-gas mass ratio and gas surface density; however, it cannot create an observed correlation if there is no physical one.

Systematic errors can also be introduced by the large difference in apertures between the FIR measurements and the CO measurements. $L_{\rm FIR}$ is a global measure-

ment, while the M_g^* reported here are the estimated gas masses in the central regions. Near and mid-IR observations (e.g., Keto et al. 1992; Wynn-Williams & Becklin 1993) suggest that most of the IR luminosity arises from the central regions of the most IR-luminous objects. This is not always the case for lower luminosity objects, however. At lower L_{FIR}, and hence lower L_{FIR}/M_g^* (see above), L_{FIR} may overestimate the luminosity associated with the central regions, and thus may overestimate the central value for L_{FIR}/M_g^*. Like systematic variations in the CO conversion factor, this effect can reduce, hide, or reverse a positive correlation between L_{FIR}/M_g^* and Σ_g^*, but cannot create an observed trend out of nothing.

Also, the lack of uniform linear CO apertures in the sample in Table 3–8 should increase scatter in the derived central gas densities, and thus may hide weak correlations involving Σ_g^*. Fortunately, no systematic bias in Σ_g^* appears to be introduced by the non-uniform apertures (Figure 3–27a; §3.5.2.3).

Due to the above effects that can reduce or hide a positive correlation between the luminosity-to-gas mass ratio and the central gas densities, the observation of a strong positive correlation in Figure 3–25 and Scoville et al. (1991) provides robust evidence for an actual physical correlation between the gas surface density and the efficiency of luminosity generation per unit gas mass in the centers of luminous galaxies.

3.5.3.3. Distance and aperture biases

The sample in Table 3–8 was not selected based on strict observational criteria, contains galaxies at a wide range of distances, and utilizes data with highly non-uniform

CO apertures. We must ask whether observational biases are affecting the trends shown in Figures 3–23 to 3–25. Figures 3–26 and 3–27ab illustrate that, despite the inhomogeneity of the data, neither Σ_g^* nor L_{FIR}/M_g^* appear to be biased by distance or aperture. The measured gas masses, M_g^* do show a trend with aperture size (Figure 3–27c), which is likely explained by interferometers resolving out some CO emission for nearby objects where the synthesized beam covers a small area. This bias, by artificially raising L_{FIR}/M_g^* for nearby galaxies, would by itself produce trends opposite to those seen for this variable with respect to Σ_g^*, L_{FIR}, and $\log(f_\nu(60)/f_\nu(100))$, and so cannot be responsible for the observed behavior. Therefore, this bias has no qualitative impact on our conclusions.

Another potential bias is the trend of increasing deconvolved CO source diameter with increasing linear beam size (Figure 3–27d). This behavior, though, can be introduced by the observational procedure and need not be the result of an artificial bias introduced by inaccurate deconvolution. Imagine a large sample of objects observed at low (e.g., several kpc) resolution. Some of these will be well resolved, but most will be either marginally resolved or completely unresolved. The ones that are re-observed at higher (e.g., 1–2 kpc) resolution will belong to the latter category. Repetition of this process will produce a trend such as that seen in Figure 3–29d, where the largest objects were observed with the largest apertures and the smallest objects with the smallest apertures. We therefore conclude that neither distance nor aperture biases corrupt the qualitative behavior of the observed trends discussed above, despite the inhomogeneity of the data in Table 3–8.

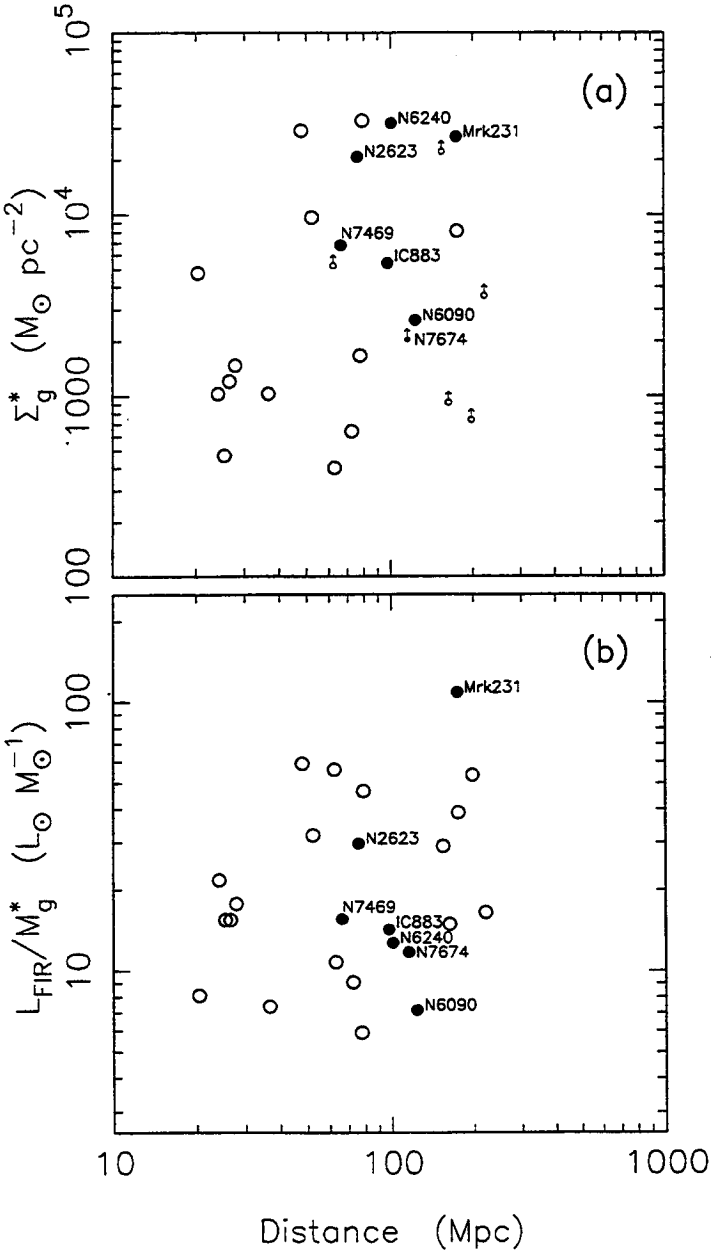

Figure 3–26. The quantities (a) Σ_g^* and (b) $L_{\rm FIR}/M_g^*$ are plotted versus the distance (H_0 = 75 km s^{-1} Mpc^{-1}) for the infrared-bright galaxies in Table 3–8 to search for possible biases in the sample of objects. Neither quantity shows a significant trend with distance. The data from this work are shown as solid symbols and are labeled with the galaxy names.

3.5.3.4. Implications for the compact starburst hypothesis

Eleven of the objects in our sample were part of the sample of infrared-luminous

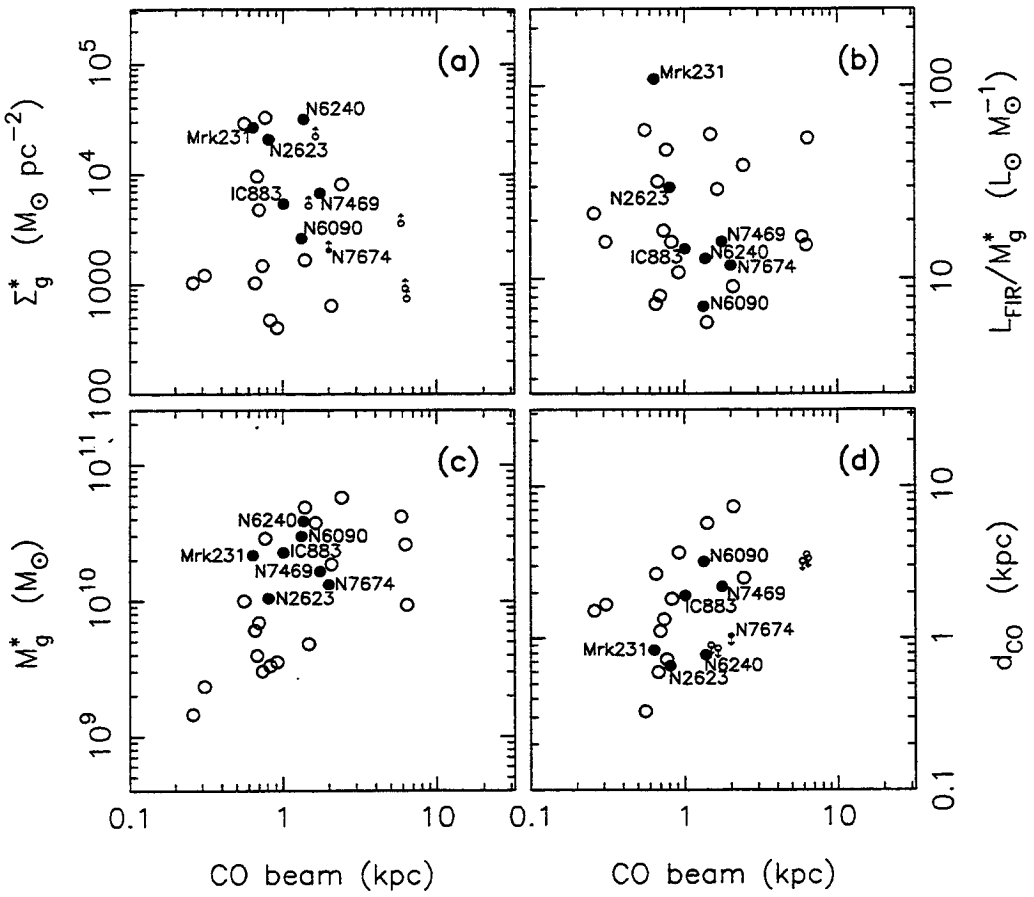

Figure 3–27. The quantities (a) Σ_g^*, (b) L_{FIR}/M_g^*, (c) M_g^*, and (d) d_{CO} (the CO source diameter) are plotted versus the linear CO beam size for the infrared-bright galaxies in Table 3–8 to search for possible biases in the sample of objects. See text for a discussion. The data from this work are shown as solid symbols and are labeled with the galaxy names.

galaxies mapped in the radio continuum by CHYT. Four, plus 10 not in our sample, were found to exhibit radio source sizes smaller than the minimum angular size required for the thermal IRAS 25–60–100 μm emission. CHYT interpret these objects as compact starbursts (CSBs), a hypothesis which *requires* that the dust be optically thick at all wavelengths shorter than 25 μm. In their model, the non-thermal radio flux and the thermal far-IR flux both arise from star formation regions, thus explaining the strong empirical correlation between these quantities. The far-IR flux

normally should be roughly coincident with the star formation since nearly all of the optical and ultraviolet radiation produced by starbursts is quickly absorbed by dust. The non-thermal radio, due to the propagation of the energetic particles produced in supernovae responsible for the synchrotron radiation, should encompass a slightly larger region. For the radio to appear *smaller* than the far-IR requires that the far-IR radiation emergent from the immediate vicinity of the star formation regions be absorbed and re-emitted by a surrounding dust layer that is optically thick in the far-IR (CHYT). CHYT also point out that, unlike starbursts, AGNs can possess smaller radio sources than far-IR sources without such optically thick dust, since the radiation emergent from their surfaces may still be in the optical and ultraviolet.

As can be seen in Figure 3–23, three of the four CSBs in Table 3–8—Arp 220, Mrk 273, and NGC 2623—exhibit three of the four reddest 12/25 μm colors: -1.09, -1.00, and -0.89, respectively (see Figures 3–23 and 3–25). The fourth "compact starburst" in our sample, IRAS 10173+0828, has an upper limit to its 12/25 μm color of -0.78, meaning it is likely as red as the other three. Zw 049.057, the only other object in Table 3–8 with so red a color, was not studied by CHYT, but it also fits the definition of CSBs: a blackbody responsible for its 60–100 μm emission must have an angular diameter greater than $0''.76$, while its 1.5 GHz emission is only $0''.5$ across (Condon et al. 1990). Such extreme red colors (see §3.4.1) suggest that the optical depths of these objects are indeed very large. The interferometric CO observations provide further evidence, in the association of high gas surface densities with the extremely

red 12/25 μm colors (Figure 3–23). The gas surface densities (from the standard conversion factor) of the three compact starbursts that have been resolved in CO emission correspond to $A_{25\mu m} \approx 8$–15. Even accounting for the additional uncertainty in the estimated $A_{25\mu m}$ of at least a factor of 2 due to the imprecise knowledge of the extinction law at 25 μm (Mathis 1990), these observations provide quantitative support for the hypothesis that the CSBs described by CHYT are optically thick at $\lambda \lesssim 25$ μm. The standard conversion factor would have to be overestimating the gas surface density by much more than a factor of 4–8 for these objects to be optically thin at 25 μm. The CO observations, along with the IRAS 12/25 μm colors, thus provide strong evidence supporting a crucial prediction of the compact starburst hypothesis of CHYT.

3.6. Conclusions

We have obtained 2–3″-resolution aperture synthesis CO 1→0 data on five merging and two strongly-interacting systems with infrared luminosities from 3.2×10^{11} $L_\odot$ to 3.5×10^{12} $L_\odot$. The CO maps reveal that all five mergers and one of the two interacting systems possess extremely compact, but massive, concentrations of gas with radii from 0.33 to 1.6 kpc. The only object to show bright CO emission extending to radii approaching the size of the optical disk is the interacting barred spiral NGC 7674.

The morphology of the CO emission varies with the interacting class of the galaxy in this small sample. The single nucleus mergers—Mrk 231, IC 883, and NGC 2623—show all their CO emission concentrated in bright, compact cores (R_c = 0.33–0.96 kpc) coincident with the peaks of the cm-wave radio continuum. The double

nucleus mergers also exhibit extremely bright, compact CO cores; however, these peak between the radio continuum nuclei and have extents nearly equal to the nuclear separation; these presumably less-evolved mergers also contain low-level CO emission features that extend over 10 kpc in length. The two interacting systems observed show very different CO morphologies from each other: NGC 7469 exhibits a compact CO core with $R_c = 0.76$ kpc and no extended emission, and thus resembles the single nucleus mergers; NGC 7674, on the other hand, is the only object in our sample that does not have a dominant CO core—instead, it exhibits a bright CO bar-like feature of 12 kpc length, roughly coextensive with the K band stellar bar.

The two double nucleus mergers studied here—NGC 6090 and NGC 6240—and also Arp 220 (Scoville et al. 1996) show single CO components peaking between the stellar nuclei and having an extent nearly equal to the nuclear separation. These observations provide the first empirical evidence that the gas nuclei merge prior to the stellar nuclei in gas-rich mergers. This behavior, likely due to dissipation in the gas, has not yet been seen in gas-dynamical simulations of mergers, and so these observations should provide useful constraints for future simulations. The lack of a morphological correlation between the non-thermal radio and CO emission in these three objects suggests that the luminous nuclei are not tapping the entire reservoir of molecular gas and thus that their luminosities may increase further as the mergers evolve.

Using the observed line widths to estimate the dynamical masses, $M_{\rm dyn}$, and the standard Galactic conversion factor to estimate the molecular gas masses, $M_{\rm g}^*$, we

find that $M_g^* \gtrsim M_{dyn}$ in the cores of all seven objects. We argue that we are viewing several of these galaxies nearly along their rotation axes, causing us to underestimate M_{dyn}—especially in Mrk 231, NGC 6090, NGC 7469, and NGC 7674. In the latter three, this geometrical argument can completely remove the discrepancy between M_g^* and M_{dyn} without any appeal to an overestimate of the gas mass.

Nonetheless, our results indicate that the standard conversion factor is indeed causing significant overestimates of the nuclear molecular gas masses in Mrk 231, NGC 6240, and perhaps also IC 883. The aspect ratio of the CO 2→1 source in Mrk 231, if interpreted as an inclined disk, implies that the actual nuclear gas mass must be at least 3.6 times smaller than M_g^*. Similarly, the edge-on optical morphology, coupled with the very broad CO line width, of NGC 6240 suggests that the observed M_{dyn} is accurate and thus that the actual nuclear gas mass must be at least 1.5 times smaller than M_g^*.

Even allowing for smaller gas masses than given by the standard conversion factor, the molecular gas is likely the dominant nuclear mass component in all seven systems except NGC 7674. For Mrk 231, even if we take the extreme case of optically-thin CO emission (with $[CO]/[H_2] = 10^{-4}$), and adopt a disk inclined 60° to our line-of-sight, the molecular gas mass constitutes 40% of the total mass in the inner 840 pc region. Realistically, this fraction may be significantly higher. In the other compact objects, gas mass overestimates of more than factors of 3–4 are needed to reduce the mass of molecular gas to a relatively small fraction of the total. In NGC 2623, the CO position-velocity diagram suggests that the rotation curve stars to turn over at a radius near

where the CO emission ceases, providing direct evidence that the molecular gas dominates the kinematics in this object. The standard conversion factor is thus unlikely to be overestimating the gas mass in NGC 2623 by more than a factor of two, if at all.

The column densities of gas implied by the CO surface brightnesses are extremely large. Using the standard conversion factor, the mean gas surface densities range from 2.1×10^3 to 3.2×10^4 $M_\odot$ pc^{-2}—one to two orders of magnitude higher than the surface density within a typical Milky Way disk GMC (e.g., Solomon et al. 1987). The corresponding mean K band extinctions range from 5.4–85 magnitudes. Only if the CO is optically thin can the mean K band extinctions be reduced below unity, and then only for the least compact objects. In Mrk 231, NGC 6240, and NGC 2623, even this extreme case cannot reduce A_K below 2.4–5.8. For such large extinctions, the resultant emission is very sensitive to the relative geometry of emission and absorption (e.g., Witt et al. 1992), and thus extreme caution must be exercised when interpreting the near-infrared emission in luminous infrared galaxies, especially when comparing emission from different components that may experience different extinction patterns.

That the nuclei can be seen at near-IR wavelengths at all in Mrk 231, NGC 6240, and NGC 2623 in spite of the extreme mean extinctions strongly suggests that the molecular gas is aspherically distributed, possibly in a nuclear disk. These disks, due to their extreme mass surface densities ($\sim 10^4$ $M_\odot$ pc^{-2}), must be thin, with half the mass contained within a full width of 30–40 pc for a vertical velocity dispersion of 90 km s^{-1} (such as that inferred for Arp 220 by Scoville et al. 1996). These scale heights are only one-tenth of the radii of the gas cores. For such thin, high

surface density gas disks, the mean volume density of molecular hydrogen must be over 10^4 cm^{-3}.

We have compiled interferometric CO data from the literature for 18 infrared-galaxies at distances over 20 Mpc in addition to the 7 studied here and have used this sample to search for empirical correlations that could provide insight into the nature of these objects. We examined the sample for distance and aperture biases and found none that significantly affect the results.

With a larger sample and improved CO data, we confirm the trend of increasing $L_{\rm FIR}/M_{\rm g}^*$ with increasing $\Sigma_{\rm g}^*$ originally noted by Scoville et al. (1991). This implies that galaxies with high gas surface densities contain either more efficient or high-mass biased star formation, or else it may signify that a luminosity source other than star formation, e.g., an AGN, becomes increasingly dominant as the gas surface density increases. In either case, the empirical trend strongly suggests that the large concentrations of molecular gas are intimately associated with the powerful activity in luminous infrared galaxies.

We also note a significant trend of redder IRAS 12/25 μm colors with higher $\Sigma_{\rm g}^*$, and suggest that extinction at mid-infrared wavelengths plays a significant role in galaxies with the most extreme observed 12/25 μm colors: $\log(f_\nu(12)/f_\nu(25)) < -0.8$. The gas surface densities estimated from high-resolution CO observations can quantitatively account for the size of the observed trend. We note that those galaxies with the reddest 12/25 μm colors are, virtually exclusively, the same objects identified by CHYT as having more compact cm-wave radio continuum than far-infrared

emission, and also that none of these "compact starbursts" (CSBs) show more normal 12/25 μm colors (except for Mrk 231, whose variable radio emission is dominated by a pc-size AGN; CHYT). Extinction thus appears to be affecting the 12/25 μm colors in the CSBs. In fact, the CO surface brightnesses of the CSBs mapped in CO at kpc-resolution—NGC 2623 (§3.4.2.1), Arp 220 (Scoville et al. 1991), and Mrk 273 (Yun & Scoville 1995)—imply that the dust is optically-thick at a wavelength of 25 μm. This confirms a crucial prediction of the compact starburst hypothesis of CHYT, though it does not yet rule out AGNs as dominant luminosity sources in the CSBs.

References

Aalto, S., Radford, S. J. E., Scoville, N. Z., & Sargent, A. I. 1996, ApJ, submitted

Aaronson, M., Huchra, J., Mould, J., Schechter, P. L., & Tully, R. B. 1982, ApJ, 258, 64

Armus, L., Heckman, T. M., & Miley, G. K. 1990, ApJ, 364, 471

Arp, H. 1966, ApJS, 14, 1

Awaki. H., Koyama, K., Inoue, H., & Halpern, J. P. 1991, PASJ, 43, 195

Barbieri, C. et al. 1993, A&A, 273, 1

Barnes, J. E. & Hernquist, L. E. 1991, ApJ, 370, L65

Batuski, D. J., Hanisch, R. J., & Burns, J. O. 1992, AJ, 103, 1077

Bernlöhr, K. 1993, A&A, 268, 25

Bicay, M. D., Kojoian, G., Seal, J., Dickinson, D. F., & Malkan, M. A. 1995, ApJS, 98, 369

Boksenberg, A., Carswell, R. F., Allen, D. A., Fosbury, R. A. E., Penston, M. V., & Sargent, W. L. W. 1977, MNRAS, 178, 451

Brinkmann, W., Siebert, J., & Boller, T. 1994, A&A, 281, 355

Calzetti, D. & Kinney, A. L. 1992, ApJ, 399, L39

Carico, D. P., Sanders, D. B., Soifer, B. T., Elias, J. H., Matthews, K., & Neugebauer, G. 1988, ApJ, 95, 356

Carral, P., Turner, J. L., & Ho, P. T. P. 1990, ApJ, 362, 434

Chini, R., Krügel, E., & Kreysa, E. 1992, A&A, 266, 177

Colbert, E. J. M., Wilson, A. S., & Bland-Hawthorn, J. 1994, ApJ, 436, 89

Condon, J. J., Condon, M. A., Gisler, G., & Puschell, J. J. 1982, ApJ, 252, 102

Condon, J. J., Helou, G., Sanders, D. B., & Soifer, B. T. 1990, ApJS, 73, 359

Condon, J. J., Huang, Z. P., Yin, Q. F., & Thuan, T. X. 1991, ApJ, 378, 65 (CHYT)

DeGeus, E. 1994, OVRO memo

DePoy, D. L., Becklin, E. E., & Geballe, T. R. 1986, ApJ, 316, L63

Désert, F. X. 1986, in Light on Dark Matter, ed. F. P. Israel (Dordrecht: Reidel) p. 213

DeVaucouleurs, G., DeVaucouleurs, A., & Corwin, H. G. 1976, Second Reference Catalogue of Bright Galaxies, (Austin: Univ. of Texas Press)

Downes, D., Reynaud, D., Solomon, P. M., & Radford, S. J. E. 1996, ApJ, 461, 186

Durret, F., Boisson, C., Petitjean, P., & Bergeron, J. 1993, A&AS, 98, 365

Eales, S. A., Becklin, E. E., Hodapp, K. W., Simons, D. A., & Wynn-Williams, C. G. 1990, ApJ, 365, 478

Fabbiano, G., Kim, D.-W., & Trinchieri, G. 1992, ApJS, 80, 531

Fosbury, R. A. E. & Wall, J. V. 1979, MNRAS, 189, 79

Fried, J. W. & Schulz, H. 1983, A&A, 118, 166

Genzel, R. et al. 1995, ApJ, 444, 129

Gordon, M. A., Baars, J. W. M., & Cocke, W. J. 1992, A&A, 264, 337

Harwit, M., Houck, J. R., Soifer, B. T., & Palumbo, G. C. C. 1987, ApJ, 315, 28

Heckman, T. M., Armus, L., Miley, G. K. 1987, AJ, 93, 276

Heckman, T. M., Van Breugel, W., Miley, G. K., & Butcher, H. R. 1983, AJ, 88, 1077

Helou, G. 1986, ApJ, 311, L33

Helou, G., Soifer, B. T., & Rowan-Robinson, M. 1985, ApJ, 298, L7

Herbst, T. M., Graham, J. R., Beckwith, S., Tsutsui, K., Soifer, B. T., & Matthews, K. 1990, AJ, 99, 1773

Hummel, E., Van der Hulst, J. M., Keel, W. C., & Kennicutt, R. C. 1987, A&AS, 70, 517

Joseph, R. D. & Wright, G. S. 1985, MNRAS, 214, 87

Joy, M. & Harvey, P. M. 1987, ApJ, 315, 480

Keel, W. C. 1985, ApJ, 90, 1449

Kenney, J. D. P., Wilson, C. D., Scoville, N. Z., Devereux, N. A., & Young, J. S. 1992, ApJ, 395, L79

Keto, E., Ball, R., Arens, J., Jernigan, G., & Meixner, M. 1992, ApJ, 387, L17

Khachikian, E. Ye. & Weedman, D. W. 1974, ApJ, 192, 581

Koerner, D. W., Sargent, A. I., & Beckwith, S. V. W. 1993, Icarus, 106, 2

Lester, D. F., Harvey, P. M., & Carr, J. 1988, ApJ, 329, 641

Liu, C. T. & Kennicutt, R. C. 1995, ApJS, 100, 325

Lonsdale, C. J., Smith, H. E., & Lonsdale, C. J. 1993, ApJ, 405, L9

Lonsdale, C. J., Smith, H. E., & Lonsdale, C. J. 1995, ApJ, 438, 632

Lutz, D. 1992, A&A, 259, 462

MacKenty, J. W. 1990, ApJS, 72, 231

Mathis, J. S. 1990, ARA&A, 28, 37

Mathis, J. S. 1993, Rep. Prog. Phys., 56, 605

Mazzarella, J. M. & Boroson, T. A. 1993, ApJS, 85, 27

Mazzarella, J. M. & Balzano, V. A. 1986, ApJS, 62, 751

Mazzarella, J. M., Graham, J. R., Sanders, D. B., & Djorgovski, S. 1993, ApJ, 409, 170

McLeod, K. K., & Rieke, G. H. 1995, ApJ, 441, 96

Mendes de Oliveira, C. M. & Hickson, P. 1994, ApJ, 427, 684

Meixner, M., Puchalsky, R., Blitz, L., Wright, M., & Heckman, T. 1990, ApJ, 354, 158

Mihos, J. C. & Hernquist, L. 1996, ApJ, 464, 641

Miller, J. S. & Goodrich, R. W. 1990, ApJ, 355, 456

Norris, R. P., Allen, D. A., Sramek, R. A., Kesteven, M. J., & Troup, E. R. 1990, ApJ, 359, 291

Padin, S. et al. 1993, IEEE Trans. Instr. Meas., 42, 793

Planesas, P., Mirabel, I. F., & Sanders, D. B. 1991, ApJ, 370, 172

Press, W. H., Teukolsky, S. A., Vetterling, W. T., & Flannery, B. P. 1992, Numerical Recipes in FORTRAN, 2nd edition, (Cambridge: Cambridge Univ. Press)

Prestwich, A. H., Joseph, R. D., & Wright, G. S. 1994, ApJ, 422, 73

Radford, S. J. E., Solomon, P. M., & Downes, D. 1991, ApJ, 368, L15

Regan, M. W., Vogel, S. N., & Teuben, P. J. 1995, ApJ, 449, 576

Ridgway, S. E., Wynn-Williams, C. G., & Becklin, E. E. 1994, ApJ, 428, 609

Rieke, G. H., Cutri, R. M., Black, J. H., Kailey, W. F., McAlary, C. W., Lebofsky, M. J., & Elston, R. 1985, ApJ, 290, 116

Rowan-Robinson, M. & Crawford, J. 1986, in Light on Dark Matter, ed. F. P. Israel (Dordrecht: Reidel) p. 421

Rowan-Robinson, M. & Crawford, J. 1989, MNRAS, 238, 523

Ruiz, M., Rieke, G. H., & Schmidt, G. D. 1994, ApJ, 423, 608

Rybicki, G. B. & Lightman, A. P. 1979, Radiative Processes in Astrophysics, (New York: John Wiley & Sons)

Sanders, D. B., Egami, E., Lipari, S., Mirabel, I. F., & Soifer, B. T. 1995, AJ, 110, 1993

Sanders, D. B. & Mazzarella, J. M. 1996, in preparation

Sanders, D. B., Scoville, N. Z., Sargent, A. I., & Soifer, B. T. 1988a, ApJ, 324, L55

Sanders, D. B., Scoville, N. Z., & Soifer, B. T. 1991, ApJ, 370, 158 (SSS)

Sanders, D. B., Soifer, B. T., Elias, J. H., Madore, B. F., Matthews, K., Neugebauer, G., & Scoville, N. Z. 1988b, ApJ, 325, 74

Sargent, A. I. & Scoville, N. Z. 1991, ApJ, 366, L1

Scoville, N. Z., Carlstrom, J. E., Chandler, C. J., Phillips, J. A., Scott, S. L., Tilanus, R. P. J., & Wang, Z. 1993, PASP, 105, 1482

Scoville, N. Z. & Good, J. C. 1989, ApJ, 339, 149

Scoville, N. Z., Sanders, D. B., Sargent, A. I., Soifer, B. T., & Tinney, C. G. 1989, ApJ, 345, L25

Scoville, N. Z., Sargent, A. I., Sanders, D. B., & Soifer, B. T. 1991, ApJ, 366, L5

Scoville, N. Z., Yun, M. S., & Bryant, P. M. 1996, ApJ, submitted

Seyfert, C. K. 1943, ApJ, 97, 28

Shepherd, M. C., Pearson, T. J., & Taylor, G. B. 1994, BAAS, 26, 987

Smith, D. A., Herter, T., Haynes, M. P., Beichman, C. A., & Gautier, T. N. 1995, ApJ, 439, 623

Soifer, B. T., Boehmer, L., Neugebauer, G., & Sanders, D. B. 1989, AJ, 98, 766

Soifer, B. T., Sanders, D. B., Neugebauer, G., Danielson, G. E., Lonsdale, C. J., Madore, B. F., & Persson, S. E. 1986, ApJ, 303, L41

Solomon, P. M. & Barrett, J. W. 1991, in Dynamics of Galaxies and Their Molecular Cloud Distributions, eds. F. Combes & F. Casoli (Dordrecht: Kluwer Academic) p. 235

Solomon, P. M., Downes, D., & Radford, S. J. E. 1992, ApJ, 387, L55

Solomon, P. M., Rivolo, A. R., Barrett, J., & Yahil, A. 1987, ApJ, 319, 730

Stanford, S. A. & Bushouse, H. A. 1991, ApJ, 371, 92

Stanford, S. A., Sargent, A. I., Sanders, D. B., & Scoville, N. Z. 1990, ApJ, 349, 492

Thronson, H. A., Majewski, S., Descartes, L., Hereld, M. 1990, ApJ, 364, 456

Toomre, A. 1977, in The Evolution of Galaxies and Stellar Populations, eds. B. M. Tinsley & R. B. Larson (New Haven: Yale Univ.) p. 401

Tran, H. D. 1995, ApJ, 440, 565

Tully, R. B. 1988, Nearby Galaxies Catalog, (Cambridge: Cambridge Univ. Press)

Unger, S. W. et al. 1988, MNRAS, 234, 745

Van der Wérf, P. P. et al. 1993, ApJ, 405, 522

Wang, Z., Schweizer, F., & Scoville, N. Z. 1992, ApJ, 396, 510

Wang, Z., Scoville, N. Z., & Sanders, D. B. 1991, ApJ, 368, 112

Witt, A. N., Thronson, H. A., & Capuano, J. M. 1992, ApJ, 393, 611

Wright, G. S., James, P. A., Joseph, R. D., & McLean, I. S. 1990, Nature, 344, 417

Wright, G. S., Joseph, R. D., & Meikle, W. P. S. 1984, Nature, 309, 430

Wynn-Williams, C. G. & Becklin, E. E. 1993, ApJ, 412, 535

Young, J. S., Claussen, M. J., & Scoville, N. Z. 1988, ApJ, 324, 115

Yun, M. S. & Scoville, N. Z. 1995, ApJ, 451, L45

Yun, M. S., Scoville, N. Z., & Knop, R. A. 1994, ApJ, 430, L109

Zwicky, F., Herzog, E., & Wild, P. 1961, Catalogue of Galaxies and of Clusters of Galaxies, (Pasadena: Caltech), vol. 1.

Chapter 4

High Density Molecular Tracers in Luminous Infrared Galaxies

4.1. Introduction

The CO molecule has dominated extragalactic observations of molecular gas ever since the CO $J = 1 \rightarrow 0$ emission line was first detected in the nearby galaxies M 82 and NGC 253 in 1975 (Rickard et al. 1975). Several other non-masing molecular emission lines were detected in these galaxies soon afterwards— including HCN $J = 1 \rightarrow 0$ (Rickard et al. 1977), HCO^+ $J = 1 \rightarrow 0$ (Stark & Wolff 1979), the NH_3 $J, K = 1, 1$ inversion transition (Martin & Ho 1979), and CS $J = 2 \rightarrow 1$ (Henkel & Bally 1985)—but have not been comprehensively studied due to their faintness relative to the CO 1→0 line. Due to its low dipole moment, the CO molecule traces gas of moderate density ($n_{H_2} \gtrsim 10^2$ cm^{-3}). In contrast, the other non-masing molecular

transitions—the brightest of which are HCN 1→0, HCO^+ 1→0, and CS 2→1—are from molecules with much higher dipole moments and need much denser gas to be excited ($n_{H_2} \gtrsim 10^4$ cm^{-3}). While CO observations can provide information on the overall distribution of molecular gas in galaxies, observations of other molecules are needed to provide information on the density and chemical properties of the gas.

Several surveys of the dense gas tracers HCN 1→0, HCO^+ 1→0, and CS 2→1 have been performed in the last few years with single dish telescopes (Mauersberger et al. 1989; Sage, Shore, & Solomon 1990; Israel 1992; Nguyen-Q-Rieu et al. 1992; Solomon, Downes, & Radford 1992, hereafter SDR; Helfer & Blitz 1993; Aalto et al. 1995). Most of these studies have concentrated on nearby spiral galaxies with bright CO emission in order to maximize detection rates. The results indicate that HCN and HCO^+ are often of comparable strength (Israel 1992; Nguyen-Q-Rieu et al. 1992), with CS about 2.5 times fainter (Helfer & Blitz 1993). Also, Helfer & Blitz (1993) find that the ratio of integrated intensities, CO/HCN $\equiv \int T_b(\mathrm{CO})dv / \int T_b(\mathrm{HCN})dv$, is very sensitive to the resolution of the observations. Lower ratios are found in smaller beams.

Two of the surveys of dense gas tracers have focused on luminous merging galaxies, rather than more normal nearby galaxies. SDR examined the HCN 1→0 emission from eight interacting and merging galaxies with high L_{FIR}/L_{CO} ratios and two normal galaxies with low L_{FIR}/L_{CO} ratios. They find that L_{HCN}/L_{IR} is relatively constant and that L_{CO}/L_{HCN} drops by an order of magnitude as L_{FIR} and L_{FIR}/L_{CO} increase by 1.5 orders of magnitude. Aalto et al. (1995), on the other hand, find no such correlation in their observations of HCN 1→0 emission from eleven interacting and

merging galaxies and one normal galaxy. In fact, in their sample, CO/HCN exhibits little variation from galaxy to galaxy.

Luminous infrared galaxies ($L_{IR} > 10^{11.5}$) are believed to contain large amounts of dense molecular gas due to the extremely compact, bright cores of molecular gas that are seen in CO 1→0 emission (e.g., Chapters 2 and 3; Scoville et al. 1991; Sargent & Scoville 1991) and the low CO/HCN ratios seen in several of these objects for which HCN data are available, such as Mrk 231 and Arp 220 (SDR; Radford et al. 1991). This class of objects, which constitutes a significant population in the local universe (Soifer et al. 1986), is often associated with strong galactic interactions and mergers (e.g., Sanders et al. 1988; Lawrence et al. 1989). The nature of the dominant luminosity source, however, remains uncertain, with nuclear starbursts and dust-enshrouded AGNs being the leading candidates (e.g., Joseph & Wright 1985; Sanders et al. 1988). The large amounts of molecular gas and dust in the cores of these objects vastly complicate probing the innermost regions at optical and near-infrared wavelengths. Fortunately, the spectral lines that trace the large amounts of molecular gas lie at wavelengths unaffected by the severe dust extinction, and thus can probe the entire nuclear regions. This gas likely serves as the fuel for the activity, especially if nuclear starbursts are the dominant luminosity source, so by using mm-wave molecular tracers to measure the gas properties, distribution, and kinematics, one can better understand whether the gas is capable of supporting an outburst of star formation luminous enough to power the bolometric luminosity, or whether a dust-enshrouded AGN is required.

Only a small number of these luminous merging galaxies have been studied in high-density tracers of molecular gas (SDR; Aalto et al. 1995), and only Arp 220 has previously been mapped in a high-density tracer at the few-arcsecond resolution necessary to resolve the dense gas distribution (Radford et al. 1991). In this paper, we present aperture synthesis observations at 4–6″-resolution of the HCN 1→0 line in six additional luminous infrared mergers, HCO^+ 1→0 in three, and CS 2→1 in one. This work is part of a larger study of the molecular gas in the dense cores of luminous infrared galaxies. Previous results on the CO 1→0 maps in six objects, and one CO 2→1 map, are described in Chapters 2 and 3. Results of additional CO 2→1 maps will be presented in a forthcoming paper (Bryant & Scoville 1996).

Basic data on the six objects studied here are listed in Table 4–1. These are among the most distant objects in which high-density molecular tracers have been detected in emission, and all except NGC 7469 are more distant than Arp 220—previously the most distant object mapped in a high-density molecular tracer with aperture synthesis.

4.2. Observations

We have obtained 4–6″-resolution HCN 1→0 data for the five brightest CO 1→0 objects of the six studied in Chapters 2 and 3. The selection of the sample is described in §3.2. For three of these objects, we were able to obtain HCO^+ 1→0 data simultaneously with HCN 1→0. In addition, we have obtained 8–10″-resolution data for CO 1→0, HCN 1→0, and CS 2→1 in NGC 7469.

Table 4–1. Basic data for the galaxy sample

object	D	L_{IR}	spectral class	interaction class[a]	nuclear separation	common aliases	reference[b]
	(Mpc)	($L_\odot$)			(″)		
(1)	(2)	(3)	(4)	(5)	(6)	(7)	(8)
NGC 2623	76.1	3.5×10^{11}	LINER	M1	...	UGC 4509, Arp 243, VV 79	1
Mrk 231	173.9	3.5×10^{12}	Sy 1	M1	...	UGC 8508	2
IC 883	97.8	4.0×10^{11}	H II	M1	...	UGC 8387, Arp 193, VV 821	3
NGC 6090	123.3	3.2×10^{11}	H II	M2	5.8	UGC 10267, Mrk 496, VV 626	4
NGC 6240	100.9	6.6×10^{11}	LINER	M2	1.5	UGC 10592, VV 617	5
NGC 7469	66.4	4.0×10^{11}	Sy 1	I	80	UGC 12332, Arp 298, Mrk 1514	6

Columns: (1) object; (2) distances, using $H_0 = 75$ km s^{-1} Mpc^{-1} and the Virgocentric flow model of Aaronson et al. 1982; (3) infrared luminosity from 8–1000 μm, as quoted in Sanders, Scoville, & Soifer 1991; (4) optical spectral class of nuclear emission lines; (5) morphological interaction class (e.g., Sanders et al. 1991); (6) angular separation of double nucleus at radio wavelengths (optical for NGC 7469/IC 5283); (7) common aliases, from the NASA/IPAC Extragalactic Database; (8) reference for the optical spectral class.

Notes:
[a] M1: merger, single nucleus; M2: merger, double nucleus; I: member of interacting pair, non-overlapping disks
[b] Spectral class references: (1) Heckman et al. 1983; (2) Boksenberg et al. 1977; (3) Liu & Kennicutt 1995; (4) Mazzarella & Boroson 1993; (5) Heckman, Armus, & Miley 1987; (6) Khachikian & Weedman 1974.

The HCN and HCO^+ observations were obtained with the Owens Valley millimeter array at Big Pine, California between 1993 July and 1995 May, as listed in Table 4–2. During this time period, the array was expanded from five to six telescopes. In order to obtain sufficient uv-coverage to produce aperture synthesis images for each object, tracks of six to twelve hours in several different configurations of the telescopes were combined into single datasets. Occasionally duplicate tracks were obtained in a single configuration in cases when poor atmospheric transparency or coherence affected the data or when scheduling conflicts caused a track to be prematurely ended. Typical on-source integration times were ~15 hours. For each object, Table 4–2 lists the pointing centers and observed central velocities, as well as the dates of each track and the number of operational telescopes for each track. Data

Table 4–2. Summary of high-density tracer observations

object	pointing center (B1950.0) α	δ	center of passband cz (km s^{-1})	spectrometer setup[a]	dates of tracks	no. of telescopes	natural-weight synthesized beam HPBW (″)	PA
NGC 2623	$8^h35^m25^s.27$	+25° 55′ 50″.2	5538	HCN/HCO$^+$	1995 Jan 23	6	6.0 × 4.5	157°
					1995 May 08	6		
					1995 May 23	6		
Mrk 231	$12^h54^m05^s.01$	+57° 08′ 38″.1	12660	HCN/HCO$^+$	1994 Nov 21	6	4.6 × 4.5	114°
					1994 Dec 18	6		
IC 883	$13^h18^m17^s.03$	+34° 24′ 04″.5	7000	HCN	1993 Nov 21	5	3.4 × 3.0	94°
					1994 Feb 05[b]	5		
					1995 Jan 03	6		
NGC 6090	$16^h10^m24^s.56$	+52° 35′ 05″.2	8831	HCN/HCO$^+$	1993 Sep 30	5	5.2 × 5.0	136°
					1995 Jan 29	6		
					1995 Apr 11	5		
					1995 Apr 14	6		
NGC 6240	$16^h50^m27^s.862$	+2° 28′ 58″.87	7335	HCN	1993 Oct 02	5	5.4 × 4.2	133°
					1994 Jan 16	5		
					1994 Mar 02	5		
					1995 Jan 30	5		
NGC 7469	$23^h00^m44^s.4$	+8° 36′ 16″.0	4963	HCN	1993 Jul 05	4	12.7 × 7.5	179°
				CS	1993 Jul 06	4	9.3 × 7.9	15°

Notes:
[a] For HCN (or CS) observed by itself, the spectrometer contains one band of 112 × 4 MHz channels (1550 km s^{-1} total bandwidth), centered at the redshifted frequency of HCN 1→0 (or CS 2→1). For HCN/HCO$^+$, it contains two bands of 56 × 4 MHz channels each (775 km s^{-1} total bandwidth), one centered at the redshifted frequency of HCN 1→0 and one at HCO$^+$ 1→0.
[b] Data affected by time round-off error; see text for explanation.

were recorded simultaneously with a digital spectrometer and a 1 GHz analog continuum correlator. (For data taken prior to 1993 Sep, the bandwidth of the continuum correlator was 500 MHz.) The digital spectrometer consists of four independent modules (Padin et al. 1993), which we arranged to cover adjacent, partially-overlapping, sections of the IF. For the three objects in which the full CO velocity width at zero intensity (FWZI) was less than about 500 km s^{-1}, we split the spectrometer into two bands of two modules each, in order to observe the HCN 1→0 and HCO$^+$ 1→0 lines simultaneously. In this setup, each band contained 56 × 4 MHz non-overlapping channels, for a velocity coverage of ∼775 km s^{-1} at 13.8 km s^{-1} resolution. For IC 883 and

NGC 6240, where the FWZI of the CO line approaches 775 km s^{-1}, all four spectrometer bands were dedicated to the HCN 1→0 transition. In this setup, the passband contained 112 × 4 MHz channels, for a velocity coverage of ~1550 km s^{-1} at the same resolution. The half-power width of the primary beam is 86″ at 87 GHz, so we used only a single pointing center for each object, centered at or near the position of the peak of the centimeter-wave continuum emission (Condon et al. 1990; Carral, Turner, & Ho 1990). To remove the time-dependent atmospheric and instrumental phase drifts, unresolved quasars near to the sample objects were observed every 30 minutes.

Phase, passband, and flux calibration were performed using the OVRO millimeter array software (Scoville et al. 1993). Instrumental passbands were derived from the spectra of bright quasars (e.g., 3C 273, 3C 454.3, 3C 345), and the absolute flux scale was obtained from integrations on Uranus or Neptune, after correcting the planet fluxes for resolution effects. The accuracy of this flux calibration is ~10%.

After the *uv* data for each track had been calibrated and the tracks for each object combined into a single dataset, maps were made using the NRAO AIPS software package. For objects in which continuum emission was detected in the line-free spectrometer channels, we subtracted a constant continuum value from the calibrated *uv* data with the AIPS task 'UVLIN.' The data were Fourier-transformed and deconvolved using the CLEAN algorithm in the AIPS task 'MX.' Varying numbers of velocity-channels were binned together to improve the signal-to-noise ratio in the channel maps. Due to the low signal-to-noise ratio, we used natural weighting of the *uv* data to produce the maps used for this analysis. The half-power synthesized beam

widths (HPBW) are listed in Table 4–2 for each object. Absolute positions should be accurate to within 0″.5.

The HCN track on IC 883 taken on 1994 Feb 05 suffered from the time round-off error in the observing software that is described in detail in §3.3. For this track, the maximum decorrelation is only slightly over 6%, and the east-west beam smearing is only 0″.8 (compared to the synthesized beam width of 3″.4). Thus, the time round-off error should have a negligible effect upon the final map, and all otherwise useable data from this track have been retained.

4.3. Results

4.3.1. HCN, HCO^+

Despite the large distances (66–174 Mpc), HCN 1→0 was detected in all six objects, and HCO^+ 1→0 was detected in the three objects in which it was attempted. The only marginal detection is for CS 2→1 in NGC 7469. Measured parameters for the HCN and HCO^+ emission lines are listed in Table 4–3. For comparison, we also list the corresponding measurements for the CO 1→0 emission (and CO 2→1 emission in Mrk 231) described in Chapters 2 and 3. Table 4–4 contains the integrated brightness temperature ratios and a lower limit to the HCN 1→0 excitation temperature (derived assuming that the HCN emission arises from an area no larger than that from which the CO emission arises). The uncertainties for the CO/HCN and CO/CS brightness temperature ratios do not include the estimated 10% relative calibration error between

Table 4–3. Spectral line data

object	transition	S_c	coordinates of peak $\Delta\alpha$	$\Delta\delta$	σ	FWHM	cz_{mid}	T_b
		(Jy km s^{-1})	(″)	(″)	(″)	(km s^{-1})	(km s^{-1})	(K)
(1)	(2)	(3)	(4)	(5)	(6)	(7)	(8)	(9)
NGC 2623	HCN 1→0	7	...	...	...	300 (80)	5592 (40)	0.09 (0.02)
	HCO$^+$ 1→0	7	...	...	...	290 (80)	5517 (40)	0.08 (0.02)
	CO 1→0	153	0.15 E	0.05 N	0.04	317 (21)	5543 (11)	4.3 (0.3)
Mrk 231	HCN 1→0	10.0	0.76 W	0.32 S	0.20	191 (25)	12613 (11)	0.42 (0.04)
	HCO$^+$ 1→0	8.3	0.46 W	0.56 S	0.33	203 (44)	12651 (21)	0.23 (0.03)
	CO 1→0	62	0.13 W	0.02 N	0.04	186 (9)	12645 (4)	4.7 (0.3)
	CO 2→1	180	0.08 W	0.04 N	0.02	189 (10)	12667 (4)	14 (1.6)
IC 883	HCN 1→0	9.5	...	...	...	200 (70)	6961 (27)	0.12 (0.03)
	CO 1→0	202	0.19 W	0.18 N	0.03	388 (18)	7014 (9)	6.6 (0.5)
NGC 6090	HCN 1→0	5.5	0.46 W	1.08 S	0.53	155 (44)	8882 (22)	0.10 (0.02)
	HCO$^+$ 1→0	6.0	1.09 W	0.98 S	0.34	125 (31)	8842 (14)	0.12 (0.02)
	CO 1→0	96	1.85 W	1.37 S	0.04	138 (6)	8835 (3)	3.8 (0.3)
NGC 6240	HCN 1→0	22	0.63 W	0.85 S	0.12	401 (47)	7345 (19)	0.09 (0.02)
	CO 1→0	185	0.55 W	0.66 S	0.03	469 (15)	7342 (7)	4.1 (0.4)
NGC 7469	HCN 1→0	15	0.00	1.50 N	0.9	334 (79)	4889 (37)	0.076 (0.018)
	CS 2→1	7[a]	0.24 E	0.06 N	1.3	...	...	0.054 (0.014)
	CO 1→0	317	0.22 E	0.16 N	0.11	273 (3)	4917 (1)	1.74 (0.06)

Columns: (1) object; (2) spectral line; (3) line flux integrated over velocity and solid angle; (4)–(5) offset of integrated flux peak from pointing center listed in Table 4–2—blanks mean that the map is too poor to yield accurate coordinates for the peak; (6) formal uncertainty in peak coordinates—does not include possible systematic errors due to calibration or baseline measurement; (7) full-width at half-maximum (FWHM) of the line profile, with the 1σ formal uncertainty in parentheses; (8) heliocentric velocity at midpoint of FWHM of profile; (9) peak brightness temperature of the line emission in the synthesized beam listed in Table 4–2 (see Chapters 2 and 3 for synthesized beams of the CO 1→0 and CO 2→1 observations)— these numbers should be compared only after correcting for the different beam sizes.

Note:
[a] Marginal detection.

the individual line measurements; the HCO$^+$/HCN T_b ratios are not subject to this error since the data for each line were obtained simultaneously.

Single dish HCN 1→0 data have been published for three of the six objects studied here: Mrk 231, NGC 6240, and IC 883 (SDR). For the other two molecules, the only published single dish data is HCO$^+$ 1→0 in Mrk 231 (SDR). Columns 6 and 7 of Table 4–4 compare our measurements with those from the IRAM 30 m telescope. Our HCN fluxes for Mrk 231 and NGC 6240 agree fairly well with the IRAM measurements, given the large uncertainties in the relative calibration of ~20%. On the

Table 4–4. Line ratios and excitation

object	OVRO CO/HCN	OVRO HCO^+/HCN	OVRO CO/CS	IRAM CO/HCN	HCN 1→0 OVRO/IRAM	HCO^+ 1→0 OVRO/IRAM	HCN 1→0 $T_{x,min}$
(1)	(2)	(3)	(4)	(5)	(6)	(7)	(8)
NGC 2623	12 (3)	1.0 (0.2)	...	...	...	...	3.8 K
Mrk 231	3.3 (0.3)	0.7 (0.1)	...	3.9	0.69	2.5	32
IC 883	18 (4)	...	...	3.8	0.38	...	2.9
NGC 6090	26 (9)	1.7 (0.6)	...	...	...	...	2.9
NGC 6240	9.2 (1.0)	...	...	6.3	0.85	...	3.5
NGC 7469	10.0 (1.4)	...	29 (10)	...	...	...	3.2

Columns: (1) object; (2) observed brightness temperature ratio of CO 1→0 to HCN 1→0, convolved to the same beam size and averaged over the CO line profile; (3) same as column 2, but for the ratio of HCO^+ 1→0 to HCN 1→0; (4) same as column 2, but for the ratio of CO 1→0 to CS 2→1; (5) single dish velocity-integrated temperature ratio of CO 1→0 to HCN 1→0, corrected for the CO source sizes measured in Chapters 2 and 3 and assuming that the HCN source size is the same as that of CO; (6) ratio of the HCN 1→0 flux detected by the Owens Valley millimeter array to that detected by the IRAM 30m telescope; (7) same as column 6 but for HCO^+ 1→0; (8) minimum excitation temperature of HCN 1→0, derived by correcting the observed peak brightness temperature for beam dilution, cosmic background, and the Rayleigh-Jeans approximation.

other hand, the HCN flux that we measure for IC 883 (Arp 193) is 2.5 times fainter than that reported by SDR, and the HCO^+ flux we measure for Mrk 231 is over 2 times brighter than that reported by SDR. Given the highly compact nature of the CO emission in these objects, and that there is there is no evidence for any missing CO flux in the aperture synthesis maps (Chapters 2 and 3), we cannot attribute the unexpectedly weak HCN flux that we see towards IC 883 to emission resolved out by the array. Instead, we suspect spectral baseline uncertainties may have contributed to the excess flux measured in the single dish data on this object. Unfortunately SDR do not publish their spectrum so a judgment of the quality of the single dish spectrum of IC 883 cannot be made. For Mrk 231, the HCN and HCO^+ aperture synthesis data were taken simultaneously, and the HCN flux agrees fairly well with the flux reported from IRAM; if anything it is somewhat less than the IRAM flux. So

the larger HCO^+ flux we measure is unlikely to be due to a relative calibration difference. We suspect that the weaker HCO^+ flux in Mrk 231 reported by SDR is also attributable to instrumental uncertainties in the single dish data, such as pointing errors.

Both the maps and the line profiles from our data suggest that the HCN, HCO^+, and CO trace similar gas distributions. The HCN maps (see Figures 4–1a, 4–3, and 4–8a) and the HCO^+ maps (see Figures 4–1b and 4–8b) are consistent with all of the high dipole moment emission lines arising from the same compact core as the CO emission. The HCN, HCO^+ and CO line profiles are also consistent to within the uncertainties. The spatial resolution and signal-to-noise ratio of the data do not allow us to state conclusively whether the HCN emission distribution differs from the CO emission distribution, though in NGC 6090 there is marginal evidence that the HCN arises from a more compact area than the CO and HCO^+. This is seen best when the maps are convolved to the same beam size (Figure 4–9a).

Below we describe the data for each object separately, in order of decreasing far-infrared luminosity.

Mrk 231. The HCN map shows a point source of emission, with a 2σ upper limit on its diameter of $<2''.3$ (Figure 4–1a). The HCN peak is offset from that of CO by $0''.8$—four times the formal uncertainty. This offset is not significant, however, since baseline measurement errors add a systematic uncertainty of around $0''.5$ to the absolute positions. No significant constraints are placed on the relative distribution

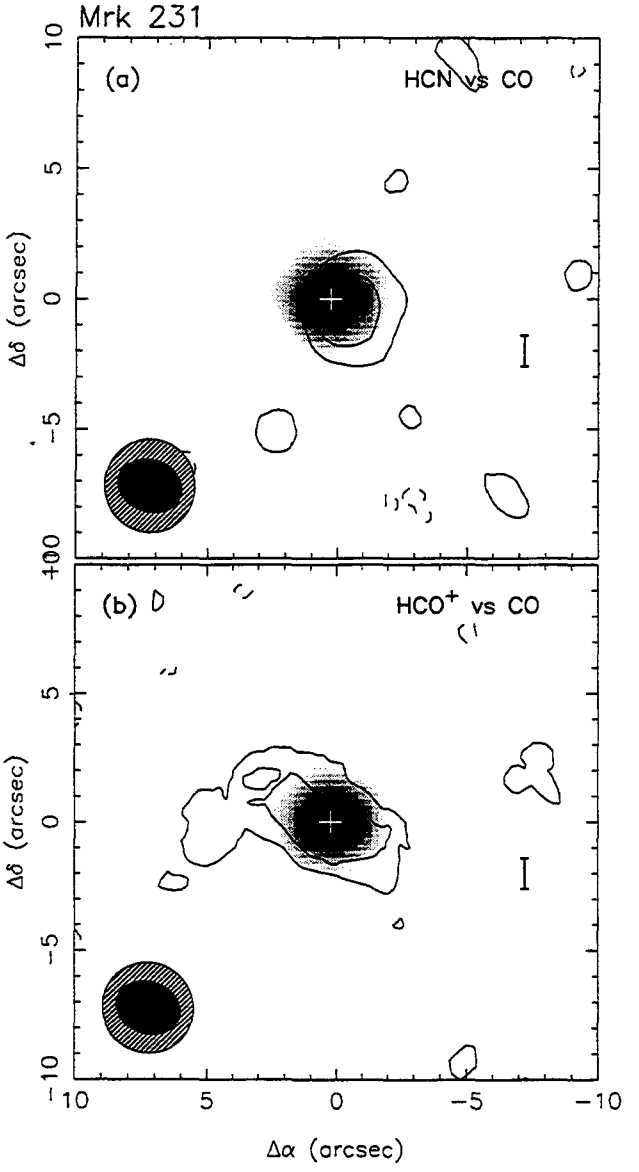

Figure 4–1. (a) The velocity-integrated HCN 1→0 emission from the natural-weight aperture synthesis map is shown in contours overlaid on a grayscale of the velocity-integrated CO 1→0 emission (uniform weight; Chapter 2). Contours are spaced linearly beginning at 3 Jy beam^{-1} km s^{-1}. (b) The velocity-integrated HCO^+ 1→0 emission from the natural-weight aperture synthesis map is shown in contours overlaid on the same grayscale image in (a). Contours are spaced linearly beginning at 1.8 Jy beam^{-1} km s^{-1}. The integrated emission line maps were produced by smoothing the frequency resolution to 32 MHz (~113 km s^{-1}) and summing over all line channels, blanking pixels below 2σ (6.4 mJy for the HCN map and 6.1 mJy for the HCO^+ map). The hatched ellipses represent the half-power beam size of the high dipole moment molecule observations, while the solid ellipses represent the beam size for the CO observations. The bars delineate 1 kpc, and the "+" symbols mark the position of the compact 1.49 GHz continuum emission (Condon et al. 1990).

of the CO and HCN emission since the CO arises from a source only 1″ in diameter (Chapter 2), much smaller than the resolution of our HCN map.

The observed peak HCN brightness temperature of 0.42 K translates into a minimum HCN 1→0 excitation temperature of 32 K if the HCN arises from a region no larger than that from which the CO 2→1 arises. Even using the conservative 3σ upper limit to the size of the CO 2→1 emission ($1''.20 \times 0''.66$) results in a lower limit of 14 K for the excitation temperature of HCN 1→0. A reasonable upper limit to the excitation is given by the upper limit to the far-infrared color temperature of the dust grains: $T_d < 85$ K (Roche & Chandler 1993). Thus, like the CO lines (Chapter 2), the HCN line probably has a large area filling factor (>0.2) in the molecular core of Mrk 231.

The HCO^+ map shows an elongation 40% longer than the 4″.7 synthesized beam at PA 70° and is unresolved in the perpendicular direction (Figure 4–1b). The elongation is roughly 2.5 times the uncertainty in the source size estimated from the signal-to-noise ratio and expected calibration uncertainties. If this elongation is real, it corresponds to a deconvolved major axis of $4''.4 \pm 1''.0$. The data were examined in detail, and no plausible calibration errors due to individual telescopes, baselines, or tracks were found that could account for this elongation.

The measured HCO^+ flux is comparable to the HCN flux, in contrast to the single dish results of SDR, which have HCO^+ several times weaker than HCN. The average CO/HCN brightness temperature ratio across the line profile of Mrk 231 is 3.3; only NGC 1068 is known to have a lower ratio. The velocity-averaged CO/HCO^+ T_b ratio

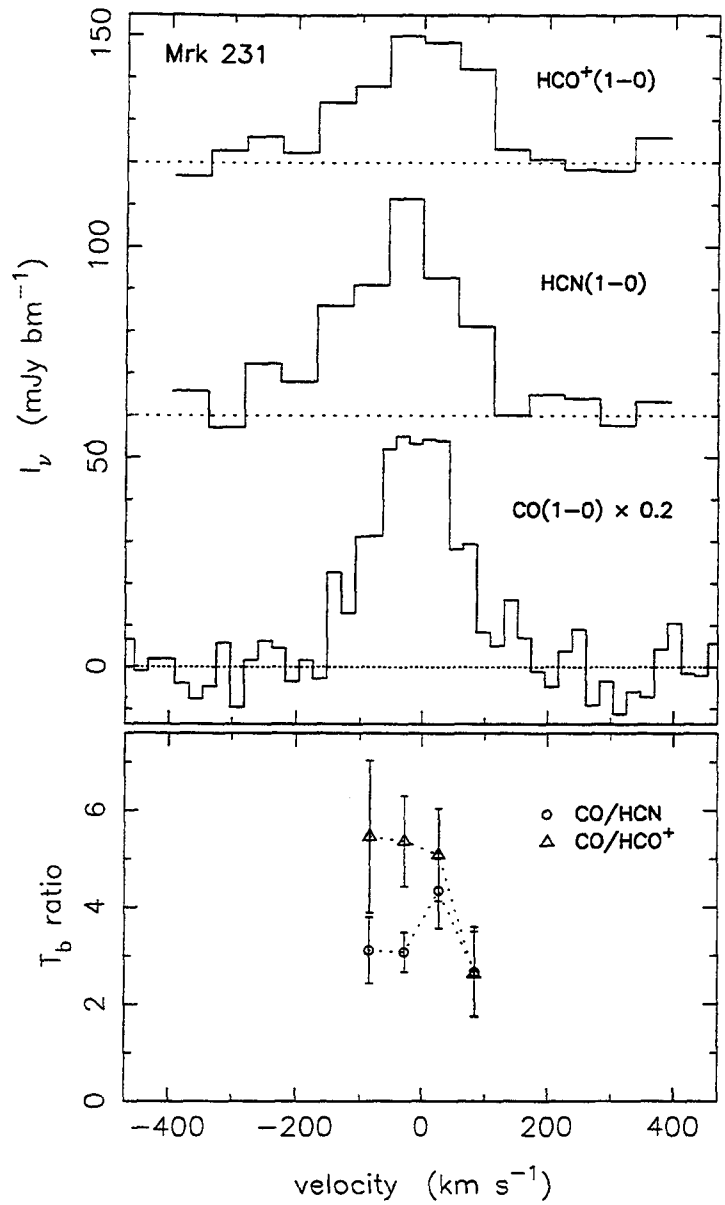

Figure 4–2. The upper panel shows the line profiles for CO 1→0, HCN 1→0, and HCO^+ 1→0 for Mrk 231. For easy display, the amplitude of CO is reduced by a factor of five, and HCN and HCO^+ are offset vertically by 60 and 120 mJy beam^{-1}, respectively. To obtain the velocity profiles, each data cube was convolved to the same spatial resolution (4″.7×4″.7) and then was sampled through a region 0″.5 east-west by 0″.25 north-south centered on the peak of the CO emission. The lower panel shows the line ratios, converted from flux to brightness temperature units, obtained after smoothing the CO profile to the same velocity resolution for which the fainter line profiles are displayed. The velocities, v, shown in this and subsequent figures are related to the observed frequencies, ν, by $v = c(\nu_0 - \nu)/\nu$, where ν_0 is the central frequency of the bandpass, given by $\nu_0 = \nu_R(1+z)^{-1}$, where ν_R is the rest frequency and z is the redshift listed in Table 4–2.

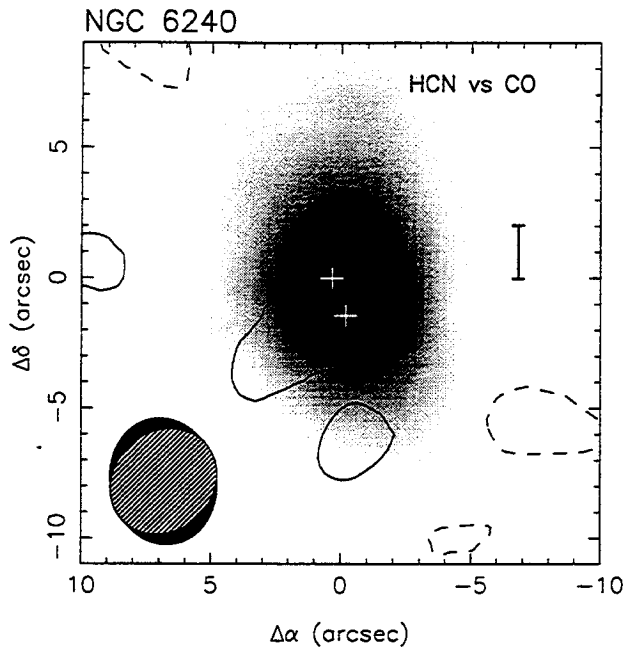

Figure 4–3. The velocity-integrated HCN 1→0 emission from the natural-weight aperture synthesis map is shown in contours overlaid on a grayscale of the velocity-integrated CO emission (natural weight; Chapter 3). Contours are spaced linearly beginning at 4 Jy beam^{-1} km s^{-1}. The HCN map was produced by smoothing the frequency resolution to 64 MHz (~222 km s^{-1}) and summing over all line channels, blanking pixels below 2σ (4.9 mJy). The hatched ellipse represents the half-power beam size of the HCN observations, while the solid ellipse represents the beam size for the CO observations. A bar delineates 1 kpc, and the two "+" symbols mark the positions of the two brightest components of the 15 GHz continuum emission (Carral et al. 1990).

is 4.7 ± 0.5, and the line profiles of both HCN and HCO^+ are consistent with the CO line profiles to within the uncertainties (Figure 4–2).

NGC 6240. The HCN map (Figure 4–3) shows a compact emission source with a maximum deconvolved diameter of $<3''.7$ (2σ), consistent with the emission arising from within the $1''.6$-diameter CO core. The line profile is similar to that of CO to within the uncertainties (Figure 4–4), as also seen by SDR. The average CO/HCN brightness temperature ratio is 9.2 ± 1.0.

IC 883. The HCN line profile agrees well with the CO line profile to within the uncertainties (Figure 4–5), but as noted above, we find only 40% of the flux reported

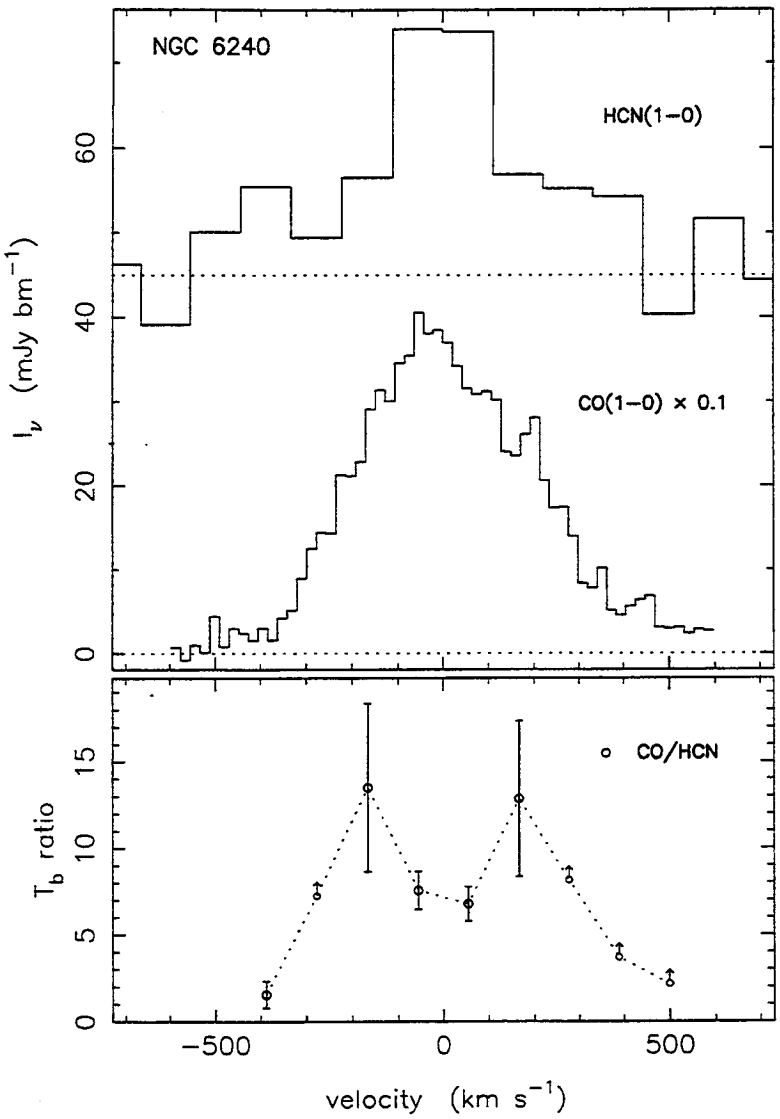

Figure 4–4. The upper panel shows the line profiles for CO 1→0 and HCN 1→0 for NGC 6240. For easy display, the amplitude of the former is reduced by a factor of ten, and the latter is offset vertically by 45 mJy beam^{-1}. To obtain the velocity profiles, each data cube was convolved to the same spatial resolution (4″.9 × 4″.9) and then was sampled through a 0″.3-square region centered on the peak of the CO emission. The lower panel shows the line ratios, converted from flux to brightness temperature units, obtained as in Figure 4–2.

by SDR. The CO/HCN brightness temperature ratio that we measure (18 ± 4) is thus rather typical of galactic nuclei (e.g., Aalto et al. 1995; Helfer & Blitz 1993), rather than the extremely small ratio reported from the IRAM observations. Due to

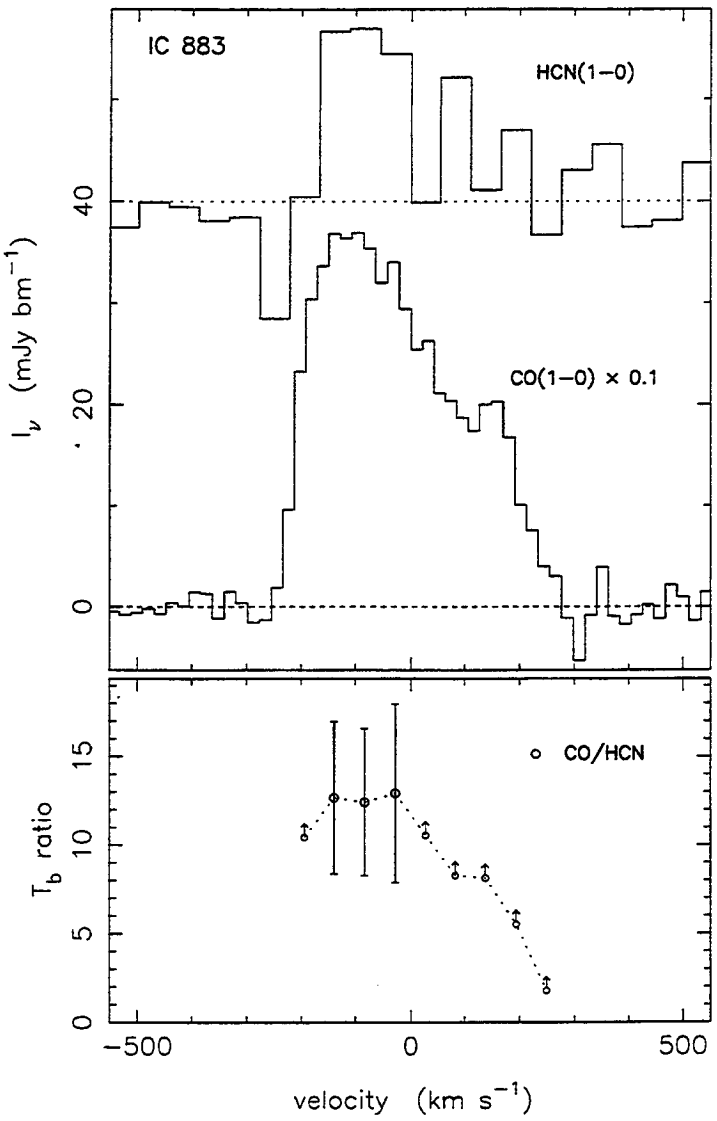

Figure 4–5. The upper panel shows the line profiles for CO 1→0 and HCN 1→0 for IC 883. For easy display, the amplitude of the former is reduced by a factor of ten, and the latter is offset vertically by 40 mJy beam^{-1}. To obtain the velocity profiles, each data cube was convolved to the same spatial resolution ($7'' \times 7''$) and then was sampled through a $6''.9$-square region centered on the peak of the CO emission. The lower panel shows the line ratios, converted from flux to brightness temperature units, obtained as in Figure 4–2.

the faintness of the HCN line in this object, the map provides no significant spatial constraints.

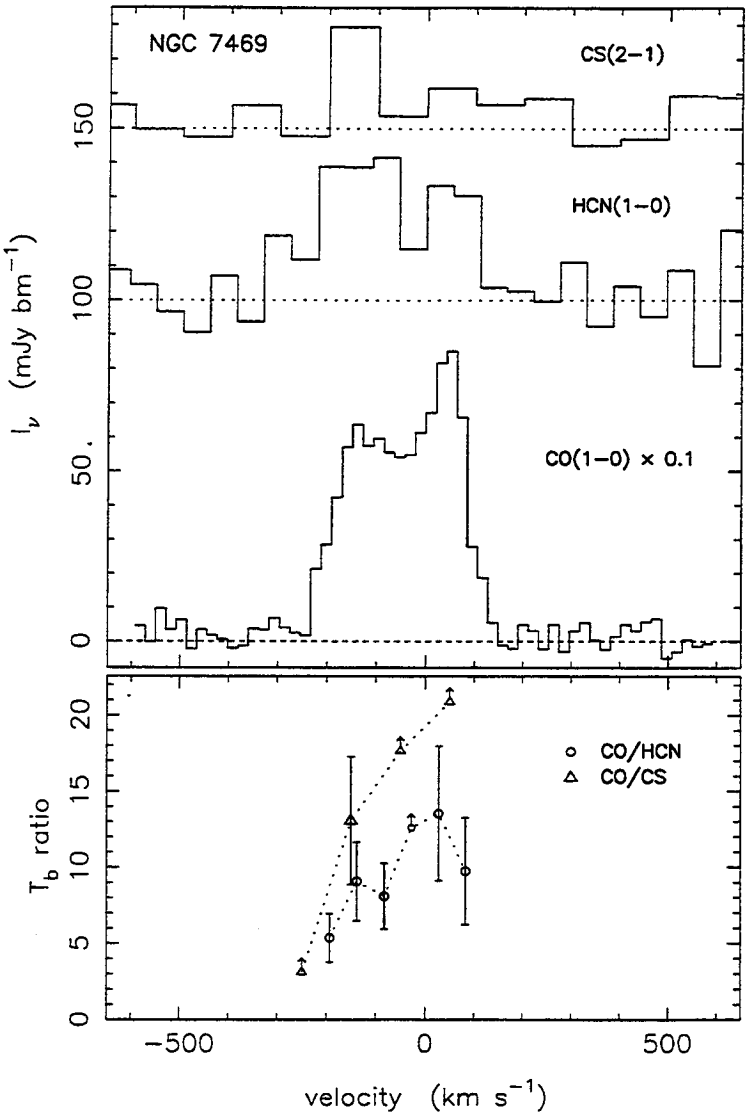

Figure 4–6. The upper panel shows the line profiles for CO 1→0, HCN 1→0, and CS 2→1 for NGC 7469. For easy display, the amplitude of CO is reduced by a factor of ten, and HCN and CS are offset vertically by 100 and 150 mJy beam^{-1}, respectively. To obtain the velocity profiles, each data cube was convolved to the same spatial resolution (12″.7 × 8″.1) and then was sampled through a 3″.75-square region centered on the peak of the CO emission. The lower panel shows the line ratios, converted from flux to brightness temperature units, obtained as in Figure 4–2.

NGC 7469. The HCN 1→0 emission is unresolved in the 12″.7×7″.5 synthesized beam. The velocity-averaged CO/HCN brightness temperature ratio is 10.0 ± 1.4 (Figure 4–6). The CS 2→1 line is seen above 3σ over only about one-third of the

CO line profile (Figure 4–6). From velocities of -200 to -100 km s^{-1}, the CO/CS brightness temperature ratio is 13.1 ± 4.2. Averaged over the full CO line profile, the ratio is 28.8 ± 10.4. Both the HCN and CS lines appear stronger relative to CO on the blue side of the CO line profile. Due to the weakness of the HCN and CS emission, however, we can only conclude that both profiles are consistent with the CO profile. At roughly 3σ, CS $2 \rightarrow 1$ in NGC 7469 is merely a tentative detection.

NGC 2623. The HCN and HCO^+ emission are nearly equal in this object, and both exhibit brightness temperatures twelve times lower than CO $1 \rightarrow 0$ (Figure 4–7). The integrated line fluxes (and the continuum flux) were obtained by comparing the total fluxes in the two digital spectrometer bands (224 MHz bandwidth each) to the total flux in the 1 GHz correlator. Due to the low signal-to-noise, the maps provide no significant spatial constraints.

NGC 6090. Despite the weakness of the HCN and HCO^+ lines in this object at a distance of 123 Mpc, we were able to produce good maps of both lines. The HCN map suggests a slightly more compact emission region than the CO map (Figure 4–8a). This is especially clear when the maps are convolved to the same beam size (Figure 4–9a). The HCO^+ map, obtained simultaneously with the HCN, agrees very well with the CO when the same comparison is made (Figure 4–9b). Subtracting the HCN from the HCO^+ data cube, the most significant difference ($>2\sigma$) is the deficiency of HCN emission in the far northeast of the molecular core. The line profile of HCO^+ agrees very well with that of CO $1 \rightarrow 0$. With less significance, the HCN profile is also consistent with the CO profile.

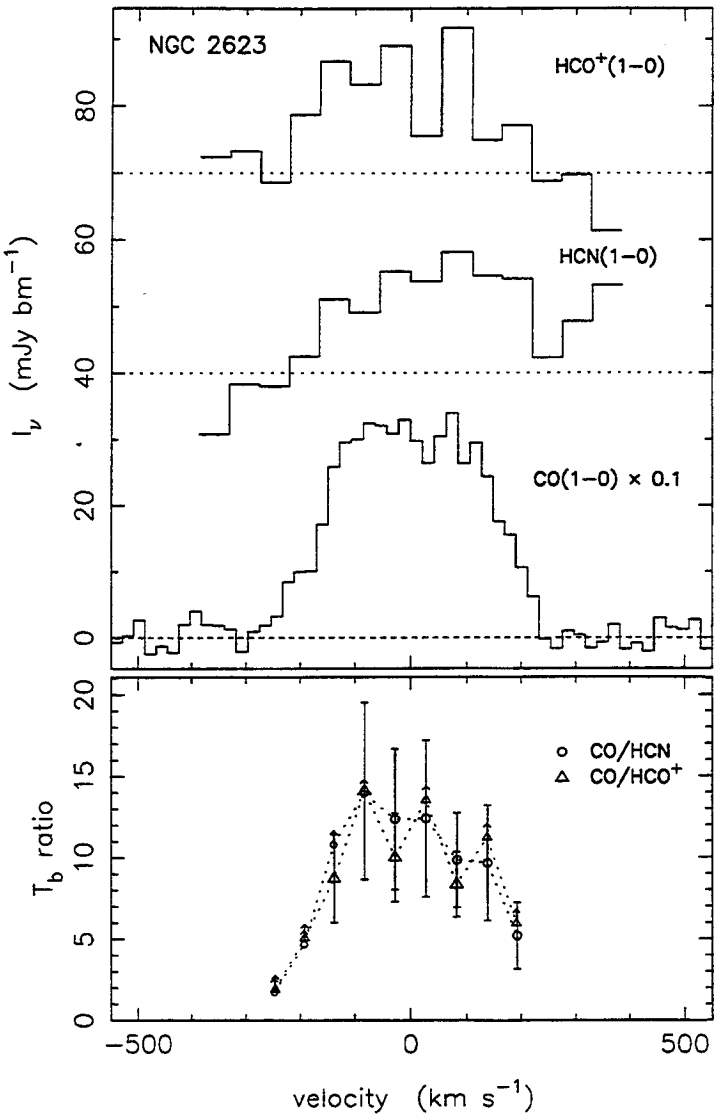

Figure 4–7. The upper panel shows the line profiles for CO 1→0, HCN 1→0, and HCO^+ 1→0 for NGC 2623. For easy display, the amplitude of CO is reduced by a factor of ten, and HCN and HCO^+ are offset vertically by 40 and 70 mJy beam^{-1}, respectively. To obtain the velocity profiles, each data cube was convolved to the same spatial resolution (6″.5 × 4″.5) and then was sampled through a region 0″.5 east-west by 0″.25 north-south centered on the peak of the CO emission. The lower panel shows the line ratios, converted from flux to brightness temperature units, obtained as in Figure 4–2.

In NGC 6090, like M 82 but unlike most other previously observed extragalactic source, HCO^+ is brighter than HCN. The velocity-averaged CO/HCN brightness

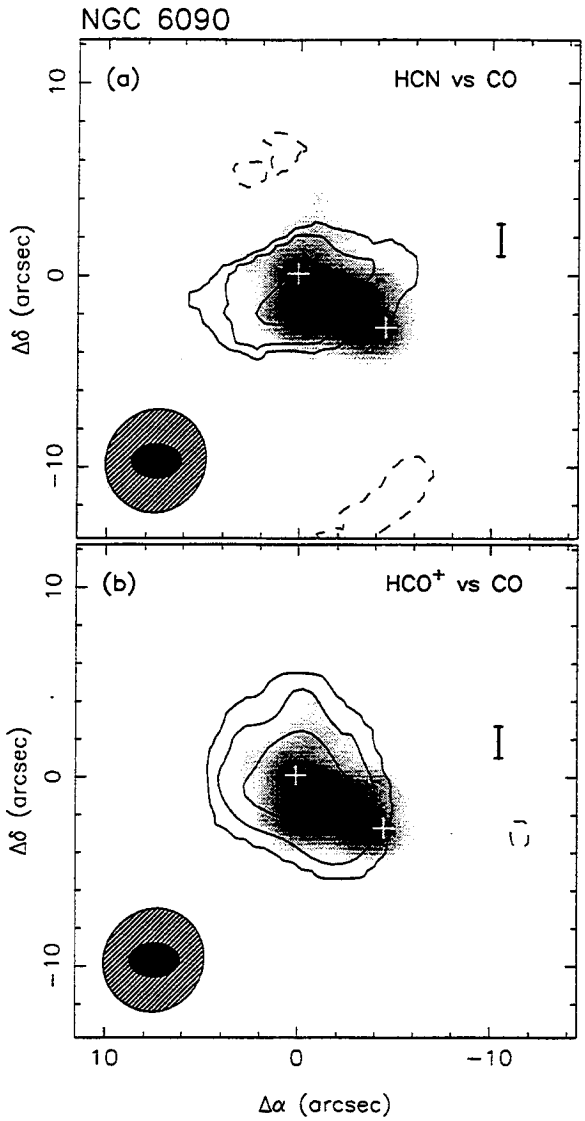

Figure 4–8. (a) The velocity-integrated HCN 1→0 emission from the natural-weight aperture synthesis map is shown in contours overlaid on a grayscale of the velocity-integrated CO emission (uniform weight; Chapter 3). Contours are spaced linearly beginning at 0.65 Jy beam^{-1} km s^{-1}. (b) The velocity-integrated HCO^+ 1→0 emission from the natural-weight aperture synthesis map is shown in contours overlaid on the same grayscale image in (a). Contours are spaced linearly beginning at 0.65 Jy beam^{-1} km s^{-1}. The integrated emission line maps were produced by smoothing the frequency resolution to 32 MHz (~111 km s^{-1}) and summing over all line channels, blanking pixels below 1.5σ (3.2 mJy for the HCN map and 2.7 mJy for the HCO^+ map). The hatched ellipses represent the half-power beam size of the high dipole moment molecule observations, while the solid ellipses represent the beam size for the CO observations. The bars delineate 1 kpc, and the two "+" symbols in each panel mark the positions of the peaks of the 1.49 GHz continuum emission (Condon et al. 1990).

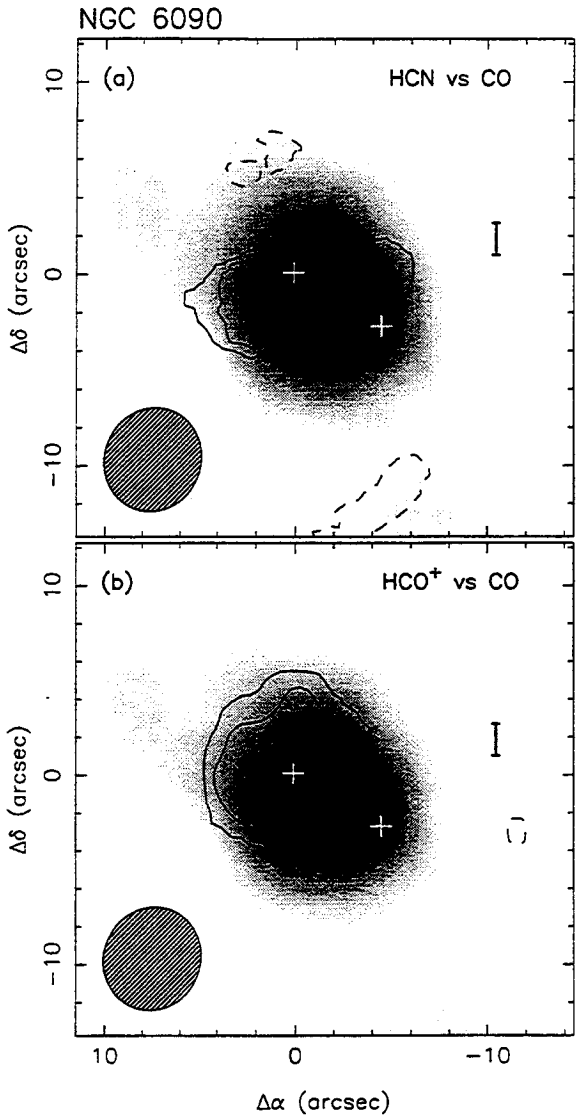

Figure 4–9. (a) and (b) Same as for Figure 4–8, except that the CO map has been convolved to the same resolution as the HCN and HCO^+ maps to ease comparison.

temperature ratio is 25.6 ± 8.7, but the same ratio for CO/HCO^+ is only 15.5 ± 2.7 (Figure 4–10).

4.3.2. Continuum

For all the objects studied here except NGC 2623, the spectrometer band was substantially wider than the spectral lines, so that continuum maps could be made by

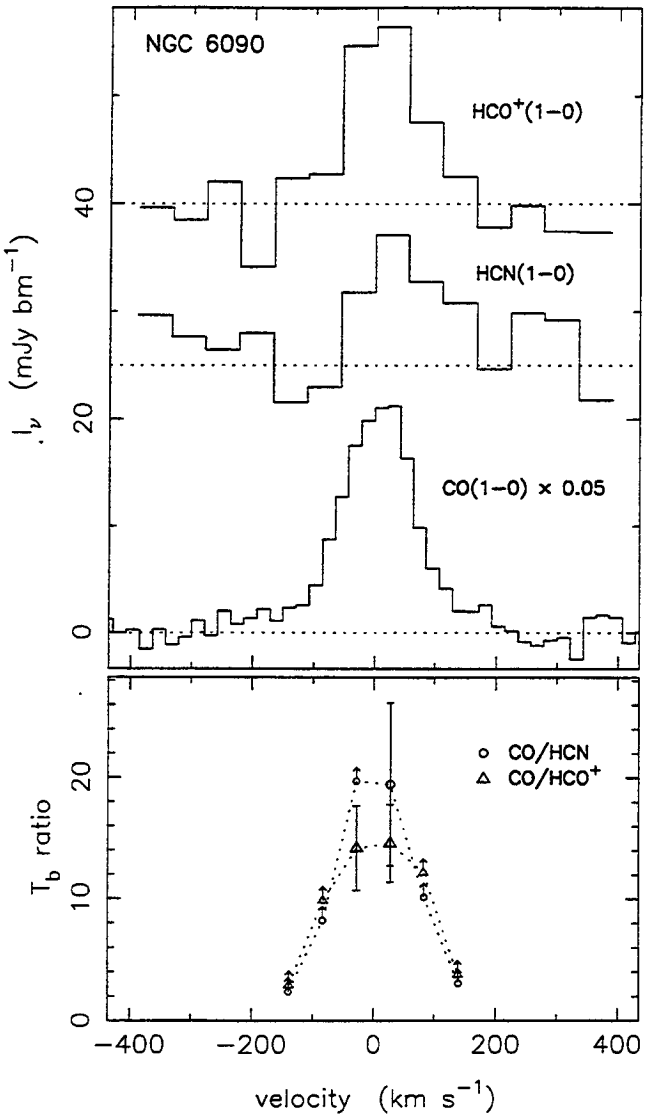

Figure 4–10. The upper panel shows the line profiles for CO 1→0, HCN 1→0, and HCO^+ 1→0 for NGC 6090. For easy display, the amplitude of CO is reduced by a factor of twenty, and HCN and HCO^+ are offset vertically by 25 and 40 mJy beam^{-1}, respectively. To obtain the velocity profiles, each data cube was convolved to the same spatial resolution (5″.5 × 5″.1) and then was sampled through a 4″.25-square region centered on the peak of the CO emission. The lower panel shows the line ratios, converted from flux to brightness temperature units, obtained as in Figure 4–2.

averaging the line-free channels. For NGC 2623, continuum maps were made by linear combinations of the channel-averaged spectrometer maps and the 1 GHz correlator maps. All objects except NGC 6090 and NGC 7469 were detected at levels of a few

Table 4–5. Radio continuum emission

object	ν (GHz)	S_ν (mJy)	SNR (peak/rms)	epoch	α	S_ν^{NT} (mJy)	S_ν^{T} (mJy)	refs[a]
(1)	(2)	(3)	(4)	(5)	(6)	(7)	(8)	(9)
NGC 2623	87.3	6.6 (3.3)	5	1995 Jan–May	−0.58 (0.04)[b]	9.2 (1.0)	< 4.3	1,2
Mrk 231	85.3	31.6 (1.7)	19	1994 Nov 21	−0.59 (0.05)[c]	21–75[d]	< 30.5[e]	3,4
	85.4	26.5 (3.3)	8	1994 Dec 18				
	85.3	30.5 (1.7)	18	average				
IC 883	86.7	8.6 (2.8)	6	1993 Nov–1995 Jan	−0.64 (0.04)[b]	7.9 (0.8)	< 6.6	2,5
NGC 6090	86.4	< 1.8[f]	...	1993 Sep–1995 Apr	−1.04 (0.16)[g]	1.0 (0.3)	< 1.8	6
NGC 6240	86.5	8.7 (3.8)	3.4	1993 Oct–1995 Jan	−0.65 (0.07)[b]	13.9 (3.0)	< 4.5	7
NGC 7469	87.2	< 6.0[f]	...	1993 Jul 5	−0.77 (0.07)[c]	6.9 (0.9)	< 4.0[h]	3
	96.4	< 5.7[f]	...	1993 Jul 6				
	92.0	< 4.0[f]	...	average				

Columns: (1) object; (2) effective frequency of continuum flux measurement; (3) continuum flux, 1σ uncertainty in parentheses does not include 10% calibration uncertainty; (4) signal-to-noise ratio of continuum detections; (5) epoch of continuum flux measurement; (6) cm-wave continuum spectral index, $S_\nu \propto \nu^\alpha$; (7) extrapolation of cm-wave continuum to frequency in column 2; (8) estimated 2σ upper limit to the thermal continuum flux at the frequency in column 2, derived by subtracting column 7 from column 3 except where noted; (9) references for cm-wave continuum flux and spectral index measurements.

Notes:

[a] Cm-wave continuum references: (1) Hummel et al. 1987; (2) Condon et al. 1991; (3) Edelson 1987; (4) Kojoian et al. 1976; (5) Condon et al. 1990; (6) Batuski, Hanisch, & Burns 1992; (7) Colbert et al. 1994.

[b] Evaluated between 1.5 and 8 GHz.

[c] Evaluated between 4.9 and 20 GHz.

[d] Extrapolation of the extreme range of the observed cm-wave variability.

[e] Due to the strong cm-wave variability of Mrk 231, the thermal contribution to the 85 GHz continuum cannot be constrained below the total observed flux;

[f] 2σ upper limit.

[g] Evaluated between 4.9 and 15 GHz.

[h] The extrapolated cm-wave flux is significantly greater than the upper limit to the 92 GHz continuum flux, so the non-thermal continuum spectral index must steepen at mm-wavelengths—hence the upper limit on the total 92 GHz continuum is also the upper limit to the thermal contribution.

times the noise (Table 4–5). The detections are all consistent with unresolved sources, as expected from the compact nature of the lower frequency radio continuum in these objects (e.g., Condon et al. 1990; Carral et al. 1990).

For NGC 2623, IC 883, NGC 6090, and NGC 6240 the observed continuum fluxes (or limits) agree remarkably well with the cm-wavelength non-thermal continuum extrapolated to 87 GHz (Table 4–5). For NGC 7469, the measured 2σ upper limit to the mm-wavelength continuum (4.0 mJy) is substantially lower than the extrapolation of the cm-wavelength continuum (6.9 ± 0.9 mJy). Thus, in these five objects, there is no

evidence for any excess continuum that could be attributed to thermal bremsstrahlung or dust emission. Estimated upper limits (2σ) to the thermal continuum contribution at 87 GHz are provided in column 8 of Table 4–5.

For Mrk 231, the non-thermal extrapolation is complicated by the fact that the central radio source varies dramatically on time scales from months to years at cm wavelengths (see §2.3.2 and references therein). We have listed the measurements for its two tracks separately in Table 4–5. The two tracks do not show evidence for significant variation during the intervening month, so we have also listed the average measurement of 30.5 mJy at 85.3 GHz. On the other hand, the 3 mm continuum did vary by ~50% over the 19 months between our measurements at 109 GHz (49 mJy; §2.3.2) and the present data at 85 GHz—variability behavior similar to that of the lower frequency continuum. Also, the 85 GHz measurements fall well within the range (21–75 mJy; §2.3.2) of non-thermal continuum at 85 GHz predicted by extrapolating earlier cm wavelength measurements. These two facts strongly suggest that the observed 85 GHz continuum in Mrk 231 is dominated by non-thermal emission, and that the thermal contributions from bremsstrahlung and dust are relatively minor. While the strict upper limit we place on the thermal continuum in Table 4–5 is the total detected flux, the actual thermal contribution is likely less than half this amount.

Table 4–6. Central CO/HCN measurements: Galaxies with $L_{FIR} > 10^{11}$ $L_\odot$

object	D	$\frac{CO}{HCN}$	σ	θ_a	d_a	Σ_g^*	log L_{FIR}	type	refs[a]
	(Mpc)			(″)	(kpc)	($M_\odot$ pc^{-2})	($L_\odot$)		
(1)	(2)	(3)	(4)	(5)	(6)	(7)	(8)	(9)	(10)
NGC 828	72.6	100	...	28	9.9	...	11.22	Sa: pec	10
NGC 1614	62.3	14.5[b]	3.8	12[b]	3.6[b]	...	11.41	SBc pec/HII Sy2	1
NGC 2623	76.1	12[c]	2	1.8	0.66	20900	11.47	/LINER	this work
NGC 3256	37.4	20	8	56	10.2	...	11.47	Pec merger/HII	7
		15.5[b]	1.2	9[b]	1.6[b]	...			1
IC 694	48.0	20	...	28	6.5	...	11.52	IBm pec/AGN	10
		9[c]	1	1.4	0.33	29000			2
Mrk 231	173.9	6.7	...	28	24	...	12.36	SAc ? pec/Sy1	10
		3.3[c]	0.3	1.0	0.84	27000			this work
IC 883	97.8	6.3	...	28	13	...	11.52	Im: pec/LINER	10
		18[c]	4	4.2	2.0	5370			this work
Arp 220	79.2	12.8	...	28	10.8	...	12.12	S ?/Sy2	10
NGC 6090	123.3	26[c]	9	5.8	3.5	2570	11.34	Sd pec/HII	this work
NGC 6240	100.9	10.7	...	28	14	...	11.69	I0: pec/LINER Sy2	10
		9.2[c]	1.0	1.6	0.78	31600			this work
IRAS 18293-3413	73.1	>16[b]	...	7[b]	2.5[b]	...	11.62	/HII	1
NGC 7130	63.0	13[b]	4	10[b]	3.1[b]	...	11.18	Sa pec/LINER Sy2	1
NGC 7469	66.4	>20	...	70	23	...	11.41	(R′)SABa/Sy1	4
		10.0[c]	1.4	4.6	1.5	6800			this work
NGC 7771	58.6	18	...	28	8.0	...	11.24	SBa/HII	10

Columns: (1) object; (2) distance—from Tully 1988 for objects closer than 40 Mpc, otherwise from Sanders, Scoville, & Soifer 1991; (3) velocity-integrated temperature ratio of CO 1→0 to HCN 1→0—not corrected for different CO and HCN beam sizes or for source sizes smaller than beam except where noted; (4) uncertainty in temperature ratio when quoted in reference; (5) angular diameter of HCN aperture to which temperature ratio applies; (6) linear diameter of HCN aperture; (7) CO surface brightness in units of gas surface density, using the standard M_g/L'_{CO} conversion factor, for the objects in Figure 4–12; (8) far-infrared luminosity (40–120μm), from Condon et al. (1990, 1996), but adjusted to the distance adopted in column 2; (9) morphological class from the NASA/IPAC Extragalactic Database—nuclear spectral classification given after the slash; (10) references for the CO/HCN line ratio in column 3.

Notes:

[a] References for CO/HCN line ratios: (1) Aalto et al. 1995; (2) Aalto et al. 1996; (4) Helfer & Blitz 1993; (7) Israel 1992; (10) Solomon, Downes, & Radford 1992.

[b] Temperature ratio and aperture corrected for source size smaller than beam.

[c] Temperature ratio derived using same beam size for CO and HCN.

4.4. Discussion

4.4.1. CO/HCN line ratios

4.4.1.1. Luminous infrared galaxies

In this study, we have measured nuclear CO/HCN ratios in six luminous interacting galaxies for which we have previously resolved the CO emission (Chapter 3). Eight additional objects with $L_{FIR} > 10^{11}$ $L_\odot$ have measurements of CO/HCN previously published (Aalto et al. 1995, 1996; SDR; Radford et al. 1991). Two of these have

been mapped at high-resolution in CO 1→0 (Arp 220, Scoville et al. 1991, Scoville, Yun, & Bryant 1996; Arp 299, Sargent & Scoville 1991, Aalto et al. 1996). The observational results for these objects are summarized in Table 4–6.

The small sample of luminous interacting galaxies in Table 4–6 display a wide range of CO/HCN ratios, implying that the molecular gas properties vary substantially amongst this class of galaxies. The lower ratios (i.e., relatively brighter HCN) are associated with the highest CO surface brightnesses. The CO surface brightness, Σ_{CO}, can be translated into a gas mass surface density, Σ_g^*, via the standard $b^* = M_g^*/L'_{CO}$ conversion factor: $\Sigma_g^* = b^*\Sigma_{CO}$. The trend we find is then consistent with the hypothesis that the HCN emission traces the high-density gas ($n_{H_2} \gtrsim 10^5$), while the CO emission traces the total molecular gas content. The high CO surface brightnesses imply large mass surface densities of gas, and it is reasonable that when the gas is so concentrated, a larger fraction will be dense as a result of both self-gravity and cloud-cloud collisions.

In Mrk 231, NGC 6240, and NGC 2623, the molecular gas may reside in thin disks with mean H_2 densities of 10^4 cm^{-3} or more (§3.6). Under these conditions, the critical density of HCN is approached or exceeded throughout the entire molecular gas content. Thus, strong HCN emission must occur, independent of the rate of star formation in the gas, contrary to the suggestion of SDR that HCN traces star formation. Further evidence against a close general association between HCN emission and star formation rate comes from the Seyfert nucleus of NGC 1068, which exhibits the lowest CO/HCN ratio yet measured (Helfer & Blitz 1995), but which is unlikely

to house a significant amount of star formation. Furthermore, a possible association between strong HCN emission and broad-line AGN is discussed below in §4.1.3.

4.4.1.2. Comparison with moderate luminosity galaxies

Several dozen nearby, moderate luminosity ($L_{\rm FIR} < 10^{11}$ $L_\odot$) galaxies have published CO/HCN ratios. These are tabulated in Table 4–7. Most of these galaxies are late-type, gas-rich, and forming stars at high rates; they also exhibit a wide range of CO/HCN ratios—a range which encompasses that seen in the very luminous galaxies. As shown in Figure 4–11, the observed ratios depend dramatically on the linear size of the region around the nucleus sampled by the observations. For nearby galaxies, apertures smaller than a kiloparsec result in a typical CO/HCN of 5–15, while larger apertures result in ratios of around 15–40. For individual galaxies, this result was first found by Helfer & Blitz (1993) and supported by Jackson et al. (1996). We confirm this result for individual galaxies, as demonstrated by the preponderance of positive slopes for the dotted lines in Figure 4–11. These lines connect measurements made with different beam sizes for the same galaxy.

The trend of increasing CO/HCN with increasing aperture from 0.2 to 2 kpc is likely due to increasing contamination of the nuclear emission by the disk emission. The values of CO/HCN in the disks of gas-rich galaxies are larger than 40 (Helfer & Blitz 1993; Kuno et al. 1995; Liszt 1995), so HCN is much brighter relative to CO in the inner kpc of gas-rich spirals than in the disks. The standard interpretation is that dense gas is more strongly concentrated towards the centers of these galaxies than is the total gas distribution (e.g., Helfer & Blitz 1993). The relative paucity of

Table 4–7. Central CO/HCN measurements: Galaxies with $L_{FIR} < 10^{11}$ $L_\odot$

object	D	$\frac{CO}{HCN}$	σ	θ_a	d_a	Σ_g^*	log L_{FIR}	type	refs[a]
	(Mpc)			(″)	(kpc)	($M_\odot$ pc^{-2})	($L_\odot$)		
(1)	(2)	(3)	(4)	(5)	(6)	(7)	(8)	(9)	(10)
Milky Way	...	14	...	...	0.4	1300	...	...	8
NGC 253	3.0	4.3	0.2	70	1.02	...	10.33	SABc	4
		10.8	1.4	56	0.81	...			7
		8.6	2.4	28	0.41	...			9
		7	...	21	0.30	3300			8
NGC 404	2.4	>15	...	70	0.81	...	...	SA0	4
NGC 520	27.8	14	...	28	3.8	...	10.78	S pec	10
NGC 660	11.8	19.5	6.3	14	0.80	...	10.33	SBa pec/LINER	1
NGC 891	9.6	29	10	70	3.3	...	10.32	SAb ?	4
		56	22	28	1.3	720			9
NGC 986	23.2	11	2	15	1.7	...	10.53	(R_1')SBb	1
Maffei 2	3.4	5.1	1.5	28	0.46	260	...	SABbc:	9
NGC 1068 (M77)	14.4	8.9	0.8	70	4.9	...	10.90	(R)SAb/Sy2	4
		2.0	...	5	0.35	1720			5
NGC 1097	14.5	27	7	70	4.9	63	10.45	$(R_1'$:)SBb/Sy1	4
IC 342	3.9	17	3	70	1.3	...	10.08	SABcd	4
		12	3.4	28	0.53	1000			9
		7	2	11.5	0.22	...			3
NGC 1808	10.8	18.1	1.3	18	0.94	3100	10.41	(R_1')SABb/Sy2	1
NGC 2146	17.2	>30	...	28	2.3	...	10.95	SBab pec	1
		17.2	3.4	24	2.0	...			9
NGC 2903	6.3	38	15	70	2.1	80	9.85	SABbc	4
		4.4	1.5	28	0.86	140			9
NGC 3034 (M82)	3.25	14	4	28	0.44	3500	10.43	I0	9
NGC 3079	20.4	24	8	28	2.8	...	10.76	SBc/Sy2	9
NGC 3147	40.9	9	...	28	5.6	...	10.83	SAbc/Sy2	10
NGC 3628	7.7	>74	...	70	2.6	...	9.92	Sb pec	4
		24	9	28	1.05	720			9
NGC 4254 (M99)	16.8	25	6	70	5.7	...	10.52	SAc	4
NGC 4303 (M61)	15.2	>43	...	70	5.2	...	10.39	SABbc/HII Sy	4
NGC 4321 (M100)	16.8	30	7	70	5.7	...	10.39	SABbc/HII	4
NGC 4527	13.5	25	4	70	4.6	...	10.19	SABbc	4
NGC 4569 (M90)	16.8	20	6	70	5.7	...	9.98	SABab/LINER Sy	4
NGC 4826 (M64)	4.1	23	8	70	1.4	...	9.22	(R)SAab/Sy	4
NGC 4945	5.2	20	4	56	1.4	...	...	SBcd:/Sy2	6
NGC 5055	7.2	>36	...	43	1.5	...	9.98	SAbc	1
NGC 5128	4.9	5.5	...	15	0.36	...	10.17	S0 pec/Sy2	7
		18	...	56	1.3	...			7
NGC 5194 (M51)	7.1	31	6	70	2.4	...	10.24	SAbc pec/Sy2.5	4
		14	4	28	0.96	490			9
NGC 5236 (M83)	4.7	29	3	70	1.6	...	10.24	SABc	4
		15	4	56	1.3	440			7
		7	2	28	0.64	850			9
NGC 5248	22.7	42	16	70	7.7	...	10.49	SABbc	4
ESO 97–G13 (Circinus)	4.2	33	6	56	1.14	...	...	SAb:/Sy2	7
		21.7	0.7	20	0.41	...			1
NGC 6946	5.5	41	5	70	1.9	...	10.10	SABcd	4
		16	5	28	0.75	1000			9
NGC 7331	14.3	41	17	28	1.9	...	...	SAb/LINER	9
NGC 7552	19.5	12.2	1.3	16	1.5	...	10.77	(R_1')SBb	1
NGC 7582	17.6	15.8	4.0	20	1.7	...	10.55	(R_1')SBab/Sy2	1

Columns: see column descriptions for Table 4–6.

Notes:

[a] References for CO/HCN line ratios: (1) Aalto et al. 1995; (2) Aalto et al. 1996; (3) Downes et al. 1992; (4) Helfer & Blitz 1993; (5) Helfer & Blitz 1995; (6) Henkel et al. 1990; (7) Israel 1992; (8) Paglione, Tosaki, & Jackson 1995; (9) Nguyen-Q-Rieuet al. 1992; (10) Solomon, Downes, & Radford 1992.

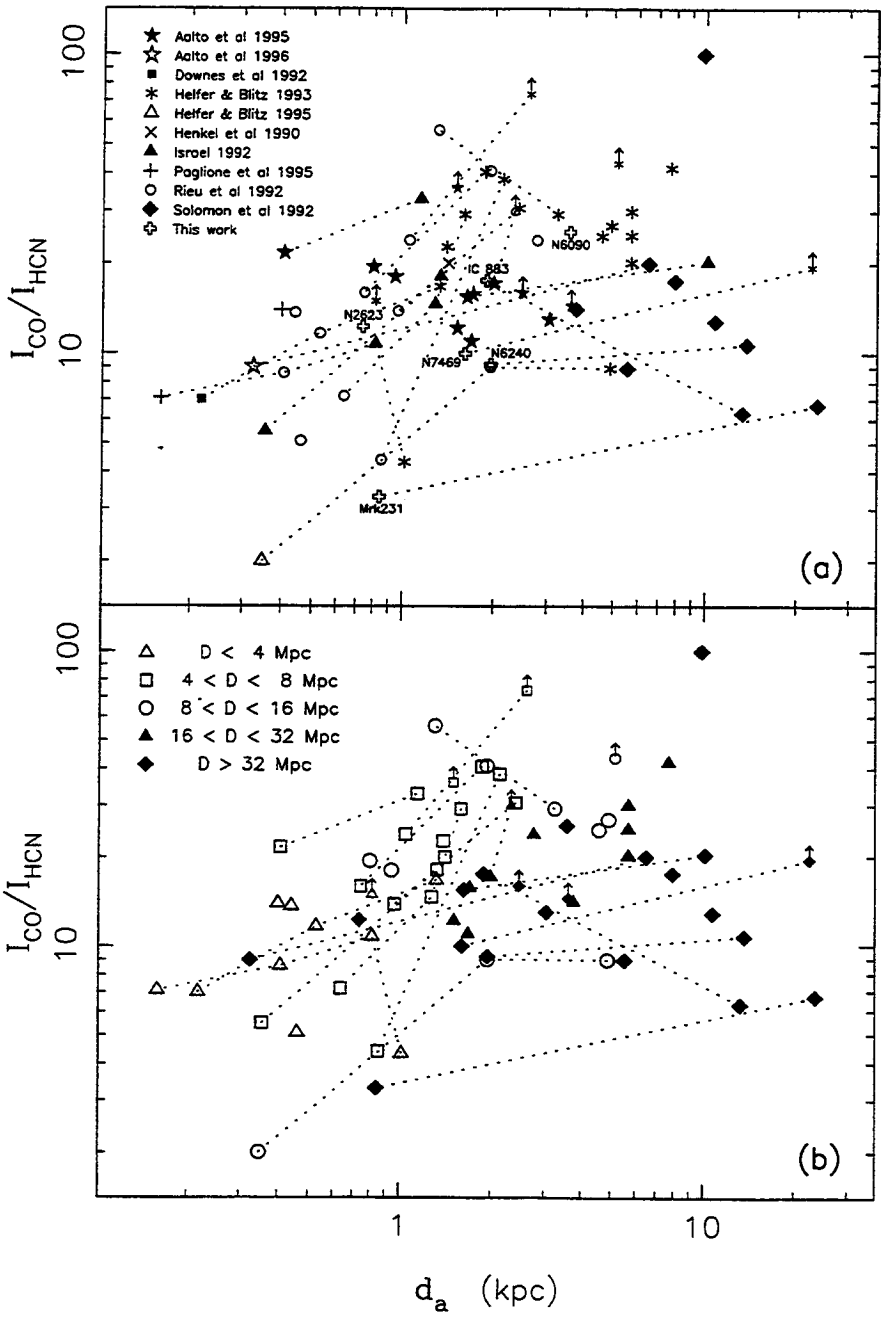

Figure 4–11. (a) CO/HCN line ratios from Tables 4–6 and 4–7 are displayed versus the linear aperture, d_a, of the measurements. Different symbols are used for the each reference. For galaxies that have been observed multiple times, the points are connected by a dotted line. Galaxies with measurements from this work are labeled. (b) Same information as in (a), but here the symbols represent the galaxy distances. Nearby galaxies (open symbols) show a strong trend towards higher CO/HCN ratios at larger apertures. The lack of many high ratios for more distant galaxies (solid symbols) is likely a selection effect. See the text for further discussion of these points.

objects with observed CO/HCN > 20 in apertures larger than 4 kpc may be largely a selection effect due to the difficulty of detecting faint HCN emission in distant galaxies.

As described above, the luminous sample shows a steep trend of decreasing CO/HCN with increasing Σ_{CO}. This trend, necessarily tentative due to the small number of objects, is shown in Figure 4–12 for the sample of luminous interacting galaxies in which both quantities have been measured (solid symbols). Since the HCN emission is effectively unresolved in our maps, and consistent with arising from the same area as the CO emission, the effective apertures of our observations are taken to be the sizes of the CO emission regions (see Chapter 3). Similarly, the apertures we adopt for the observations of IC 694 (Arp 299A; Aalto et al. 1996) and Arp 220 (Radford et al. 1991; Scoville et al. 1996) are the deconvolved sizes of the CO emission regions.

With the data available, it is impossible to distinguish whether Figure 4–12 reflects a trend of CO/HCN ratio with CO surface brightness in luminous interacting galaxies, or whether it reflects an aperture effect similar to that seen in the lower luminosity galaxies. If the HCN can be imaged at higher resolution and spatially resolved (as is the CO emission), it becomes possible to distinguish between the two cases above by directly comparing CO/HCN with the CO surface brightness at different locations and in different size regions. The result can provide extra constraints on models of the molecular gas emission and hence on the state and properties of the molecular gas.

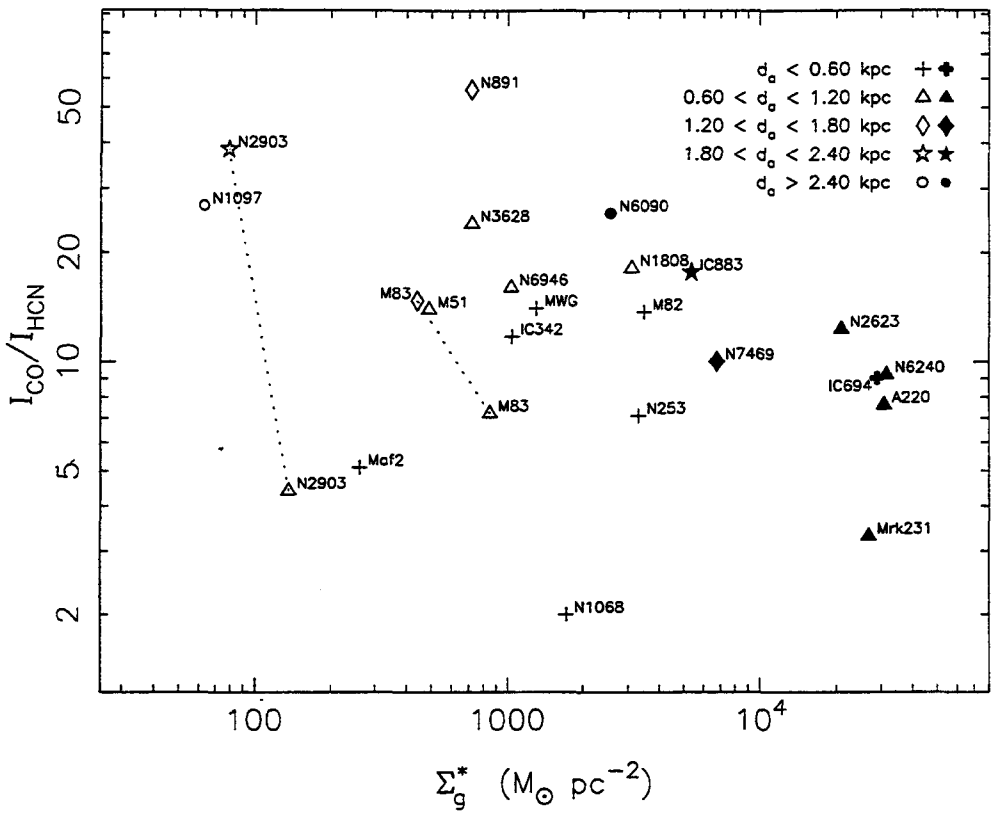

Figure 4–12. CO/HCN line ratios versus CO surface brightness, parameterized as a gas mass surface density, Σ_g^*, via the standard M_g/L'_{CO} conversion factor. The symbols represent the linear aperture sizes of the measurements. Also, solid symbols represent galaxies with $L_{FIR} > 10^{11}$ $L_\odot$, and open symbols represent those with $L_{FIR} < 10^{11}$ $L_\odot$. All luminous galaxies with CO/HCN measurements and resolved CO emission maps are shown—6 of the 8 are from this work (see Table 4–6). For comparison, a random sampling of galaxies nearby enough so that single dish telescopes significantly resolve the CO distribution are also shown (see Table 4–7). "MWG" is the Milky Way Galaxy.

Fourteen of the moderate luminosity galaxies in which CO/HCN has been measured and which are nearby enough so that single dish telescopes significantly resolve the central CO distributions are also shown in Figure 4–12. In contrast to the tentative, but steep, variation of CO/HCN with Σ_g^* in luminous galaxies, the moderate luminosity galaxies show no correlation between these quantities. In fact, while the higher luminosity galaxies exhibit an order of magnitude higher Σ_g^* than do the moderate luminosity galaxies in similar apertures, they have about the same CO/HCN

(perhaps marginally lower). The variations in CO/HCN within both samples are much greater than between them. The intense CO emission in the luminous galaxies requires very unusual gas properties, because either the gas is over an order of magnitude more concentrated than in the center of the Milky Way or its emissivity is over an order of magnitude greater or some combination of these effects. Nonetheless, the similarity of the range of CO/HCN ratios in the luminous and moderate luminosity galaxies suggests that, in the inner kpc, these galaxies have similar fractions of dense gas.

This similarity in CO/HCN ratios between otherwise rather dissimilar samples raises the possibility that the deep gravitational potential well and high hydrostatic pressure of the nucleus (cf. Spergel & Blitz 1992; Helfer & Blitz 1993) dictate the amount of dense gas in galactic nuclei. While these conditions appear to play a role in determining the fraction of dense gas in galactic nuclei, the large scatter of CO/HCN ratios in similar apertures for nuclei of galaxies of similar Hubble type—from as small as 2.0 in NGC 1068 (Helfer & Blitz 1995) to as large as 22 in ESO 97-G13 (Aalto et al. 1995)—suggests that they are not the sole determinants (Figure 4–11). The CO/HCN ratios in galactic nuclei thus must be affected by something in addition to the hydrostatic pressure. The elemental abundances, the dust temperature, the star formation rate, or the luminosity of an AGN can all affect the excitation and chemistry of the molecular gas and hence the molecular line radiation from the different species. This then results in a large dispersion in the observed CO/HCN ratios.

4.4.1.3. Very low CO/HCN line ratios and Seyfert nuclei

Prominent Seyfert nuclei are associated with the two lowest CO/HCN ratios published to date: 2.0 in NGC 1068 (Helfer & Blitz 1993) and 3.3 in Mrk 231 (§4.3.1). These two galaxies differ by a factor of 30 in luminosity and by over an order of magnitude in Σ_g^*; their most dramatic similarity is that both host a broad-line AGN at their cores (e.g., Antonucci & Miller 1985; Boksenberg et al. 1977). NGC 7469, the only other obvious broad-line AGN (Seyfert 1943; Khachikian & Weedman 1974) with a measured CO/HCN ratio, also has a low ratio (10) over a 1.5-kpc region (§4.3.1). Of all objects measured in a 1.1-kpc or larger aperture, only Mrk 231, NGC 1068, and NGC 6240 have CO/HCN ratios confirmed to be below 10. (The low ratio for IC 883 from SDR conflicts with our measurement, and that for NGC 3147 from the same authors is unconfirmed).

While very low CO/HCN ratios appear to be associated with broad-line AGNs, the presence of an AGN does not *guarantee* low ratios. According to the NASA/IPAC Extragalactic Database, 18 of the 47 objects shown in Figure 4–11 have a Seyfert nucleus at some level (all are these are Seyfert 2s except Mrk 231, NGC 7469, and possibly NGC 1097). This sub-sample exhibits the same variation in CO/HCN as the rest of the sample; however, the bulk of these are relatively weak AGN which may not have as strong an impact on their surrounding gas as the AGN in Mrk 231, NGC 1068, and NGC 7469.

4.4.1.4. Interpreting line ratios

Without a detailed model of the molecular gas emission, it is very hard to infer any quantitative properties of the molecular gas. Since CO 1→0 and HCN 1→0 have different critical densities, their emission likely arises in different gas components. Smaller CO/HCN ratios are conventionally attributed to larger fractions of the total molecular content being in high density cloud cores. Because the CO and HCN emission arise in different regions, however, the two molecules probably have different excitation conditions and beam filling factors, both of which can strongly affect the observed line intensities. Radiative transfer models, along with measurements of multiple molecular line ratios, are required to place detailed constraints on the state and properties of the molecular gas. Single component models of the gas have been used often when only a small number of line ratios are known, but these models are certainly a vast over-simplification of the true state of the observed molecular gas. Recently, Aalto et al. (1995) studied emission from several dozen galaxies in six molecular transitions, and used a two-component (core/envelope) molecular gas ensemble—described in Aalto et al. (1994) for NGC 1808—to successfully model the behavior of the line ratios. With studies in even more transitions, especially the sub-mm transitions which will tightly constrain the excitation, increasingly realistic models might be developed.

The low CO/HCN values in the presence of prominent AGN can best be explained by boosting the emission from the higher-density "core" component, from

which most of the HCN emission arises, relative to that from the lower-density "envelope" component, from which most of the ^{12}CO emission arises (Aalto et al. 1995). The alternative—decreasing the emission from the envelope component—is unattractive due to the high CO surface brightnesses in NGC 1068 and NGC 7469, and especially in Mrk 231, where the CO filling factor implied by the brightness temperature is $\gtrsim 0.2$ (Chapter 2). The core component can be boosted in several ways. For example, almost all of the molecular gas may be dense, so that most of the CO emission arises from a medium which has a density far exceeding its critical density. It is hard to see how an AGN can force this state on the molecular gas without being able to strip most of the low-density gas originally in the envelope component. Instead, we speculate that the existence of large amounts of dense gas in the central nuclear disk may in fact enhance the accretion rate and hence the luminosity of the AGN.

Whatever scenario is favored, the molecular gas model of Aalto et al. (1995) makes definite predictions for molecular line ratios in addition to CO/HCN (e.g., ^{12}CO/^{13}CO and CO $2 \rightarrow 1$/CO $1 \rightarrow 0$ for both ^{12}CO and ^{13}CO). Thus, while CO/HCN ratios alone are unable to significantly constrain the properties of molecular gas, when they are combined with a variety of other molecular line ratios they should be a powerful probe of the conditions in the center of active galaxies. At this time, only a handful of the very nearest galaxies have been measured in a sufficient number of line ratios to usefully constrain multiple-component gas models such as that of Aalto et al. described above.

4.4.2. Near-infrared extinction

The large amounts of dust in the cores of luminous infrared galaxies have inspired many studies of these objects in the near-infrared J, H, and K-windows. Since the emission in these bands is much less affected by extinction than is the emission in the optical bands, it is generally hoped that the NIR observations directly probe the nuclear regions. The extremely large column densities of molecular gas seen towards the cores of these objects, however, suggest that extinctions are extreme even at wavelengths of 2 μm (e.g., see Chapter 3). In contrast, estimates from optical and infrared reddening measurements imply that the NIR extinction is less than a magnitude at K. Clumping of the ISM, though, may cause reddening measurements to severely underestimate the true extinction, since the light we see predominantly arises in regions of low extinction. In cases where the extinction is patchy, observational selection will always tend towards an apparent extinction of order unity at the observed wavelength. Furthermore, forward scattering by large columns of dust may completely negate the reddening caused by extinction, and thus exacerbate the underestimate of the true column density of dust (Witt, Thronson, & Capuano 1992). More reliable estimates of the effective dust content require observations at longer wavelengths.

Millimeter-wavelength free-free radiation provides an optically-thin tracer of ionized gas that is unaffected by extinction. Its ratio relative to NIR hydrogen recombination lines such as Brγ can thus provide an estimate of the extinction factor, $X \equiv F^{\rm intrinsic}/F^{\rm observed}$, suffered by NIR recombination lines. Knowledge of extinction factors for the NIR recombination lines will greatly assist interpretation of the

NIR emission and hence of the nature of the nuclear phenomena in luminous infrared galaxies. Care must still be taken when interpreting NIR emission that arises from regions other than the ionized gas (such as the H_2 ro-vibrational lines). The relative distribution of emission from these regions and extinction may be significantly different than for the ionized gas, and a different extinction factor may apply.

Measuring the thermal bremsstrahlung is difficult, however, because it is weak and is contaminated by non-thermal synchrotron emission or thermal dust emission at most radio frequencies. At centimeter and longer wavelengths, radio emission from galaxies is dominated by non-thermal synchrotron emission, which decreases with increasing wavelength. At sub-millimeter wavelengths, thermal emission from dust rises very steeply to quickly dominate the other continuum emissions. Continuum observations at millimeter wavelengths thus provide the best hope for placing significant constraints on thermal bremsstrahlung in galaxies (cf. Carlstrom & Kronberg 1991).

Using case B recombination (e.g., Osterbrock 1989), the radio thermal bremsstrahlung continuum emission can be related to the total intrinsic near-infrared Brγ recombination line emission by the expression

$$F^{\rm i}_{\rm Br\gamma}\,[10^{-18}{\rm Wm^{-2}}] = 14.96\,T_4^{-0.86}\,\nu_{11}^{0.16}\,S^{\rm T}_{\nu}[{\rm mJy}]\ , \qquad (4\text{–}1)$$

where $F^{\rm i}_{\rm Br\gamma}$ is the intrinsic Brγ line flux, T_4 is the temperature of the ionized gas in units of 10^4 K, and $S^{\rm T}_{\nu}$ is the bremsstrahlung flux at frequency ν_{11}, given in units of 100 GHz. Our observational upper limits to the $S^{\rm T}_{\nu}$, obtained by subtracting power law extrapolations of the cm-wave non-thermal spectrum from the observed mm-wave continuum fluxes, are listed in Table 4–5. Table 4–8 lists the corresponding upper

Table 4–8. Near-infrared extinction constraints

object	$F^{i}_{Br\gamma}$	$F^{o}_{Br\gamma}$	$X_{Br\gamma}$	$\tau_K(X_{Br\gamma})$	$\lvert\tau_K(\Sigma_g)\rvert$		τ_K
	(10^{-18} W m^{-2})	(10^{-18} W m^{-2})		mixture	standard	minimum	reddening
(1)	(2)	(3)	(4)	(5)	(6)	(7)	(8)
NGC 2623	< 63	9.6 (0.5)	< 6.6	< 6.6	51	2.6	0.42
Mrk 231	< 445	24.7 (5.0)	< 18	< 18	103	5.7	0.46
IC 883	< 97	13.5 (0.5)	< 7.1	< 7.1	13	0.54	0.41
NGC 6090	< 26	16.0 (1.9)	< 1.6	< 1.1	6.3	0.26	0.17
NGC 6240	< 66	18.9 (4.5)	< 3.5	< 3.4	78	4.0	0.49
NGC 7469	< 60	45.7 (2.4)	< 1.3	< 0.6	17	0.8	0.00
Arp 220.....	< 152[a]	5.9 (1.3)	< 26	< 26	120 48[b]	5.7	1.00

Columns: (1) object; (2) predicted intrinsic Brγ flux predicted by the thermal bremsstrahlung flux and case B recombination for $T_e = 10^4$ K; (3) observed Brγ flux in a 3″ slit from Goldader et al. 1995; (4) Brγ extinction factor, defined as the ratio of the predicted intrinsic Brγ flux to the observed Brγ flux; (5) dust optical depth at the near-infrared K band, assuming that the dust is uniformly mixed with the ionized gas so that $X = \tau/(1-e^{-\tau})$; (6) K-band dust optical depth, derived from the CO 1→0 emission using the standard M_g/L'_{CO} conversion factor and extinction law (see Chapters 2 and 3); (7) lower limit to the K-band dust optical depth, derived from the CO 1→0 emission by assuming that the line is optically thin and that [CO]/[H_2] = 10^{-4} (see Chapters 2 and 3); (8) K-band dust optical depth, derived from optical or near-infrared broad-band reddening measurements—based on A_K estimated by Goldader et al. 1995.

Notes:
[a] Based on the upper limit of 10 mJy for the thermal flux at 110.3 GHz from Scoville et al. 1991.
[b] From preferred conversion factor of 40% times the standard value (Scoville, Yun, & Bryant 1996).

limits for the intrinsic Brγ line flux (using $T_4 = 1$), as well as the observed Brγ line fluxes in a 3″ slit (Goldader et al. 1995), which should encompass the bulk of the ionized gas emission in these compact objects. The upper limit to the extinction factor for Brγ emission, $X_{Br\gamma}$, is tabulated, and the results from millimeter continuum measurements of the ultraluminous merger Arp 220 (Scoville et al. 1991) are also shown.

The most significant constraints on the Brγ extinction factor are for NGC 6090 and NGC 7469. In these objects, our radio continuum observations imply that the NIR observations are seeing at least 61% and 76% of the total intrinsic Brγ flux. Extinction is thus not a dominant factor in the appearance of the NIR recombination line emission in NGC 6090 and NGC 7469. In the other objects, the possibility

remains that the Brγ emission may be being extinguished by a large factor. More sensitive mm-wave continuum observations are needed to confirm or rule out such large extinction factors in these objects.

If the relative distribution of the dust and the ionized gas is known, the extinction factor can be converted into an estimate of the dust optical depth and hence the into an estimate of the gas column density in the nucleus. As a simple but reasonable starting point, we assume that the dust and the ionized gas are distributed similarly, in a uniform spherical mixture. For this case, the dust optical depth τ is related to the extinction factor by

$$X = \frac{\tau}{1 - e^{-\tau}}. \tag{4–2}$$

For $\tau \gg 1$, $X \approx \tau$. Table 4–8 lists the upper limits to the K-band dust optical depths, $\tau_{\rm K}(X_{\rm Br\gamma})$, that correspond to the upper limits to the extinction factors for the assumed uniform mixture of dust and ionized gas. Also shown are the K-band optical depths determined from the gas column densities implied from the CO observations, $\tau_{\rm K}(\Sigma_{\rm g})$, both for use of the standard $M_{\rm g}/L'_{\rm CO}$ conversion factor and for the case of optically-thin CO 1$\rightarrow$0 emission (see Chapters 2 and 3). The latter serves as a lower limit to the total dust column though the nucleus of these galaxies for $[{\rm CO}]/[{\rm H_2}] \leq 10^{-4}$. A standard extinction law (Mathis 1993) is assumed to apply in all these objects. For comparison, the K-band optical depths derived from optical or NIR reddening measurements, assuming a foreground screen of dust, are also shown (Goldader et al. 1995).

In each object studied here, the upper limits to $\tau_{\rm K}(X_{\rm Br\gamma})$ derived assuming a uniform mixture of dust and ionized gas are several times lower than the values for

$\tau_K(\Sigma_g^*)$ derived using the standard CO conversion factor. As long as the dust and ionized gas are indeed uniformly mixed, this result would imply that the standard conversion factor is overestimating the mass of molecular gas by factors from 1.8 to 23, at a minimum. Yet, if the large-scale distribution of the dust in the nucleus is more confined than that of the ionized gas, the upper limits to $\tau_K(X_{Br\gamma})$ may be *severely* underestimated by the above procedure. To take an extreme example, if the dust is confined to a region several times smaller in radius than the ionized gas, the dust can have a (practically) infinite column density and still extinguish only a few percent of the recombination line emission.

Indeed, we have evidence that a similar, though much less extreme, geometry exists in NGC 6240 and NGC 7469. In these objects, the upper limit on τ_K for the uniform mixture hypothesis is smaller than the lower limit on τ_K derived by assuming that the CO emission is optically thin. So either CO is super-abundant, thus lowering the minimum τ_K for the optically thin CO case, or the dust is more compactly distributed than the ionized gas in NGC 6240 and NGC 7469. We favor the latter alternative since it does not require the extreme case of optically thin CO emission. The dust may be more compactly distributed than the ionized gas on either a large or small scale and still satisfy the above geometrical requirement. For example, individual clouds of arbitrarily small size may consist of dusty cores surrounded by less dusty regions of ionized gas, or the dust and molecular gas may be distributed in a dense, thin disk (not viewed edge-on), with the ionized gas either having a larger scale height or concentrated in a nuclear source.

Such geometries may well also apply in the other objects studied here. If so, the upper limits to $\tau_{\rm K}(X_{\rm Br\gamma})$ would be raised into better agreement with the $\tau_{\rm K}$ derived from the standard conversion factor. Thus we are unable to rule out the large molecular gas masses implied by the standard conversion factor.

4.4.3. Starburst constraints

The limits on thermal bremsstrahlung can be used to place constraints on nuclear starbursts. Since bremsstrahlung should be optically thin at mm wavelengths, measurements of its strength provide an estimate of the rate of production of ionizing photons, Q. If the bulk of the IR luminosity is powered by a nuclear starburst (i.e., $L_{\rm IR} \approx L_{\rm sb}$), the ratio $L_{\rm IR}/Q$ then provides a constraint on the starburst's age and initial mass function (IMF). This is because $L_{\rm IR}$ is dominated by moderately long-lived intermediate mass stars and Q is dominated by short-lived high mass stars. Figure 4–13 shows the variation of the $L_{\rm sb}/Q$ ratio as a function of the upper mass limit of the IMF, $m_{\rm u}$, and the age of the starburst, $t_{\rm sb}$. The figure was produced using the power law parameterization given by Scoville & Soifer (1991) for their constant rate, modified Miller-Scalo IMF starburst model.

For case B recombination, the rate of production of ionizing photons is related to the thermal bremsstrahlung flux by

$$Q[{\rm s}^{-1}] = 1.33 \times 10^{50} \, \frac{\alpha_{\rm B}(T)}{\alpha_{\rm B}(10^4 K)} \, \nu_{11}^{0.16} \, D_{\rm Mpc}^2 \, S_\nu^{\rm T}[{\rm mJy}] \, , \qquad (4\text{–}3)$$

where $\alpha_{\rm B}(T)$ is the hydrogen recombination coefficient for case B as a function of the temperature of the ionized gas and $D_{\rm Mpc}$ is the distance to the object in Mpc.

Table 4–9. Starburst constraints

object	$S_\nu^{\rm T}$ (mJy)	Q (10^{54} s^{-1})	$L_{\rm IR}/Q$ (10^{-44} L$_\odot$ s)
(1)	(2)	(3)	(4)
NGC 2623	< 4.3	< 3.2	> 10.8
Mrk 231	< 30.5	< 120	> 2.9
IC 883	< 6.6	< 8.2	> 4.9
NGC 6090	< 1.8	< 3.6	> 9.0
NGC 6240	< 4.5	< 5.9	> 11.1
NGC 7469	< 4.0	< 2.3	> 17
Arp 220	< 10[a]	< 8.5[b]	> 18[b]

Columns: (1) object; (2) upper limit to the thermal mm-wave continuum flux, from column 8 of Table 4–5; (3) upper limit to the rate of production of ionizing photons, derived assuming case B recombination at $T_{\rm e} = 10^4$ K and that the dust continuum contribution to $S_\nu^{\rm T}$ is negligible; (4) lower limit to the ratio of infrared luminosity to the rate of production of ionizing photons.

Notes:

[a] From Scoville et al. 1991.

[b] Based on estimates of Scoville et al. 1991, but slightly modified by the use of a distance of 79.2 Mpc (Sanders, Scoville, & Soifer 1991) instead of 77 Mpc and by the use of a more accurate power law expression for the gaunt factor at mm wavelengths.

For $T = 10^4$ K, the upper limits to Q and the lower limits to $L_{\rm IR}/Q$ are shown in Table 4–9. The latter limits are also depicted in Figure 4–13, with the assumption that $L_{\rm IR} = L_{\rm sb}$.

For a constant rate starburst to account for the both $L_{\rm IR}$ and the $L_{\rm IR}/Q$ ratios, the starburst's age must be greater and its upper mass limit must be less than those given by the lines plotted for each galaxy in Figure 4–13. If the nuclear starbursts account for only a fraction, $f_{\rm sb}$, of the total $L_{\rm IR}$, the limits on $L_{\rm IR}/Q$ are lowered by the same fraction, and the starburst constraints are loosened. With the current limits on $S_\nu^{\rm T}$, the luminosities of all six galaxies studied here can be explained by starbursts with reasonable values of $m_{\rm u}$ and $t_{\rm sb}$. The strongest constraint is for NGC 7469. In this galaxy, $f_{\rm sb} = 1$ rules out young starbursts ($t_{\rm sb} < 5 \times 10^7$ yr) unless $m_{\rm u}$ is smaller than 30 M$_\odot$. A similar constraint is placed on the ultraluminous galaxy Arp 220 by Scoville et al. (1991, 1996). The constraints on NGC 6240, NGC 2623, and NGC 6090

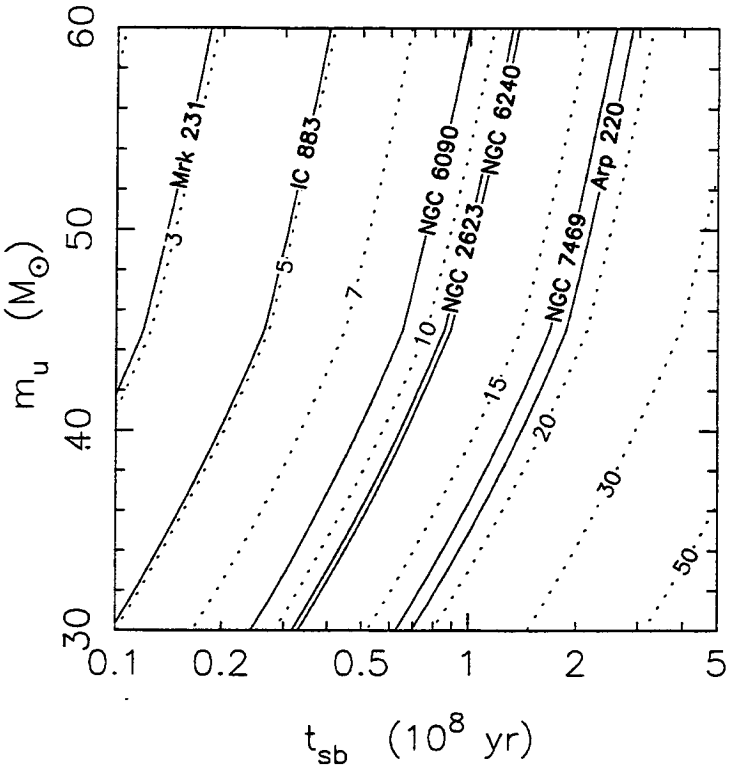

Figure 4–13. Contour plot of L_{IR}/Q (see Table 4–9) as a function of the upper mass limit, m_u, and the age of the starburst, t_{sb}, for the constant rate starburst model of Scoville & Soifer (1990). The contours are labeled in units of 10^{-44} $L_\odot$ s. If a starburst accounts for 100% of L_{IR}, the observational limits in Table 4–9 permit only solutions below and to the right of the lines shown for each luminous infrared galaxy . If a starburst accounts for 50% or less of L_{IR}, the observational limits are shifted to the left by a factor of two or more, significantly loosening any constraints on the starburst parameters. The limit for Arp 220 is based on data from Scoville et al. (1991).

are somewhat looser but still significant in requiring either relatively old ages ($t_{sb} > 10^8$ yr) or IMFs truncated at $m_u < 50$ $M_\odot$. The starburst parameters remain virtually unconstrained by the limits on L_{IR}/Q in IC 883 and Mrk 231, primarily due to the high upper limit on the free-free fluxes.

In order to tighten the constraints on the starburst parameters, it is crucial to obtain measurements of the radio continuum at frequencies between 8 and 100 GHz. With these measurements, the thermal and non-thermal contributions can be disentangled. Since the thermal contribution is expected to be less than a few mJy,

these observations will require high sensitivity. When the thermal continuum can be directly measured, it promises to yield more reliable constraints on the Lyman continuum than NIR recombination lines such as Brγ, since the radio emission is not subject to dust extinction exterior to the H II regions. We do note that dust inside H II regions will compete with the gas for the ionizing photons, and can reduce the resultant emission of both Brγ and thermal bremsstrahlung.

Genzel et al. (1995) perform a detailed comparison of optical and infrared observations of NGC 7469 with starburst models similar to that of Scoville & Soifer (1991). For their constant rate starburst with a Salpeter IMF slope, adopting a uniform mixture extinction model with $A_V = 15$, measurements of $L_{bol}/L_{Br\,\gamma}$ and $L_K/L_{Br\,\gamma}$ yield constraints consistent with, but somewhat tighter than, our constraints from L_{IR}/L_ν^T: t_{sb} from several 10^7 to several 10^8 yr and m_u from 30 to 40 $M_\odot$. This is not surprising given the strong agreement of our upper limit on the thermal bremsstrahlung with the observed Brγ flux. Genzel et al. also try a rapidly decaying starburst model, with an adopted exponential decay time of 5×10^6 yr, simulating a very brief burst. For this model, their observations require much younger ages of $1\text{–}2 \times 10^7$ yr. These authors prefer this decaying starburst model, because it does not require an upper mass cutoff to the IMF to explain the current lack of ionizing stars, and also thus explains the relatively low He I/Brγ ratio they observe (though they note that this observational parameter is very sensitive to the density, dust content, and velocity structure of the H II regions). Since the derived starburst age is much younger than the presumed interaction age of 1.5×10^8 yr for NGC 7469 and its companion IC 5283,

Genzel et al. suggest that the present burst in NGC 7469 is not the original one, or else that there has been a long delay between the tidal trigger and the beginning of the starburst. This then raises the minor problem that it would be unlikely for us to catch the starburst at this very special decaying, but still luminous, phase.

We suggest that the exceptionally young age that Genzel et al. determine for their decaying starburst model is the direct result of their choice of a very short decay time. Their age constraint depends upon the observed ratio of bolometric luminosity ($L_{\rm bol}$~$L_{\rm IR}$) to Lyman continuum luminosity ($L_{\rm Lyc} \propto L_{\rm Br\gamma}$). The modeled Lyman continuum luminosity is extremely sensitive the amount of very high mass stars remaining, so a burst which terminates after only a few 10^6 yr will lose most of its ionizing stars after an additional few 10^6 yr, leading to a rapid decrease in $L_{\rm Lyc}$. Since $L_{\rm bol}$ is dominated by intermediate mass stars for a Salpeter IMF, it only decreases slowly at this point, so $L_{\rm bol}/L_{\rm Lyc}$ rises rapidly through the observed value and beyond. If Genzel et al. had adopted a longer decay time of, say, 3×10^7 yr, new ionizing stars will be produced to replace the early generations, and the rapid increase of $L_{\rm bol}/L_{\rm Lyc}$ is postponed until a few 10^7 yr. There is no obvious mechanism to terminate a starburst after only 10^7 yr or less; in fact, if the starburst is dynamically triggered, then the decay time cannot be less than a dynamical timescale, $\sim 3 \times 10^7$ yr for the nucleus of NGC 7469. Thus, we find the ages suggested by constant rate or slowly decaying starburst models more plausible. There is then no need for the long delay between the initial tidal trigger and the onset of the starburst postulated by Genzel et al.. We note that if such long delays ($> 10^8$ yr), followed by short starbursts

(few 10^7 yr), were common, we would expect to find large numbers of gas-rich tidally interacting galaxies without starburst activity. Previous studies indicate that this is not the case, and that most such interacting galaxies host substantial activity: Xu & Sulentic (1991) find that close optically-selected spiral-spiral pairs with morphological signs of an interaction exhibit enhanced FIR to optical luminosity ratios and warmer FIR colors when compared with isolated spirals and more widely separated spiral-spiral pairs; and Combes et al. (1994) find enhanced $L_{\rm FIR}$, $L_{\rm CO}$, and $L_{\rm FIR}/L_{\rm CO}$ in tidally-perturbed, optically-selected binary galaxies. These results suggest that any delay between the trigger and the beginning of the starburst much be substantially less than the time elapsed since the interaction and that the starburst persists for timescales similar to that of the interaction.

4.5. Conclusions

In this paper, we have presented new, high-resolution observations of high-density molecular tracers in six luminous infrared galaxies, greatly increasing the sample of such observations. We have observations of HCN 1→0 in all six, HCO^+ 1→0 in three, and a tentative detection of CS 1→0 in one. The primary conclusions from this study are as follows.

1. The CO/HCN ratios cover nearly an order of magnitude, ranging from as low as 3.3 in Mrk 231 to 26 in NGC 6090. This requires that the properties of the molecular gas, specifically the fraction of the gas which is at high density, vary substantially among our sample.

2. The line profiles and spatial extent of the high-density tracers are consistent with those of the CO 1→0 emission to within the uncertainties. So the high-density tracer emission can arise from the same nuclear region as does the CO emission.

3. For Mrk 231, the most luminous object in our sample, the excitation temperature of the HCN 1→0 line is greater than 32 K if the HCN emission arises from a region equal to or smaller than the 1″.0 diameter (440 pc radius) CO 2→1 source measured in Chapter 2. Using the conservative 3σ upper limit to the CO 2→1 source size of 1″.2 × 0″.66 still results in a minimum HCN 1→0 excitation temperature of 14 K. The equivalent constraints on the CO 1→0 excitation temperature are 83 K and 34 K (§2.3.1). Both the CO and HCN emissions in this galaxy must arise in hot gas with a moderate to large filling factor.

4. The mm-wavelength continuum is detected in four of the six objects. All detections and limits are consistent with or slightly lower than the extrapolation of the cm-wave non-thermal continuum. We are able to place significant limits on the free-free contribution to the mm-wave continuum in all objects except IC 883 and Mrk 231. In Mrk 231, the 3 mm continuum decreased by ∼50% in the 19 months between 1993 May and 1994 Dec. This is similar to the variability seen by previous investigations at cm wavelengths. Both measurements of the 3 mm continuum fall within the range predicted by extrapolation of the historical range of cm-wave continuum variation. The observed 3 mm continuum emission of Mrk 231 is therefore likely to be dominated by non-thermal emission.

5. We find a trend of decreasing CO/HCN with increasing CO surface brightness for the higher luminosity infrared galaxies. This may suggest that the fraction of dense gas in molecular gas clouds increases as the surface density of clouds increases. Alternatively, the trend could be produced by an aperture effect due to the nuclear gravitational potential if the dense gas is more concentrated towards the nucleus than the overall molecular gas distribution.

6. The CO/HCN ratios in luminous IR galaxies cover a range similar to the ratios measured in galaxies with $L_{\rm FIR} < 10^{11}$ $L_{\odot}$, despite the extreme properties of the molecular gas in luminous IR galaxies. The large scatter in CO/HCN ratios in each class of objects may be caused by differences in abundances, dust content, star formation rates, or AGN luminosity, among other effects.

7. The strength of HCN emission relative to CO is not necessarily related to the rate of massive star formation in a galaxy, as suggested by SDR, but may simply reflect the preponderance of high-density (10^4 cm^{-3}) gas in the nuclei of objects like Mrk 231, NGC 6240, and NGC 2623.

8. The lowest CO/HCN ratios are associated with prominent broad-line AGN: NGC 1068, Mrk 231, NGC 7469. The presence of an AGN, however, does not guarantee low CO/HCN ratios. This may be a function of the luminosity of the AGN and the amount of gas in close proximity to the AGN. We speculate that the existence of large masses of dense gas in the central nuclear disk may in fact enhance the accretion rate and hence the luminosity of the AGN.

9. In NGC 6240 and NGC 7469, the maximum dust τ_K derived from the Brγ extinction factor and a uniform mixture extinction model is less than the lower limit to τ_K, derived from assuming that the CO 1→0 emission is optically thin. Thus either CO is super-abundant ($[CO]/[H_2] > 10^{-4}$) and still optically thin, which we view as improbable, or, more likely, the dust is distributed more compactly than the ionized gas, on either a small or large scale. Such an extinction geometry may also apply in the other objects, resulting in a larger τ_K than implied by the application of the uniform mixture extinction model to the Brγ extinction factor.

10. Using the observed constraints on the ratio of starburst luminosity to the rate of production of ionizing photons in conjunction with constant rate star formation models, we are able to place significant constraints on the age and upper mass limits of nuclear starbursts in four objects, assuming that the starburst contributes most of L_{IR}. In NGC 7469, $L_{IR}/Q > 17 \times 10^{-44}$ $L_\odot$ s rules out starbursts younger than 10^8 yr unless $m_u < 35$ $M_\odot$. We find no reason to favor a young age for rapidly decaying starburst, as suggested by Genzel et al. (1995) for this object. In NGC 2623, NGC 6090, and NGC 6240, somewhat lower constraints on L_{IR}/Q require either relatively old starbursts with $t_{sb} > 10^8$ yr or truncated IMFs with $m_u < 50$ $M_\odot$. The starburst parameters for IC 883 and Mrk 231 are essentially unconstrained by the observed limits on L_{IR}/Q. Reasonable-parameter nuclear starbursts remain a viable explanation for the bolometric luminosity of all six luminous infrared galaxies studied here.

References

Aalto, S., Booth, R. S., Black, J. H., & Johansson, L. E. B. 1995, A&A, 300, 369

Aalto, S., Booth, R. S., Black, J. H., Koribalski, B., & Wielebinski, R. 1994, A&A, 286, 365

Aalto, S., Radford, S. J. E., Scoville, N. Z., & Sargent, A. I. 1996, ApJ, submitted

Aaronson, M., Huchra, J., Mould, J., Schechter, P. L., & Tully, R. B. 1982, ApJ, 258, 64

Antonucci, R. R. J. & Miller, J. S. 1985, ApJ, 297, 621

Batuski, D. J., Hanisch, R. J., & Burns, J. O. 1992, AJ, 103, 1077

Boksenberg, A., Carswell, R. F., Allen, D. A., Fosbury, R. A. E., Penston, M. V., & Sargent, W. L. W. 1977, MNRAS, 178, 451

Bryant, P. M. & Scoville, N. Z. 1996, in preparation

Carlstrom, J. E. & Kronberg, P. P. 1991, ApJ, 366, 422

Carral, P., Turner, J. L., & Ho, P. T. P. 1990, ApJ, 362, 434

Colbert, E. J. M., Wilson, A. S., & Bland-Hawthorn, J. 1994, ApJ, 436, 89

Combes, F., Prugniel, P., Rampazzo, R., & Sulentic, J. W. 1994, A&A, 281, 725

Condon, J. J., Helou, G., Sanders, D. B., & Soifer, B. T. 1990, ApJS, 73, 359

Condon, J. J., Helou, G., Sanders, D. B., & Soifer, B. T. 1996, ApJS, 103, 81

Condon, J. J., Huang, Z. P., Yin, Q. F., & Thuan, T. X. 1991, ApJ, 378, 65

Downes, D., Radford, S. J. E., Guilloteau, S., Guélin, M., Greve, A., & Morris, D. 1992, A&A, 262, 424

Edelson, R. A. 1987, ApJ, 313, 651

Genzel, R. et al. 1995, ApJ, 444, 129

Goldader, J. D., Joseph, R. D., Doyon, R., & Sanders, D. B. 1995, ApJ, 444, 97

Heckman, T. M., Armus, L., Miley, G. K. 1987, AJ, 93, 276

Heckman, T. M., Van Breugel, W., Miley, G. K., & Butcher, H. R. 1983, AJ, 88, 1077

Helfer, T. T. & Blitz, L. 1993, ApJ, 419, 86

Helfer, T. T. & Blitz, L. 1995, ApJ, 450, 90

Henkel, C. & Bally, J. 1985, A&A, 150, L25

Henkel, C., Whiteoak, J. B., Nyman, L.-Å., & Harju, J. 1990, A&A, 230, L5

Hummel, E., Van der Hulst, J. M., Keel, W. C., & Kennicutt, R. C. 1987, A&AS, 70, 517

Israel, F. P. 1992, A&A, 265, 487

Jackson, J. M., Heyer, M. H., Paglione, T. A. D., & Bolatto, A. D. 1996, ApJ, 456, L91

Joseph, R. D. & Wright, G. S. 1985, MNRAS, 214, 87

Khachikian, E. Ye. & Weedman, D. W. 1974, ApJ, 192, 581

Kojoian, G., Sramek, R. A., Dickinson, D. F., Tovmassian, H., & Purton, C. R. 1976, ApJ, 203, 323

Kuno, N., Nakai, N., Handa, T., & Sofue, Y. 1995, PASJ, 47, 745

Lawrence, A., Rowan-Robinson, M., Leech, K., Jones, D. H. P., & Wall, J. V. 1989, MNRAS, 240, 329

Liszt, H. S. 1995, ApJ, 442, 163

Liu, C. T. & Kennicutt, R. C. 1995, ApJS, 100, 325

Martin, R. N. & Ho, P. T. P. 1979, A&A, 74, L7

Mathis, J. S. 1993, Rep. Prog. Phys., 56, 605

Mauersberger, R., Henkel, C., Wilson, T. L., & Harju, J. 1989, A&A, 226, L5

Mazzarella, J. M. & Boroson, T. A. 1993, ApJS, 85, 27

Nguyen-Q-Rieu, Jackson, J. M., Henkel, C., Truong-Bach, & Mauersberger, R. 1992, ApJ, 399, 521

Osterbrock, D. E. 1989, Astrophysis of Gaseous Nebulae and Active Galactic Nuclei, (Mill Valley, CA: University Science Books)

Padin, S. et al. 1993, IEEE Trans. Instr. Meas., 42, 793

Paglione, T. A. D., Tosaki, T., & Jackson, J. M. 1995, ApJ, 454, L117

Radford, S. J. E. et al. 1991, in Dynamics of Galaxies and Their Molecular Cloud Distributions, eds. F. Combes & F. Casoli (Dordrecht: Kluwer Academic) p. 303

Rickard, L. J., Palmer, P., Morris, M., Zuckerman, B., & Turner, B. E. 1975, ApJ, 199, L75

Rickard, L. J., Palmer, P., Turner, B. E., Morris, M., & Zuckerman, B. 1977, ApJ, 214, 390

Roche, P. F., & Chandler, C. J. 1993, MNRAS, 265, 486

Sage, L. J., Shore, S. N., & Solomon, P. M. 1990, ApJ, 351, 422

Sanders, D. B., Scoville, N. Z., & Soifer, B. T. 1991, ApJ, 370, 158

Sanders, D. B., Soifer, B. T., Elias, J. H., Madore, B. F., Matthews, K., Neugebauer, G., & Scoville, N. Z. 1988, ApJ, 325, 74

Sargent, A. I. & Scoville, N. Z. 1991, ApJ, 366, L1

Scoville, N. Z., Carlstrom, J. E., Chandler, C. J., Phillips, J. A., Scott, S. L., Tilanus, R. P. J., & Wang, Z. 1993, PASP, 105, 1482

Scoville, N. Z., Sargent, A. I., Sanders, D. B., & Soifer, B. T. 1991, ApJ, 366, L5

Scoville, N. Z. & Soifer, B. T. 1991, in Massive Stars in Starbursts, eds. C. Leitherer, N. R. Walborn, T. M. Heckman, & C. A. Norman (Cambridge: Cambridge Univ. Press) p. 233

Scoville, N. Z., Yun, M. S., & Bryant, P. M. 1996, ApJ, submitted

Seyfert, C. K. 1943, ApJ, 97, 28

Soifer, B. T., Sanders, D. B., Neugebauer, G., Danielson, G. E., Lonsdale, C. J., Madore, B. F., & Persson, S. E. 1986, ApJ, 303, L41

Solomon, P. M., Downes, D., & Radford, S. J. E. 1992, ApJ, 387, L55 (SDR)

Spergel, D. N. & Blitz, L. 1992, Nature, 357, 665

Stark, A. A. & Wolf, R. S. 1979, ApJ, 229, 118

Tully, R. B. 1988, Nearby Galaxies Catalog, (Cambridge: Cambridge Univ. Press)

Witt, A. N., Thronson, H. A., & Capuano, J. M. 1992, ApJ, 393, 611

Xu, C. & Sulentic, J. W. 1991, ApJ, 374, 407

Chapter 5

Summary and Future Work

5.1. Thesis summary

My dissertation research has focused on the observation and interpretation of spectral lines that trace the molecular gas in luminous infrared galaxies (LIRGs). This class of objects ($L_{\rm IR}$[8–1000μm] $> 10^{11}$ L$_\odot$) consists primarily of gas-rich galaxies that are undergoing strong interactions or merger events (Sanders, Scoville, & Soifer 1991; Leech et al. 1993; Sanders et al. 1988). It remains unclear whether prodigious bursts of star formation or more exotic phenomena such as dust-enshrouded AGNs account for the bulk of the luminosity in these systems (e.g., Joseph & Wright 1985; Condon et al. 1991, hereafter CHYT; Sanders et al. 1988; Lonsdale, Smith, & Lonsdale 1995); yet by studying the spatial distribution, kinematics, and physical properties of the molecular

gas—which likely serves as the fuel for both forms of activity—constraints can be placed on the size, duration, and nature of the luminosity-generating mechanism.

Previous to my dissertation work, only a handful of luminous IR galaxies had been mapped in the best tracer of the entire molecular gas content, CO 1→0, with the resolution necessary (2–4″) to resolve the molecular gas distributions; these observations showed very compact CO distributions well under a kiloparsec in radius (e.g., Scoville et al. 1991; Sargent & Scoville 1991). Also, only a single object had been mapped at few-arcsecond resolution in a high-density molecular gas tracer (Arp 220 in HCN 1→0; Radford et al. 1991). Using the Owens Valley millimeter array, I have made 2″-resolution (970 pc at 100 Mpc) aperture synthesis maps of the CO 1→0 emission in six luminous IR galaxies, five of which are mergers—Mrk 231, NGC 6240, IC 883, NGC 2623, NGC 6090—and one of which is a member of an interacting pair—NGC 7674 (Chapter 3). I have also made a 0″.8-resolution map of the CO 2→1 emission in Mrk 231, thereby achieving the first sub-arcsecond resolution CO map of an extragalactic object (Chapter 2). Finally, I have mapped the five mergers in HCN 1→0 and three in HCO^+ 1→0 (Chapter 4). A qualitative estimate of the density of the molecular gas is obtained from these observations due to the high dipole moment of these two molecules: their lowest rotational transitions require densities of around 10^4–10^5 cm^{-3} to be excited—nearly two orders of magnitude greater than the densities required to excite CO 1→0.

The CO observations reveal that the morphology of the molecular gas emission varies with the IR/radio interaction morphology. The three mergers with a single

IR/radio nucleus all show very bright and very compact CO cores, with resolved radii of 0.33–0.96 kpc; these CO cores peak at the same position as the non-thermal radio continuum. The two mergers with double IR/radio nuclei also show very bright CO cores, but these peak roughly midway between the radio continuum components and show an extent roughly equal to the nuclear separation. These objects—NGC 6090 and NGC 6240, plus also Arp 220 based on the work of Scoville, Yun, & Bryant (1996)—provide the first observational demonstration that the gas nuclei merge prior to the stellar nuclei. This behavior is not previously seen in gasdynamical simulations of gas-rich mergers and will provide constraints for future merger simulations. Additionally, the lack of a morphological correlation between the radio/IR components and the CO in the three double nucleus mergers mentioned above implies that the activity is not tapping the entire reservoir of gas. This suggests that the luminosity of these objects can increase further as the merger progresses.

Two crucial parameters for constraining starburst models for luminous IR galaxies are the total nuclear mass (stars and gas) and the molecular gas mass. The CO emission, unaffected by dust extinction, provides a reliable dynamical estimate of the total nuclear mass. I have found that the standard Galactic conversion factor from CO luminosity to molecular gas mass is overestimating the gas mass in Mrk 231 by at least a factor of 3.6 and in NGC 6240 by at least a factor of 1.5. The strong overestimate in Mrk 231 is most likely explained by the high temperature of the molecular gas: the brightness temperature of the CO $1 \rightarrow 0$ emission is at least 34 K and probably as high as 80 K. If the filling factor is less than unity, the excitation

temperature must be even higher. This exceptionally warm molecular gas in Mrk 231 constitutes the majority of the total nuclear mass within a radius of 440 pc. The molecular gas appears to constitute the majority of the total nuclear mass in all the other mergers studied as well, even if the gas mass conversion factor is several times less than the standard Galactic value.

The extreme CO surface brightnesses observed in the objects with the most compact gas cores—Mrk 231, NGC 6240, and NGC 2623—imply large mean optical depths even at near-IR wavelengths. The mean visual extinction must be $\gtrsim$20–50 magnitudes in these objects and likely is substantially higher. Extreme caution is therefore required when interpreting optical and near-IR observations of compact LIRGs, since the unknown extinction geometry can play a dominant role in their appearance at those wavelengths. Because the nuclei of Mrk 231, NGC 6240, and NGC 2623 can be seen at near-IR wavelengths despite these extreme mean extinctions, the gas cannot be uniformly distributed; instead, it may form thin (30–40 pc), dense (10^4 cm^{-3}) molecular disks of $\sim$400 pc radius.

Combining the data presented in this work with earlier CO data in IR-bright galaxies has confirmed the suggestion by Scoville et al. (1991) that the IR-to-CO luminosity ratio increases with the CO surface brightness. If starbursts provide the dominant sources of luminosity, the higher $L_{\rm IR}/L_{\rm CO}$ ratios at higher CO surface brightnesses can be interpreted as due to an increased efficiency of star formation at higher gas surface densities. On the other hand, if AGNs dominate the luminosities, this empirical correlation suggests that higher accretion rates result from higher

gas surface densities in the nuclear gas disk. Whatever the nature of the luminosity source, the high concentrations of molecular gas appear to be intimately related to its strength.

The HCN observations reveal that the gas properties vary significantly from object to object, even in this small sample of five luminous mergers. The CO/HCN intensity ratio varies by nearly an order of magnitude, requiring strong variations in the mean density of the gas or in the fraction of the gas which is at higher densities. The lowest CO/HCN ratios are associated with the objects that contain the most prominent broad-line AGN. This is inconsistent with the suggestion of Solomon et al. (1992), who interpreted HCN as a tracer of star-forming gas in galactic nuclei.

In Mrk 231, the two molecular line ratios currently known are hard to reconcile when interpreted separately: the mean CO 2→1/CO 1→0 temperature ratio is only 0.7, which, given the very high brightness temperature of the emission, suggests sub-thermal excitation at densities no higher than $\sim 10^3$ cm^{-3} (Aalto 1996); yet the CO 1→0/HCN 1→0 ratio is among the lowest ever seen in extragalactic objects, naively suggesting a large fraction of dense gas ($\gtrsim 10^4$ cm^{-3}). To reconcile these line ratios and provide quantitative density determinations in Mrk 231 and other luminous galaxies requires further multi-species, multi-transition molecular line observations (see §5.2.1).

Nuclear starbursts remain a viable option for powering the activity in most luminous mergers, but are likely to be substantially aged—over 10^8 yr—in most of the objects studied. Measurements of the 3 mm continuum, obtained simultaneously with

the HCN observations, allow upper limits to be placed on the thermal free-free emission. For the free-free emission to be produced by H II regions around ionizing stars, constant-rate starbursts (e.g., Scoville & Soifer 1991) in four systems—NGC 2623, NGC 6090, NGC 6240, and NGC 7469—are required either to be over 10^8 yr old or to be several 10^7 yr old and have IMFs truncated at masses over 30–40 $M_\odot$.

Also, the results of this work support a crucial prediction of CHYT's hypothesis that virtually all luminous IR galaxies are powered by star formation. CHYT argue that those luminous IR galaxies that exhibit non-thermal radio source sizes smaller than their minimum far-IR blackbody sizes are not necessarily powered by AGNS. They point out that starbursts can actually explain these objects, which they therefore call "compact starbursts." This hypothesis requires that the dust be optically thick at wavelengths as long as $\sim$25 μm. The CO observations reported here support this prediction for those objects with the most compact CO distributions, and thus, while not ruling out AGNs as the dominant luminosity source, provide a crucial piece of evidence in favor of CHYT's "compact starburst" hypothesis.

There is one luminous IR galaxy, however, that is unlikely to be dominated by a starburst; it is the unusual Seyfert 1 Mrk 231—the most luminous object in the local universe. The starburst model of Scoville & Soifer (1991) suggests that the stellar mass of a starburst that can account for the bulk of the 3.5×10^{12} $L_\odot$ of Mrk 231 will be larger than the observational limit on the dynamical mass minus the minimum gas mass unless the starburst is younger than a few 10^7 yr and has an exceptionally top-heavy IMF. This result is consistent with the suggestion by CHYT that Mrk 231 is

the only one of the forty most luminous galaxies in the IRAS Bright Galaxy Sample that is dominated by a compact AGN—a suggestion based upon the strength and strong yearly variability of Mrk 231's non-thermal radio continuum.

5.2. Ideas for future work on luminous infrared galaxies

In order to resolve the controversy of the luminosity source of luminous IR galaxies, a useful set of objects to concentrate on are those identified by CHYT as having radio source sizes smaller than their minimum far-IR blackbody size (hereafter called "CHYT objects"). While CHYT claim that 13 of the 14 such objects they studied can be explained by powerful, optically thick, compact starbursts, AGN-dominance is not ruled out. In fact, CHYT admit that one ultraluminous system—Mrk 231—is probably AGN-dominated: its highly-variable radio source implies a source size of only $\sim$1 pc. Non-CHYT LIRGs show more extended radio emission (and hence, via the empirical radio-FIR correlation, similarly extended far-IR radiation is implied), so the CHYT LIRGs are those most likely to be AGN dominated. Studies such as those outlined below can be used to learn about the nature of any sample of LIRGs, but are likely to provide the most profound results when applied to CHYT LIRGs.

5.2.1. Molecular gas and dust

Given the highly compact sizes of the molecular gas distributions around most LIRGs (see Chapters 2 and 3), improving the spatial resolution of the observations is crucial to improving our understanding of the condition and properties of the molecular gas. In the immediate future, the best prospects for this lie in aperture synthesis

mapping of the CO 2→1 transition, with which sub-arcsecond resolution is currently obtainable. Such observations have already been performed for Mrk 231 (Chapter 2) and Arp 220 (Scoville et al. 1996), and we are currently reducing similar observations for several other LIRGs. With the improved resolution, the size, structure, and kinematics of the molecular gas distributions can all be more accurately determined. Furthermore, in the most compact objects—such as Mrk 231 (Chapter 2)—important lower limits can be placed on the excitation temperature of CO, providing crucial constraints for gas cloud models. The higher angular resolution obtainable with CO 2→1 observations also greatly increases the distance to which compact molecular gas cores are resolvable, thus significantly increasing the number of LIRGs whose molecular gas can be studied in detail. Eventually these observations, plus further CO 1→0 observations of more nearby LIRGs, will provide a statistically-significant sample with which to test the suggestion of a morphological CO sequence presented in Chapter 3.

Another important direction for future work is to obtain multi-transition measurements of several molecular species. Only when a wide variety of line ratios are available will it be feasible to produce quantitative radiative transfer models of the state of the molecular gas (e.g., Aalto et al. 1994; Aalto et al. 1995). With such models, the mass of molecular gas can be reliably estimated without reliance upon the conversion factor for Galactic GMCs. Geometrical and dynamical constraints on the gas mass, such as those for Mrk 231 and NGC 6240 explained in Chapters 2 and 3, can then be used as a reality check on the molecular gas models. As explained in

Chapter 1, knowledge of the mass of molecular gas is a crucial constraint for starburst models that account for the luminosity. Detailed gas cloud models will also shed light on the feedback between the energetics of the luminosity source and the interstellar medium. This should lead to better understanding of the nature and evolution of the luminosity source.

5.2.2. Extinction models

A primary difficulty in understanding the nature and evolution of the energy source(s) in LIRGs has been penetrating the thick shroud of dust surrounding the central engines. Only observations at wavelengths between cm-wave and the far-infrared can directly probe the core. At near- and mid-infrared wavelengths, we obtain a partial view of the core, but the mean extinction is still so large (e.g., Chapter 3; Goldader et al. 1995) that the factor by which emission is reduced is extremely sensitive to the relative geometry of the emission-region and the absorbing dust (e.g., Witt, Thronson, & Capuano 1992). This geometry has been virtually unconstrained by observations to date. If future observations can place constraints on the extinction factors for near- and mid-IR emission features, a great deal more quantitative information will be available for modeling the nature of LIRGs: a wealth of diagnostic spectral lines are available at these wavelengths and the imaging technology has been rapidly improving.

In fact, due to the improved sensitivity of mm-wave receivers and infrared detector arrays, it is rapidly becoming practical to directly map the effects of extinction on emission from the ionized gas in LIRGs. The thermal continuum at millimeter

wavelengths is essentially unaffected by optical depth affects. It therefore traces the entire content of ionized gas, and its strength should be proportional to the rate of production of ionizing photons. In the absence of extinction, the integrated flux of near-IR and optical recombination lines should also be proportional to the rate of production of ionizing photons, and thus to the thermal radio continuum. By measuring the actual ratio of the recombination lines to the free-free mm-wave continuum and comparing it to the ratio predicted by case B recombination, the extinction factor can be directly measured. With high-resolution maps of Brγ (and other optical/IR recombination lines) and similar resolution maps of the free-free radio continuum, the extinction distribution can be directly constrained. Interpretations of the near-IR spectra and maps will thus be greatly strengthened. The results of such observations on CHYT objects will also provide a direct test of CHYT's compact starburst hypothesis, which predicts exceptionally large optical depths at near-IR wavelengths.

Whatever the answers to the questions concerning the nature and evolution of the luminosity source of luminous merging galaxies, they are likely to have a profound impact on our understanding of the creation and evolution of normal galaxies. The coming years promise to be an exciting time; I am eagerly looking forward to them.

References

Aalto, S. 1996, private communication

Aalto, S., Booth, R. S., Black, J. H., & Johansson, L. E. B. 1995, A&A, 300, 369

Aalto, S., Booth, R. S., Black, J. H., Koribalski, B., & Wielebinski, R. 1994, A&A, 286, 365

Condon, J. J., Huang, Z. P., Yin, Q. F., & Thuan, T. X. 1991, ApJ, 378, 65 (CHYT)

Goldader, J. D., Joseph, R. D., Doyon, R., & Sanders, D. B. 1995, ApJ, 444, 97

Joseph, R. D. & Wright, G. S. 1985, MNRAS, 214, 87

Leech, K. J., Rowan-Robinson, M., Lawrence, A., & Hughes, J. D. 1993, MNRAS, 267, 253

Lonsdale, C. J., Smith, H. E., & Lonsdale, C. J. 1995, ApJ, 438, 632

Radford, S. J. E. et al. 1991, in Dynamics of Galaxies and Their Molecular Cloud Distributions, eds. F. Combes & F. Casoli (Dordrecht: Kluwer Academic) p. 303

Sanders, D. B., Soifer, B. T., Elias, J. H., Madore, B. F., Matthews, K., Neugebauer, G., & Scoville, N. Z. 1988, ApJ, 325, 74

Sanders, D. B., Scoville, N. Z., & Soifer, B. T. 1991, ApJ, 370, 158

Sargent, A. I. & Scoville, N. Z. 1991, ApJ, 366, L1

Scoville, N. Z., Sargent, A. I., Sanders, D. B., & Soifer, B. T. 1991, ApJ, 366, L5

Scoville, N. Z. & Soifer, B. T. 1991, in Massive Stars in Starbursts, eds. C. Leitherer, N. R. Walborn, T. M. Heckman, & C. A. Norman (Cambridge: Cambridge Univ. Press) p. 233

Scoville, N. Z., Yun, M. S., & Bryant, P. M. 1996, ApJ, submitted

Solomon, P. M., Downes, D., & Radford, S. J. E. 1992, ApJ, 387, L55

Witt, A. N., Thronson, H. A., & Capuano, J. M. 1992, ApJ, 393, 611

Appendix A

Estimating Molecular Gas Mass from CO Luminosity

In this Appendix, we present in detail an analysis of how the molecular gas mass to CO luminosity conversion factor, M_g/L'_{CO}, depends upon assumptions of the physical properties and geometrical configuration of the gas. We begin in §A.1 by discussing the assumption of optically thin emission, which provides a lower limit to the amount of CO. Optically thick emission is discussed in §A.2. In this case, the assumed geometry of the gas can significantly affect the conversion factor; several cases are looked at in detail. The estimation of the dynamical mass is discussed in §A.3. This estimate provides an upper limit to the amount of molecular gas. Finally, a summary of the results of the analysis is provided in §A.4.

A.1. Optically thin emission

A firm lower limit on the amount of CO present can be derived by assuming that the CO $J = 1 \rightarrow 0$ emission is optically thin at all velocities. In this case, the detected specific intensity will be (e.g., Linke et al. 1977; Goldsmith et al. 1992)

$$I_\nu = \tau_\nu [B_\nu(T_x) - B_\nu(T_{bg})] \ , \tag{A-1}$$

where $B_\nu(T)$ is the Planck function at temperature T, T_x is the excitation temperature of the transition, T_{bg} is the cosmic background blackbody temperature, 2.73 K (e.g., Mather et al. 1994), and τ_ν is the optical depth of the transition. Equation A–1 holds both for single dish measurements, where the cosmic background is directly subtracted from the data by position-switching, and for interferometric measurements, where the uniform cosmic background is resolved out. Converting to brightness temperature and integrating over velocity and area leads to the relation:

$$\frac{M_g}{L'_{CO}} = \frac{8\pi k \mu m_{H_2}}{hc^3} \frac{\nu_{ul}^2}{A_{ul}} X_{CO}^{-1} \xi_{ul} \ , \tag{A-2a}$$

where μm_{H_2} is the mean mass per H_2 molecule, ν_{ul} is the frequency of the transition, A_{ul} is the spontaneous emission rate of the transition, X_{CO} is the relative abundance of CO to H_2 molecules, and

$$\xi_{ul} = f_u^{-1} \left(1 - \frac{e^{h\nu/kT_x} - 1}{e^{h\nu/kT_{bg}} - 1} \right)^{-1} \ , \tag{A-2b}$$

where f_u is the fraction of CO molecules in the upper ($J = 1$) state. Note that equation A–2a can be applied to any molecular line by substituting the appropriate

abundance and the appropriate molecular constants. For CO 1→0, equation A–2a evaluates to

$$\frac{M_{\rm g}}{L'_{\rm CO}} = 0.079 \left(\frac{X_{\rm CO}}{10^{-4}}\right)^{-1} \xi_{\rm ul} \quad {\rm M}_\odot \ ({\rm K\ km\ s^{-1}\ pc^2})^{-1} \ . \tag{A–3}$$

In this case, the conversion factor depends upon both the CO abundance and the excitation of the gas. We can place limits on the excitation term, $\xi_{\rm ul}$, even with no detailed knowledge of the conditions. For non-LTE excitation, $\xi_{\rm ul}$ can drop as low as $4/3 \approx 1.333$ (unless level populations are inverted); however, this requires that the $J = 1$ level be fully populated while all $J > 1$ levels are empty—an unrealistic situation. A more realistic lower limit is obtained by assuming LTE level populations. For this case, $\xi_{\rm ul}$ reaches a minimum of 2.546 at $T_{\rm x} = 8.35$ K. The lower limit to the conversion factor is therefore

$$\frac{M_{\rm g}}{L'_{\rm CO}} > 0.20 \left(\frac{X_{\rm CO}}{10^{-4}}\right)^{-1} \quad {\rm M}_\odot \ ({\rm K\ km\ s^{-1}\ pc^2})^{-1} \ . \tag{A–4}$$

Further refinement of this lower limit is possible if constraints can be placed on the excitation or abundance. For instance, the excitation can be partially constrained using the observed brightness temperature, which provides a lower limit to $T_{\rm x}$.

We now check the lower limit in equation A–4 for consistency with the original assumption that the gas is optically thin. The optical depth is the integral of the absorption coefficient along the line of sight, and for a gaussian profile, the optical depth of CO $(1 \rightarrow 0)$ at line center is

$$\tau_0 = 2.08 \left(\frac{N_{\rm H_2}}{10^{20}\ {\rm cm^{-2}}}\right) \left(\frac{\sigma_v}{1\ {\rm km\ s^{-1}}}\right)^{-1} \left(\frac{X_{\rm CO}}{10^{-4}}\right) \psi_{\rm ul} \ , \tag{A–5}$$

where N_{H_2} is the column density of H_2 molecules, σ_v is the gaussian velocity dispersion, and $\psi_{ul} \equiv f_u\ (e^{h\nu/kT_x} - 1)$ varies roughly like T_x^{-2}. (ψ_{ul} = 1.85, 0.321, 0.0171, and 0.00442 for T_x = 2.73, 10, 50, and 100 K, respectively, for LTE populations.) Now, for a given total gas mass, source radius, and total line width, the optical depth is minimized by spreading the gas uniformly throughout a spherical region. Using the lower limit on M_g given in equation A–4, the minimum possible optical depth at line center is

$$\tau_{min} = 0.46\ T_b\ \psi_{ul}\ , \qquad \text{(A–6)}$$

where T_b is the intrinsic brightness temperature of the emission. If τ_{min} exceeds unity, then it is impossible for the CO to be optically thin, and the actual conversion factor will significantly exceed the lower limit in equation A–4.

A.2. Optically thick emission

For optically thick emission, it is not immediately obvious that the CO line luminosity should trace the total amount of material; however, use of the virial theorem enables the observed size and line-width to be related to the total amount of gravitating mass. Most analyses in the literature have only considered gravitational forces in virial analyses, but pressure and magnetic forces may also be significant in real molecular clouds in galactic nucleus environments. Below we examine how inclusion of these non-gravitational forces affects the virial relation.

A.2.1. Virial theorem

The virial theorem for a cloud in equilibrium can be expressed as (see Spitzer 1978, ch. 10)

$$-W \;=\; 2T \;+\; 3\Pi \;+\; \mathcal{M} \;+\; \int_{\mathcal{S}} \tfrac{1}{4\pi}(\vec{r}\cdot\vec{B})(\vec{B}\cdot d\vec{S}) \;-\; \int_{\mathcal{S}} (p^2 + \tfrac{B^2}{8\pi})(\vec{r}\cdot d\vec{S})\;, \quad \text{(A–7a)}$$

where

$$-W = \int_{\mathcal{V}} \rho\vec{r}\cdot\vec{\nabla}\phi\, dV, \quad T = \int_{\mathcal{V}} \tfrac{1}{2}\rho v^2\, dV,$$

$$\Pi = \int_{\mathcal{V}} p\, dV, \quad \text{and} \quad \mathcal{M} = \int_{\mathcal{V}} \frac{B^2}{8\pi}\, dV\;. \qquad \text{(A–7b)}$$

In this equation, $\mathcal{S}$ is the surface of volume $\mathcal{V}$, $\vec{r}$ is the position vector, ρ is the gas density, ϕ is the gravitational potential, v is the bulk velocity, p is the thermal gas pressure, and $\vec{B}$ is the magnetic field vector.

To approximate a molecular cloud, we consider a spherical, "turbulent" cloud of radius R containing gas and stars. For the computational surface $\mathcal{S}$, we take a spherical surface immediately outside the radius of the cloud. We assume that mass external to the cloud has little effect on the gravitational term (i.e., we neglect tidal shear since the cloud would then be unstable). Thus $-W = \alpha_1 G M_{\rm dyn} M_{\rm g}/R$, where $M_{\rm dyn}$ is the total mass contained in the cloud, $M_{\rm g}$ is the gas mass, and α_1 is a constant of order unity ($\alpha_1 = (3-\gamma)/(5-2\gamma)$ for $\rho \propto r^{-\gamma}$). The quantity $2T + 3\Pi$ integrated over the volume of the clump, $\mathcal{V}_{\rm c}$, can be rewritten as $\int_{\mathcal{V}_{\rm c}} (v^2 + \frac{3p}{\rho})\, dM$, which is simply the intrinsic, three-dimensional velocity dispersion of the cloud gas averaged over the entire cloud, $< v_{\rm 3d}^2 >$, multiplied by the gas mass. For simplicity, we assume that the

magnetic field, B, is uniform throughout the volume of the cloud. The expression of virial equilibrium then reduces to

$$\alpha_1 \frac{GM_{\rm dyn}}{R} = < v_{\rm 3d}^2 > - \left(\frac{3p_{\rm e}}{\rho_{\rm g}} - \frac{B^2 - B_{\rm e}^2}{8\pi\rho_{\rm g}} \right) , \qquad \text{(A–8)}$$

where $\rho_{\rm g}$ is the mean gas density of the cloud, $p_{\rm e}$ is the external gas pressure at the surface of the cloud, and $B_{\rm e}$ is the magnetic field immediately outside the cloud.

In order to make this expression relevant to observations of molecular clouds, we need to relate the intrinsic velocity dispersion of the gas to an observed line width. Shu & Lizano (1987) argue that the turbulent gas velocities in molecular clouds are sub-alfvenic, and that due to photon trapping in the ^{12}CO line, observations select the highest velocities, $v \sim v_{\rm A} = B^2/4\pi\rho_{\rm g}$. The observed FWHM will then be slightly less than twice the alfven velocity; to parameterize this, $\delta v^2 = \alpha_2 v_{\rm A}^2$. If we further assume that the amount of mass possessing (three-dimensional) velocities in a given velocity interval decreases linearly with velocity up to $v_{\rm A}$, then $< v_{\rm 3d}^2 >= v_{\rm A}^2/\alpha_3$, with $\alpha_3 = 2$. (For a mass per velocity interval ranging from constant to decreasing as the square of velocity, α_3 varies from 5/3 to 3.) Now, we can group the $< v_{\rm 3d}^2 >$ and $B^2/8\pi\rho_{\rm g}$ terms of equation A–8 together on the left-hand side, leaving the expression

$$\frac{\delta v^2}{\alpha_2\alpha_3} \left(1 + \frac{\alpha_3}{2} \right) = \alpha_1 \frac{GM_{\rm dyn}}{R} + \frac{3p_{\rm e}}{\rho_{\rm g}} + \frac{B_{\rm e}^2}{8\pi\rho_{\rm g}} . \qquad \text{(A–9)}$$

The terms on the left-hand side—kinetic and magnetic pressure—represent the support of the cloud against the terms on the right-hand side—gravity, external thermal pressure, and external magnetic pressure.

The observed line width can now be expressed as

$$\delta v^2 \;=\; \alpha\,\frac{GM_{\rm dyn}}{R} \;+\; \frac{\alpha}{\alpha_1}\frac{\Pi_{\rm e}}{\rho_{\rm g}}\,, \qquad \text{(A–10)}$$

where $\alpha = \alpha_1\alpha_2\alpha_3/(1+\frac{1}{2}\alpha_3)$ and $\Pi_{\rm e} = 3p_{\rm e} + B_{\rm e}^2/8\pi$. Rewriting (A10),

$$\delta v^2 \;=\; \alpha\frac{GM_{\rm dyn}}{R}\,(1+q)\,, \qquad \text{(A–11)}$$

where $q \equiv (4f/3\pi\alpha_1 G)(\Pi_{\rm e}/\Sigma_{\rm g}^2)$ is the factor that corrects gravitational virial equilibrium for non-gravitational forces; $f = M_{\rm g}/M_{\rm dyn}$ is the gas mass fraction of the cloud, and $\Sigma_{\rm g} = (4/3)\rho_{\rm g}R$ is the gas surface density of the cloud. Rewriting the expression for the pressure-confinement term is convenient units:

$$q \;=\; 0.0201\,\frac{f}{\alpha_1}\,\frac{\Pi_{\rm e}/k\ [{\rm cm^{-3}\,K}]}{\Sigma_{\rm g}^2\ [{\rm M_\odot\,pc^{-2}}]}\,. \qquad \text{(A–12)}$$

The relationship between the size, line width, and cloud mass expressed in equation A–11 enables the determination of relations between $L'_{\rm CO}$ and $M_{\rm g}$ for optically thick gas.

A.2.2. Clumpy gas distribution

We first examine the case where the optically-thick molecular gas exists in discrete clouds, as in our Galaxy, rather than as a smoothly distributed medium. A useful discussion of this case applied to observations of other galaxies is given in Dickman, Snell, & Schloerb (1986; hereafter DSS); however, they do not discuss the effects of non-gravitational forces, which can significantly alter the $M_{\rm g}/L'_{\rm CO}$ conversion factor in certain environments. For observations of other galaxies, many molecular clouds will be averaged together in a single beam. If we assume that the clouds do not

shadow each other, then the CO luminosity can be calculated by simply summing over all $\mathcal{N}$ clouds in the beam, so that in general (DSS),

$$\frac{M_{\rm g}}{L'_{\rm CO}} = \left(\frac{4\mu m_{\rm H_2}}{3}\right) \frac{\sum_{i=1}^{\mathcal{N}} \bar{n}_i r_i^3}{\sum_{i=1}^{\mathcal{N}} \bar{T}_{{\rm b},i} \delta v_i r_i^2} , \tag{A–13}$$

where $\bar{n}_i$, $\bar{T}_{{\rm b},i}$, δv_i, and r_i are the mean density, mean peak brightness temperature, FWHM line width, and radius, respectively, of the ith cloud. We now can use the virial theorem, as given in equation A–11, to express the δv_i in terms of $M_{{\rm dyn},i} = M_{{\rm g},i} f_i^{-1}$, r_i, and q_i. $M_{{\rm g},i}$ can then be expressed in terms of n_i and r_i, leading eventually to a general expression for the conversion factor for clouds in virial equilibrium:

$$\frac{M_{\rm g}}{L'_{\rm CO}} = \left(\frac{4\mu m_{\rm H_2}}{3\pi\alpha G}\right)^{1/2} \frac{\sum_{i=1}^{\mathcal{N}} \bar{n}_i r_i^3}{\sum_{i=1}^{\mathcal{N}} \bar{T}_{{\rm b},i} \bar{n}_i^{1/2} r_i^3 f_i^{-1/2} (1+q_i)^{1/2}} . \tag{A–14}$$

In order to simplify this relation, we must make further assumptions. A common assumption in the literature, supported by observations of Galactic clouds, is that the mean brightness temperature of each cloud is roughly the same: $\bar{T}_{{\rm b},i} \approx \bar{T}_{{\rm b},0}$. In our more general analysis, we make the further assumptions that the gas mass fraction and the pressure term are roughly constant for all clouds: $f_i \approx f$, $q_i \approx q$. Both of these assumptions are consistent with observations of Galactic clouds (e.g., Solomon et al. 1987), which appear to be in gravitational virial equilibrium with a constant molecular gas mass fraction of unity, and which appear to have nearly constant surface density; since both f and Σ are constant, q should also be constant

as long as the confining pressure Π_e defined above does not vary from cloud to cloud. The conversion factor now becomes

$$\frac{M_g}{L'_{CO}} = \left(\frac{4\mu m_{H_2}}{3\pi\alpha G}\right)^{1/2} \left(\frac{f}{1+q}\right)^{1/2} \frac{1}{\bar{T}_{b,0}} \frac{\sum_{i=1}^{\mathcal{N}} \bar{n}_i r_i^3}{\sum_{i=1}^{\mathcal{N}} \bar{n}_i^{1/2} r_i^3} . \quad \text{(A–15)}$$

If we assume a power law for the variation of mean cloud density with cloud size, $\bar{n} = \bar{n}_0 (r/R_{max})^{-\gamma}$, and a power law distribution of clouds with size, $P(r) \propto r^{-\delta}$, over a size range R_{min} to R_{max}, the quotient of summations in equation A–15 simplifies to $\bar{n}_{eff}^{1/2} = A\bar{n}_0^{1/2}$, with the constant A given by $A = [(4-\delta-\gamma/2)/(4-\delta-\gamma)]\ [(1-\epsilon^{4-\delta-\gamma})/(1-\epsilon^{4-\delta-\gamma/2})]$, where $\epsilon \equiv R_{min}/R_{max}$. The conversion factor now reduces to

$$\frac{M_g}{L'_{CO}} = \left(\frac{4\mu m_{H_2}}{3\pi\alpha G}\right)^{1/2} \frac{\bar{n}_{eff}^{1/2}}{\bar{T}_{b,0}} f^{1/2}(1+q)^{-1/2} , \quad \text{(A–16)}$$

where $\bar{n}_{eff}$ acts as an effective mean density of the gas averaged over the entire cloud population. Equation A–16 is similar to the traditional gravitational virial equilibrium expression for the conversion factor (e.g., DSS; Solomon et al. 1987), except for the additional factors f and q, which respectively account for the possibilities that the gas mass fraction of a cloud may be less than one or that the clouds may be pressure-confined.

The conversion factor can be rewritten in observational units as

$$\frac{M_g}{L'_{CO}} = \frac{2.57}{\alpha^{1/2}} \frac{\bar{n}_{eff}^{1/2}}{\bar{T}_{b,0}} f^{1/2}(1+q)^{-1/2} \quad M_\odot\ (\mathrm{K\ km\ s^{-1}\ pc^2})^{-1} , \quad \text{(A–17)}$$

where we have used $\mu = 1.36$. Equation A–17 agrees well with the empirically determined value for the conversion factor in the Galactic disk, 4.9 $M_\odot$ (K km s^{-1} pc^2)$^{-1}$ (Solomon & Barrett 1991), if we take $f = 1$ and $q \ll 1$. To estimate α, we use

$\alpha_1 = 1.0$, $\alpha_2 = 1.5$, and $\alpha_3 = 2.0$, giving $\alpha = 1.5$ (§A.2.1). (Using a range of likely values for these parameters yield values for α from 0.55 to 2.4.) Observations of Galactic clouds serve to constrain other parameters: $\bar{n}_0 \approx 50$ cm^{-3}, $\gamma \approx 1$ (Solomon et al. 1987), $\delta \approx 2.3$, and $\epsilon < 0.1$ (Sanders et al. 1985), implying that $A \approx 1.5$–1.7, and hence that $\bar{n}_{\rm eff} \approx 130$ cm^{-3}. Substituting these numbers, plus $\bar{T}_{\rm b,0} = 6$ K (DSS), into equation A–17 results in $M_{\rm g}/L'_{\rm CO} \approx 4.0$ M$_\odot$ (K km s^{-1} pc^2)$^{-1}$, about four-fifths of the empirical value. The difference is likely explained by uncertainties in the estimation of the parameter α.

The gravitational virial mass often used in the literature on molecular clouds, $M_{\rm VT} \equiv R\delta v^2/(\alpha G) = M_{\rm dyn}(1+q)$, can be very different from $M_{\rm dyn}$ if q is larger than one. Then, non-gravitational effects will dominate the dynamics of the cloud, and hence increase the velocity width of the emission line. In this case, the gravitational virial equilibrium analysis produces a significant overestimate of the cloud mass. This is not the situation for Galactic molecular clouds, however. For Galactic disk clouds, $M_{\rm VT}$ agree well with masses derived by independent methods, implying that both $f \approx 1$ and $q \ll 1$ (Solomon & Barrett 1991). Solomon et al. (1987) use the empirical size-line-width relation to derive a constant surface density, $\Sigma_{\rm g} \approx 170$ M$_\odot$ pc^{-2}, for Galactic disk molecular clouds. Using this value of $\Sigma_{\rm g}$ and a representative Galactic disk interstellar medium pressure of $p_{\rm e} = 4000$ cm^{-3} K (Jenkins, Jura, & Loewenstein 1983) in equation A–12, neglecting magnetic terms (which are comparable and thus will not raise q to an appreciable level), gives $q \approx 0.008$, consistent with the original interpretation that Galactic disk molecular clouds are in gravitational virial

equilibrium. If one were to observe a hypothetical galaxy with similar $\bar{n}_0$ and $\bar{T}_{b,0}$ for its molecular clouds, but with a much lower gas mass fraction per cloud or, more probable, a much higher confining pressure, the CO mass conversion factor would be significantly decreased. If ignored, high external pressures or small gas mass fractions can therefore lead to significant overestimates of the molecular gas mass corresponding to a given CO luminosity.

A.2.3. Smooth gas distribution—spherical configuration

Downes et al. (1993) suggest that the molecular gas in the nucleus of Arp 220 may consist of a single huge molecular cloud. The expression for the conversion factor for a spherical cloud of smoothly-distributed gas is the same as that for a single clump in the clumpy distribution discussed above. Setting $\mathcal{N} = 1$ in equation A–13 for clouds in virial equilibrium leads to

$$\frac{M_g}{L'_{CO}} = \left(\frac{4\mu m_{H_2}}{3\pi\alpha G}\right)^{1/2} \frac{\bar{n}^{1/2}}{T_b} f^{1/2} (1+q)^{-1/2} , \qquad \text{(A–18)}$$

which is of exactly the same form as the expression for the conversion factor for the clumpy gas case in equation A–16, with $\bar{n}_{eff}^{1/2}$ replaced by $\bar{n}^{1/2}$, the square root of the mean density of the cloud, and $\bar{T}_{b,0}$ replaced by T_b, the mean peak brightness temperature of the cloud.

For Arp 220, the standard conversion factor gives $\Sigma_g > 2 \times 10^4$ $M_\odot$ pc^{-2} (Scoville et al. 1991). From equation A–12, $q > 1$ only for $\Pi_e/k > 2\times10^{10}$ cm^{-3} K. This requires thermal pressures of nearly 10^{10} cm^{-3} K or magnetic fields of nearly 10 mG throughout a region several hundred kiloparsecs in radius. For Arp 220 and other luminous

galaxies with dense nuclear concentrations of molecular gas which lack evidence for such extreme pressure, neglecting q in the derivation of M_g is self-consistent. Downes et al. (1993) point out, however, that f may be significantly less than one for their proposed single molecular cloud several hundred parsecs in radius, as such a cloud would likely encompass a large mass of stellar and other CO-dark matter. If this material contributes more to the gravitating mass of the cloud than the molecular gas itself, the gas mass will be overestimated by use of the Galactic conversion factor (ignoring possible differences in $\bar{n}$ and T_b from Galactic clouds).

A.2.4. Smooth gas distribution—thin disk configuration

The expression for the M_g/L'_{CO} conversion factor will be somewhat different in the case of optically-thick gas distributed smoothly in a rotating disk than for the smooth spherical case for two reasons: (1) there will be an inclination effect since a more highly-inclined disk will present less surface area to the observer and thus show a lower L'_{CO} for a given M_g than a more face-on disk; (2) the line width that determines the observed L'_{CO} is the local velocity dispersion (not an observable quantity unless the disk is well resolved) and not the observed line width as in the spherical case. Note that if the molecular gas exists in a rotating disk, but is arranged in non-shadowing clumps rather than smoothly distributed, the conversion factor will be given by equation A–16 above.

For gas in a smooth thin disk observed in a single beam, basic geometrical arguments give the following expression for the conversion factor:

$$\frac{M_g}{L'_{CO}} = 4\mu m_{H_2} \frac{\bar{n} H_{1/2}}{T_b \delta v} \sec i, \qquad \text{(A–19)}$$

where i is the angle that the disk axis makes with the line-of-sight, $H_{1/2}$ is the distance from the midplane between which half of the disk gas mass is contained, and $\bar{n}$ is the mean density averaged over this region. If we can relate $H_{1/2}$ and δv to $\bar{n}$, equation A–19 can be simplified further. There are at least three different extreme scenarios for relating the vertical scale height to the local velocity dispersion and mean density (Spitzer 1942): (a) a self-gravitating gas disk; (b) a thin gas disk embedded in a much broader and denser (stellar) disk that has an essentially constant density, ρ_{*0}, over the extent of the gas; (c) a thin gas disk of radius R circling a dominant central point mass, M_c. The first two scenarios are examined further below. Case (c) yields the same form for the conversion factor as case (b), with ρ_{*0} in case (b) replaced by $M_c/4\pi R^3$ in case (c).

A.2.4.1. Self-gravitating thin disk

Spitzer (1942) gives the solution for the distribution of gas density with height in the self-gravitating disk. $H_{1/2}$ for this solution is given by

$$H_{1/2} = \left(\frac{c_1 \sigma_z^2}{12\pi G \mu m_{\mathrm{H}_2} \bar{n}} \right)^{1/2}, \qquad \text{(A–20)}$$

where $c_1 = \tanh^{-1}(0.5) \approx 0.5493$ and σ_z is the vertical velocity dispersion, which is related to the local FWHM line width in a thin disk by $\delta v^2 = \alpha' \sigma_z^2$, where $\alpha' \approx 10$ is a constant that accounts for the conversion from a velocity dispersion to FWHM and for the increase in observed line width due to saturation (here using line center optical depth of 50–100 and a ratio of line-of-sight velocity dispersion to overall local velocity

dispersion of 0.5, following the discussion in DSS). Using this relation between the scale height and the local line width to rewrite $H_{1/2}/\delta v$ in terms of $\bar{n}$:

$$\frac{M_g}{L'_{CO}} = \left(\frac{4c_1\mu m_{H_2}}{3\pi\alpha' G}\right)^{1/2} \frac{\bar{n}^{1/2}}{T_b} \sec i \ . \tag{A-21}$$

In observational units,

$$\frac{M_g}{L'_{CO}} = \frac{1.90}{\alpha'^{1/2}} \frac{\bar{n}^{1/2}}{T_b} \sec i \quad M_\odot \ (\mathrm{K\ km\ s^{-1}\ pc^2})^{-1}. \tag{A-22}$$

The ratio between the conversion factor for a smooth self-gravitating disk and that for Galactic disk clouds (equation A–17 with $f \approx 1$ and $q \ll 1$) is $0.74(\alpha/\alpha')^{1/2} \sec i$. Using likely ranges for the parameters, α/α' can vary roughly from 0.04 to 0.36; hence the ratio of conversion factors can range from $0.15 \sec i$ to $0.44 \sec i$. Therefore, for a smooth, face-on self-gravitating disk, the molecular gas mass conversion factor is somewhat reduced from the Galactic one, assuming similar values of $\bar{n}$ and T_b; however, as such a disk becomes more edge-on to our line-of-sight, the CO luminosity decreases and hence the conversion factor increases. At $i \approx 65$–$80°$, the conversion factor becomes comparable to the Galactic value.

A.2.4.2. Thin gas disk embedded in a thicker, denser stellar disk

Spitzer (1942) also gives the solution for the distribution of gas density with height for a gas disk embedded in a much broader and denser stellar disk, where the stellar mass density can be assumed constant over the extent of the gas. For the stellar mass to dominate the vertical dynamics of the disk requires $\rho_{*0} \gg \rho_0$, where ρ_0 is

the gas mass density at the midplane (otherwise, the gas disk would become partially self-gravitating). In this situation,

$$H_{1/2} = c_2 \left(\frac{\sigma_z^2}{6\pi G \rho_{*0}} \right)^{1/2} , \tag{A-23}$$

where $c_2 \approx 0.4769$. The conversion factor now becomes

$$\frac{M_{\rm g}}{L'_{\rm CO}} = c_2 \left(\frac{16 \mu m_{\rm H_2}}{3\pi\alpha' G} \right)^{1/2} \frac{\bar{n}^{1/2}}{T_{\rm b}} f_\rho^{1/2} \sec i \, , \tag{A-24}$$

where $f_\rho = \rho_0 / \rho_{*0}$. In observational units,

$$\frac{M_{\rm g}}{L'_{\rm CO}} = \frac{2.45}{\alpha'^{1/2}} \frac{\bar{n}^{1/2}}{T_{\rm b}} f_\rho^{1/2} \sec i \quad {\rm M}_\odot \ ({\rm K\ km\ s^{-1}\ pc^2})^{-1}. \tag{A-25}$$

For this case, the ratio between the conversion factor for a face-on disk and that for Galactic clouds is $0.19\text{–}0.57 f_\rho^{1/2}$. Since $f_\rho \ll 1$, a molecular gas disk embedded in a thicker, denser stellar disk will show a much higher line luminosity for a given amount of mass, similar to the case of pressure-confined clouds. In both of these cases, the effective line width is determined by conditions external to the gas and thus the gas mass cannot be determined without additional information (e.g., $\Pi_{\rm e}$, f_ρ).

A.3. Dynamical mass

The total mass in the CO emission region can be estimated dynamically using the observed size and line width of the CO source, and serves as an upper limit to the amount of molecular gas. The derived dynamical mass will depend upon the assumed

configuration of the molecular gas. We consider here the cases for a sphere and a rotating thin disk. Assuming the molecular gas occupies a spherical region, we can use the virial theorem as discussed above. Rearranging equation A–11 yields

$$M_{\rm dyn}({\rm sphere}) = \frac{\delta v^2 R}{\alpha G}\,(1+q)^{-1}\ . \qquad \text{(A–26)}$$

If the molecular gas occupies a rotationally-supported disk, however, slight differences arise, because the rotational speed for a disk relates differently to the observed line width than does the intrinsic velocity dispersion for a sphere. To begin, we assume that the line full-width at zero-intensity, $\delta v_{\rm fwzi}$, represents twice the maximum rotational speed, $v_{\rm rot}$, corrected for inclination effects, and we relate the observed FWHM line width, δv, to $\delta v_{\rm fwzi}$ by defining a line profile parameter $a \equiv \delta v_{\rm fwzi}/\delta v$, leading to $\delta v = (2/a) v_{\rm rot} \sin i$. (We ignore the saturation correction because the source line width is determined by the rotational velocity, not the much smaller local dispersion where saturation may be important.) Next, the rotational velocity can be related to the dynamical mass by centrifugal equilibrium, $v_{\rm rot}^2 = \alpha_{\rm 1,d} G M_{\rm dyn}({\rm disk})/R$. The parameter $\alpha_{\rm 1,d}$ is slightly under unity since the rotational velocity for a disk is generally somewhat higher than that for a sphere of the same mass distribution with radius (see Binney & Tremaine 1986, ch. 2). Solving for the dynamical mass gives

$$M_{\rm dyn}({\rm disk}) = \frac{\delta v^2 R}{\alpha_{\rm d} G}\,\frac{1}{\sin^2 i}\ , \qquad \text{(A–27)}$$

where $\alpha_{\rm d} \equiv (2/a)^2 \alpha_{\rm 1,d}$ is a correction factor of order unity very similar to α for the spherical case. While α ranges from 0.55 to 2.4, with a representative value

of 1.5 (§A.2.2), $\alpha_{\rm d}$ takes on values close to unity. Note that if the peak rotational velocity is reached at a radius less than the observed source size, R, then the actual dynamical mass of the disk will be less than the derived value in equation A–27. The principal difference between the two cases is that, for spherical gas distributions, $M_{\rm dyn}$ cannot be larger than $\delta v^2 R/\alpha G$ and may be significantly smaller, while for disks, the value of $M_{\rm dyn}$ can be much larger than $\delta v^2 R/\alpha_{\rm d} G$ if i is small.

A.4. Summary

Many factors can cause the $M_{\rm g}/L'_{\rm CO}$ conversion factor in other galaxies to depart from the value measured for Galactic disk clouds. It has been long understood that differences in the mean cloud properties $\bar{n}$ and $T_{\rm b}$ can lead to such variations, but we wish to emphasize that differences in the cloud environment and in the geometrical configuration of the gas can lead to even more significant variations. Except for the cloud shadowing and the inclination effect for optically-thick gas distributed smoothly in a disk, ignorance of which cause underestimates of the gas mass, ignorance of these additional factors tend to cause overestimates of the gas mass if the Galactic conversion factor is applied blindly. The properties of the material surrounding the molecular gas and the geometrical configuration of the molecular gas itself thus need to be well understood in order to accurately determine the amount of molecular material from molecular line observations alone. High-resolution millimeter interferometry observations can place lower limits on the gas mass fraction, using the lower limit on

M_g derived by assuming optically thin CO emission and M_{dyn} derived from the CO source size and line width. Such constraints on the molecular gas mass fraction, f, plus constraints on the external pressure, Π_e, allow one to make reasonable estimates of M_g, subject to the traditional uncertainties in $\bar{n}^{1/2}/T_b$.

References

Binney, J. & Tremaine, S. 1986, Galactic Dynamics, (Princeton: Princeton Univ. Press)

Dickman, R. L., Snell, R. L., Schloerb, F. P. 1986, ApJ, 309, 326 (DSS)

Downes, D., Solomon, P. M., & Radford, S. J. E. 1993, ApJ, 414, L13

Goldsmith, P. F., Margulis, M., Snell, R. L., & Fukui, Y. 1992, ApJ, 385, 522

Jenkins, E. B., Jura, M., & Loewenstein, M. 1983, ApJ, 270, 88

Linke, R. A., Goldsmith, P. F., Wannier, P. G., Wilson, R. W., & Penzias, A. A. 1977, ApJ, 214, 50

Mather, J. C. et al. 1994, ApJ, 420, 439

Sanders, D. B., Clemens, D. P., Scoville, N. Z., & Solomon, P. M. 1985, in The Milky Way Galaxy, eds. H. Van Woerden, R. J. Allen, & W. B. Burton (Dordrecht: Kluwer Academic) p. 329

Scoville, N. Z., Sargent, A. I., Sanders, D. B., & Soifer, B. T. 1991, ApJ, 366, L5

Shu, F. H. & Lizano, S. 1987, in Interstellar Matter, eds. J. M. Moran & P. T. P. Ho (New York: Gordon & Breach Science Publishers) p. 65

Solomon, P. M. & Barrett, J. W. 1991, in Dynamics of Galaxies and Their Molecular Cloud Distributions, eds. F. Combes & F. Casoli (Dordrecht: Kluwer Academic) p. 235

Solomon, P. M., Rivolo, A. R., Barrett, J., & Yahil, A. 1987, ApJ, 319, 730

Spitzer, L. 1942, ApJ, 95, 329

Spitzer, L. 1978, Physical Processes in the Interstellar Medium, (New York: John Wiley & Sons)